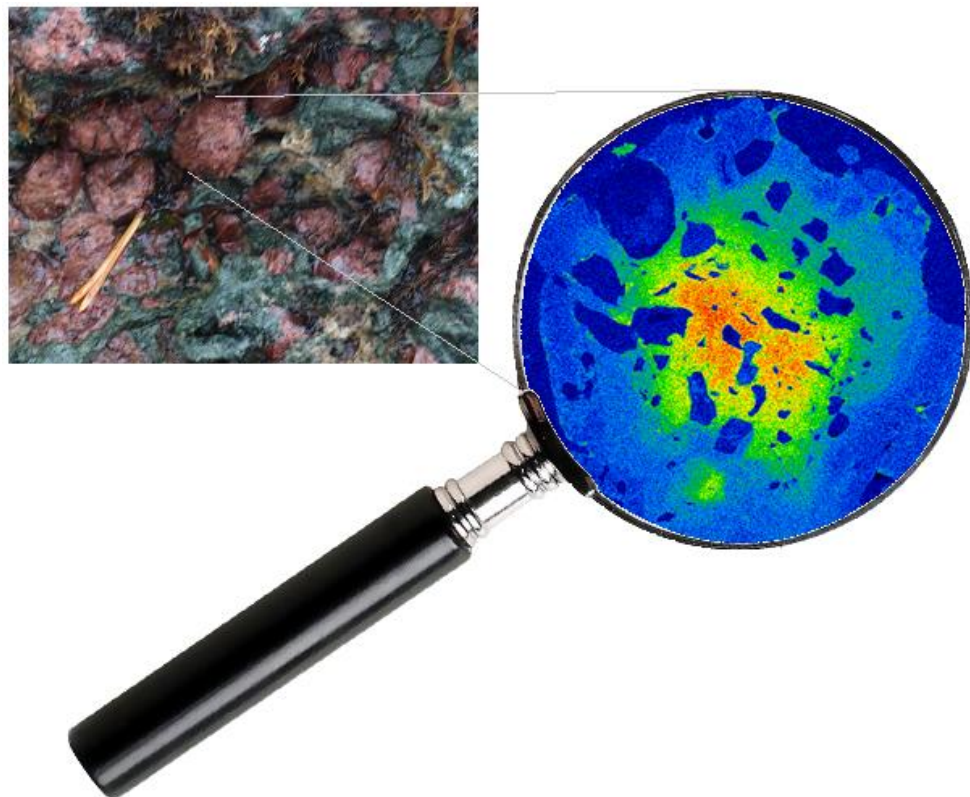


Master Thesis, Department of Geosciences

The Engebøfjellet Eclogite, Sunnfjord

*Petrology and modal analysis of a
world class rutile-ore deposit*

Steinar Kleppe



UNIVERSITY OF OSLO
FACULTY OF MATHEMATICS AND NATURAL SCIENCES

Front page shows a coarse grained eclogite, and a Mn-map of a garnet from coarse grained eclogite. Maginfying glass is found at <http://scarletjames.wordpress.com/2012/03/20/photoshop-background/magnifying-glass-2/>
(Accessed: 16.05.2013)

The Engebøfjellet Eclogite, Sunnfjord

*Petrology and modal analysis of a
world class rutile-ore deposit*

Steinar Kleppe



Master Thesis in Geosciences

Discipline: Geology

Department of Geosciences

Faculty of Mathematics and Natural Sciences

University of Oslo

30.05.2013

© Steinar Kleppe, 2013

This work is published digitally through DUO – Digitale Utgivelser ved UiO

<http://www.duo.uio.no>

It is also catalogued in BIBSYS (<http://www.bibsys.no/english>)

All rights reserved. No part of this publication may be reproduced or transmitted, in any form or by any means, without permission.

Forewords

A small step for geology, a giant leap for me as a geologist. This first sentence summarizes my feelings when I now write the last words in my master thesis. I feel that I have contributed to a deeper understanding of the Engebøfjellet Eclogite, but books will probably not be rewritten. For me, however, things have changed. I know that there are things that I could have done otherwise, or at least better, in the early phases of the data acquisition. When I realized that, it was too late to reproduce and process those data. On countless occasions I felt that a dataset, an observation or an idea could mean something, but I did not know what. This taught me how to put words on geological problems, and further how to find references in scientific databases. If I was to do this, or another, thesis again I now have many more tools in my toolbox. Due to the tools I have discovered during the last year, I can now work more independent and with much more confidence and that is what separates me as a geologist from me as a geology student.

This master thesis was written in the time between August 2012 and June 2013 with excellent supervision from Dr. Muriel Marie Laure Erambert at the Institute of Geosciences, University of Oslo – Thank you very much, Muriel! I feel that I could not have done this without you, your impressive knowledge, your patience and your thorough (sometimes a bit brutal, but I like it) feedback.

I sincerely want to thank Maarten Aerts for spending many hours teaching me how to prepare sample for XRD and XRF as well as interpreting the results with me. Thanks to Salahalldin Akhavan for preparing my thin sections, and to Dani Schmid for good advices on my Matlab issues. A big thank to Are Korneliussen at the Geological Survey of Norway (NGU) for spending a day with me answering my questions and giving me thin sections and reports of his previous work at Engebøfjellet. Thank you, Eugene Gerald Grosch from the University of Bergen, for your help on XMapTools, and for the interesting conversation regarding eclogite petrology and everyday stuff.

I also want to thank my fellow student Øyvind Sunde for good collaboration and company during the five years at this master program. Thanks to you it was a jolly good time!

Last, but not least want to thank my fantastic, rock loving wife, Katarina, who I met outside the geology building in September 2009. You have enthusiastically supported me through the process, and gave birth to our lovely daughter Andrina in February 2013. She lived her four first months with a father not present at all time, but she kept smiling to me every day I got home. Hopefully she will adapt her parents' interests on rocks (Preferably hard rocks)!

To my dear Andrina

(Melody: Bæ, bæ, lille lam)

Bank, bank eklogitt, hva har du til meg?
Jo, jo, geobarn, det skal jeg si deg:
Fin grønn omfasitt, og fin rød pyralspitt.
Og hvit kvarts og glimmer, og masse amfibol

Steinar Kleppe

Abstract

The Engebøfjellet Eclogite is situated in the Western Gneiss Region, and is found in Naustdal, Sunnfjord, Norway. It is typically fine grained, and is dominated by almandine-grossular-pyrope-garnet, omphacite and the sodic-calcic amphiboles barroisite and magnesio-katophorite. In addition minor rutile, quartz and phengitic mica occur in varying amounts. The difference in the bulk rock chemistry affects the mineralogy as well as the mineral chemistry significantly. In general the FeTi-poor eclogite is richer in felsic minerals like quartz and mica, and the minerals are lower in Fe relative to the FeTi-rich. The FeTi-rich eclogite is rich in rutile, and from image processing techniques, the Engebøfjellet eclogite contains up to 5.5 mineable weight percent rutile in addition to up to 50 weight percent garnet.

In this master thesis, the petrology and mineralogy of the eclogite and the veins within is studied using EMP for mineral chemical and petrological purposes, quantitative XRD for bulk rock mineralogy, XRF for bulk rock chemistry, optical microscopy for petrological purposes, and image processing for detection of rutile and garnet. During the thesis field description, mineralogy and petrology of eclogite facies veins are done. Finding the abundance and grain size distribution of rutile by image processing is never been done at Engebøfjellet and is concluded as better for a mining purpose than XRD and XRF. Quantitative bulk rock XRD are done in this thesis as the first time at Engebøfjellet.

From XMapTools and thermobarometric calculations on the mineral assemblage, the Engebøfjellet protolith is known to have undergone prograde metamorphism reaching eclogite facies conditions at 600 (± 100) °C and at least 15 kbar, with garnet crystallization starting in garnet amphibolite facies. During exhumation, at least the core of the eclogite retained its eclogite facies mineralogy well, except locally where fracturing and veining caused amphibolite/greenschist facies alteration. In contact to, or close to amphibolite/greenschist facies veins, the eclogite mineralogy (Omphacite + garnet + primary amphibole + phengite + rutile) is partly to completely altered to secondary amphibole + plagioclase + biotite + ilmenite.

Eclogite facies quartz rich veins of variable size are abundant, and omphacite, mica and rutile are commonly found in these veins. Similar veins are also found in pressure shadows, where eclogite facies minerals have precipitated. Ti is thought to have been dissolved from the eclogite and reprecipitated in the vein due to the sudden drop in pressure within the vein or in pressure shadows.

Lack of measurements on $\text{Fe}^{2+}:\text{Fe}^{3+}$ caused large spans in the temperature calculations. For quantitative XRD better mineral refinements would give more accurate results. Further research should be done on the veins, including structural geology and fluid inclusions.

Contents

1. INTRODUCTION	1
1.1 GENERAL INTRODUCTION	1
1.2 ECLOGITES	1
1.3 ENGEBOFJELLET	2
1.4 RUTILE MINING	3
2. GEOLOGIC BACKGROUND	4
2.1 LITHOLOGY OF THE WGR	4
2.2 TECTONIC EVOLUTION OF THE WGR	5
2.3 THE GEOLOGY OF SUNNFJORD	8
2.4 ENGEBOFJELLET	9
3. METHODS.....	11
3.1 ANALYTICAL METHODS	11
3.1.1 Basic Principles of X-ray methods	11
3.1.2 X-ray diffraction (XRD)	11
3.1.3 X-ray fluorescence (XRF)	12
3.1.4 Electron microprobe (EMP)	13
3.2 OPTICAL MICROSCOPY	14
3.3 PREPARATION OF SAMPLES FOR XRD/XRF	14
3.4 MATLAB	15
4. FIELD WORK.....	17
4.1 SAMPLES	18
4.2 DESCRIPTION OF VEINS AND LAYERS	21
4.2.1 Eclogite facies veins	21
4.2.2 Late fractures and veins	26
5. BULK ROCK ANALYSES.....	27
6. PETROLOGY.....	29
6.1 ECLOGITE FACIES	35
6.2 AMPHIBOLITE TO GREENSCHIST FACIES	38
7. MINERALOGY.....	40
7.1 GARNET	40
7.2 PYROXENE	43
7.3 PRIMARY AMPHIBOLE	47
7.4 SECONDARY AMPHIBOLES	49
7.5 CLINOZOISITE	50
7.6 RUTILE	51
7.7 CARBONATE	52
7.8 QUARTZ	52
7.9 MICA	53
7.10 FELDSPAR	55
7.11 SULFIDES	55
7.12 ZIRCON	56
8. THERMOBAROMETRY.....	57
8.1 PRINCIPLES OF THERMOBAROMETRY	57
8.2 APPLICATIONS OF THE GENERAL THERMODYNAMICS ON NATURAL SYSTEMS	59
8.2.1 Garnet-Clinopyroxene geothermometer	59
8.2.2 Application of Grt-Cpx geothermometers on samples from Engebøfjellet	60
8.2.3 Garnet – Amphibole geothermometer	60
8.2.4 Application of Grt-Amp geothermometers on samples from Engebøfjellet	61
8.2.5 Zirconium-in-rutile geothermometer	62
8.2.6 Application of zirconium-in-rutile-geothermometer on samples from Engebøfjellet	62
8.2.7 Plagioclase-omphacite-quartz geobarometer	62
8.2.8 Application of the Pl-Omp-Qz geobarometer for minimum pressure estimate at Engebøfjellet	63
8.3 SUMMARY ON THERMOBAROMETRY	64
9. XMAPTOOLS.....	64
9.1 INTRODUCTION ON XMAPTOOLS	64
9.2 APPLICATION OF XMAPTOOLS ON A SAMPLE FROM ENGEBOFJELLET	65
9.2.1 Garnet	65
9.2.2 Pyroxene	66
9.2.3 Amphibole	68
9.2.4 Thermometry	70
10. DISCUSSION.....	71
10.1 NET MINERAL REACTION FROM ECLOGITE FACIES TO AMPHIBOLE FACIES	71
10.2 THE DETECTION OF RUTILE THROUGH IMAGE PROCESSING	72

10.3 CONSEQUENCES OF CALCULATED Fe ³⁺ :Fe ²⁺ RATIO	73
10.4 GROWTH OF GARNETS BASED ON INCLUSIONS AND THERMOMETRY	74
10.5 RECRYSTALLIZATION OF GARNET	75
10.6 QUANTITATIVE XRD ON ECLOGITES	75
10.7 MOBILITY OF Ti IN HYDROTHERMAL FLUIDS	75
10.8 DEVELOPMENT OF VEINS AT ECLOGITE FACIES	77
10.9 LACK OF AMPHIBOLITIZED SAMPLES	78
10.10 PROBLEMS DUE TO BAD THIN SECTION POLISH	78
11. CONCLUSION.....	79
12. SUGGESTIONS FOR FURTHER RESEARCH.....	79
13. REFERENCES.....	80
APPENDIX 1 – MINERAL ABBREVIATIONS	85
APPENDIX 2 – THIN SECTION SCANS	86
APPENDIX 3 – MINERAL CHEMICAL TABLES	96
3.1 FERRO GABBROIC GARNETS	96
3.2 LEUCO GABBROIC GARNETS	100
3.3 FERRO GABBROIC, PRIMARY PYROXENES.....	101
3.4 LEUCO GABBROIC, PRIMARY PYROXENES	106
3.5 FERRO GABBROIC, PRIMARY AMPHIBOLES	107
3.6 LEUCO GABBROIC, PRIMARY AMPHIBOLES	111
3.7 SECONDARY AMPHIBOLES.....	112
3.8 MICAS.....	114
3.9 CLINOZOISITES	116
3.10 FELDSPARS.....	118
APPENDIX 4 – RESULTS FROM IMAGE PROCESSING IN MATLAB.....	119
4.1 MODAL PERCENTAGES OF RUTILE AND GARNET	119
4.2 RUTILE GRAIN SIZE DISTRIBUTION	125
APPENDIX 5 – STRUCTURAL FORMULA RECALCULATIONS	131
5.1 PREPARATION OF ANALYSES FOR RECALCULATION	131
5.2 RECALCULATION STRUCTURAL FORMULA.....	131
5.3 CALCULATING END-MEMBERS.....	131
5.4 CALCULATING AMPHIBOLES	132
APPENDIX 6 – MATLAB SCRIPTS WRITTEN FOR THIS THESIS	134
6.1 RUTILE AND GARNET DETECTION.....	134
6.2 STRUCTURAL FORMULA RECALCULATION OF GARNET	135
6.3 STRUCTURAL FORMULA RECALCULATION OF FELDSPAR	136
6.4 STRUCTURAL FORMULA RECALCULATION OF MICA	137
6.5 STRUCTURAL FORMULA RECALCULATION OF CLINOPYROXENE.....	138
6.6 STRUCTURAL FORMULAE RECALCULATION OF AMPHIBOLE	138
6.7 STRUCTURAL FORMULA RECALCULATION OF CLINOZOISITE.....	139
APPENDIX 7 – LIST OF FIGURES AND TABLES	140

1. Introduction

1.1 General introduction

This master thesis will focus on the petrology and mineral chemistry of the Engebøfjellet Eclogite. Since the Engebøfjellet Eclogite is a potential high grade TiO_2 -ore, it seems natural to investigate the rutile-ore potential in the samples collected. Veins and fractures are abundant in the eclogite, and some of them alter the eclogite mineral assemblage. The veins will be described and analyzed, and where they alter the eclogite wall rock, this alteration is described.

The purpose of the thesis is to give a contribution to the previous work done by NGU, by primarily focusing on the mineralogy and petrology of the eclogite instead of the presence of rutile. A comparable work for this thesis is the mineralogical and petrological contribution from Muriel Erambert in Korneliussen *et al.* (1998).

Samples collected during field work represent the variations within the eclogite, as well as in the veins described in this thesis. By using quantitative XRD for bulk rock mineralogy, XRF for bulk rock chemistry, EMP for mineral chemistry, optical microscopy for petrology purposes and image processing for quantification of rutile, a large data set can be produced. Weight percent of rutile from quantitative XRD, XRF and image processing will be compared to each other to see what method is the most reliable for a mining purpose. Thermobarometric calculations will be done in order to place the formation of the Engebøfjellet Eclogite in a pressure-temperature-setting.

1.2 Eclogites

Due to the high pressure (P) origin of eclogite facies rocks, studies of these rocks are important for the

understanding of deep crustal processes. Figure 1 shows the location of eclogite facies within a pressure – temperature (T) space, including geothermal gradients from different environments. As seen in figure 1, eclogite facies can be reached from blueschist, amphibolite or granulite facies, primarily by an increase in P and secondary by an increase in T.

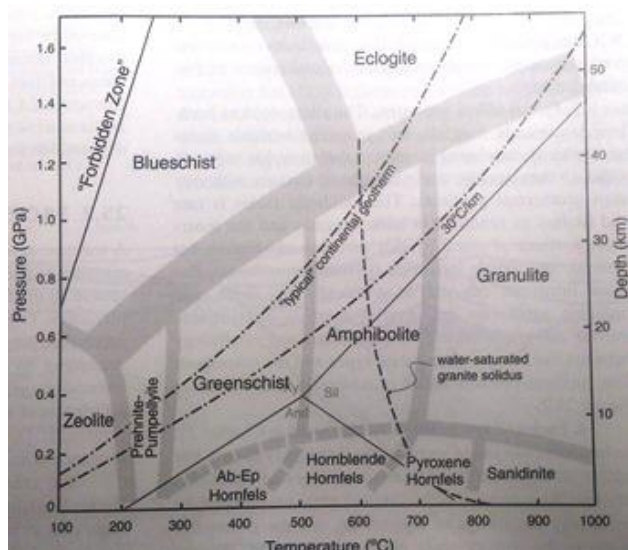


Figure 1 - Phase diagram showing the locations of the metamorphic facies (Winter, 2010)

The average continental geothermal gradient suggests an amphibolite facies – eclogite facies transition, whereas a geothermal gradient in subduction zones will be steeper, and cause a blueschist facies – eclogite facies transition. When mafic rocks are exposed to eclogite facies

conditions, the mineral assemblages from the previous metamorphic facies break down to form omphacite + garnet \pm quartz \pm amphibole \pm clinzoisite \pm phengite \pm kyanite \pm rutile (Foreman *et al.*, 2005). Due to the pressure, mafic eclogites are by definition rocks without plagioclase, that at eclogite facies conditions breaks down to form the Na-rich omphacite and/or amphiboles (Winter, 2010). Figure 2 shows a coarse grained sample

from the Engebøfjellet Eclogite composed primarily of green omphacite and red almandine-rich garnet. Due to HP recrystallization, and especially if the protolith is mafic, eclogites are dense rocks with specific gravities up to 3.5gcm^{-3} (Korneliussen *et al.*, 1999) and higher for more Fe-Ti-rich rocks.



Figure 2 - Typical eclogite minerals from Engebøfjellet. Grain size in the rock is larger than in typical eclogite at Engebøfjellet. Hammer head as scale.

Eclogites are usually found as lenses of varying sizes that have been exposed to the pressure and temperature in a subduction zone below an orogeny. By analyzing the minerals in eclogites one can calculate the pressure and temperature of the metamorphism, as well as the evolution of the pressure and temperature as a function of time during metamorphism and deformation. This is achieved by looking at for example the Fe^{2+} , Mg and Ca distribution in garnet and clinopyroxene (Ellis & Green, 1979). Minerals that grow during metamorphism may evolve a zoning with respect to chemistry. By analyzing for example the mineral inclusions in garnet from core to rim, the different element ratios yield different P,T-conditions, and the metamorphic evolution of the body can be calculated.

When finding deformation structures containing eclogite facies minerals in equilibrium, it is reasonable to believe that the structures are developed at eclogite facies conditions. Hence, these structures give valuable information on deformation mechanisms in the deep crust below an ancient orogeny, and may give indications on the processes acting below modern orogenies like the Himalayas.

A common problem when studying structures and mineralogy in eclogites is that deformation events after eclogite formation overprint the eclogite facies structures and minerals. The temperature in the deep crust is high, which causes rapid retrogression reactions as well as the disappearance of structures during exhumation. This retrogression is widespread in WGR, where amphibolite facies rocks dominate (Cuthbert *et al.*, 2002).

1.3 Engebøfjellet

The Engebøfjellet Eclogite is situated in Veiring, Naustdal, Sogn og Fjordane, Western Norway. It forms the southern side of the 330 meters high Engebøfjellet Mountain and is located next to Førdefjorden (Figure 3).



Figure 3 - Helicopter view of Engebøfjellet (Korneliussen et al., 2007).

The eclogite is surrounded by the gneisses that define the WGR (Korneliussen *et al.*, 1998), and is hence exposed to the same metamorphic evolution as the rest of the WGR (see section 2.2).

Since rutile (TiO_2) was discovered by Hans-Peter Geis in 1974 (Korneliussen, 2001) the Engebøfjellet Eclogite has been considered a potential major rutile-ore deposit. At present, the Norwegian mining company Nordic Mining ASA is waiting for permission to establish a mine at Engebøfjellet with a capacity of approximately 400 million tons ore containing 15 million tons of rutile over a 50 year period (Tenold, 2009). The Geological Survey of Norway has done an extensive work at Engebøfjellet over the last 15-20 years, mainly focusing on the resource potential of the eclogite, but also with respect to petrology, geochemistry, mineralogy and structural geology (Korneliussen *et al.*, 1998).

1.4 Rutile mining

The world's need of TiO_2 is today primarily covered by extraction of TiO_2 from ilmenite ($FeTiO_3$) and secondary by mining on one of the natural occurring TiO_2 polymorphs, rutile. Ilmenite is mined from placer deposits (e.g. Brand-se-baai – South Africa, Gulf of Tonkin – Vietnam & Playstein – Germany) (Dill, 2006) and from hard rock anorthosite massifs (e.g. Rogaland - Norway and Quebec - Canada) (Charlier *et al.*, 2006), while rutile primarily is mined from placer deposits.

From ilmenite, artificial rutile is produced through an energy consuming processes separating the TiO_2 from the $FeTiO_3$. In eclogites, however, this is done when ilmenite breaks down to form rutile and excess Fe that goes into other minerals. Hence, the rock can be mined for relatively pure rutile. The benefits of mining rutile from eclogite is that the vast amount of energy required in the processing from ilmenite can be saved, and the process becomes both cheaper and cleaner.

2. Geologic Background

2.1 Lithology of the WGR

The Western Gneiss Region (WGR) (Figure 4) is primarily composed of two generations of Fennoscandian orthogneisses, compositionally ranging between granodioritic and tonalitic (Kylander-Clark *et al.*, 2008), with ages of ca. 1650 Ma (Austrheim *et al.*, 2003, Skår & Pedersen, 2003) and ca. 950 Ma (Skår & Pedersen, 2003). The WGR contains the lowest exposed structural level in the Scandinavian Caledonides (Cuthbert *et al.*, 2000) and is hence an important study area. The WGR is overlain by continental and oceanic allochtones thrusted onto the bedrock during the initial stage of the Caledonian Orogeny between 430 and 410 Ma (Tucker *et al.*, 2004), and is exposed through a tectonic window in the Caledonian allochton. A relative recent study by Kylander-Clark *et al.*, (2009) shows that HP to UHP eclogite facies metamorphism peaked between 413.9 ± 3.7 Ma and 397 ± 4.8 Ma. There is no systematic age difference in the eclogites situated in the allochton and the basement, indicating eclogitization after thrusting (Cuthbert *et al.*, 2000).

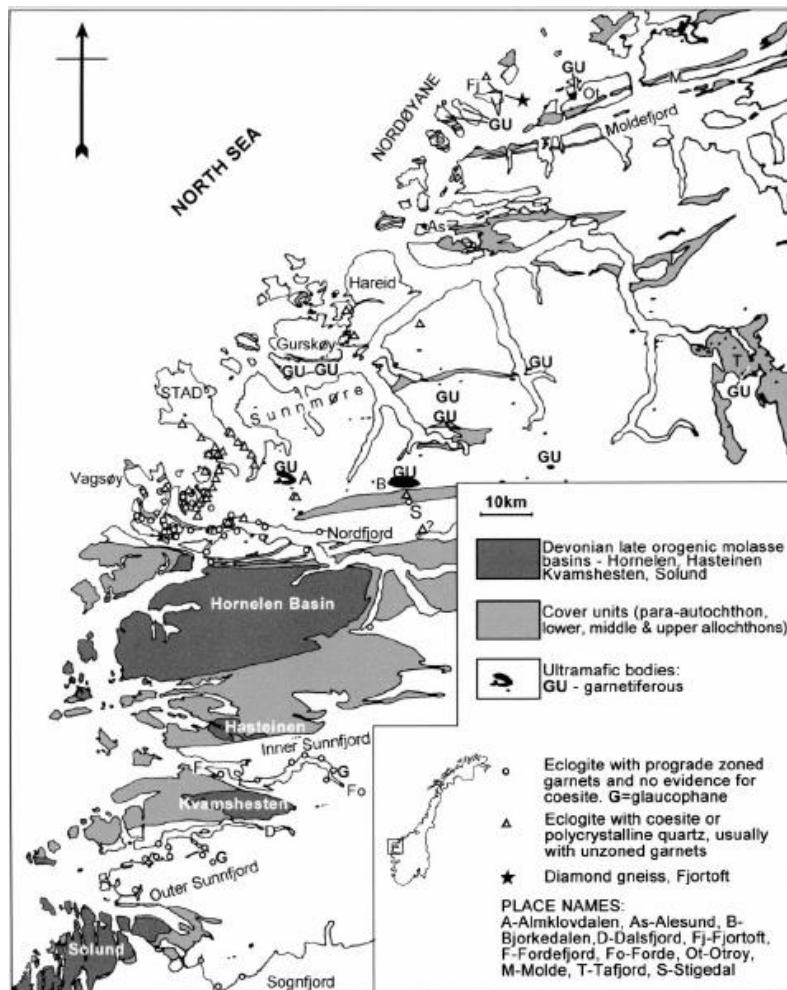


Figure 4 - Petrographic map of the coastal part of the WGR and the distribution of eclogites (Cuthbert *et al.*, 2000).

To the south eastern margin of the WGR and the Caledonian allochtones, lies the Baltic foreland, primarily consisting of high grade gneisses of Proterozoic age as well as metasediments and metavulcanites (Cuthbert *et al.*, 2000). The allochton thrust sheets consist of Baltic gneisses and their lower sedimentary cover of Paleozoic age. During the Caledonian orogenic event, WGR was overthrusted by several different units, such as ophiolites and island arcs (Stephens, 1988).

The WGR consists primarily of metastable amphibolite facies rocks. Despite this, several areas were not re-equilibrated during post-Caledonian exhumation and are preserved in eclogite facies (Austrheim *et al.*, 1997). Some areas have also escaped the reworking during the Caledonian Orogeny, and thus show pre-Caledonian structures and parageneses.

2.2 Tectonic evolution of the WGR

Going from SE towards NW, the WGR shows increasing metamorphic grade due to the Caledonian reworking. In the very SE of the WGR Caledonian metamorphism is nearly absent and Proterozoic structures and mineral assemblages are preserved (Milnes *et al.*, 1997). Moving in a NW direction, the Caledonian deformation and metamorphism becomes more pervasive (Figure 5 and 6), and the older Proterozoic structures and parageneses generally become wiped out. About 40 km NW of the edge of the nappe, eclogites are first discovered and become increasingly common in the rest of the WGR (Cuthbert *et al.*, 2000).

The general increasing metamorphic grade towards NW suggest that the WGR was subducted under, and overthrust by the Laurentian continent with a NW transport direction (Figure 5) during the development of the Caledonian Orogeny (Cuthbert *et al.*, 1983).

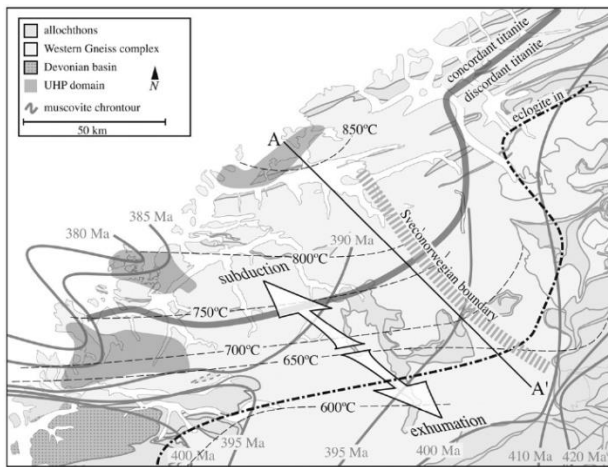


Figure 5 - Map showing the direction of the subduction and exhumation during and after the Caledonian orogeny (Kylander-Clark *et al.*, (2008).

According to Hacker *et al.* (2010) there are three UHP domains in the WGR where pressure exceeds 32 kbar. These domains extend between 300km^2 and 1200km^2 , and are located 1) east of Måløy, 2) south of Ålesund and 3) west of Molde. A detailed map (Figure 7) by Hacker *et al.* (2010) show the P,T-condition at peak metamorphism in the WGR. It shows the general trend with increasing metamorphic grade towards NW, along with the UHP domains. UHP allows coesite (Smith, 1984) and microdiamonds (Dobrzhinetskaya *et al.*, 1995) to be stable, and both are found in the WGR.

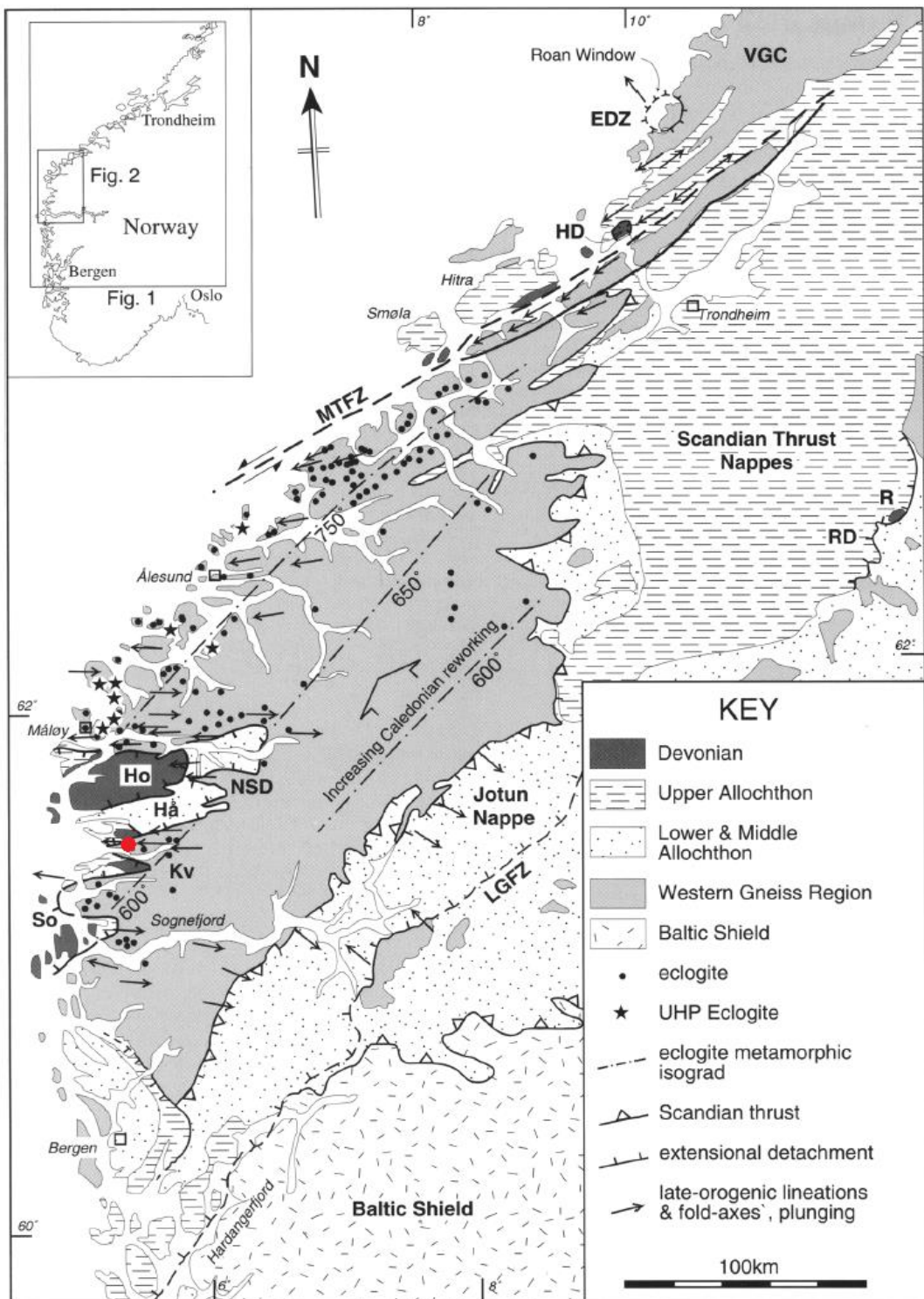


Figure 6 - Geological map of WGR with T-gradients and eclogite localities. Red dot marks Engebøfjellet. (Krabbendam & Dewey, 1998).

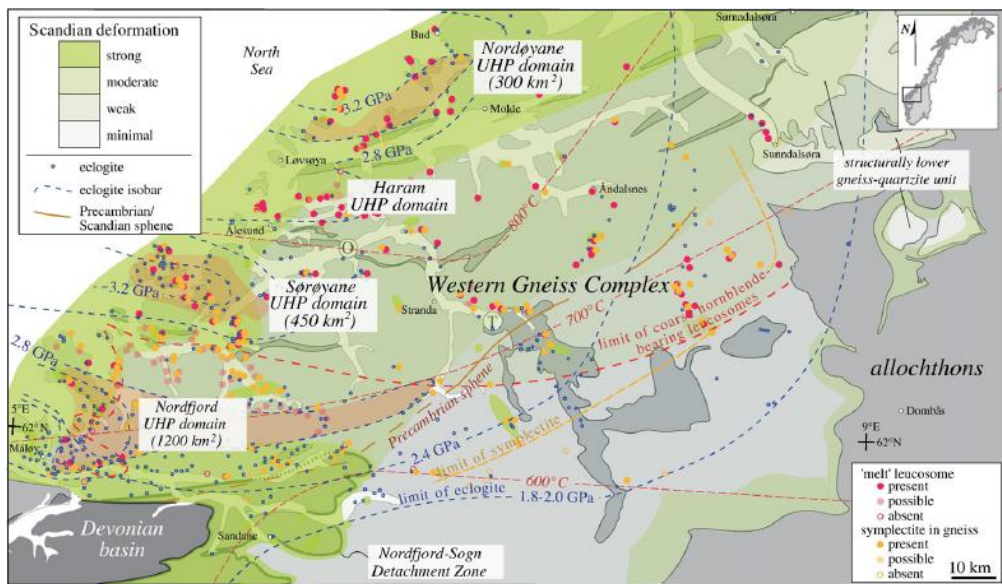


Figure 7 - Metamorphic overview of the WGR, showing UHP domains (Hacker *et al.*, 2010).

The evolution of the metamorphic condition in the WGR is illustrated in figure 8 (Hacker *et al.*, 2010). It shows that prior to the HP to UHP metamorphism, the WGR was subjected to a Barrovian style metamorphism up to about 10 kbar and ca. 620°C. After this, the metamorphic conditions increased to >30 kbar and ca. 730°C due to

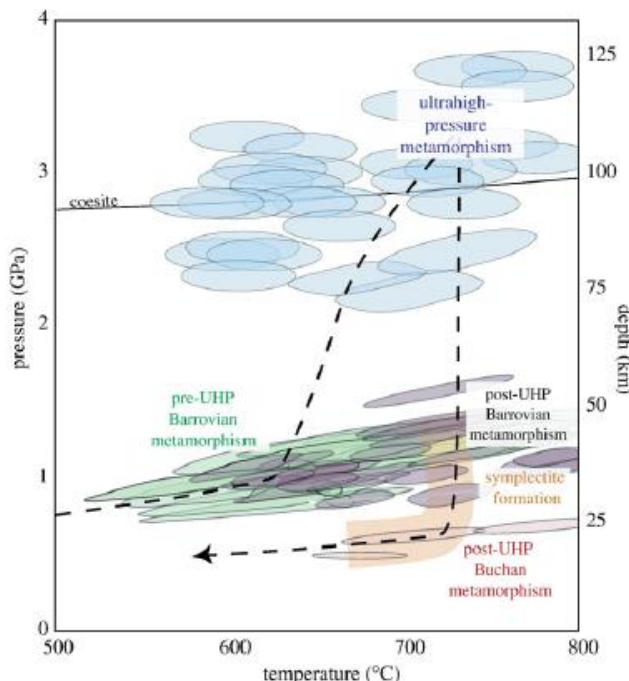


Figure 8 - P-T path for several HP to UHP eclogites in the WGR (Hacker *et al.*, 2010).

rapid burial and crustal thickening (Hacker *et al.*, 2010). This event was followed by a near isothermal pressure drop to below 10 kbar caused by rapid exhumation of the WGR. At last a Buchan style metamorphism at amphibolite facies (Hacker *et al.*, 2010) retrograded the whole WGR to a large extent.

According to Walsh and Hacker (2004) the exhumation of the WGR occurred in two stages. The first stage was probably a buoyancy driven flattening of the subducted WGR in a ductile environment close to the Moho. This could possibly flatten a 20 km thick unit of rock to a few km during 1-5 million years. The second stage was exhumation from Moho to middle- to upper-crustal depths through large scale shear

zones like the Nordfjord-Sogn Detachment Zone (NSDZ). The cause of these major shear zones is unknown, but Walsh and Hacker (2004) suggests a rapid change in crustal thickness to activate the shear zones. Associated with the NSDZ is an up to 5 km wide mylonite zone (Johnston *et al.*, 2007), witnessing the amount of deformation along this shear zone. Walsh and Hacker (2004) states that without the shear zones, the mafic bodies would have remained near the Moho forever, due to the high difference in density relative to the surrounding gneisses.

By studying the contact between the basement gneisses and the allochthon cover, information about the evolution of the WGR can be extracted. Such studies show evidences of a complex tectonic evolution. According to Hossack and Copper (1986) the allochton experienced a shortening of more than 400 km when being thrusted almost 100 km onto the Baltic craton towards the east. After the peak eclogite facies metamorphism, the motion reversed and the nappes were backslicing so that the load covering the WGR decreased. This motion followed older thrust faults through the nappe pile, and in the lower to middle allochton significant ductile deformation took place (Wilks & Cuthbert, 1994). The result of this extensional phase was that the WGR was brought up towards the surface, and now lies within a large metamorphic core complex (Cuthbert *et al.*, 2000).

2.3 The geology of Sunnfjord

Krogh (1980) classified the eclogites in the Sunnfjord area as rather low temperature eclogites formed under P, T-conditions increasing from 12.0 ± 2.5 kbar and $510-520^\circ\text{C}$ in the SSE to 15.0 ± 2.5 kbar and $630 \pm 35^\circ\text{C}$ moving towards NNW in the Sunnfjord area. Krogh (1980) also found zoning in eclogite minerals, and interpreted the cores to have formed at lower P-T conditions than the rims characteristic for a prograde metamorphism.

The NSDZ splits the geology of Sunnfjord into two major units: The unit above and the unit below NSDZ (Norton, 1986). The eclogite at Engebøfjellet is situated within the Precambrian basement (Figure 9), in two geological units called the Hegreneset and Helle complex (Korneliussen, 2001). The Hegreneset complex is primarily composed of metamorphosed mafic and felsic intrusions preserved at amphibolite and eclogite facies. It is surrounded by the Helle complex consisting of granitic to granodioritic gneisses and augen gneisses (Korneliussen, 2001, after Lutro and Ragnhildstveit, 1997). The mafic and felsic rocks are folded and mixed into each other and a banded mafic-felsic rock, possibly of volcanic origin, appears in contact with the Engebøfjellet Eclogite (Korneliussen, 2001).

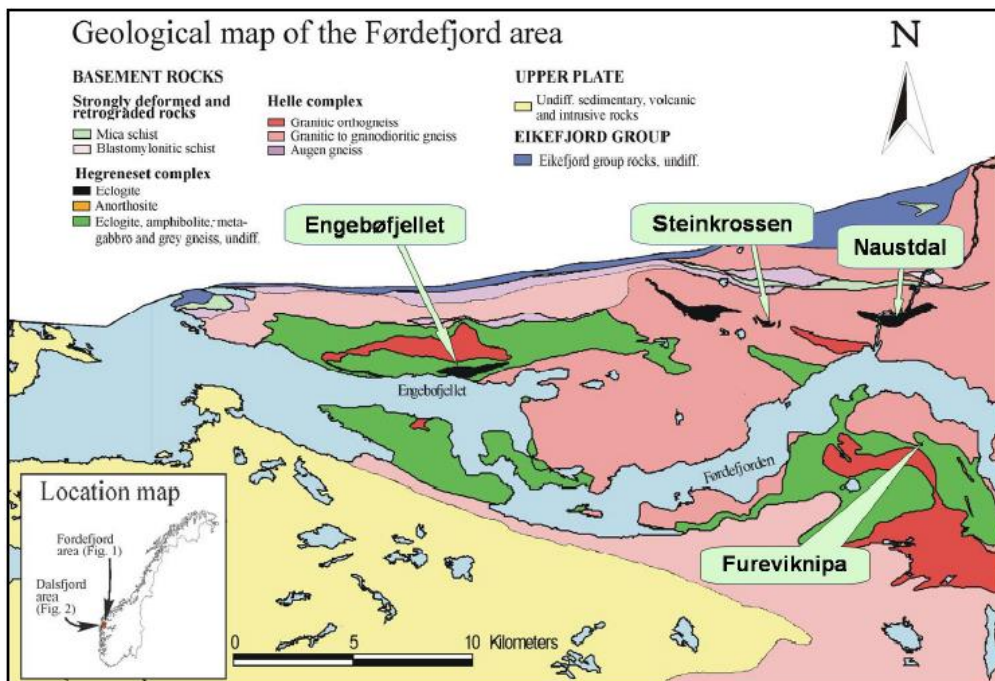


Figure 9 - Geological map of the Førdefjord area (Korneliussen *et al.*, 2001).

Eclogites in the Førdefjord area appears to be distributed in the surrounding gneiss through a boudinage process. Many eclogites are elongated in E-W direction and several lenses are found along approximately the same strike (Foreman *et al.*, 2005). The eclogite bodies usually appear as smaller lenses, but some of the larger lenses occur as more or less massive bodies with outgoing outcrops in excess of 10^5 m² as is the case for the Engebøfjellet Eclogite.

2.4 Engebøfjellet

Based on observations of relict textures and geochemistry, the protolith of the Engebøfjellet Eclogite is known to be a gabbroic intrusion enriched in Fe and Ti due to fractionated crystallization. During the Caledonian Orogeny the protolith was metamorphosed under eclogite facies condition at 15-17 kbar and ca 600°C (Korneliussen *et al.*, 1998). The eclogite is today found as a relatively well preserved eclogite facies outcrop, cut by zones more or less retrograded to amphibolite facies. These zones vary from thin, but pervasive fractures up to larger shear zones.

Based on varying contents of Fe and Ti, the Engebøfjellet Eclogite has been subdivided into two different types. The ferro eclogite is defined by $\text{Fe}_2\text{O}_3 > 14\%$ and $\text{TiO}_2 > 3\%$, while the leuco eclogite is defined by $\text{Fe}_2\text{O}_3 < 14\%$ and $\text{TiO}_2 < 3\%$ (Korneliussen *et al.*, 1998). The ferro eclogite is dark and the leuco eclogite is bright in color. For field work, the term transitional eclogite is used on rocks that are difficult to classify as either of the two end-members. The different eclogite types at Engebøfjellet are complexly folded as shown in the map below (figure 10), from Korneliussen *et al.*, (2007).

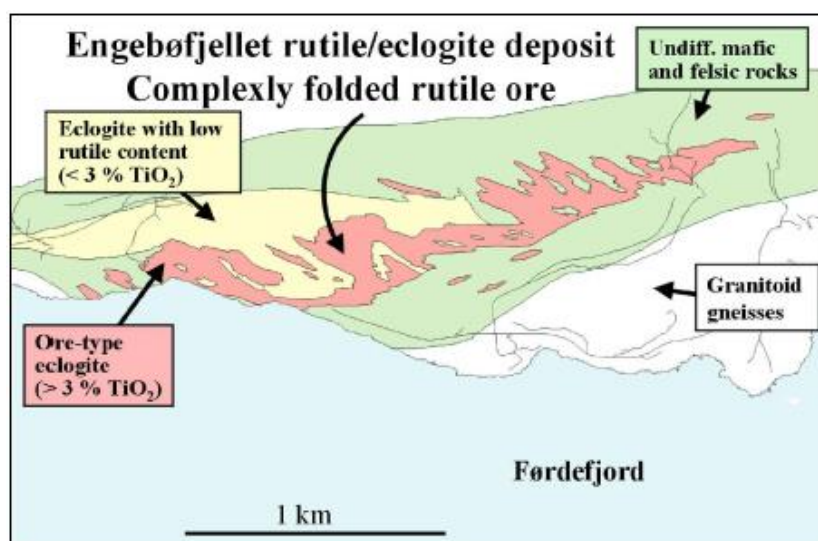


Figure 10 - Simplified geological map of Engebøfjellet (Korneliussen *et al.*, 2007).

Due to a complete mineralogical recrystallization during eclogite facies condition, no magmatic minerals were found in Engebøfjellet (Korneliussen *et al.*, 1998). It is, however, possible that coarse grained minerals have preserved mineral inclusions showing traces of metamorphic events prior to the peak Caledonian metamorphism. The textural equilibrium on the other hand is dependent on the deformation during eclogite facies. In zones where the strain has been low, pseudomorphs of magmatic minerals are found.

According to Korneliussen *et al.* (1998) there are six stages of deformation (D_1 to D_6) observed at Engebøfjellet, ranging from eclogite to greenschist facies condition. Table 1 below will briefly sum up these six stages in chronological order along with the respective structures.

Table 1-Overview of the deformation history at Engebøfjellet (After Korneliussen *et al.*, 1998).

Deformation event	Structures	Metamorphic Facies
D_1	Isoclinal folding (F_1) of protolith mineralogical banding. F_1 -axes are E-W, indicating N-S shortening. Transposition foliation (S_1) parallel to this banding.	Increasing up to Eclogite.
Post- D_1	Randomly oriented omphacite show evidences for a static growth. These larger omphacites cut S_1 -foliation.	Eclogite
D_2	S_1 is folded into tight isooclinal F_2 -folds. Spaced cleavages near hinges. Fold limbs experienced the most strain, and S_2 -foliation formed. Both sinistral and dextral sense of shear parallel to WNW-ESE. May be explained by N-S shortening.	Eclogite
D_3	S_2 folded into tight F_3 -folds. Spaced cleavages near hinges, and up to meter wide shear zones (S_3) in fold limbs. S_2 reactivated as shear zones.	Decreasing down to garnet-amphibolite
D_4	Meter wide shear zones (S_4) is developed, and cuts through F_3 -folds. Maybe progressive continuation of D_3 .	Amphibolite to greenschist
D_5	Sub-vertical N-S striking joints. N-S shortening and E-W extension.	Epidote-amphibolite to greenschist
D_6	N-S striking brittle normal faults, dipping towards E and W. Also sub-vertical NNW-SSE and NE-SW striking strike-slip fault. Indications on slip surfaces suggest N-S shortening and E-W extension.	Greenschist or lower P-T.

Several of the deformation structures found in Engebøfjellet are also found in the Drøsdal eclogite (Foreman *et al.*, 2005) several kilometers towards west. This indicates that the deformation mechanisms working at Engebøfjellet also worked on a regional scale.

Referring to a personal comment from Thomas Krogh, Korneliussen (2001) claims that a relict magmatic zircon from Engebøfjellet yields an age of 1500 Ma. This approximates the U-Pb zircon ages obtained by Walsh *et al.* (2007), yielding 1612 ± 22 Ma (Discordia age) for an eclogite protolith 100 km NE of Engebøfjellet.

3. Methods

3.1 Analytical methods

For this master thesis, the following analytical methods are used: Quantitative X-ray diffraction (XRD) for bulk rock mineral determination, X-ray fluorescence (XRF) for bulk rock chemical compositions, Electron microprobe (EMP) for petrological purposes and for determining mineral chemistry, Matlab for detection of rutile and garnet, and optical microscopy for petrological purposes. The principles behind the methods used will be described below. Prior to analysis, the samples need to be prepared differently for the different methods. All the analytical instruments described and used are available at the Department of Geosciences of the University of Oslo. Reference for principles and EMP is Reed (2005), for XRD is Dutrow and Clark (2012) and for XRF is Wirth and Barth (2012). In addition to these references is information from Muriel Erambert and Maarten Aerts during preparation and analyses.

3.1.1 Basic Principles of X-ray methods

XRD, XRF and EMP use the unique properties of the electron configuration in the different elements to give information about the material that is analyzed. From the Bohr's atom model, we know that the electrons are distributed in different shells, denoted K, L, M etc. By irradiating a mineral with for example X-rays, inner shell electrons of the atoms can be dislodged from their positions causing a vacancy in the electron distribution. Inner electrons are stronger bound to the nucleus than outer electrons, and thus have lower potential energy. Hence, an outer electron will benefit –energetically– on moving in and occupy this vacancy. Since the energy needs to be preserved, the excess energy is released as X-ray photons (Figure 11). Several electron transitions are possible, and the set of X-ray signals received is characteristic for an element.

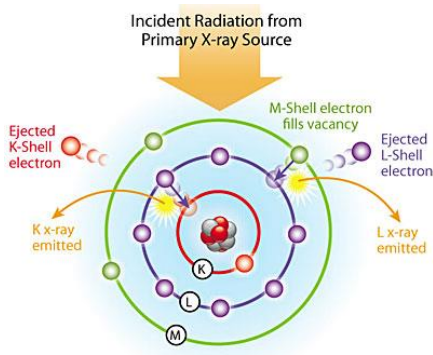


Figure 11 - Illustration of the process from ionizing the atom to the emitting of a characteristic X-ray. (www.azom.com).

3.1.2 X-ray diffraction (XRD)

XRD is a method used primarily for identifying crystal structures and symmetry in crystalline material. In order to perform a XRD analysis a representative part of the sample needs to be crushed into clay size particles. A primary X-ray is generated by a copper source, and focused onto the sample.

XRD is based on the principle of Bragg's law

$$n\lambda = 2dsin\theta \quad (\text{Eq. 1.1})$$

Where n is an integer λ is the wave length of the incident radiation, d is the distance between the planes in the atomic lattice, and θ is the angle between the incoming X-rays and the scattering planes (See figure 12) Eq. 1.1 states that two parallel beams of the same wavelength will positively interfere when the equation is satisfied.

The sample is rotated in the plane along an angle Φ while the X-ray tube is rotated through a range of angles (θ). By varying θ , all d -values are recorded, and by varying Φ , a more representative selection of the material is analyzed due to the random orientation of the grains in the powder. By capturing the θ -values a conversion to the d -values can be done. Since each mineral has a set of unique d -spacings an identification of the mineral is possible (eq. 1.2). The results are correlated up against a database containing crystal lattice data for minerals. Both Crystallographic Open Database (COD) and Powder Diffraction File, International Centre for Diffraction Data (PDS-4) were used to identify phases present in the samples.

$$d = \frac{n\lambda}{2\sin\theta} \quad (\text{eq. 1.2})$$

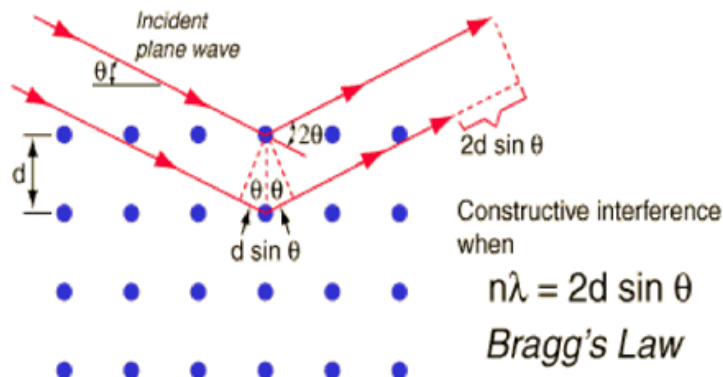


Figure 12 - Figure shows how Bragg's equation is fulfilled when positive interference occurs. (www.photonicmicrodevices.com).

3.1.3 X-ray fluorescence (XRF)

XRF is a method used, among others; by geologists primarily for quantitatively determine the chemical composition of rocks and minerals. The primary X-rays are generated in the same way as in the XRD, but where the XRD captures the diffracted incident beam, the XRF captures secondary X-rays generated from electron transitions within the sample. This radiation is termed fluorescence, and from an irradiated sample a whole spectrum of X-ray, known as white X-ray, results. Two basic methods are used to treat this white X-ray: Energy-dispersive spectroscopy (EDS) and wave-dispersive spectroscopy (WDS).

EDS uses a semi-conductor to detect the different photons in the white X-ray. By being capable of detecting and analyzing at a fast rate, the EDS is able to treat the incoming beam as a pulse of single photons. When an energetic photon hits the semi-conductor it dislodges a valence electron out to the conducting band and generates a current. A counting system will count the number of pulses, and display them as an EDS spectrum.

WDS is distinguished from EDS by the fact that the white X-ray is analyzed according to the wavelength by means of Bragg's equation (eq. 1.1). The WDS works by the principle that an analyzer crystal with a known d -spacing (d) is rotated (θ) relative to the sample, along with the detector. In this way, individual wavelengths can be recorded, corresponding to characteristic lines belonging to the different chemical element within the sample.

3.1.4 Electron microprobe (EMP)

Where the XRF only analyze a larger crushed sample, the EMP has the possibility to do chemical analyzes on a $1-2\mu$ wide spot on a thin section, since the EMP uses a focused electron beam to excite atoms, yielding characteristic X-rays. The EMP is usually fitted with 3-5 WDS containing different analyzing crystals, so it has the possibility to analyze a large range of elements at both major and trace element concentrations. Being able to do chemical point analyses on the thin section, the chemical variation in for example a zoned porphyroblast can be analyzed. In addition to the quantitative WDS an EDS is also fitted to the EMP to qualitatively investigate mineral grains in the thin section. The EDS was used to determine mineral grains not analyzed; primarily quartz, feldspar, sulfide and zircon.

The EMP also works as a scanning electron microscope (SEM) since the electron beam can be scanned over the thin section. When the electrons hit the minerals in the thin section, some are backscattered according to a function that positively correlates with the atom number (Z). Hence, minerals containing heavy elements will appear brighter than minerals containing light elements (Figure 13). The advantage of BSE relative to the optical microscope also fitted to the EMP is that zoning in minerals is easier seen, which is important for a petrological study of a rock.

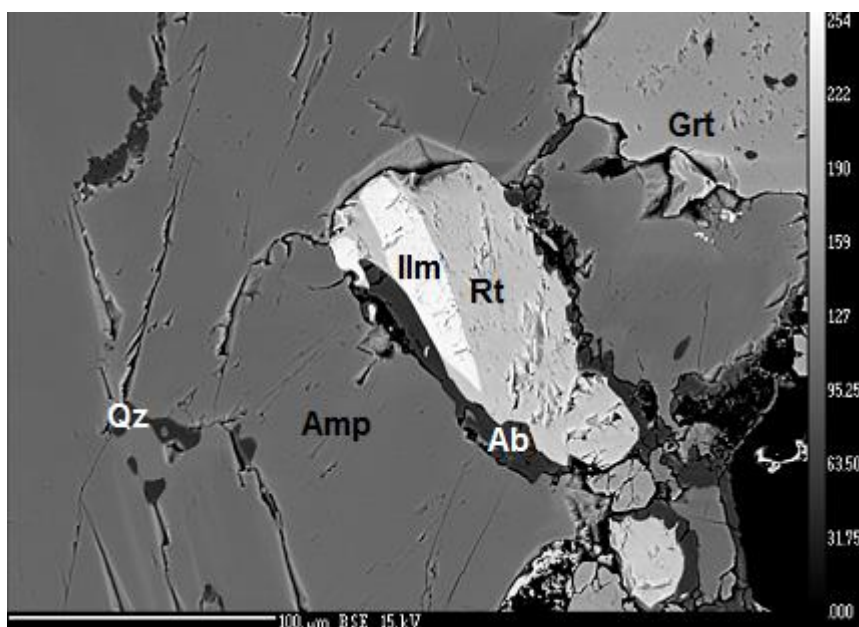


Figure 13 - BSE image of partly altered rutile in amphibole from SK-7.

The EMP also allows X-ray mapping for visual investigation of the elemental distribution between or within mineral phases in the map. The WDS spectrometers are set to detect the intensity of the elements of interest. The mapped area is defined, together with beam current, counting time on each pixel and the step size. For the high quality quantitative mapping for XMapTools (See section 9), longer count time is used than for qualitative mapping. The smaller the step size is, the more pixels the map will contain. Higher number of pixels within an area yield higher resolution. High resolution is required for detailed studies along grain boundaries and for tiny inclusions within minerals. The drawback of achieving a high resolution X-ray map is that it requires several hours of mapping. The map produced for the XMapTools (see section 9) ran for 16 hours.

When the required parameters are set, the sample is moved below the static beam, detecting intensity of all the elements of interest in each pixel. The result is one intensity matrix for each element. From the matrices elemental concentration maps can be created.

For this thesis the Cameca SX100 electron microprobe at the Department of Geosciences, University of Oslo was used. For calibration, the following standards are used: Ca and Si (Wollastonite), Na (Albite), K (Orthoclase), Ti and Mn (Pyrophanite), Fe (Native Fe), C (Cr_2O_3), Al (Corundum), Mg (Periclaste), Zr (Rutile) and Nb (niobium metal). Na and K were analyzed first in order to reduce the effect of the loss due to burning on the sample. All analyses were performed in WDS mode. For routine analyses 15 kV (Acceleration voltage), 15 nA (Beam current), 10 sec counting time on both peak and background was used. Zr in rutile: 20 kV, 100 nA, 5 μm beam size and 240 second counting time on peak was used. Quantitative mapping: 15 kV, 60 nA, 6 μm step size, 300 ms per pixel and focused beam (stage motion). Qualitative mapping: 15 kV, 40 nA, 5 μm step size, 50 ms per pixel and focused beam (stage motion).

For Zr and other trace elements in rutile, a trace element procedure was used, with Ti and O wt. % as input for calculating matrix corrections, done according to the Cameca PAP method (Pouchou & Pichoir, 1985). The PAP method was also used on matrix corrections for major element analyses.

3.2 Optical microscopy

Optical microscopy was primarily used early in the process to get a good overview of the samples, including veining, mineralogy and petrology. Getting good observations on the microscope causes the EMP analyses to be more time efficient. Cameras can also be fitted to the microscope allowing good photos of texture etc. to be taken.

3.3 Preparation of samples for XRD/XRF

Representative samples with different bulk chemistry were chosen for XRD and XRF analysis. This was done after investigating thin sections, where the differences are easily estimated by the modal compositions of

Table 2 - Table giving the weight of the samples used for XRD/XRF.

Weight (grams)		
Sample	After sawing	After crushing
SK-2	497	461
SK-3	460	427
SK-7	536	465
SK-8	407	382
SK-9	291	260
SK-11	274	256
SK-12	355	334
SK-20	336	325
SK-29	151	136
SK-30	259	242
SK-31	220	207

The altered surfaces were first cut off with a diamond saw, and the samples dried. Further they were crushed in a sling mill to a fine grained powder. The samples were weighted before and after the crushing (Table 2) to ensure that they could be considered representative with respect to the rock grain size.

To obtain a grain size small enough for accurate XRD and XRF measurements, the powder from the sling mill was further crushed in a micronizer agate mill. This mill crushed the sample to $>5\mu\text{m}$ in ethanol. After crushing, the samples were dried in a heating cabinet until the ethanol was vaporized. Bulk rock XRD mounts were first

made from a small fraction of the crushed material, and since the results from the XRD and XRF should be compared to each other, exactly the same material would have to be subsequently analyzed by the XRF.

Before the sample material from the XRD samples could be used for making XRF pellets, it had to be stored in the heating cabinet at 110°C for at least 24 hours, in order to evaporate all absorbed free fluids. The sample was then accurately weighted before it was fired in an oven at 1050°C for at least 1 hour in order to oxidize all elements. Further the sample was weighted again to control the weight loss or gain due to dehydration of minerals and oxidation respectively. 0.75 g sample and 3.75 g flux (lithium tetraborat) was then mixed and melted in a platinum crucible at 1200°C and cooled down in a mold to form the finished XRF pellet. The fusion process was automated using a Philips PerlX.

Since the minerals should be quantified by XRD, representative minerals from all samples were analyzed at the EMP. At least 25 point analyses per sample were done in order to get a good overview of the mineral chemistry in each sample.

After the XRF analyses the results needed to be recalculated to account for the loss on ignition. Loss on ignition (LOI) is defined as sample weight after ignition (1050°C oven) minus the weight before ignition, divided by the weight before ignition. All XRF results are multiplied by a factor

$$F = (\text{Analysis total} - 100 \cdot \text{LOI}) / \text{Analysis total}$$

3.4 Matlab

Matlab R2007b was used to quantify the rutile and garnet in thin sections and find the grain size distribution. This was done by comparing the thin section with three predefined images of rutile and one of garnet (Figure 14), cropped out of the scanned thin sections. In order to determine the size of each rutile and garnet grain, a scale was implemented. This scale was the area of each pixel, calculated by dividing the area of the thin section by the number of pixels in the thin section scan.

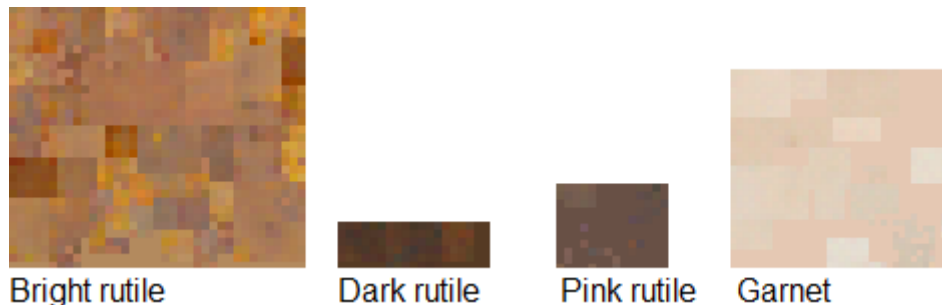


Figure 14 - The garnet and the three different rutile standards used in the classification.

The motivation for making this script was primarily to be able to quickly determine the amount of rutile and garnet in an arbitrary thin section without doing any modifications to the script except the actual file input. The only requirements for an input file is that 1) it is a scan of the whole thin section, mounted on a plate of the same size as those crafted at the Department of Geosciences, University of Oslo (48x28 mm). This is important to get the size of the rutile grains correct, but will not affect the modal %. If the sizes are different one can easily correct for this in the script. 2) The thin section must be scanned in normal light, and no color corrections should be done. 3) To obtain the best result one should use for example Photoshop to delete everything within the scanned thin section except the rock slab.

Since the color of rutile and garnet varies in each thin section and from thin section to thin section, the standards were made by combining rutile and garnet grains from several thin sections. Based on visual control (Figure 15), the program was able to detect most of the rutile and garnet in most of the samples.

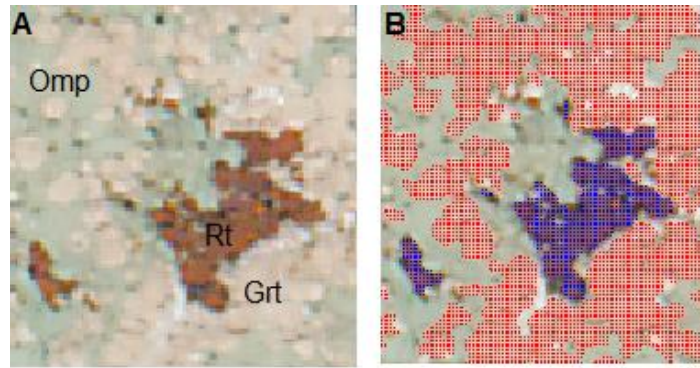


Figure 15 - Image showing how well the program detects rutile (blue) and garnet (red) in SK-2.

The biggest issue regarding rutile was in sample SK-4 and SK-16 where the garnet and amphibole had a rusty appearance. Matlab counted much of this rust as rutile (Figure 16), and in order to remove this error the standards needs to be changed causing rutile from other thin sections to remain undetected.

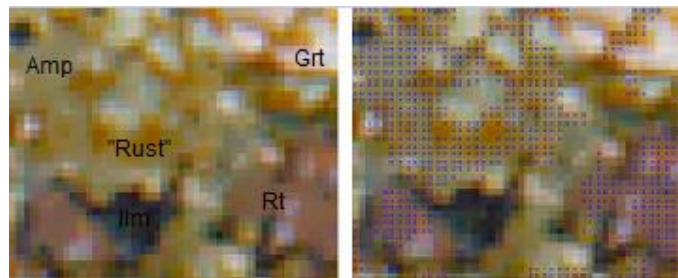


Figure 16 - Example of how the program wrongly can classify rusty garnet and amphibole in sample SK-16 as rutile. Original thin section scan to left, and processed image to the right.

The biggest issue regarding garnet was in samples where the minerals appeared pale, possibly due to thinner thin sections. This especially caused the visual difference between garnet and omphacite to be less significant, and the program often had problems separating the two (Figure 17). Also towards the edges of many thin sections the colors were paler, and hence caused detection issues.

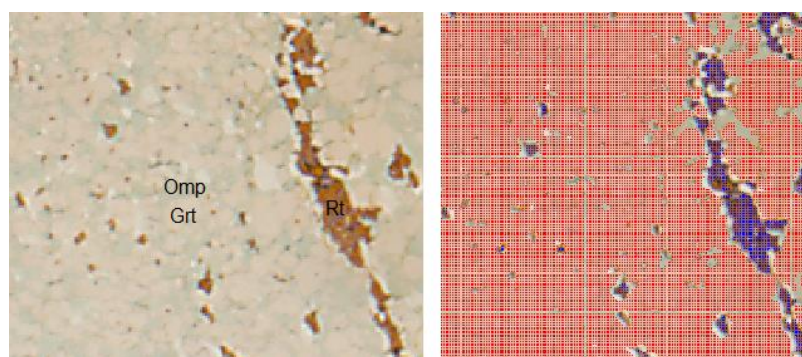


Figure 17 - Figure showing how pale thin sections can be problematic for identifying garnet correctly. Sample SK-20.

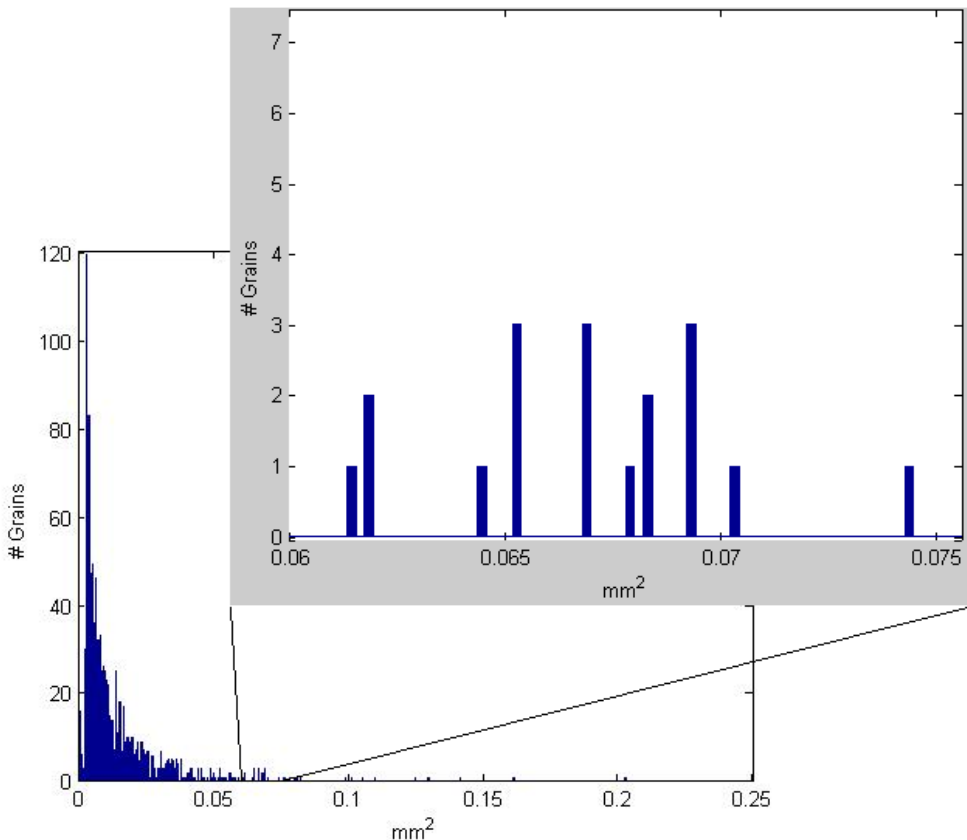


Figure 18 - Output histogram of the grain size distribution in SK-19.

Figure 18 shows the rutile grain size distribution from SK-19, with an additional outcrop between 0.06 and 0.075 mm². All grain size distributions show a higher density of grains in the fine grained area. Due to the issues on detecting garnet, grain size distributions are not made, but can easily be produced on request.

In order to produce the script some general advices were offered by Daniel W. Schmid at the PGP. The script is presented in appendix 6.1 and the results from the image processing are found in appendix 4.

4. Field work

For a master thesis study on a location where not much work has been done before, an extensive mapping is required in order to produce a proper result. At Engebøfjellet, however, geological surveying has been carried out more or less continuously since the mid 90's. From 1996 to 1997 the Geological Survey of Norway (NGU) mapped the eclogite to a great detail including structural geology, geochemistry, petrology, drilling and gravimetry (Korneliussen *et al.*, 1998). Therefore, in order to add any significant results to the previous work, months of field work could be required.

The field work was done in two parts. The first trip to Engebøfjellet was done at august 6th and 7th 2012, together with the supervisor Muriel Erambert. The focus was to collect samples, taking pictures and to get familiar with the Engebøfjellet Eclogite. A total of 31 samples of variable sizes were collected for thin section, EMP and bulk rock XRD and XRF. The samples were marked SK (1-31) – 12. The second period of field work

was done between September 10th and 14th 2012. The focus was to study the different vein types present. Due to heavy rainfall good observations were difficult to achieve.

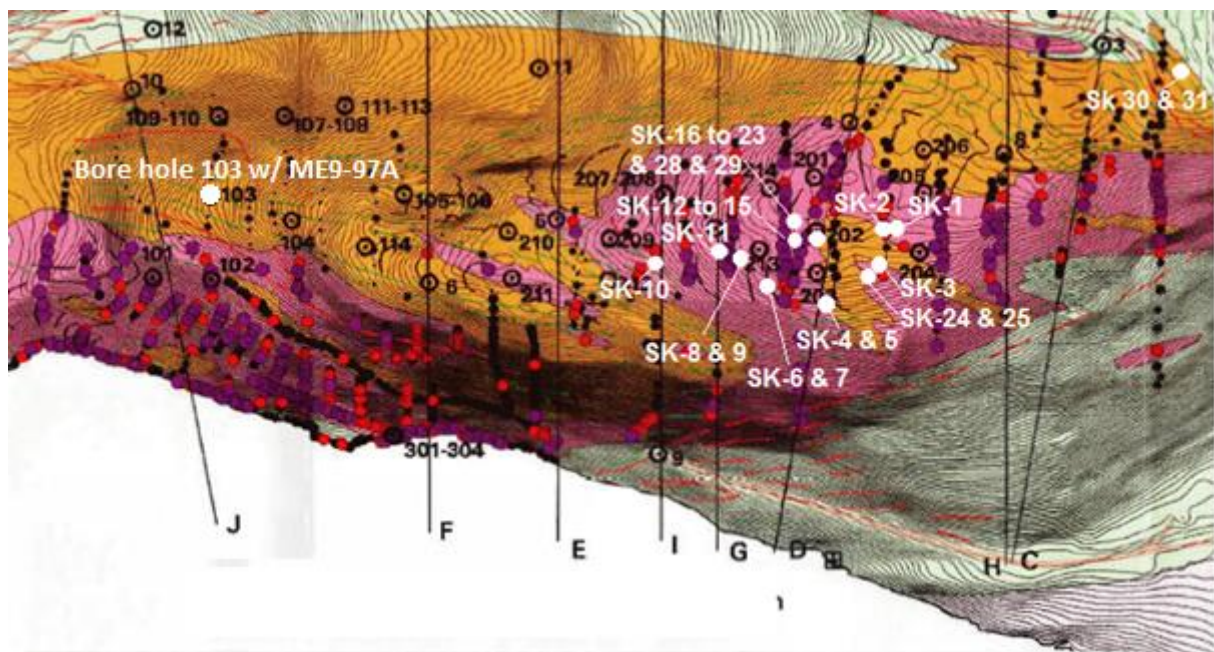
4.1 Samples

The samples were primarily collected in the western part of the Engebøfjellet Eclogite (Figure 19), where the eclogite is considered transitional to Fe-Ti-eclogite (Figure 20). The object was to collect representative samples from the different eclogite types, some of them large enough for bulk rock XRD and XRF. The different vein types occurring at Engebøfjellet were also sampled along with apparently more amphibolitized samples in a small pit (SK-30 and SK-31).



Figure 19 - Air photo of Engebøfjellet shows how well exposed the rock is. (Photo from Norgeskart.no).

Figure 20 shows where all collected samples are collected within the geological map of Korneliussen *et al.* (1998). Earlier samples collected by Korneliussen *et al.* (1998) are marked on the map, and explained in the legend of the map.



LEGEND

- | | | | |
|---|--|-----|--|
| 1 | Ferro eclogite (ore type) | — | D1 fabric |
| 2 | Leuco - and transitional eclogite | — | D2 fabric |
| 3 | Amphibolite unit (undiff. amphibolite, eclogite and gray gneiss) | — | D3 and D4 fabric |
| 4 | Granitoid gneisses, undiff. | | Vertical profile (See NGU-report 97.014) |
| • | Samples (TiO ₂) | 3 ○ | Drillhole position with number |
| • | < 1% TiO ₂ | ■ | End of gravimetric profile |
| • | 1 - 2% TiO ₂ | — | Roads |
| • | 2 - 3% TiO ₂ | | |
| • | 3 - 4% TiO ₂ | | |
| • | > 4% TiO ₂ | | |

Figure 20 - Geological map showing where the samples were collected (white dots). Map is from Korneliussen et al. (1998).

Table 3 shows the GPS coordinates and a brief description of all the samples collected.

Table 3 - GPS coordinates for samples, with brief descriptions.

Sample	X	Y	Description
SK-1	310229	6822843	Ferro-eclogite
SK-2	310219	6822843	Fresh eclogite with alteration veins
Sk-3	310214	6822802	Intermediate, fresh eclogite with some rutile
SK-4	310162	6822750	"Pegmatite vein"
SK-5	310162	6822750	Omphacite in quartz
SK-6	310100	6822764	Ferro-eclogite. Garnet concentration around vein.
SK-7	310100	6822764	Ferro-eclogite. Garnet concentration around vein..
SK-8	310067	6822789	Ferro-eclogite. Fresh eclogite
SK-9	310067	6822789	Ferro-eclogite. More fine grained than above.
SK-10	309981	6822772	Ferro-eclogite with larger omphacite
SK-11	310047	6822794	Finegrained ferro-eclogite/transitional
SK-12	310130	6822824	Quartz+ omphacite vein
SK-13	310130	6822824	Layered Fe-Ti eclogite
SK-14	310130	6822824	Ferro-eclogite
SK-15	310130	6822824	Ferro-eclogite with late vein.
SK-16	310130	6822847	Garnet and rutile rich eclogite
SK-17 a + b	310130	6822847	Two small samples of amphibole and mica.
SK-18	310130	6822847	Coarse grained ferro eclogite
SK-19	310130	6822847	Coarse grained ferro-eclogite with late fracture.
SK-20	310130	6822847	Garnet rich band
SK-21	310130	6822847	Omphacite segregation
SK-22	310130	6822847	Amphibole
SK-23	310130	6822847	Quartz/mica
SK-24	310208	6822789	Garnet + quartz vein
SK-25	310208	6822789	Eclogite with large amphibole porphyroblasts.
SK-26	310149	6822824	Fresh eclogite and rutile bearing quartz vein
SK-27	310130	6822824	Partially retrograded eclogite
SK-28	310130	6822847	Sample with quartz vein
SK-29	310130	6822847	High density of late veins in ferro-eclogite.
SK-30	310508	6823037	Apparently amphibolitized
SK-31	310508	6823037	Apperantly amphibolitized

4.2 Description of veins and layers

On both micro and meso scale, veins and distinct layers are common in the Engebøfjellet Eclogite, and they range widely in composition and metamorphic facies. Several types were investigated in field and sampled, and the observed layers and vein types are described below.

4.2.1 Eclogite facies veins

Several veins at Engebøfjellet are developed during eclogite facies conditions. The indication is that the wall rock still is unaltered, and that the veins in some cases contain eclogite facies minerals, for example omphacite (Figure 21). The quartz rich veins are interpreted to have formed due to brittle deformation (explained in section 10.8) and in pressure shadows based on the structural setting they are located in.

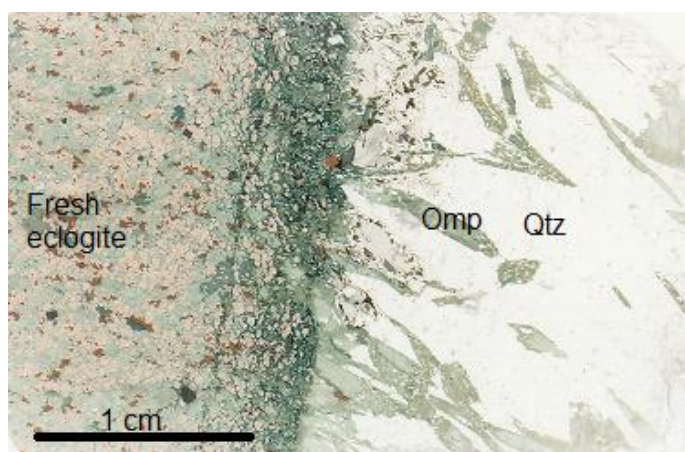


Figure 21 - Eclogite facies vein in SK-28 containing omphacite.

4.2.1.1 Garnet + quartz veins

The garnet veins consist of primarily garnet and quartz (Figure 22). They are usually less than 0.5 cm wide, sometimes wider. On weathered surfaces the garnet and to some extent the quartz sticks out, maybe due to the weathering of a third mineral, possibly carbonate. In fresh surfaces these veins contain a bright, soft mineral also suggesting carbonate as the third mineral. They are interpreted as veins since they are found with a large range in orientation within a small outcrop. They also cut the foliation, hence postdating the foliation developing event.

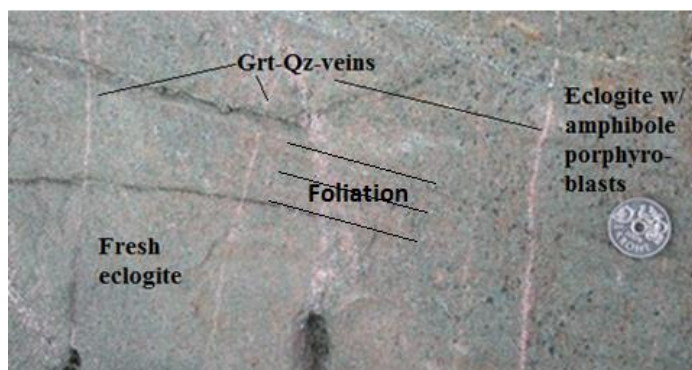


Figure 22 - Field image of the garnet veins.

The orientations (Figure 23) of the veins vary, but two sets are common, one that is sub parallel to the foliation and one that is close 40-80° to the foliation.

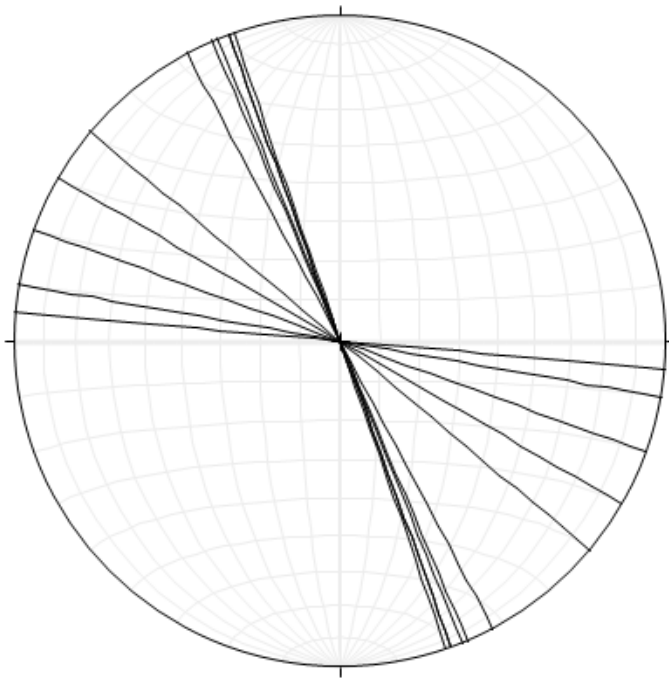


Figure 23 - Stereonet plot of the strikes of the garnet veins (Rick Allmendinger's Stereonet).

4.2.1.2 Layer with large omphacites

A layer was found that contained euhedral omphacite crystals up to several cm long, in a fine grained matrix possibly consisting of amphibole and quartz (Figure 24). The layer was oriented approximately E-W and folded due to compression, also in E-W direction. The internal distribution of the elongated omphacite crystals were, however, not systematic, indicating a static regime locally within the layer during deformation (Figure 24).

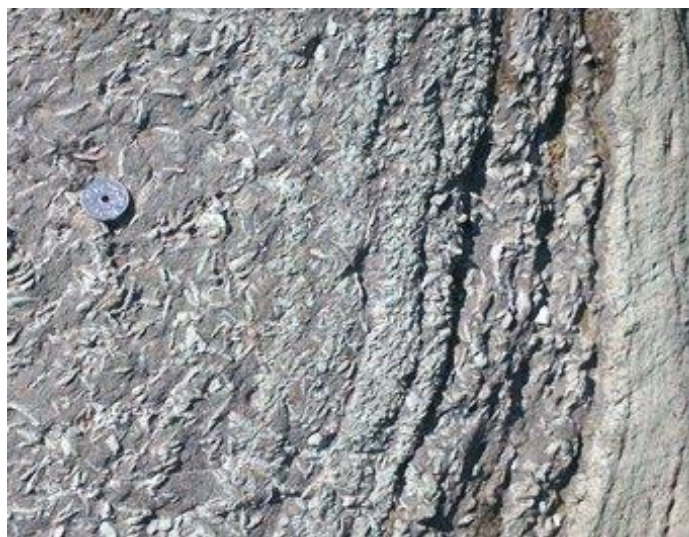


Figure 24 - Layer with large omphacite crystals in amphibole matrix.

4.2.1.3 Coarse grained quartz + omphacite + rutile veins

When studying the blasted outcrop where samples SK-16 to SK-23 were collected, several quartz rich hand specimens containing omphacite and rutile crystals up to 4 cm across were found. Similar material was found in situ, often occurring as smaller quartz + omphacite + rutile domains (Figure 25 A). They are often found in association with boudin appearing structures, and may hence be considered as mineral precipitation in the pressure shadows around competent material as eclogite boudins during deformation (figure 25 B)

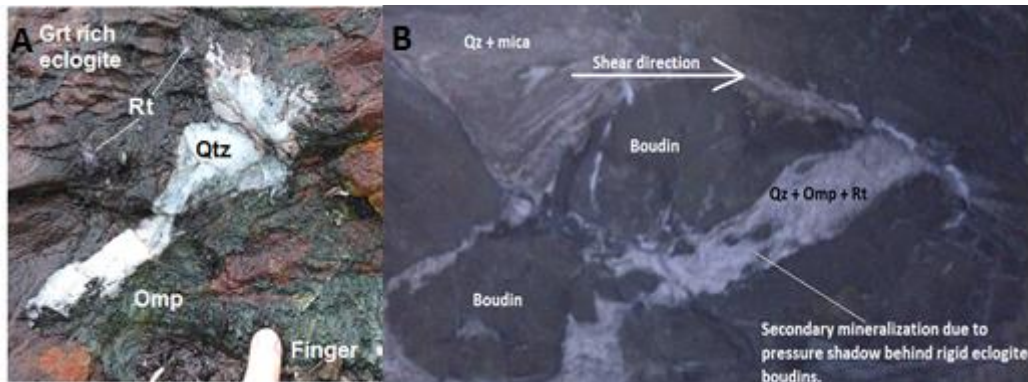


Figure 25 - A) Quartz, omphacite, rutile vein possibly developed in a pressure shadow between boudins (B).

Continuous veins up to 10-15 meters long were found inside the Vevring tunnel (Figure 95 in Section 10.8). Since the veins do not show any alteration of the eclogite wall rock (Figure 26) in addition to containing omphacite, they are considered eclogite facies veins. The veins often occur in garnet rich zones, maybe indicating a more competent composition.



Figure 26 - 1 cm large rutile crystal in quartz vein. Notice the absence of alteration of the wall rock.

4.2.1.4 Quartz/mica veins

The quartz/mica veins are a common vein type at Engebøfjellet. They are most likely close related to the quartz + omphacite + rutile veins described above. The veins usually consist of a quartz core, with increasing mica content towards the contact to the eclogite wall rock. Larger rutile crystals are also found in these veins. No significant alteration of the surrounding eclogite is observed, indicating eclogite facies. The mica appears to be strongly oriented towards parallelism with the vein, and show intense folding. This indicates a deformation within the vein, most likely syntectonic. Within some of the veins, larger clasts of eclogite are found, and these

appear to have been rigid during internal deformation of the vein, and cause quartz fillings in the pressure shadows (Figure 27).

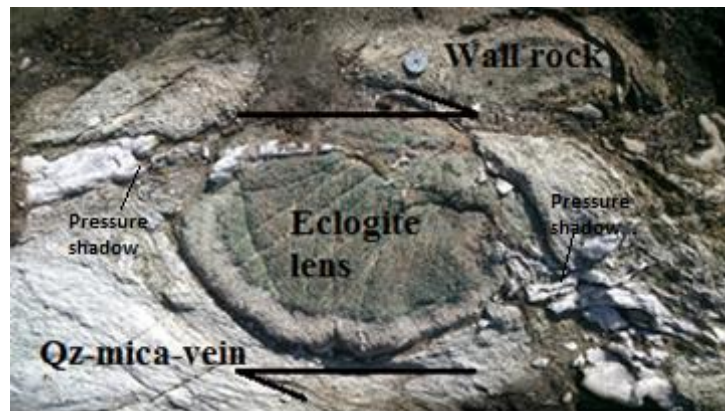


Figure 27 - Eclogite inclusion in quartz/mica vein. The eclogite behaved rigid during ductile deformation of the vein.

The mica and boudinages indicate a high overall strain, and the veins are interpreted to have formed as brittle structures due to a high rate of deformation in a fluid rich system (See section 10.8). This high rate of deformation would be possible in a shear zone, maybe associated with flanks of larger folds. Similar smaller veins are observed in fold flanks of asymmetric folds (Figure 28) at several locations.



Figure 28 - quartz/mica vein developed in the flank of asymmetric fold.

Based on the strike of 7 quartz/mica-veins they show a systematic orientation (Figure 29).

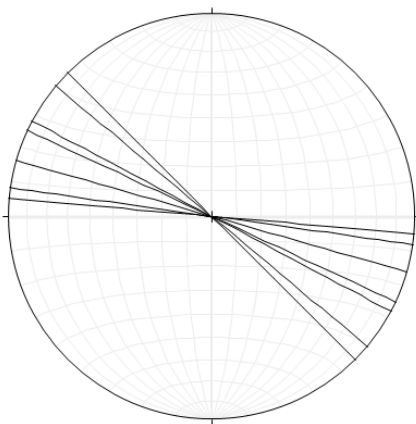


Figure 29 - Stereonet plot of the strikes of 7 quartz/mica veins (Rick Allmendinger's Stereonet).

4.2.1.5 Rutile layers

Layers are found in the eclogite, containing close to 100 % rutile. The layers follow the foliation within garnet segregations containing >80% garnet (Figure 30 and figure 31). They are narrow, rarely exceeding 1-2 mm width, and can be followed for up to 1 meter more or less continuous. Even though they are usually fine grained, several larger rutile grains can be found associated to them. These layers may be results of FeTi-rich layers in the fractionated gabbroic protolith.

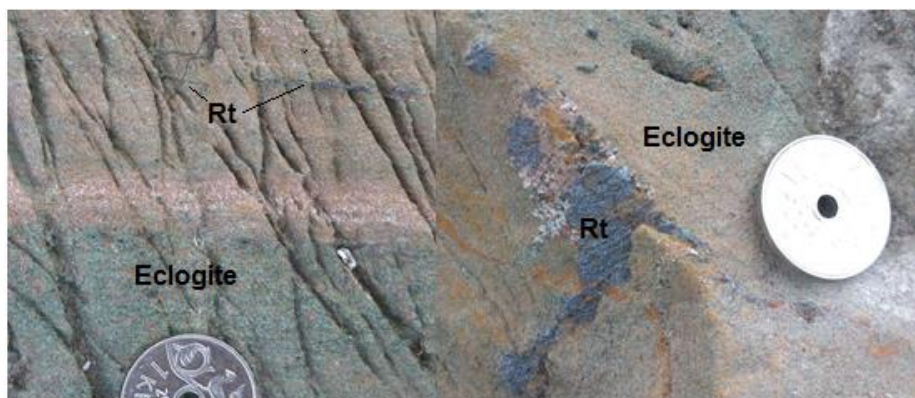


Figure 30 - Rutile layering following the foliations in garnet rich zone of the eclogite.

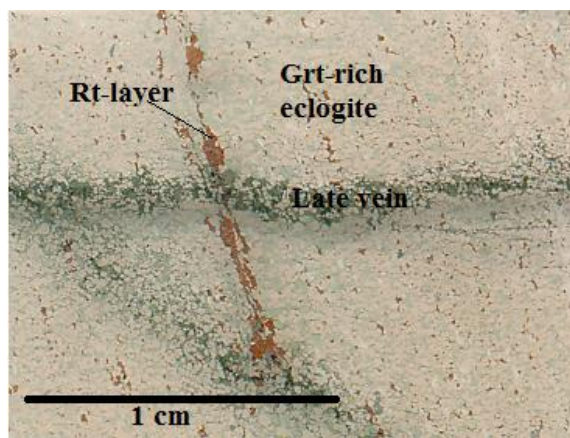


Figure 31 - Outcrop from thin section of sample SK-20, showing part of a rutile layer in garnet rich eclogite.

The orientations of the veins are based on 6 measurements and are presented in figure 32.

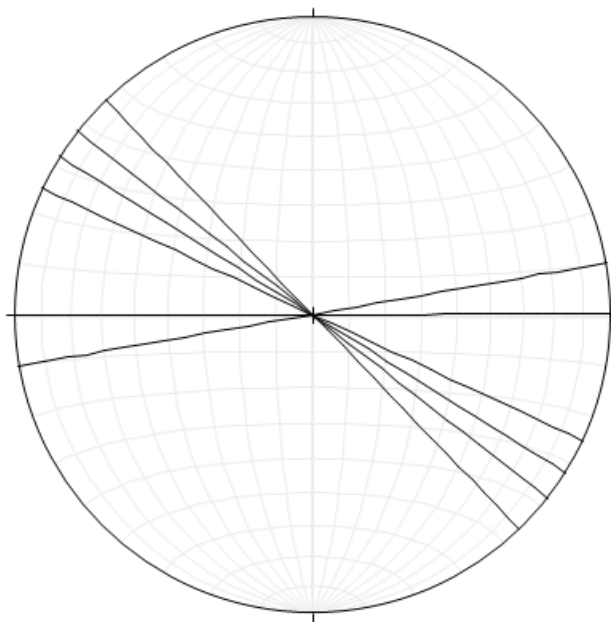


Figure 32 - Stereonet plot showing orientation of 6 rutile veins. (Rick Allmendinger's Stereonet).

4.2.2 Late fractures and veins

Furrows (Figure 33 A) observed in the surface are often associated with later veins and fractures. They get their characteristic surface appearance due to the weathering of weaker minerals. In fresh surfaces they appear as narrow veins typically <0.5 cm wide with a dark green color due to the alteration of pyroxene to amphibole (Figure 33 B). Some wider zones up to 20 cm are also observed (Figure 34). The wider zones may be considered as alteration around veins associated with higher fluid fluxes than the narrow ones.

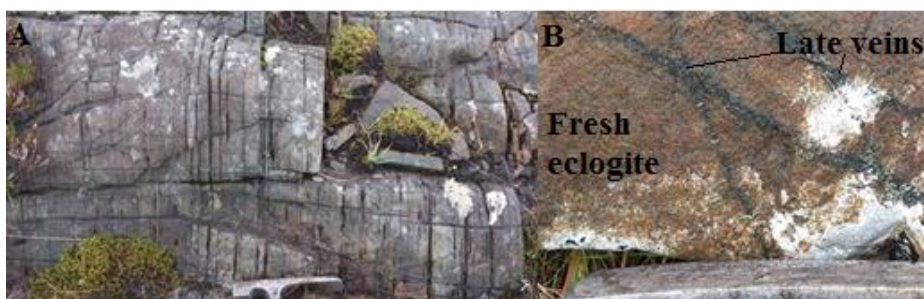


Figure 33 - A) Furrow found in the Engebøfjellet Eclogite due to weathering of late fractures. B) How the late fractures appear on unaltered surfaces. Hammer head as scale.



Figure 34 - Later vein of considerably larger size than normal.

They tend to form two sets almost perpendicular to each other. Within each set the fractures are more or less parallel suggesting a tensile origin.

On some surfaces the dip of the late veins are visible, and they usually show a dip between 30° and 50°. Strike/dip (Figure 35 A) and strike (Figure 35 B) measurement of the late veins are displayed in the stereo nets below. The strike/dip-measurements were done at a relatively small area (ca 50x50 meters), and they show a strong clustering towards NE-SW, indicating tension in NW-SE direction. The strike-measurements were done at a larger area (ca 200x200 meters), and show a general clustering towards NNE-SSW.

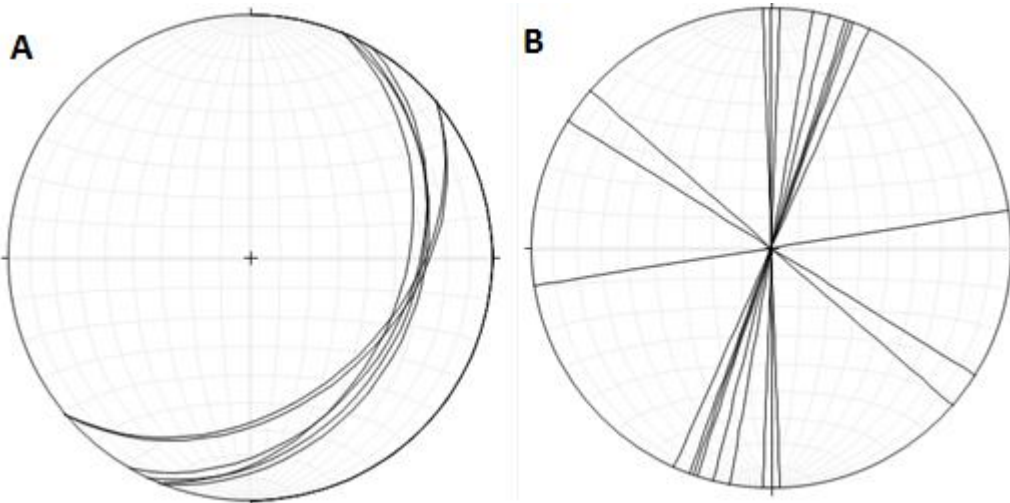


Figure 35 - Stereonet plot of A) Strike/dip of late veins and B) Strike directions of late veins. (Rick Allmendinger's Stereonet).

5. Bulk rock analyses

The bulk rock chemistry from XRF of 9 samples is presented in table 4, showing the differences in the low FeTi leuco-eclogites (SK-30 and SK-31) relative to the high FeTi ferro-eclogites. The table is recalculated with respect to loss on ignition (see section 3.3).

Table 4 - Bulk rock chemistry from XRF of 9 samples from the Engebøfjellet Eclogite.

	SK-7	SK-8	SK-9	SK-11	SK-12	SK-20	SK-29	SK-30	SK-31
SiO ₂	44,27	43,80	43,91	43,56	42,91	41,71	44,24	45,85	48,74 %
TiO ₂	5,37	4,89	5,21	3,04	4,23	3,34	4,76	2,19	0,98 %
Al ₂ O ₃	13,63	13,77	13,55	13,04	14,42	15,78	13,39	15,18	17,23 %
Fe ₂ O ₃	18,44	17,68	18,25	17,71	21,50	23,45	18,04	14,84	9,48 %
FeO	0,00	0,00	0,00	0,00	0,00	0,00	0,00	0,00	0,00 %
MnO	0,21	0,20	0,20	0,21	0,23	0,21	0,20	0,21	0,15 %
MgO	5,65	5,29	5,66	5,74	5,78	4,56	5,89	7,04	6,38 %
CaO	9,97	9,91	9,76	9,53	8,86	7,83	10,56	9,32	8,33 %
Na ₂ O	2,54	2,37	2,28	3,08	2,33	1,43	3,08	2,80	4,43 %
K ₂ O	0,26	0,41	0,21	0,36	0,09	0,02	0,17	0,36	0,54 %
P ₂ O ₅	0,02	0,05	0,06	0,04	0,01	0,03	0,02	0,24	0,12 %
LOI	-0,68	0,51	-0,85	0,97	-0,65	-1,51	-0,15	0,19	2,05 %
Total	99,68	98,89	98,26	97,30	99,74	96,89	100,22	98,24	98,48 %

Samples SK-30 and SK-31 were considered in the field to be amphibolitized. From thin section studies, however, these two samples are found to be well preserved leuco-eclogite. SK-30 is very fine grained and SK-31 is coarser grained with abundant amphibole, causing the hand specimen to appear amphibolitized (See section 10.9). The other samples are considered ferro-eclogite. Applying the classification from Korneliussen *et al.* (1998) on the samples in table 4, only SK-31 is a true leuco-eclogite, while SK-30 is slightly too rich in Fe₂O₃. The leuco-eclogite is also richer in Si, Al, Na and P than the ferro-eclogite.

Recorded diffractogram were quantified using the Bruker-AXS's Topas R 3.0 software package (Total Pattern Analysis Software), which uses a Rietveld method. Crystal structure information used for the refinements was taken from the Bruker Structure Database. The default mineral structural formulas in Topas were refined from EMP analyses in order to resemble the actual mineral chemistry in the Engebøfjellet Eclogite. Since refinement of the mineral structures is time consuming, one set of structural formulas was made. The mineral chemistry varies from leuco-eclogites to ferro-eclogites (See section 7). Hence the refined structural formulas are not perfectly fitted to every sample. Topas fitted the refined minerals to the X-ray diffractogram and from the intensities the weight percent of the minerals were calculated (Table 5).

Table 5 - Results from quantitative XRD of samples from the Engebøfjellet Eclogite. Quantification is done using a Rietveld method.

Phase	SK-7	SK-8	SK-9	SK-11	SK-12	SK-20	SK-29	SK-30	SK-31
Garnet	38,32 ($\pm 1,17$) %	37,63 ($\pm 1,26$) %	40,37 ($\pm 1,08$) %	35,59 ($\pm 1,20$) %	41,22 ($\pm 1,47$) %	57,73 ($\pm 1,77$) %	33,28 ($\pm 1,14$) %	32,48 ($\pm 1,35$) %	18,88 ($\pm 0,87$) %
Omphacite	47,1 ($\pm 1,35$) %	43,19 ($\pm 1,46$) %	45,57 ($\pm 1,32$) %	46,72 ($\pm 1,47$) %	32,05 ($\pm 1,62$) %	26,24 ($\pm 1,26$) %	33,87 ($\pm 1,38$) %	38,25 ($\pm 1,95$) %	28,11 ($\pm 1,48$) %
Amphibole	4,21 ($\pm 1,08$) %	2,81 ($\pm 0,93$) %	3,56 ($\pm 0,99$) %	9,74 ($\pm 1,11$) %	19,37 ($\pm 1,32$) %	4,63 ($\pm 1,71$) %	12,80 ($\pm 1,14$) %	20,56 ($\pm 1,32$) %	18,64 ($\pm 1,26$) %
Pyrite	0,64 ($\pm 0,45$) %	0,37 ($\pm 2,07$) %	0,35 ($\pm 0,36$) %	0,61 ($\pm 0,36$) %	0,73 ($\pm 0,51$) %	0,39 ($\pm 0,45$) %	-	0,65 ($\pm 0,45$) %	0,11 ($\pm 1,48$) %
Rutile	5,33 ($\pm 0,61$) %	4,31 ($\pm 0,45$) %	5,17 ($\pm 0,45$) %	3,16 ($\pm 0,48$) %	3,45 ($\pm 0,51$) %	3,20 ($\pm 0,42$) %	4,61 ($\pm 0,45$) %	1,98 ($\pm 0,39$) %	2,21 ($\pm 0,72$) %
Quartz	4,05 ($\pm 0,54$) %	5,65 ($\pm 0,54$) %	4,99 ($\pm 0,51$) %	3,16 ($\pm 0,51$) %	-	6,90 ($\pm 0,57$) %	1,52 ($\pm 0,33$) %	5,64 ($\pm 0,57$) %	6,37 ($\pm 0,51$) %
Phengite	0,35 ($\pm 0,87$) %	1,42 ($\pm 1,35$) %	-	1,03 ($\pm 1,5$) %	-	0,27 ($\pm 0,54$) %	0,33 ($\pm 0,69$) %	0,44 ($\pm 1,98$) %	2,08 ($\pm 0,90$) %
Epidote	-	3,89 ($\pm 1,26$) %	-	-	-	-	4,13 ($\pm 1,20$) %	-	-
Ilmenite	-	-	-	-	-	0,63 ($\pm 0,75$) %	0,39 ($\pm 0,54$) %	-	0,13 ($\pm 0,60$) %
Paragonite	-	-	-	-	-	-	-	-	7,36 ($\pm 1,20$) %
Albite	-	-	-	-	-	-	8,39 ($\pm 1,17$) %	-	16,14 ($\pm 1,41$) %

From Table 4, only SK-31 is a true leuco-eclogite. However, SK-30 will further be treated as a leuco-eclogite since it is close to 14 wt. % Fe₂O₃, and hence significantly poorer in Fe₂O₃ than other ferro-eclogitic samples. SK-30 and SK-31 are significantly lower in rutile. SK-30 is in the lower range of the garnet abundances, while SK-31 is significantly lower. The mica content of SK-31 is, as expected, significantly higher than in the other samples. The two leuco-eclogitic samples are higher in amphibole than the ferro-eclogite, and also relative high in quartz. Based on BSE and EDS, the abundance of albite in SK-31 must be considered a wrong estimate. Some albite is found in symplectites around omphacites, but not enough to account for 16 wt. %. BSE and EDS determination of mica showed that paragonite was found in SK-30 (one observation) and abundantly in SK-31. However, a ratio of almost 4:1 between paragonite and phengite in SK-31 is significantly higher than expected. Ilmenite is, as expected, most abundantly found in the two most retrograded samples (SK-20 and SK-29).

The total weight percent is always normalized to 100%, and all phases found in table 5 are identified either directly from the XRD diffractogram or from BSE/EDS analyses. Several phases were observed at the BSE/EDS but could not be fitted to the diffractogram. This includes albite in SK-20 and epidote in SK-31. If an abundant phase in the sample is not fitted to the XRD diffractogram, the included phases will be overestimated due to the normalization.

For several phases, the uncertainty is greater than actual abundances showing the weakness of this quantification for the minor phases. For phases with abundances >5 wt. %, the method at least gives results that can be compared between samples. The results in table 5 are estimates from a best possible fit to the XRD-diffractogram, and overlapping peaks in the diffractogram can thus cause errors when estimating the abundances.

From scatter plots of oxides versus mineral abundances, several strong correlations were observed: Garnet correlates positively with Fe_2O_3 , and negatively with MgO , SiO_2 , Na_2O and K_2O . Omphacite correlates positively with CaO and negatively with Al_2O_3 . Rutile correlates positively with TiO_2 and negatively with Al_2O_3 . These observations conclude that the bulk rock chemistry affects the abundances of the mineral phases present.

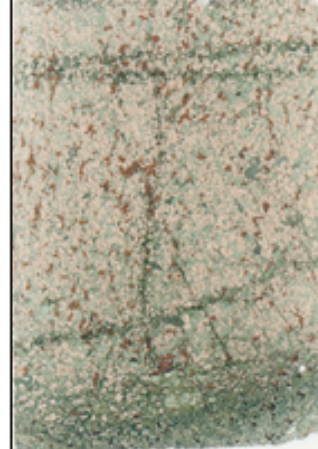
6. Petrology

In the petrology section, the mineral assemblages and texture of the different metamorphic facies found in samples from Engebøfjellet are described. In the core of the Engebøfjellet lens, the eclogite is well preserved. Towards the contact to the gneissic host rock and within later shear zones, however, the eclogite is extensively retrograded. In the following pages, a table describing mineralogy, texture and veining based on optical microscopy is presented. Larger images of the thin sections are found in Appendix 2.

Sample	Thin section	Mineralogy	Texture	Veining
SK-2		Garnet, pyroxene, amphibole, rutile, mica and ilmenite.	Euhedral to subhedral Grt 0.1 to 0.5 mm in diameter. Eclogite facies Amp may grow up to several mm. Elongated minerals make up foliation ESE-WNW in thin section.	Several narrow amphibolite facies veins cutting foliation. Also Grt seems to alter in contact with veins. Narrow alteration zone. No significant alteration.
SK-3		Garnet, pyroxene, amphibole, rutile, ilmenite, hematite (?), pyrite and plagioclase.	Dominated by euhedral to subhedral Grt and subhedral to anhedral Px. Grt and Px from 0.1 to 0.3 mm. Foliation defined by elongated Rt and Px and is NE-SW in thin section.	Two significant veins, approx. parallel to E-W in thin section. 1 and 2 mm alteration zone of Px (to Amp) and Rt (to Ilm). Also some alteration of Grt and eclogite facies Amp.
SK-4		Garnet, pyroxene, amphibole, rutile, pyrite, mica and quartz.	Dominated by cm size Px with Grt and Amp inclusions. Near euhedral Px and Amp. Some orientation into a SW-NE foliation. Grt rarely exceed 0.25 mm. Sub-Euhedral Px, Mca and small Amp.	Alteration along grain boundaries of large Px to symplectitic Amp and Pl.
SK-6		Garnet, pyroxene, amphibole, rutile, quartz, mica and ilmenite.	Sub to euhedral Grt. Up to 2.5 mm, but in general 0.25 to 0.6 mm. 1) Fresh eclogite. 2) 7-8 mm > 90% Grt. 3) Vein zone with SBM Qtz, Grt and Amp. 4) partly oriented Px and Mca growing around Grt.	Vein seems to change the mineralogy and chemistry in the surrounding eclogite by extraction of Px and Amp, and enrichment in Grt. No alteration of eclogite wall rock, hence eclogite facies vein.

SK-7		Garnet, pyroxene, amphibole, rutile, ilmenite, pyrite, quartz and mica.	Sub to euhedral Grt generally < 0.5 mm. Px grows in between Grt with no systematic orientation. Amp typically as larger sub to anhedral crystals up to a couple of mm. No observed foliation.	No observed veining, and sample appears to be fresh eclogite.
SK-8		Garnet, pyroxene, amphibole, rutile, ilmenite, pyrite, mica, quartz and calcite.	Close to euhedral Grt and mica. Sub to anhedral Px and Amp. Grt typically from 0.1 to 0.7 mm. On thin section scale layered with respect to Grt and Px + Amp. E-W foliation in thin section.	Several narrow veins sub parallel to foliation. Within one zone several smaller fractures. Making up alteration zones up to 2 mm. Dominated by Amp and Ilm. Some alteration of Grt. In contact, Rt is altered.
SK-9		Garnet, pyroxene, amphibole, rutile, ilmenite, pyrite, quartz and mica.	Sub to euhedral Grt generally between 0.2 and 0.3 mm. Px and mica appears subhedral and elongated into E-W foliation in thin section. Larger randomly distributed eclogite facies Amp grains.	No specific veining, but areas with Qtz concentration show minor alteration of Px into symplectites.
SK-11		Garnet, pyroxene, amphibole, rutile, ilmenite, pyrite, mica, calcite and quartz.	Grt are mostly subhedral and between 0.25 and 0.5 mm. Px are sub to anhedral up to 3 mm. Strongly fractured in NNW-SSW direction best observed in the Grt.	The only veining are the fractures. There is some alteration of Px to Amp and of Rt to Ilm.

SK-12		Garnet, pyroxene, amphibole, rutile, ilmenite, quartz and pyrite.	Sub to euhedral Grt from 0.05 to 0.5 mm. Generally fine grained. Rt, Px and Amp are generally elongated and define an E-W foliation.	The only veinings are two vein appearing rutile aggregates parallel to foliation. Often associated with larger Amp, and can be tracked or traced for over 1 cm.
SK-13		Garnet, pyroxene, amphibole, rutile, ilmenite, quartz and apatite.	Dominated by fine grained sub to euhedral Grt and sub to anhedral Px. Grt is typically between 0.05 and 0.2 mm. Several zones contain Px and Amp exceeding 1 mm.	Several veins with alteration zones up to 1.5 mm. The largest contain a visible core of Pl. Px is completely altered to Amp, while Grt and Rt in general remain unaltered. In direct contact, Rt is altered to Ilm. Grt-amphibolite facies?
SK-15		Garnet, pyroxene, amphibole, rutile, ilmenite, quartz and calcite.	Grt are typically euhedral and between 0.3 and 0.5 mm. Px and Amp is sub- to anhedral and together with rutile aggregates they make up E-W foliation. Zones of fine grained garnet, maybe due to shear zones?	Two types of veins: 1) Narrow fractures with almost no alteration zone and 2) wider zone with approx. 1 mm alteration zone. Both alter eclogite facies minerals. Ilm with Rt core within vein zone.
SK-16		Garnet, pyroxene, amphibole, rutile, ilmenite, quartz and hematite (?).	Dominated by sub to euhedral Grt between 0.25 and 0.5 mm. Grt found as coronas around Rt. Some zones with primarily Amp. Foliation is not observed.	Two sub parallel veins of presumably the same generation and facies. Alters Grt, Px and Rt. Some relict Grt within vein zone. Large rutile grains are only altered at grain boundaries and where vein physically cut the grains.

SK-19		Garnet, pyroxene, amphibole, rutile, ilmenite and quartz.	Sub to euhedral Grt typically < 0.5 mm, but also significantly smaller. Sub to anhedral Prx and Amp without strong orientation. Rutile aggregates defines a vague SW-NE foliation.	Several E-W and N-S cracks. Only one of the E-W cracks shows significant alteration. Ca 0.5 mm alteration zone where Prx is altered to Amp and cut Rt grains are altered to Ilm. N-S are more fluid migration along grain boundaries and alters Ptx to Amp, but not Rt.
SK-20		Garnet, amphibole, pyroxene, rutile, ilmenite, quartz, epidote, calcite and pyrite (?).	Sub to euhedral Grt < 0.5 mm. Some zones contain very fine grained (0.05 to 0.2 mm) Grt and Qtz. Elongated Ptx and traces of Grt, Rt and Qtz yield an approx. E-W foliation.	Two alteration veins cutting each other. Seems to be of same facies based on mineralogy. From 1 to 1.5 mm wide alteration zones and Ptx is readily altered to Amp and Pl. Mineral growth approx. perpendicular to vein. Rtx is altered to Ilm. Larger Rt aggregate sub parallel to foliation.
SK-27		Garnet, pyroxene, amphibole, rutile, ilmenite, quartz, calcite and pyrite.	Sub to euhedral Grt between 0.2 and 0.4 mm. Sub to anhedral Ptx and Amp grow in between. Also larger (ca 1 mm) Amp commonly with Rt and Grt inclusions. Symplectitic texture of Amp and Pl in wide alteration zone.	Appears to be two major generations of veining. NE-SW: pervasive without larger alteration zones. Ptx, Rt and Grt are altered. E-W: > 5 mm alteration zone. Complete alteration of Ptx and Rt. Small veins only alter Rt in grain boundaries, but larger veins alter more (>75%) as well as Grt → Greenschist-Amp facies.

SK-28		Garnet, pyroxene, amphibole, rutile, ilmenite, quartz, calcite, plagioclase and pyrite.	Eclogite: Sub to euhedral Grt <0.5 mm. Sub to anhedral Prx and Amp that grow in between Grt. Also Grt inclusions in Amp. No foliation. In vein: Coarser grained minerals, with up to 1.5 cm Omp. Also >3 mm Cal.	Half of thin section is vein dominated by large heavily altered Omp crystals and Qtz. Approx. 5 mm. Amp dominated zone towards the eclogite is heavily altered with respect to Prx, Grt and Rt. Some relict Rt and Grt remains.
SK-29		Garnet, pyroxene, amphibole, rutile, ilmenite, mica, quartz, feldspar and pyrite.	Sub to euhedral Grt > 0.5 mm and sub to anhedral Amp and Prx. Some Amp is rather large (1x1 mm). Amp and Prx is elongated due to the approx. N-S foliation.	Three major amphibolite facies veins in thin section. 3-5 mm alteration zones. Strong alteration of Prx, Rt and Grt. Core with Qtz and Pl. Fluids along grain boundaries around vein cause minor alteration.
SK-30		Garnet, pyroxene, rutile, mica, quartz and pyrite.	Dominated by sub to euhedral Grt (<0.25 mm) and sub to anhedral Prx. E-W foliation defined by elongated Prx and Rt. Alternating layers of coarse and fine grained Grt. Vague kinematic indicators yield dextral sense of shear.	Minor veining, but one perpendicular to the foliation have a 0.1 mm alteration zone, where Prx is altered to Amp and Rt is altered to Ilm in direct contact to the vein.
SK-31		Garnet, pyroxene, amphibole, rutile, mica and calcite.	Large sub to euhedral Prx up to 3 mm dominates the thin section. Two types: 1) Needle shaped, and 2) more rounded. Oriented into sub parallelism with E-W foliation. Prx typically have inclusions of euhedral Grt. Several shear zones (?) containing mica.	Some mica rich shear zone appearing veins are the only veins present in this thin section. No alteration of eclogite facies mineralogy indicating eclogite facies structures.

6.1 Eclogite facies

Eclogite facies samples from Engebøfjellet consist of garnet (Grt, 20-50%), omphacite (Omp, 10-40 %), amphibole (Amp, 10-40 %) in addition to minor rutile (Rt), quartz (Qz), carbonate (Cb), sulfides and zircon (Zrn). The abundance of mica and epidote (Ep) varies from minor phases in ferro-eclogite to major phases, at least mica, in the leuco-eclogite. The listed minerals coexists in textural equilibrium (Figure 36), meaning they show a metamorphic texture with triple junctions at contacts between minerals.

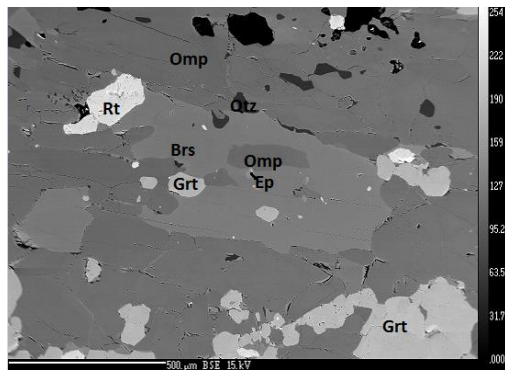


Figure 36 - BSE image from sample SK-28.

The modal sum of Amp and Omp varies somewhat from sample to sample, but the ratio between the two, however, varies strongly. Some samples are almost completely dominated by Amp (Figure 37 A), and some are almost completely dominated by Omp (Figure 37 B).

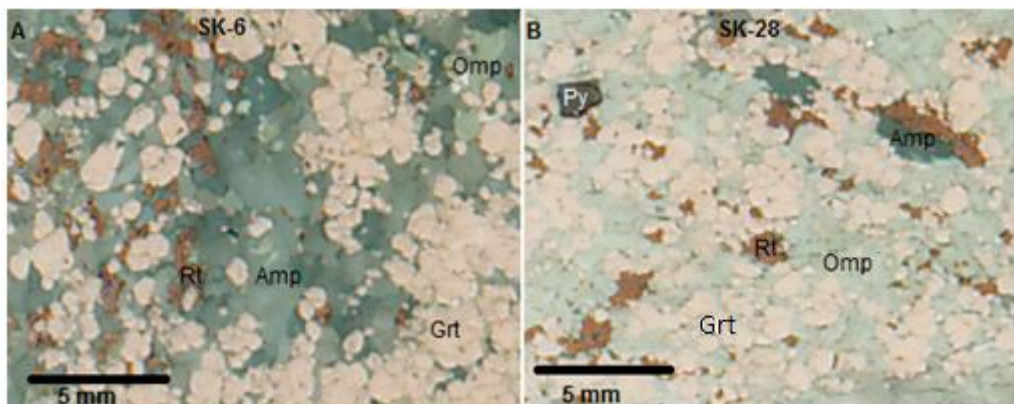


Figure 37 - Figure showing difference in modal abundance of Omphacite and Amphibole. A is from SK-6, and B is from SK-28.

In general, ferro-eclogite is richer in Grt and Rt, reflecting its FeTi-rich composition (Korneliussen *et al.*, 1998) while leuco-eclogite is richer in Qz and mica. This causes the leuco-eclogite to be paler and less dense than the ferro-eclogite, hence the definition.

The garnet is typically fine grained (0.1-1 mm) and euhedral to subhedral. At a few localities larger (>1 cm) Grts are found. In hand specimens the Grt is dark red, and pale red in thin sections. They are often found in clusters or layers parallel to the foliation if well developed, and are hence not always homogenously distributed. Mineral inclusions in Grt are common, and more common in larger Grt. The inclusions (Figure 38) are composed of Omp, Amp, Rt and minor Qz, Cb, Zrn and sulfides. The eclogite facies inclusions are anhedral, and often show a strong zoning towards the rim.

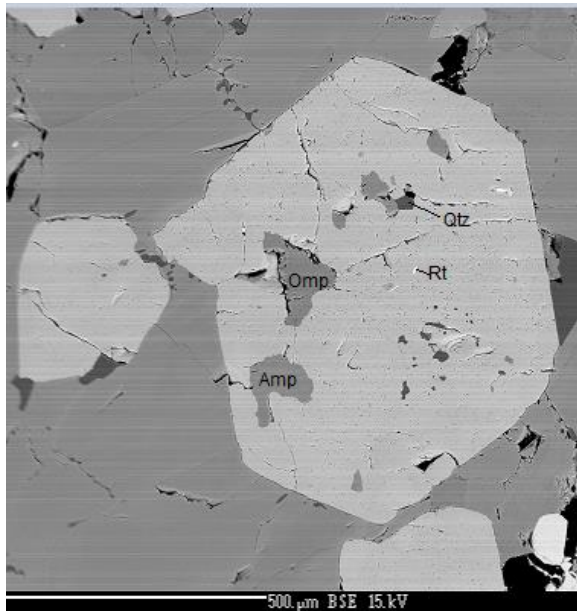


Figure 38 - BSE image of ca. 1 mm Grt with several different inclusions. Sample SK-6.

The omphacite is pale green (relative to Amp) and typically occur as elongated, subhedral to anhedral grains. In some samples euhedral to subhedral cm sized Omp (Figure 39 A) are found with abundant eclogite facies mineral inclusions. Omp in textural equilibrium tends to make up the foliation (Figure 39 B), indicating an eclogite facies deformation event. Pyroxenes reaching several cm long with Omp cores are found in veins. They show random orientation, indicating static growth at eclogite facies conditions. Later alteration, however, has altered the Omp, and they are strongly zoned (see section 7.2), often leaving a relict Omp core and symplectitic rims.

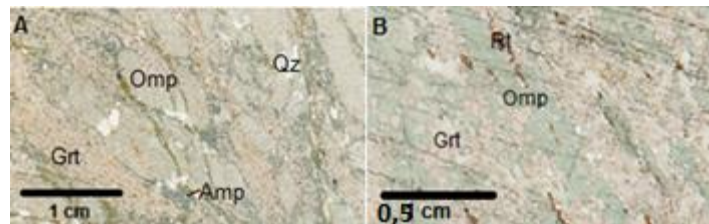


Figure 39 - A) Large Omp from SK-4. B) Matrix foliation developing Omp from SK-2.

Amphibole is usually abundant, and found in textural equilibrium with eclogite facies minerals. It is distinguished from Omp by showing a blue-green color and strong pleochroism in thin sections. Amp is found as both sub mm sized subhedral to anhedral matrix minerals (Figure 40 A) and as several mm sized euhedral to subhedral porphyroblasts (Figure 40 B). Inclusions in the porphyroblastic Amp are abundant, composed of primarily Grt, Omp and Rt (Figure 40 B). Whether or not the porphyroblastic Amp is a late (but still eclogitic) phase is unclear. The Grt inclusions are rounded, and thus not in textural equilibrium, and the amphibole appears to be growing around garnet when in contact to Omp. This implies a later growth of the porphyroblasts.

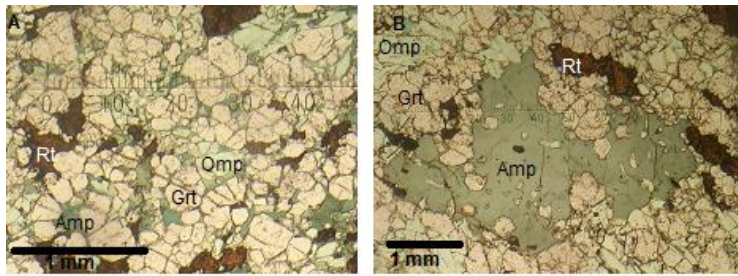


Figure 40 - A) Matrix amphibole from SK-12. B) Porphyroblastic amphibole from SK-3.

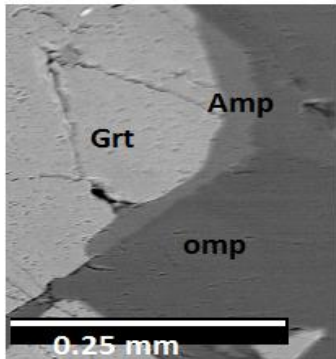


Figure 41 - BSE image showing late eclogitic amphibole after reaction of Grt and Omp.

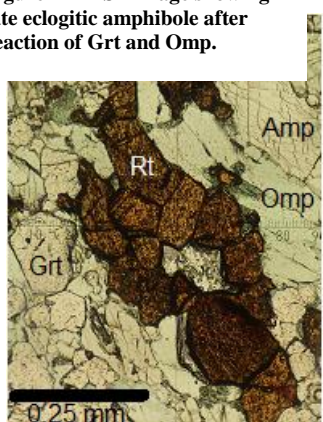


Figure 42 - Rutile cluster composed of several smaller rutile crystals from SK-29.

When in contact to Grt, Omp often reacts to form Amp (Figure 41). In optical light this amphibole is more distinct green than the bluer porphyroblastic and matrix Amp, and the pleochroism is weaker. The formation of these secondary Amp is not associated with later fractures or veins. The Amp in figure 41 appears to have grown into the Grt, and hence is a reaction product between the Grt and Omp. This reaction may be the same reaction as formed the large porphyroblasts, but the textural differences does not suggest this relationship.

In ferro-eclogitic samples, Rt is typically the fourth most abundant mineral. The modal abundance in these samples is 2-6 % causing the eclogite itself to be considered a rutile-ore. In leuco-eclogites the modal abundance of Rt is typically < 1%. In fresh eclogite the Rt is in textural equilibrium with the eclogite mineral assemblage, and often occurs as clusters composed of several sub grains (Figure 42). The rutile grain sizes vary widely from microscopic grains <0.01 mm to single grains >0.2 mm (For grain size distributions, see Appendix 4.1). The Rt clusters, however, may reach up to 5x5mm. In most of the ferro-eclogitic samples, the rutile is typically represented in grains ranging in size from 0.05 – 0.25 mm. The shape strongly depends on the amount of deformation; in mylonitized samples, the Rt is strongly elongated (Figure 43 A), while rounded in samples exposed to less deformation (Figure 43 B).

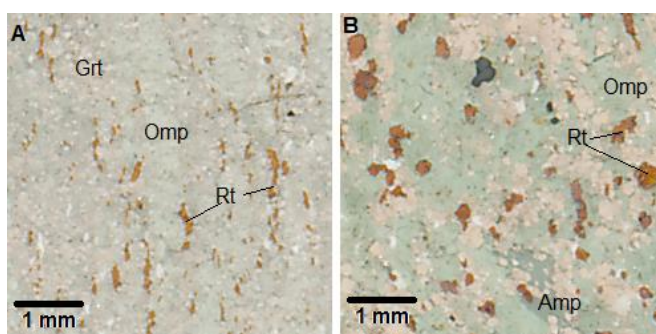


Figure 43 - A) Elongated rutile in mylonitized samples (SK-30) and B) rounded rutile from less deformed sample (SK-8).

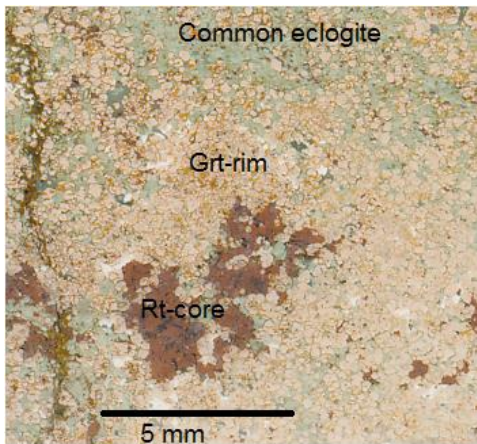


Figure 44 - Rt - Grt corona in SK-16.

Figure 44 shows a cluster of Rt surrounded by Grt. This corona structure is common and Rt rich zones are typically also rich in Grt. Since the core represents a Ti rich domain, and the Grt represents a Fe rich domain, this corona structure is considered a possible result of the in situ breakdown of ilmenite, leaving the Ti in the Rt and the Fe in the Grt. No relict Ilm from the precursor is found; hence documenting this reaction is difficult.

6.2 Amphibolite to greenschist facies

Fractures developed late during the exhumation are common to the eclogite (see section 4.2.2). These veins consist of albite ($An_{4.5-8.3}$) cores surrounded by an alteration zone up to several mm wide. Within the vein zones, Grt and Omp is absent –or remain as relicts– and the zones are dominated by Fsp of varying composition ($An_{0.9}$.

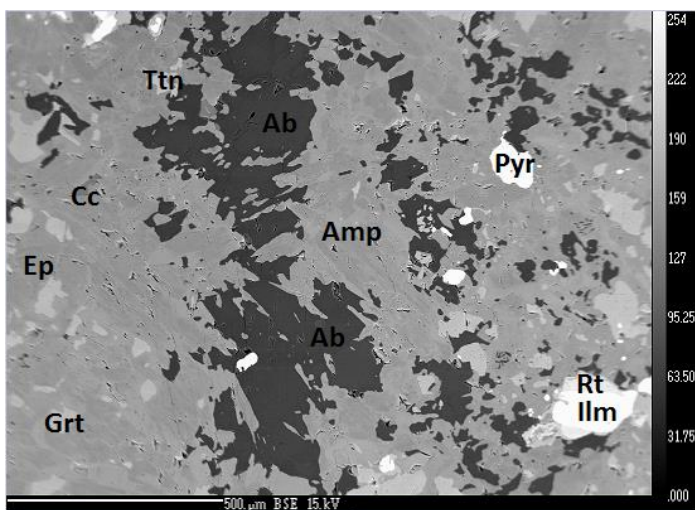


Figure 45 - BSE image showing symplectitic Amp and Ab from SK-29.

17.4), Amp, Ilm and Ttn showing symplectitic texture (Figure 45). Unfortunately, too few Fsp are analyzed during this thesis. How well the Fsp in the symplectites are equilibrated are not sure, but the Fsp in the veins are considered to be in equilibrium. In extensively retrograded areas, the eclogite mineral assemblages are completely replaced by amphibolite to greenschist facies parageneses dominated by Amp \pm Fsp ($An_{0.9-17.4}$) \pm Ep \pm Ilm \pm Cb \pm Ttn.

The symplectite grain size varies, but is usually cryptocrystalline with mineral grains only visible in microscope or with BSE imaging. In some cases the zones are several cm wide, and the symplectited area can be seen by the naked eye (Figure 46). Often the symplectites are limited to micrometer scale zones around relict omphacites and amphiboles (Figure 47).

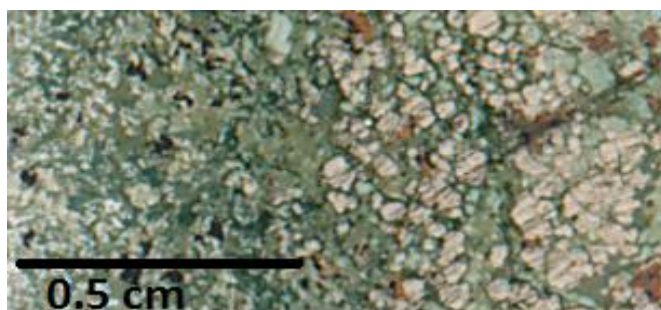


Figure 46 - Large symplectitic area from SK-27.

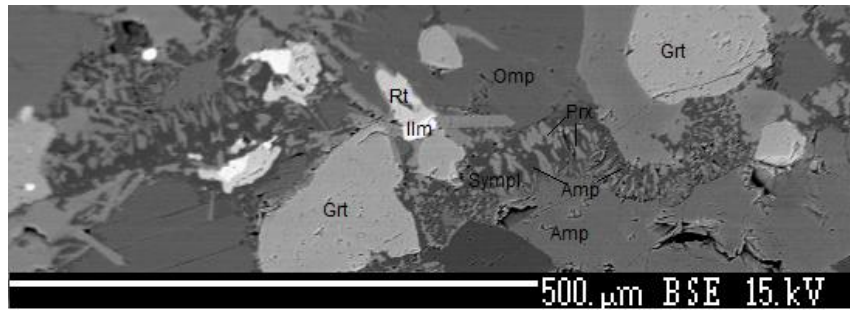


Figure 47 - Micrometer scale symplectites around relict Omp and Amp from SK-4.

The grain size within the symplectited area appears to depend on the size of the alteration zones. Narrow zones show low degree of alteration and also fine grained symplectites, whereas wide zones show high degree of alteration, and coarser grained symplectites. The minerals within the zones are usually the same, independent on the size, which indicates that the alteration zones of different sizes are of same metamorphic facies.

Figure 48 A shows a BSE image of a relict phengite (see section 7.9) grain surrounded by biotite and plagioclase symplectite in sample SK-28 (Figure 48 B). This indicates a breakdown of phengite, possible in association with the alteration of the wall rock.

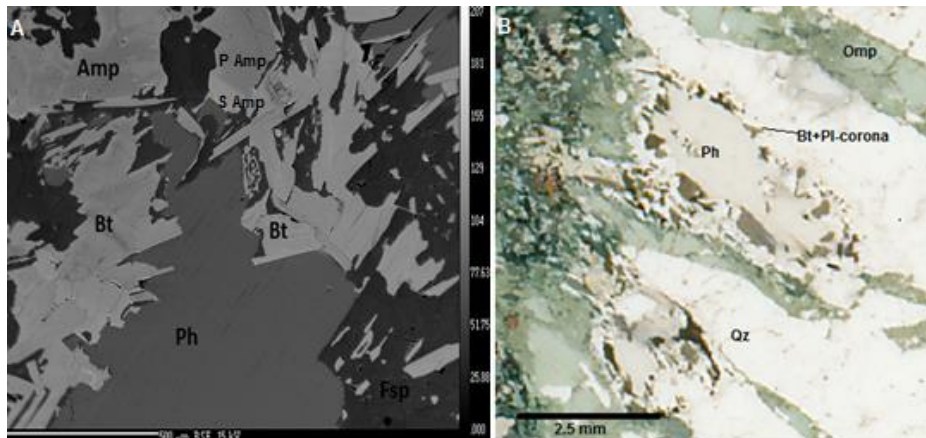


Figure 48 - Relict Ph with symplectitic Bt+Pl corona from SK-28.

Rutile breaks down in the wide alteration zones are more pervasive than in narrow alteration zones. The Rt grains are often partially altered, resulting in either coronas of IIm around Rt cores (Figure 49 A), or growth of IIm through the Rt, possibly due to fractures in the Rt grain (Figure 49 B).

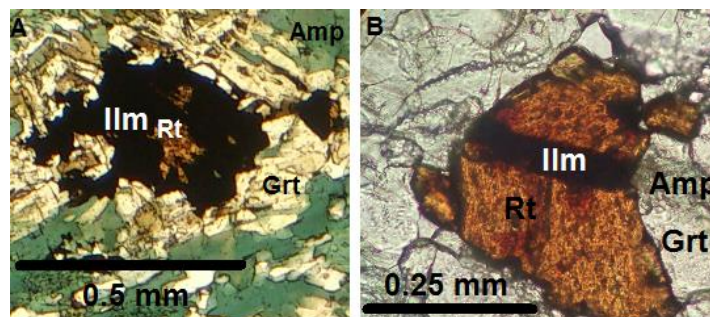


Figure 49 - A) Relict Rt with IIm corona from alteration zone in SK-28. B) Alteration of Rt along fracture in SK-8.



Figure 50 - Section of SK-6 with fresh eclogite (left), Grt concentration (middle) and Qz+Grt vein (right).

Within the vein zone in SK-6 (Figure 50), Grt is breaking down to form an Amp (Figure 51). Since Grt is not in contact to other eclogite facies minerals, except the quartz in the vein, the reactants forming this Amp are Grt \pm Qz \pm elements from a fluid present during alteration. This fluid might, of course, contain dissolved material, either from an external source, or from the breakdown of eclogite facies minerals in the wall rock.

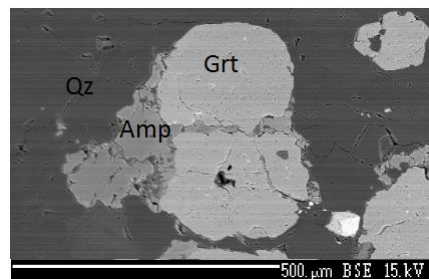


Figure 51 - Alteration of garnet to amphibole in quartz vein i SK-6.

7. Mineralogy

Based primarily on optical microscopy and EMP, the mineralogy and mineral chemistry is described. 13 thin sections from both ferro-eclogite and leuco-eclogite are analyzed at the EMP, and from the 650 analyses the chemistry of the minerals are determined. The mineral structural formulas are recalculated in Matlab (See appendix 6) based on the ideal number of cations and oxygens (see appendix 5). Since the microprobe detects all Fe as Fe^{2+} , Fe^{3+} is calculated based on charge balance, and is hence an assumption. For extended mineral chemical tables, see appendix 3.

7.1 Garnet

The garnets in the Engebøfjellet (Figure 52) eclogite do not show a wide variance in chemistry. Figure 53 is a

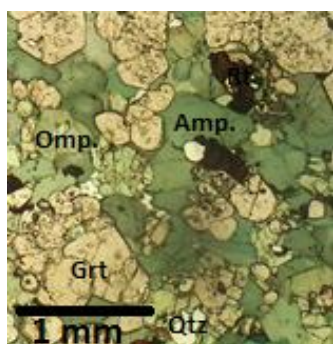


Figure 52 - Garnets from SK-6.

triangular plot of 224 garnets, represented by the end members almandine, grossular and pyrope. Figure 53 combines garnets from 15 samples distributed between ferro-eclogite and leuco-eclogite, as well as rim and core analyses. Garnets from ferro-eclogites are plotted in black, while garnets from leuco-eclogites are plotted in red. The garnets from ferro-eclogitic samples show compositions in the range of $\text{Alm}_{54.2-65.0}\text{Gro}_{17.5-29.8}\text{Pyr}_{8.8-19.0}\text{Spes}_{0.7-2.8}\text{And}_{0.0-2.1}$. Garnets from leuco-eclogitic samples show compositions in the range of $\text{Alm}_{51.0-60.4}\text{Gro}_{17.4-29.5}\text{Pyr}_{15.4-23.2}\text{Spe}_{0.6-3.1}\text{And}_{0.0-1.2}$. Figure 53 indicates that the leuco-eclogitic garnets are enriched in pyrope (Mg) relative to the ferro-gabbroic eclogite.

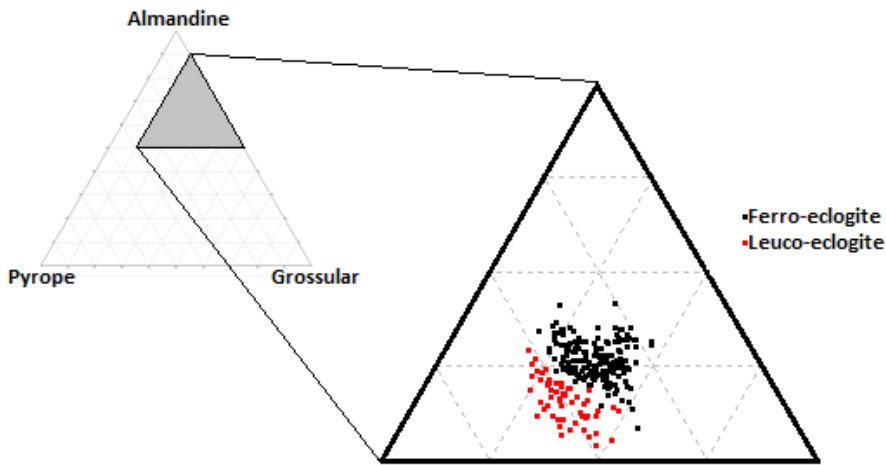


Figure 53 - Triangular plot in the Alm-Pyr-Gro system.

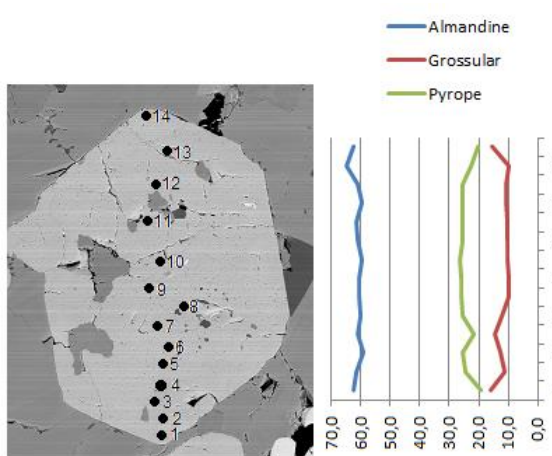


Figure 54 - Chemical profile across 1 mm Grt from SK-6.

Effort was put in finding zoning in the garnets but this rarely occurred in the fine grained eclogite representative for the samples. In SK-6, however a 1 mm euhedral garnet surrounded by amphibole was found, showing a weak zoning (Figure 54). 14 analyses were taken across the diameter of the garnet, and the graph within figure 54 shows the pyrope, grossular and almandine end member. The almandine component does not indicate any consistent zoning, while pyrope and grossular tend to vary opposite to each other. The pyrope content increases towards the rim, while the grossular component decreases.

A 3 mm garnet, also from SK-6, shows the opposite feature, and displays a lowered pyrope and elevated grossular content towards the rim. The garnet is in contact to a pyroxene, which may be the reason for the opposite zoning. The amount of the two components, however, are oscillating along the profile from the core to the rim, and the variation is less prominent than in figure 54. A plot of the Fe^{2+} , Ca and Mg is in agreement with the statement, that there is a coupled substitution between $\text{Ca} \leftrightarrow \text{Fe}^{2+} + \text{Mg}$.

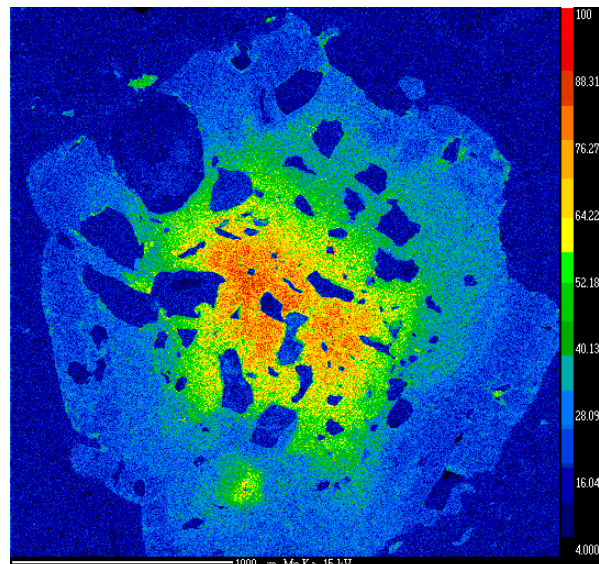


Figure 55 - Garnet from ME9.97-A showing strong Mn zoning.

Garnets from coarse grained eclogite at Engebøfjellet did show strong zoning. Figure 55 shows a ca 3 mm garnet from ME 9.97-A (Korneliussen *et al.*, 1998)

with a strong zoning with respect to Mn. Except from a small deviation, the Mn zoning is concentric with decreasing Mn towards the rim. A Mn map of a 1 mm garnet (Figure 56) from SK-6 show two distinct Mn concentrations. For an detailed chemical description of a zoned coarse grained garnet, see section 9.2.1.

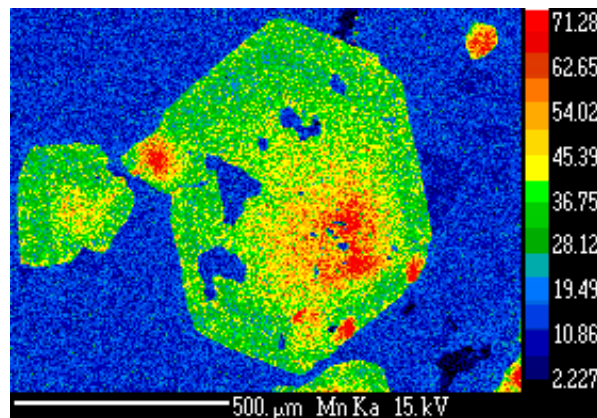


Figure 56 - Mn map of 1 mm garnet from sample SK-6.

Table 6 - Selection of analyses of garnets from ferro- and leuco-eclogite.

		Ferro-gabbroic eclogite				Interm. eclogite		Leuco-eclogite	
		SK-7		Sk-28		SK-31		SK-4	
Wt.% EMP	Comment	Rim	Core	Rim	Core	Rim	Core	Rim	Core
	SiO₂	38,02	38,22	38,17	38,13	38,94	38,44	38,18	37,64
	TiO₂	0,04	0,08	0,06	0,14	0,10	0,11	0,15	0,06
	Al₂O₃	21,13	21,05	21,71	21,07	21,78	21,57	21,44	21,47
	Cr₂O₃	0,00	0,00	0,03	0,01	0,03	0,00	0,00	0,00
	FeO	28,87	28,15	28,06	28,45	24,34	24,57	27,28	26,95
	MnO	0,33	0,61	0,50	0,57	1,01	0,91	0,75	0,82
	MgO	2,84	3,10	4,11	3,83	5,58	5,06	5,37	5,18
	CaO	9,34	9,29	8,30	8,34	9,11	9,22	7,03	7,31
	Na₂O	0,00	0,02	0,04	0,07	0,04	0,06	0,07	0,00
	K₂O	0,00	0,00	0,00	0,02	0,03	0,00	0,00	0,00
	Total	100,56	100,49	100,98	100,63	100,94	99,95	100,28	99,43
Structural formula 8 oxygen	Si	2,99	2,99	2,97	2,99	2,99	3,01	2,97	2,96
	Ti	0,00	0,01	0,00	0,01	0,01	0,01	0,01	0,00
	Al	1,96	1,96	1,99	1,94	1,97	1,98	1,97	1,99
	Cr	0,00	0,00	0,00	0,00	0,00	0,00	0,00	0,00
	Fe³⁺	0,05	0,06	0,07	0,08	0,04	0,00	0,08	0,09
	Fe²⁺	1,85	1,77	1,76	1,79	1,53	1,59	1,70	1,68
	Mn	0,02	0,03	0,03	0,04	0,07	0,09	0,05	0,05
	Mg	0,33	0,42	0,48	0,45	0,64	0,54	0,62	0,61
	Ca	0,79	0,75	0,69	0,70	0,75	0,78	0,59	0,62
	Na	0,00	0,00	0,00	0,00	0,00	0,00	0,00	0,00
	K	0,00	0,00	0,00	0,00	0,00	0,00	0,00	0,00
	Sum	8,00	7,99	7,99	7,99	7,99	8,00	7,99	8,00
Garnet endmember	Almandine	61,9	60,6	59,4	60,1	51,2	52,5	57,4	56,9
	Pyrope	11,1	12,1	16,1	15,0	21,5	19,7	21,1	20,5
	Grossular	25,6	25,6	22,6	22,6	24,6	25,3	19,0	19,9
	Spessartine	0,7	1,3	1,1	1,3	2,2	2,0	1,7	1,8
	Andradite	0,6	0,4	0,7	0,9	0,5	0,4	0,8	0,9
	Sum	100,0	99,9	99,9	99,9	99,9	99,9	99,9	100,0

Table 6 gives analyses of four garnets, two of them from ferro-eclogite and two from a leuco-eclogite. These garnets are smaller (<0.5 mm), but represent the average sizes in their respective thin sections. The zoning in these four garnets is less obvious than in Figure 54, but two show a higher pyrope content towards the rim.

7.2 Pyroxene

To give an impression of the chemistry of pyroxenes in Engebøfjellet, 120 pyroxenes from several samples are plotted in a triangular (Figure 57). The pyroxenes represent the eclogite facies, rock-forming pyroxenes, and thus excludes pyroxenes found in veins and altered pyroxene. These pyroxenes are treated below. All pyroxenes plot within the omphacite field, and figure 57 shows how the chemistry vary between ferro-eclogite (black) and leuco-eclogite (red). The leuco-eclogite hosts omphacite with higher jadeite (Jd_{36-42}) content relative to the ferro-eclogite (Jd_{24-36}). This difference, however, is due to a lower Fe^{3+} content in leuco-eclogitic omphacites rather than a higher Na content.

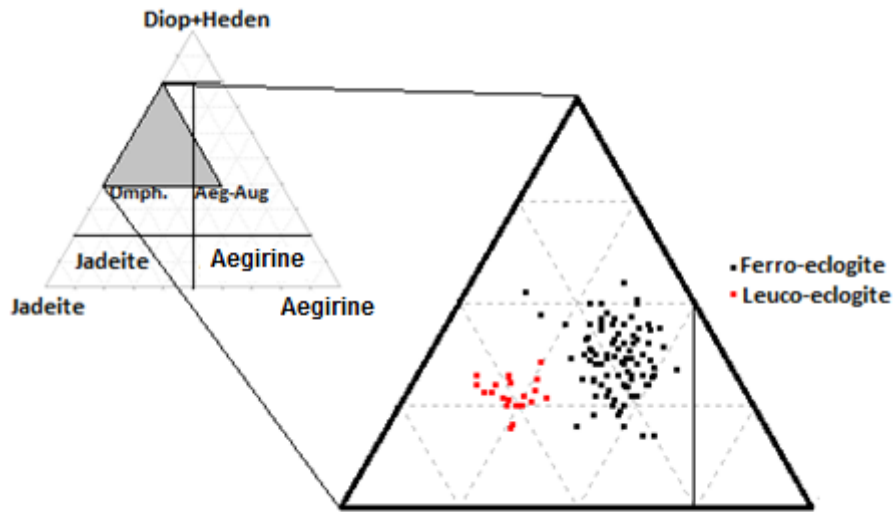


Figure 57- Triangular plot of pyroxenes in the Jd-Aeg-Di+Hd system.

Figure 58 shows a part of a cm long pyroxene in a quartz+pyroxene+mica+rutile vein from sample SK-28. The pyroxenes are strongly altered, but relict omphacite remains in the core.

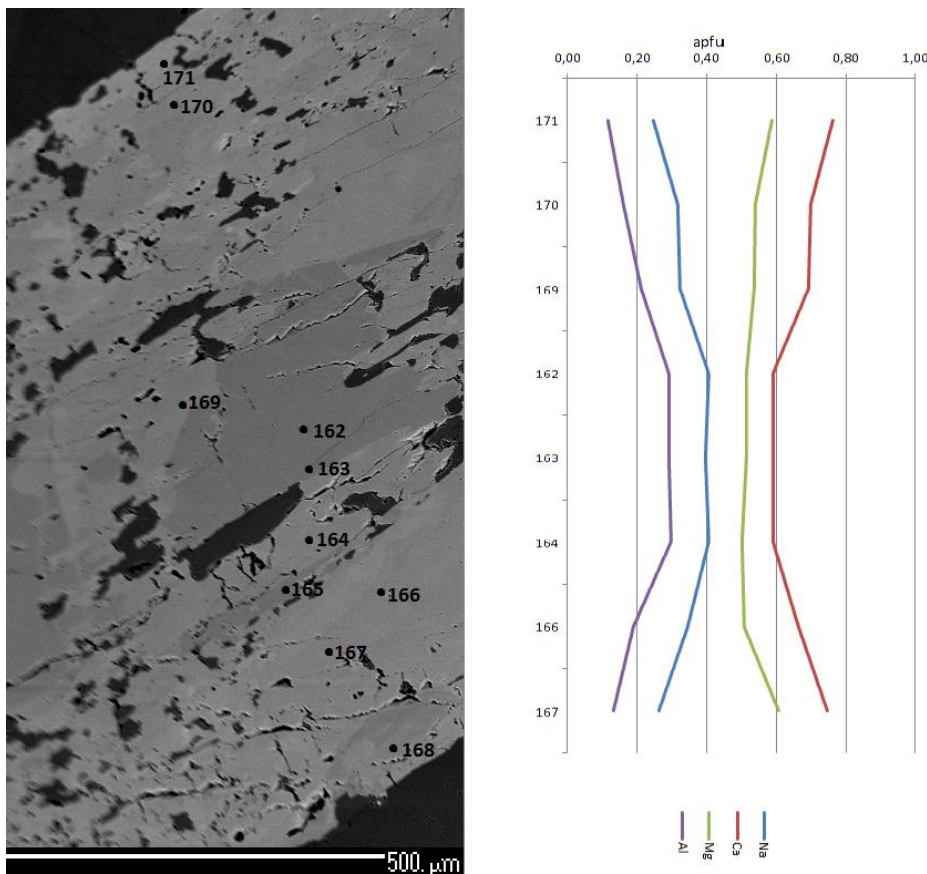


Figure 58 - Chemical profile across large vein Omp in SK-28.

Al (purple) and Na (blue) correlates and decreases from core to rim, while Mg (green) and Ca (red) also correlate, but increases from core to rim. This implies a coupled substitution of



explained by a higher jadeite component in the relict core relative to the re-equilibrated rim and secondary pyroxene.

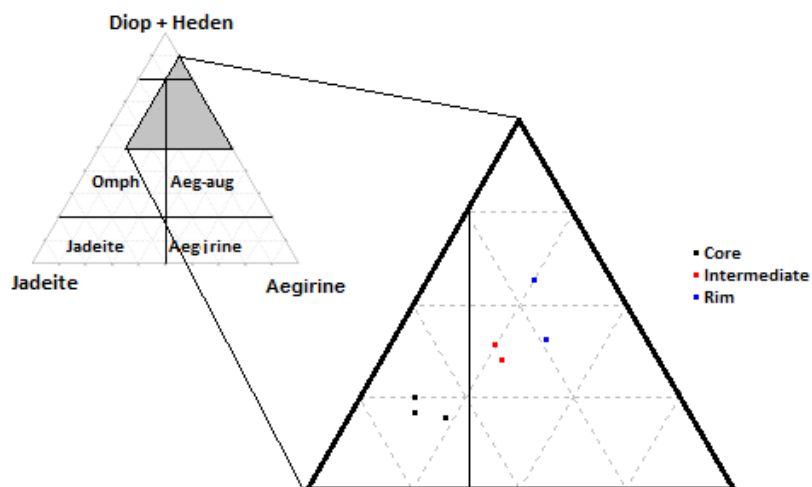


Figure 59 - Triangular plot from core, intermediate and rim of large vein Omp in SK-28.

Figure 59 shows where core (black), intermediate (red) and rim (blue) analysis of the large vein pyroxene (Figure 58) plot in the pyroxene classification triangle. The figure shows the relict omphacite core, but is enriched in Diopside + Hedenbergite component at the expense of the jadeite component towards the rim, and hence is shifted into the aegerine-augite field.

The cm-size pyroxenes (Figure 60 A) in the vein are texturally different from the relatively fine grained matrix pyroxene (Figure 60 B). Chemically, however, the two apparently different pyroxenes are similar, which is shown in figure 61.

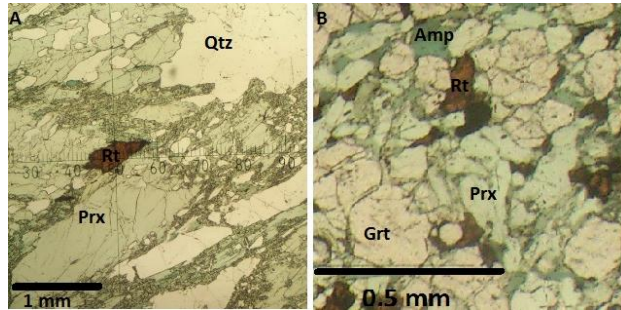


Figure 60 - Image showing the visual difference in the vein Omp (SK-28) and matrix Omp (SK-7).

The red squares represent fine-grained pyroxene from the unaltered ferro-gabbroic wall rock and the black squares represent the core analyses of the larger vein pyroxene. The small dots in the background represent the same points as in figure 61, showing that the scatter in the chemistry of vein omphacite and matrix omphacite is within the scatter of the pyroxenes in ferro-eclogite (black dots).

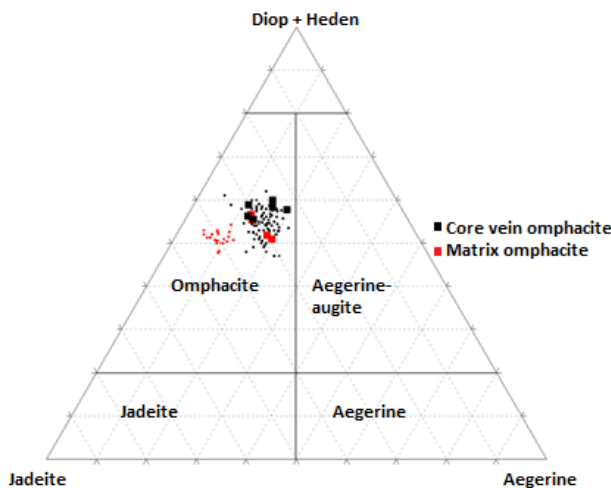


Figure 61 - Triangular plot of core of vein Omp (black squares) and matrix Omp (red squares) both from SK-28. Background points are from figure 59.

Table 7 presents analyses of several representative pyroxenes from the Engebøfjellet Eclogite. Since sample SK-28 is a highly complex sample with veining, several pyroxenes from this thin section were selected. The selection of analyses shows how the pyroxene chemistry varies when the texture and indeed the mineralogy varies within one sample. Table 7 confirms what is observed in figure 57 – the pyroxene chemistry is dependent on whether the sample is ferro-gabbroic or leuco-gabbroic.

Table 7 - Table with several Omp analyses from both ferro- and leuco-eclogite.

		Ferro-gabbroic eclogite						Leuco-eclogite			
Wt.% EMP	Comment	SK-28			SK-9			SK-4			Core in garnet rich field
		Inclusion in Amphibole	Core in fresh eclogite close to small vein	Core in relict vein	Core in large vein omphacite	Rim in large vein omphacite	Core	Rim, close to rutile	Within large omphacite	Within large omphacite	
SiO ₂	SiO ₂	55,30	54,78	54,98	52,82	54,54	52,34	55,35	55,77	56,07	55,27
TiO ₂	TiO ₂	0,06	0,07	0,04	0,05	0,08	0,07	0,31	0,07	0,05	0,07
Al ₂ O ₃	Al ₂ O ₃	8,19	7,72	7,71	5,18	6,92	2,65	7,85	7,20	10,30	10,41
Cr ₂ O ₃	Cr ₂ O ₃	0,00	0,00	0,02	0,03	0,00	0,05	0,04	0,00	0,00	0,03
FeO	FeO	7,14	9,16	7,93	11,36	7,61	10,89	7,96	8,20	4,98	5,03
MnO	MnO	0,02	0,02	0,00	0,09	0,02	0,07	0,02	0,04	0,02	0,04
MgO	MgO	8,94	7,75	8,71	9,01	9,58	10,62	8,57	8,81	8,41	8,34
CaO	CaO	14,34	13,28	14,25	17,45	15,33	19,19	14,23	14,79	13,32	13,38
Na ₂ O	Na ₂ O	6,23	6,88	6,31	4,24	5,85	3,46	6,43	5,98	7,14	7,18
K ₂ O	K ₂ O	0,01	0,01	0,00	0,00	0,00	0,00	0,00	0,01	0,01	0,00
Total		100,22	99,65	99,90	100,23	99,85	99,34	100,51	100,39	99,99	100,49
Structural formula 6 oxygen	Si	1,98	1,98	1,98	1,94	1,96	1,94	1,98	1,98	1,98	1,97
	Ti	0,00	0,00	0,00	0,00	0,00	0,00	0,01	0,00	0,00	0,00
	Al	0,35	0,33	0,33	0,22	0,29	0,12	0,33	0,30	0,43	0,41
	Cr	0,00	0,00	0,00	0,00	0,00	0,00	0,00	0,00	0,00	0,00
	Fe ³⁺	0,13	0,19	0,15	0,19	0,19	0,24	0,15	0,13	0,10	0,10
	Fe ²⁺	0,09	0,08	0,08	0,15	0,04	0,09	0,09	0,11	0,05	0,06
	Mn	0,00	0,00	0,00	0,00	0,00	0,00	0,00	0,00	0,00	0,00
	Mg	0,48	0,42	0,47	0,49	0,51	0,59	0,46	0,47	0,44	0,46
	Ca	0,55	0,51	0,55	0,69	0,59	0,76	0,55	0,57	0,51	0,52
	Na	0,43	0,48	0,44	0,30	0,41	0,25	0,45	0,42	0,49	0,47
	K	0,00	0,00	0,00	0,00	0,00	0,00	0,00	0,00	0,00	0,00
Sum		4,00	4,00	4,00	4,00	4,00	4,00	4,00	4,00	4,00	4,00
Pyroxene endmember	Jadeite	33	32	21	28	11	32	30	42	42	40
	Acmite	12	19	15	18	23	15	13	10	9	10
	Diop + heden	55	49	53	61	54	65	53	57	48	50
Sum		100,0	100,0	100,0	100,0	100,0	100,0	100,0	100,0	100,0	100,0
Mg/Mg+Fe ²⁺		0,84	0,83	0,85	0,76	0,92	0,86	0,84	0,81	0,91	0,89

7.3 Primary amphibole

The primary amphiboles of the Engebøfjellet Eclogite can be grouped into three texturally distinct types. Figure 62 shows these three texturally different amphiboles.

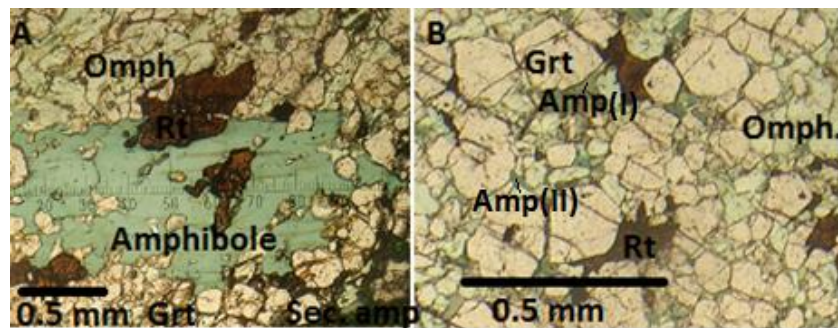


Figure 62 - Figure showing the textural difference in porphyroblastic Amp (SK-3) and matrix Amp (SK-27). Amp(I) is the amphibole from reaction between Grt and Omph, while Amp (II) is the common matrix amphibole.

Figure 62 A shows the porphyroblastic amphibole, and figure 62 B shows the common matrix amphibole and the amphibole often found at grain boundaries between garnet and omphacite. From BSE investigation the latter amphibole appear to be in chemical equilibrium with the surrounding eclogite facies minerals, and are hence not classified as secondary amphibole, but rather as later eclogite facies amphibole. This observation is in agreement with Korneliussen *et al.* (1998).

From the EMP analyses, the amphibole structural formulas are recalculated as described in appendix 5. The amphiboles are plotted and classified after the nomenclature of Leake *et al.* (1997). Figure 63 shows where the amphiboles plot, subdivided into the following groups: Primary, zoning in primary, inclusion in garnet, zoning towards secondary amphibole and zoning towards garnet.

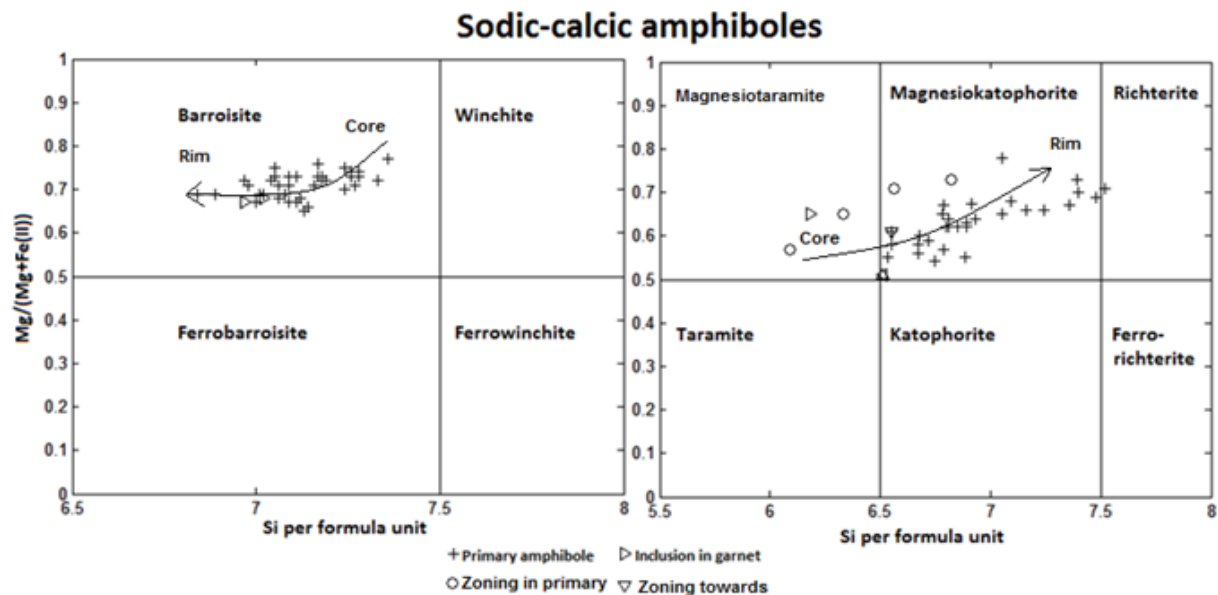


Figure 63 - Primary sodic-calcic amphiboles from the Engebøfjellet Eclogite (After Leake et al.1997). Arrows show trends from core to rim.

The core-rim trend in the right diagram is quite consistent, whereas the core-rim trend in the left diagram is less consistent. The trend in the latter case is general, but in several amphibole grains, the trend is opposite. All

primary amphiboles observed are within the sodic-calcic amphiboles, and barroisite and magnesio-katophorite is the two most abundant primary amphiboles. In addition, one analysis classify as richterite. When considering zoning in the primary amphiboles along with amphibole inclusions in garnets, magnesiotaramite is also added to the list.

After Leake *et al.* (1997), Brs and Mkp are separated by a $(\text{Na}+\text{K})_A$ threshold of 0.5 atoms per formula unit (pfu). Brs has $<0.5 \text{ Na}+\text{K}$ pfu and Mkp has $\geq 0.5 \text{ Na}+\text{K}$ pfu. All the primary amphiboles analyzed have 0.29 - 0.76 $\text{Na}+\text{K}$ pfu. Since Na_A is a calculated value (see appendix 5) errors in the recalculation may be sufficient to shift an amphibole to either of the two fields. The occurrence of Brs or Mkp does not seem to correlate with any of the following factors: Ferro / leuco – eclogite, core/rim relationship, texture, distance to veins and what mineral the amphibole is in contact to (primarily garnet or omphacite). Some samples are dominated by Brs (SK-4, SK-7, SK-8, SK-9 and SK-31), Mkp (SK-11, SK-12, SK-20, SK-30, SK-28 and SK-29,) or both (SK-2, SK-3 and SK-6).

Zoning in primary amphiboles occur both in contact to eclogite facies minerals and in contact to veins and phases from retrogression. Amphiboles are sensitive to local bulk compositions, and when they re-equilibrate the trend may vary dependent on the adjacent mineral or fluid present. This is easily recognized when amphiboles are in contact to rutile; the amphiboles typically contain 0.1 to 0.4 weight percent TiO_2 , but when in contact to rutile, TiO_2 often exceeds 1.2 weight percent. When in contact to secondary amphiboles or veins where fluids were present, a strong zoning (Figure 66) will occur from the pristine core towards the contact to the vein or secondary amphibole. Table 8 below shows the chemistry of a selection of amphiboles from Engebøfjellet.

Table 8 - Analyses of primary amphiboles from ferro- and leuco-eclogite.

Wt.% EMP		Ferro-gabbroic eclogite						Leuco-eclogite			
		SK-9		SK-7		SK-28		SK-31		SK-4	
		Core in Brs	Core in Brs	Core in Brs	Rim in Brs towards Grt and Omp	Core in Mkp	Rim in Mkp towards rutile	Core in zoned Brs	Zonation in Brs => Mkp	Core in Brs	Rim in Brs
SiO ₂	49,94	50,93	49,81	48,89	47,00	44,87	49,84	47,96	48,57	48,39	
TiO ₂	0,26	0,19	0,24	0,31	0,37	1,12	0,23	0,26	0,34	0,28	
Al ₂ O ₃	8,32	7,61	8,03	9,89	11,08	12,16	11,67	12,56	10,88	11,43	
Cr ₂ O ₃	0,03	0,00	0,02	0,00	0,03	0,01	0,02	0,04	0,01	0,03	
FeO	12,13	11,96	12,80	13,28	14,13	15,12	9,97	11,01	12,55	11,49	
MnO	0,03	0,05	0,00	0,04	0,03	0,02	0,09	0,12	0,07	0,00	
MgO	13,90	14,46	14,00	13,05	11,43	10,08	13,55	13,24	12,82	12,85	
CaO	8,73	8,77	8,50	8,78	8,33	9,13	7,69	8,65	7,86	7,83	
Na ₂ O	3,28	3,11	3,16	3,43	3,92	3,78	4,17	3,94	3,56	3,96	
K ₂ O	0,43	0,36	0,43	0,41	0,48	0,55	0,30	0,39	0,37	0,41	
Total	97,05	97,44	96,95	98,05	96,79	96,83	97,52	98,18	97,02	96,67	
Structural formula 23 oxygen	Si	7,18	7,28	7,18	7,01	6,67	7,05	6,82	6,98	6,97	
	Ti	0,02	0,02	0,03	0,03	0,13	0,02	0,03	0,04	0,03	
	Al IV	0,82	0,72	0,82	0,99	1,11	1,33	0,95	1,18	1,02	1,03
	Al VI	0,57	0,62	0,54	0,68	0,80	0,80	1,00	0,92	0,82	0,91
	Fe ³⁺	0,33	0,28	0,41	0,33	0,26	0,12	0,24	0,27	0,41	0,29
	Fe ²⁺	1,17	1,12	1,14	1,26	1,47	1,76	0,94	1,04	1,10	1,09
	Mn	0,00	0,01	0,00	0,00	0,00	0,00	0,01	0,01	0,01	0,00
	Mg	3,01	3,04	3,01	2,79	2,50	2,23	2,86	2,80	2,75	2,76
	Ca	1,35	1,33	1,31	1,35	1,31	1,45	1,17	1,32	1,21	1,21
	NaA	0,36	0,30	0,31	0,40	0,50	0,58	0,38	0,48	0,32	0,40
	NaM4	0,56	0,59	0,57	0,56	0,62	0,51	0,77	0,61	0,67	0,71
	K	0,07	0,07	0,08	0,08	0,09	0,10	0,05	0,07	0,07	0,07
	Sum	15,43	15,37	15,39	15,47	15,59	15,68	15,43	15,55	15,39	15,48
	Mg/(Mg+Fe ²⁺)	0,72	0,73	0,73	0,69	0,63	0,56	0,75	0,73	0,71	0,72

7.4 Secondary amphiboles

The secondary amphiboles most often occur around later veins. The secondary amphiboles typically occur as fibrous masses replacing eclogite facies pyroxenes, amphiboles and garnets (Figure 64).

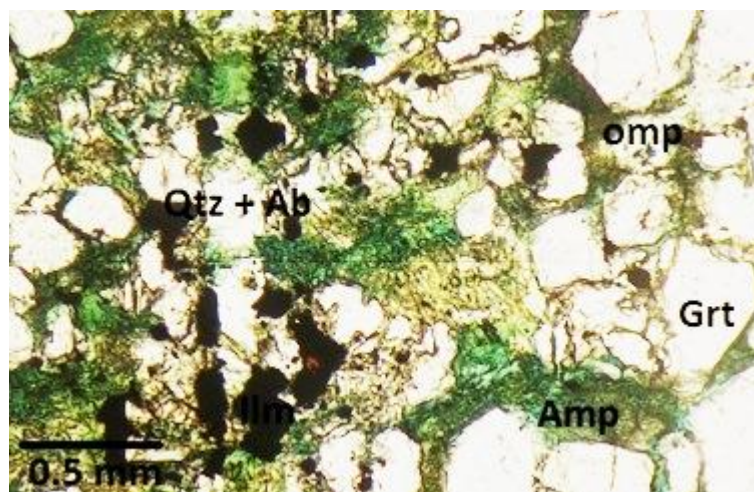


Figure 64 - Image showing how late amphiboles occur (SK-20).

The Cl and F contents of secondary amphiboles were analyzed on the microprobe in order to be able to say anything about the chemistry of the fluids present in the veins (See section 10.7). All analyses, both on primary and secondary amphiboles, yielded Cl and F contents below detection limit. Whether or not the fluids contained any Cl or F is hence not documented, but should be further investigated.

Figure 65 shows that the secondary amphiboles all plot within the fields of calcic amphiboles after Leake *et al.* (1997). The secondary amphiboles include pargasite, magnesiohastingsite, edenite, ferropargasite, hastingsite, ferro-edenite, ferrotschermakite, magnesiohornblende and actinolite.

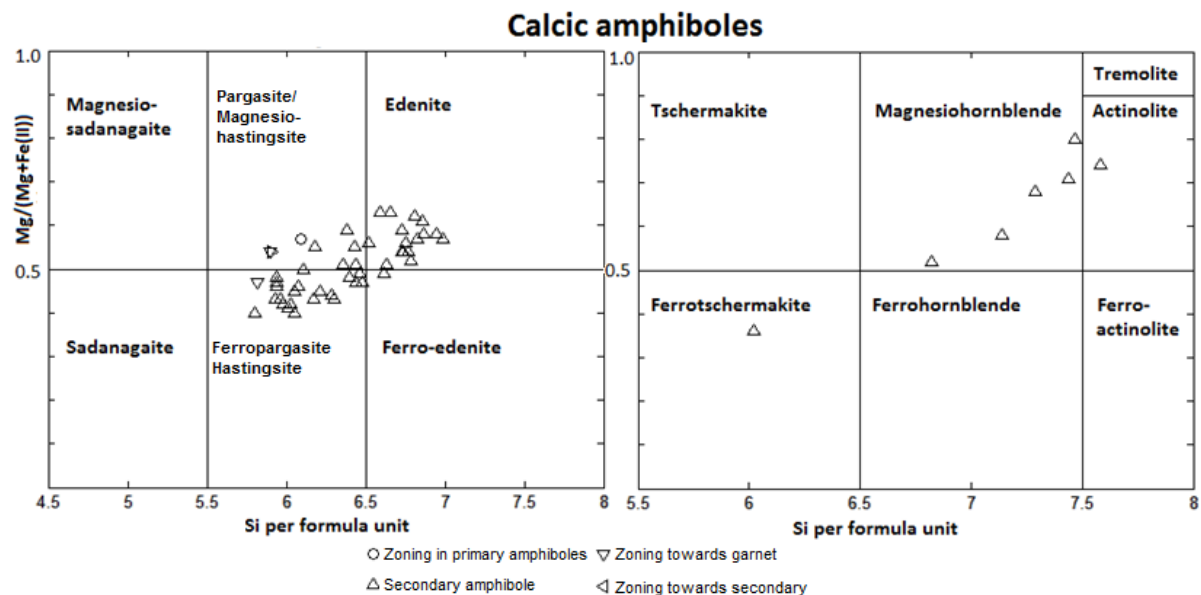


Figure 65 - Zoning to, and secondary amphiboles from the Engebøfjellet Eclogite (After Leake *et al.* 1997).

Where veins cut primary porphyroblastic amphiboles, the effect of these veins on the amphibole can be investigated. Figure 66 shows a profile across a porphyroblastic amphibole, and what effect the alteration related to the vein has on the mineral chemistry. The primary amphibole is a magnesiokatophorite (point 99-103), and it is zoned to ferropargasite (point 104) towards the vein, where a secondary amphibole, edenite (105) crystallized. On the other side of the vein, the ferropargasite (point 106) is found again, resembling the chemistry of the ferropargasite in point 104.

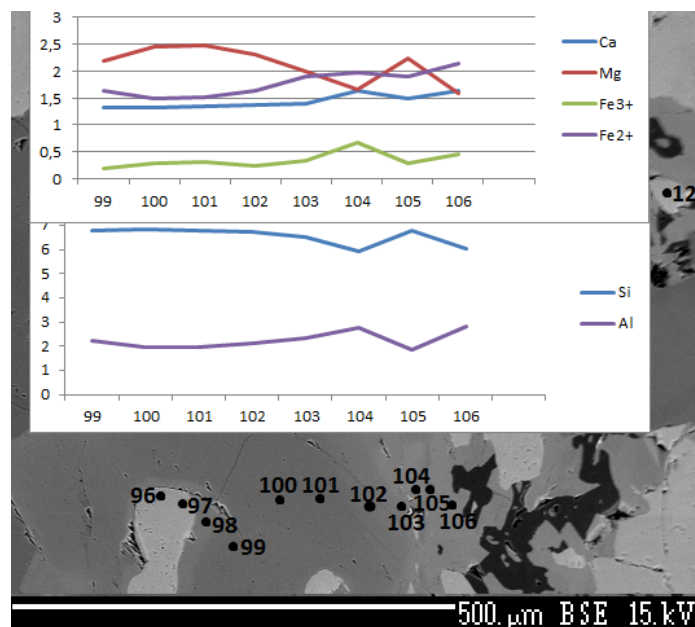


Figure 66 - Chemical profile across zoned primary Amp, cut by later vein causing development of a secondary amphibole (SK-28).

7.5 Clinzoisite

Clinzoisite/epidote is a common minor phase in the Engebøfjellet Eclogite. It occurs as matrix mineral and as inclusions, primarily in the leuco-eclogite. Figure 67 shows a primary epidote in the contact between garnet and omphacite. It is assumed to be primary based on the large grain size relative to the symplectite.

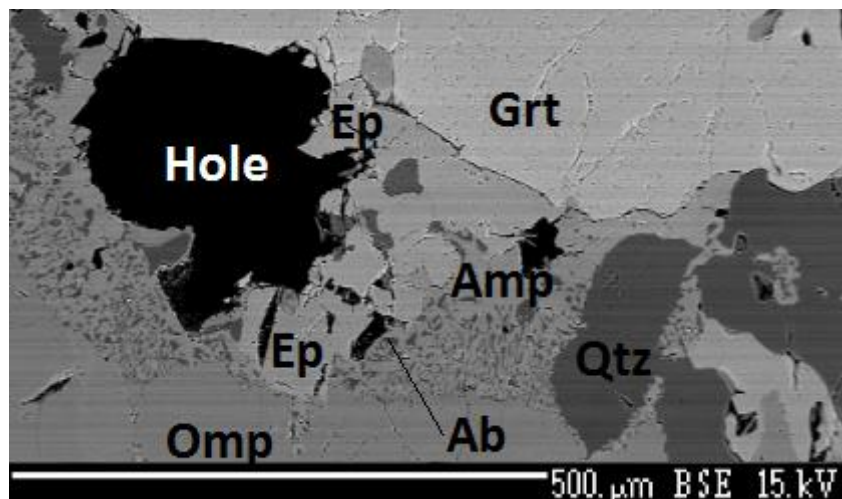


Figure 67 - Primary epidote within symplectite between Grt and Omp in SK-6.

The epidote is typically fine grained, and difficult to find in an optical microscope, rarely exceeding 0.1 mm, usually subhedral to anhedral. Table 9 lists 5 epidotes from ferro-eclogite to leuco-eclogite.

Table 9 - Table with analyses of epidotes from ferro- and leuco-eclogites at Engebøfjellet.

		Ferro-gabbroic eclogite		Leuco-eclogite		
		SK-8	SK-28	SK-30	SK-4	
Wt.% EMP	Comment	Epidote in Omp. Contact to Grt.	Small inclusion in barroisite	Core in epidote in contact to Grt.	Epidote incl. in large omphacite	Epidote in garnet rich field
SiO ₂		37,66	37,96	38,76	38,16	37,76
TiO ₂		0,10	0,14	0,12	0,11	0,12
Al ₂ O ₃		25,03	24,86	28,12	27,17	26,20
Cr ₂ O ₃		0,01	0,04	0,00	0,01	0,01
FeO		9,58	10,94	6,46	6,97	8,47
MnO		0,01	0,01	0,00	0,00	0,04
MgO		0,12	0,05	0,05	0,05	0,10
CaO		22,48	23,24	23,97	23,69	23,13
Na ₂ O		0,00	0,02	0,01	0,02	0,00
K ₂ O		0,01	0,00	0,02	0,01	0,02
Total		94,97	97,25	97,48	96,15	95,83
Structural formula 12.5 oxygen	Si	2,99	2,96	2,99	2,99	2,97
	Ti	0,01	0,01	0,01	0,01	0,01
	Al	2,34	2,28	2,55	2,51	2,43
	Cr	0,00	0,00	0,00	0,00	0,00
	Fe ³⁺	0,71	0,79	0,46	0,51	0,62
	Mn	0,00	0,00	0,00	0,00	0,00
	Mg	0,01	0,01	0,01	0,01	0,01
	Ca	1,91	1,94	1,98	1,99	1,95
	Na	0,00	0,00	0,00	0,00	0,00
	K	0,00	0,00	0,00	0,00	0,00
	Sum	7,98	8,00	8,00	8,00	8,00
*100*Fe ³⁺ /(Fe ⁽³⁺⁾ +Al)	Ps*	23,18	25,76	15,33	16,82	20,31

Table 9 shows that epidotes in ferro-eclogites are higher in pistacite component than epidotes in Leuco-eclogites.

7.6 Rutile

Chemically the rutile is very pure, typically with >99.5% TiO₂ from EMP analyses. Table 10 gives oxide weight percent of four rutile grains.

Table 10 - Chemical analyses of four rutile grains from the Engebøfjellet Eclogite.

SiO ₂	Na ₂ O	Al ₂ O ₃	K ₂ O	CaO	FeO	MnO	Cr ₂ O ₃	TiO ₂	MgO	Total
0,04	0,00	0,00	0,00	0,03	0,47	0,00	0,00	99,55	0,00	100,00
0,00	0,00	0,03	0,01	0,02	0,37	0,03	0,00	99,96	0,01	100,42
0,00	0,01	0,01	0,00	0,05	0,40	0,01	0,05	99,77	0,02	100,26
0,02	0,00	0,02	0,00	0,08	0,49	0,00	0,00	99,73	0,00	100,27

Trace element analyses of the rutile are presented in table 11, and are primarily done for using the Zr-in-rutile geothermometer (Tomkins *et al.*, 2007). Si is also analyzed in order to ensure that a zircon inclusion is not analyzed.

Table 11 - Trace element analyses of rutile from Engebøfjellet, primarily of thermobarometric purposes.

Sample	Zr (ppm)	Cr (ppm)	Nb (ppm)	Si (ppm)	Fe (wt. %)
SK2	92	76	62	27	0,2625
SK2	73	108	72	67	0,2223
SK2	63	104	82	48	0,4206
SK2	31	109	71	69	0,2852
SK2	44	95	37	83	0,6465
SK6 wall-rock	111	84	277	41	0,315
SK6 wall-rock	63	78	89	61	0,3774
SK6 wall-rock	93	79	236	54	0,3376
SK6 wall-rock	100	68	254	55	0,366
SK6 Grt-Qtz vein	40	81	1288	40	0,3504
SK6 Grt-Qtz vein	36	82	1402	64	0,4037
SK12	89	631	0	33	0,2759
SK12	69	677	12	39	0,3069
SK12	66	687	39	38	0,1944
SK28	52	71	82	55	1,1212
Detection limits (ppm)					
	Zr	Cr	Nb	Si	Fe
	49	28	50	19	75
Uncertainties in ppm (2 sigma)					
	27	16	28	11	60-150

7.7 Carbonate

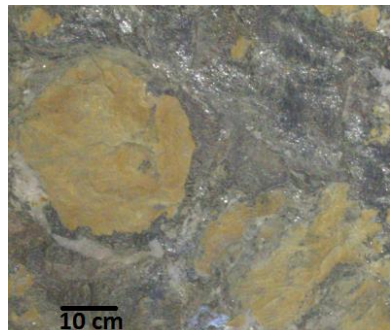


Figure 68 - Carbonate clast in quartz+mica vein from the Vevring tunell.

The presence of carbonate varies greatly from accessory mineral in the eclogite, only visible in BSE to large masses up to 50 cm in diameter in veins (Figure 68).

Carbonate is also found as inclusions in garnets and pyroxenes. Chemically the carbonates are dolomites and ankerites, typically with Mg>Fe, indicating a higher dolomite component. Beam current during analyses of Carbonates was 15nA that is too high for ideal carbonate analyses.

7.8 Quartz

The amount of quartz varies in different samples. Leuco-eclogite has more and larger quartz (Figure 69 A) than ferro-eclogite (Figure 69 B).

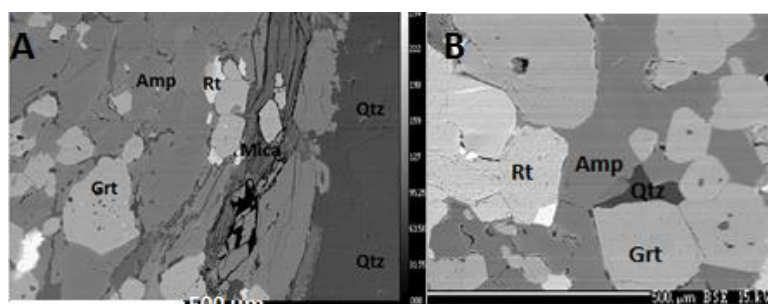


Figure 69 - A) Large quartz from SK-4. B) Small quartz inclusion in SK-6.

Quartz dominates the mineralogy of the veins in both types of eclogite. In the quartz + omphacite + rutile vein in SK-28, the quartz clearly shows grain boundary migration (Figure 70), indicating deformation at temperatures of >500°C (Stipp *et al.*, 2002).

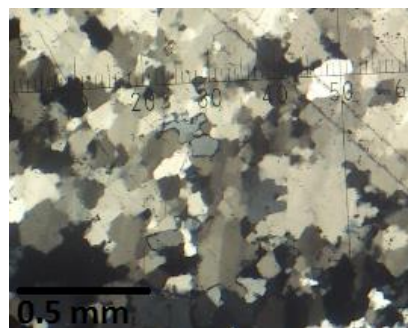


Figure 70 - Quartz showing GBM in vein in SK-28.

7.9 Mica

Mica is a common mineral in the Engebøfjellet Eclogite, and is typically dominated by phengitic mica and single grains of paragonitic mica. According to quantitative XRD SK-31, as the only sample, is significantly richer in paragonite than in phengite. Phengite is different from muscovite by a $(\text{Mg}, \text{Fe}^{2+}) \rightarrow \text{Al}$ substitution in M-site, and a $\text{Si} \rightarrow \text{Al}$ substitution in T-site. The phengite is hence richer in Si (>3 apfu) and lower in Al than a muscovite (Mindat.org). Paragonite is different from muscovite by having Na instead of K in A-site (from mindat.org). Leuco-eclogite is significantly richer in mica than ferro-eclogite, and in some samples (SK-31 and SK-4) it is a major mineral. Biotite is found together with plagioclase as an alteration product after phengite. For analyses of mica, see table 12.

Table 12 - Analyses of mica from the Engebøfjellet Eclogite.

Wt.% EMP	Comment	Ferro-gabbroic eclogite												Leuco-eclogite					
		SK-7			SK-8			SK-2			SK-28			SK-31			SK-4		
		Pg from fresh eclogite	Ph from fresh eclogite	Ph incl. from large Amp.	Ph incl. from large Amp.	Ph from vein-rock contact	Ph from vein-rock contact	Bt from alteration of Ph	Bt from alteration of Ph	Relict Ph	Relict Ph	Ph incl. in Bts	Ph incl. in Bts	Ph incl. in large Crmp	Ph incl. in large Crmp	Pg between Amp. And Qtz.			
SiO ₂	SiO ₂	50,59	48,84	49,12	50,16	35,74	49,01	36,42	47,95	47,13	48,96	48,96	48,96	48,96	48,87				
TiO ₂	TiO ₂	0,50	0,47	0,48	0,45	0,87	0,48	1,22	0,08	0,11	0,50	0,50	0,50	0,50	0,46				
Al ₂ O ₃	Al ₂ O ₃	26,15	27,36	27,66	25,94	17,63	25,43	17,45	40,73	40,24	29,19	29,19	29,19	29,19	28,67				
Cr ₂ O ₃	Cr ₂ O ₃	0,02	0,00	0,01	0,00	0,00	0,00	0,03	0,05	0,04	0,00	0,00	0,00	0,00	0,03				
FeO	FeO	3,22	3,42	3,08	3,29	15,55	3,47	15,94	0,46	0,58	2,64	2,64	2,64	2,64	2,88				
MnO	MnO	0,00	0,00	0,01	0,00	0,05	0,02	0,04	0,00	0,00	0,04	0,04	0,04	0,04	0,00				
MgO	MgO	4,08	3,70	3,76	3,76	13,27	3,81	12,52	0,17	0,19	3,12	3,12	3,12	3,12	2,93				
CaO	CaO	0,00	0,00	0,03	0,00	0,00	0,00	0,00	0,34	0,24	0,00	0,00	0,00	0,00	0,08				
Na ₂ O	Na ₂ O	0,33	0,30	0,46	0,31	0,10	0,42	0,12	7,31	7,06	0,65	0,65	0,65	0,65	0,50				
K ₂ O	K ₂ O	11,06	10,79	10,25	10,56	9,97	10,78	10,02	0,74	0,98	10,35	10,35	10,35	10,35	10,33				
Total	Total	95,90	94,85	94,84	94,52	93,16	93,36	93,76	97,82	96,56	95,38	95,38	95,38	95,38	94,74				
Structural formula		Si	3,39	3,31	3,31	3,40	2,74	3,38	2,78	2,99	3,33	3,28	3,28	3,28	3,30				
11 oxygen	Ti	0,03	0,02	0,02	0,02	0,05	0,02	0,07	0,00	0,01	0,02	0,02	0,02	0,02	0,02				
	Al	2,06	2,19	2,20	2,07	1,60	2,07	1,57	2,99	2,24	2,30	2,30	2,30	2,30	2,28				
Cr	Cr	0,00	0,00	0,00	0,00	0,00	0,00	0,00	0,00	0,00	0,00	0,00	0,00	0,00	0,00				
Fe ²⁺	Fe ²⁺	0,18	0,19	0,17	0,19	1,00	0,20	1,02	0,02	0,10	0,15	0,15	0,15	0,15	0,16				
Mn	Mn	0,00	0,00	0,00	0,00	0,00	0,00	0,00	0,00	0,00	0,00	0,00	0,00	0,00	0,00				
Mg	Mg	0,41	0,37	0,38	0,38	1,52	0,39	1,43	0,02	0,37	0,31	0,31	0,31	0,31	0,30				
Ca	Ca	0,00	0,00	0,00	0,00	0,00	0,00	0,00	0,02	-0,01	0,00	0,00	0,00	0,01	0,01				
Na	Na	0,04	0,04	0,06	0,04	0,01	0,06	0,02	0,88	0,10	0,08	0,08	0,08	0,07	0,07				
K	K	0,94	0,93	0,88	0,92	0,98	0,95	0,98	0,05	0,87	0,88	0,88	0,88	0,89	0,89				
Sum	Sum	7,05	7,06	7,03	7,02	7,90	7,06	7,86	6,98	7,02	7,03	7,03	7,02	7,02	7,02				
Mg/Mg+Mn+Fe ²⁺	Mg/Mg+Mn+Fe ²⁺	0,69	0,66	0,69	0,67	0,60	0,66	0,58	0,40	0,78	0,68	0,68	0,68	0,68	0,64				

7.10 Feldspar

Feldspars commonly occur as alteration products in the eclogite. Most of the feldspar ($An_{0.9-1.4}$) occurs in symplectites of amphibole + feldspar (albite and plagioclase) after omphacite (Figure 71).

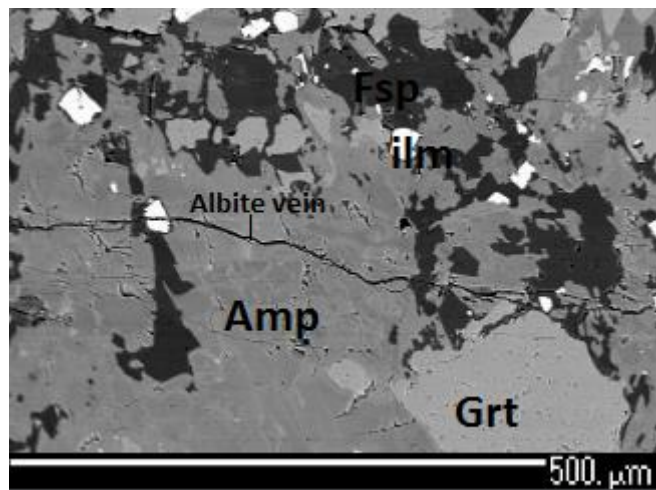


Figure 71 - Ab occurring in both vein and in symplectite in SK-20.

In the vein in SK-28, there is at least one large grain of albite (Figure 72). If it is primary, it gives the maximum pressure possible at Engebøfjellet (Holland, 1980), see section 8.2.7. Based on the texture of the Ab and the position close to the contact to the altered wall rock, the grain is considered secondary, and can hence not give an upper pressure limit of the formation of the eclogite / vein.

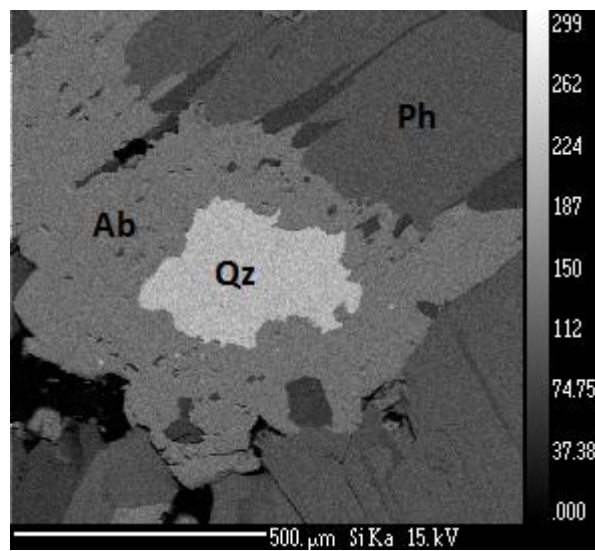


Figure 72 - Albite occurring close to contact between vein and wall rock in SK-28.

7.11 Sulfides

Sulfides are common in both ferro-gabbroic and leuco-gabbroic eclogite. They are determined using EDS on the microprobe, and are not analyzed. Pyrite is the most common of the sulfides and typically occurs as up to 5 mm sized euhedral to subhedral crystals easily recognized in thin section (Figure 73).

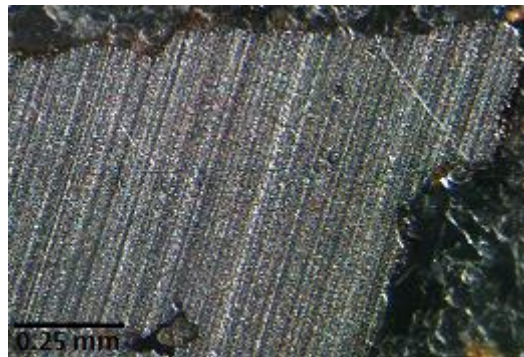


Figure 73 - Pyrite in SK-7 in reflected light.

Chalcopyrite is observed as a minor phase on BSE images. When Chalcopyrite is found it usually occurs as inclusions in garnets.

7.12 Zircon

Zircon is a common accessory mineral in the Engebøfjellet Eclogite, and it typically occur as tiny inclusions ($<20 \mu\text{m}$) only visible on BSE images (Figure 74). Zircons are detected using the EDS on the microprobe, and are not analyzed.

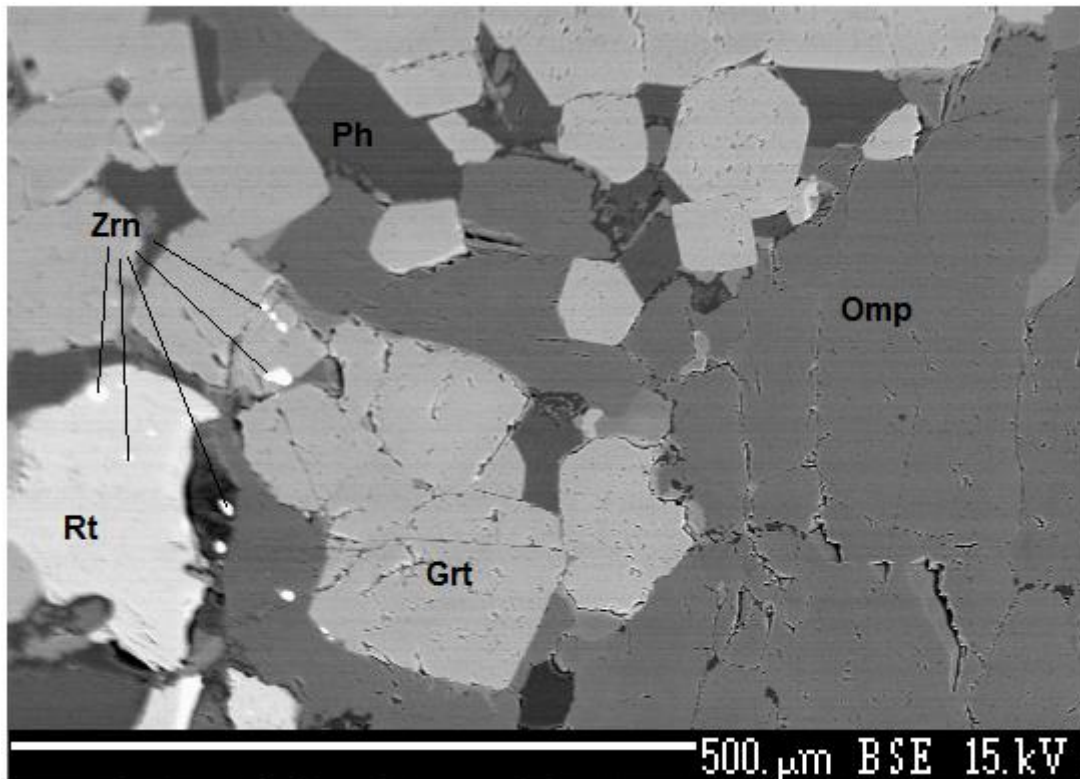


Figure 74 - Zircon inclusions in SK-2.

8. Thermobarometry

8.1 Principles of thermobarometry

Thermobarometry is used to determine the P-T conditions for the formation and/or evolution of rocks. It is based on equilibrium thermodynamics on the mineral assemblage in the rock of interest. Since it is impossible to prove that a mineral assemblage has ever been in equilibrium, the equilibrium mineral assemblage is a geological assumption (Powell & Holland, 2008). The metamorphic conditions of a rock are estimated by an extrapolation of experimental data by fitted equations. Hence, an error should be added to the result, both due to the uncertainty in this extrapolation as well as the uncertainty of composition analysis (Powell & Holland, 2008).

The conventional geothermobarometry is recently more and more overtaken by P-T pseudosections (Powell & Holland, 2008). P-T pseudosections require thermodynamic parameters as a-x properties and bulk rock composition of the equilibration volume. The equilibration volume is the volume where one can assume that the minerals were in equilibrium (Powell & Holland, 2008). If the rock sample collected is homogenous, often due to fine grained texture, an equilibration volume is not needed, and one can use whole rock XRF analyses (Powell & Holland, 2008).

For this master thesis, conventional thermobarometry is used instead of pseudosections. Due to lack of good geobarometers (Krogh Ravna & Piquin, 2003), thermobarometric calculations will only yield a minimal pressure, and no upper limit. Conventional thermobarometry is usually an empirical correlation of a mineral reaction considered a thermobarometer with a thermodynamic equation (e.g. Eq. 8.1), yielding either P or T. For a mineral reaction at equilibrium, $\Delta G = 0$, yielding

$$\Delta G(P, T, X) = 0 = \Delta H(298,1) + \int_{298}^T \Delta C_P dT + \int_1^P \Delta C_P dP - T \left(\Delta S(298,1) + \int_{298}^T \frac{\Delta C_P}{T} dT \right) + RT \ln K_{eq}$$

(Eq. 8.1, Spear, 1995).

Eq. 8.1 describes the relationship between pressure (P), temperature (T) and the activity (within the composition (X)). In addition to these parameters, eq. 8.1 includes the change in free energy (ΔG), enthalpy (ΔH), entropy (ΔS), volume (ΔV), and heat capacity (ΔC_P). The only unknowns in this equation should be P and T, so by solving eq. 8.1 for one mineral equilibrium one has to give either the P or T in order to calculate the other. In addition, the activity of mineral components or mineral phases in non-ideal solid solution cannot easily be measured, and models must be used to get as correct activities as possible (Ganguly, 2001). Empirical calibration of the thermobarometers may by-pass the problems around complex activity models. By solving the equation for two sets of mineral equilibria in a mineral assemblage, both P and T can be calculated (Spear, 1995). If the whole phase equilibria system is defined, with equations balanced with respect to both chemistry and mass, eq. 8.1 can yield P,T, mineral composition and even the mineral abundance in the system (Spear, 1995).

For the reaction $2A + 3B \leftrightarrow C + 4D$, the equilibrium constant (K_{eq}) is defined as

$$K_{eq} = \frac{a_C \cdot a_D^4}{a_A^2 \cdot a_B^3} \quad (\text{Eq. 8.2, Winter, 2010})$$

Where a_i^j is the activity of phase i raised to the power of the stoichiometry of that phase. The activity is a function of the concentration (X) and the activity coefficient (γ)

$$K_{eq} = K_D K_\gamma = \frac{X_C \cdot X_D^4 \gamma_C \cdot \gamma_D^4}{X_A^2 \cdot X_B^3 \gamma_A^2 \cdot \gamma_B^3} \quad (\text{Eq. 8.3, Winter, 2010})$$

For ideal solid solution in the minerals, the activity equals the concentration, X, (Ellis & Green, 1979), and Eq 3.3.2 can be rewritten to

$$K_{eq} = K_D = \frac{X_C \cdot X_D^4}{X_A^4 \cdot X_B^3} \quad (\text{Eq. 8.4})$$

Eq. 8.1 can be rewritten to

$$\Delta G^0(P, T, X) = 0 = \Delta H^0 - T\Delta S^0 + (P - 1)\Delta V^0 = -RT\ln K \quad (\text{Eq. 3.5, Ellis & Green, 1979})$$

Not all mineral reactions are suitable for thermobarometric studies. According to Eq. 8.5, the effect of variation in the temperature will be greater when ΔS^0 for the reaction is great. Large entropy for the reaction is hence important for a geothermometer. For an ideal geothermometer, ΔV^0 should have been zero, resulting in a pressure independent mineral reaction. If this was fulfilled, $(P-1)\Delta V^0$ would cancel, leaving a thermometer where K_D was the only variable. For ideal geobarometers the two criteria are opposite; they should have a high ΔV^0 and sufficiently low ΔS^0 to neglect the $T\Delta S^0$. Natural systems are not ideal, causing the ideal situations described above to be invalid. Hence, geobarometers and geothermometers often require inputs of T and P respectively. Mineral assemblages used for thermobarometric purposes should also be relative insensitive to variation in bulk rock chemistry, in order to be used on several rock types.

For geothermometry in this thesis, as well as in many other works (Krogh Ravna & Paquin, 2003), Fe^{2+} -Mg exchange reactions are used. They have very low ΔV^0 , due to similarities in effective radii. In 6-coordination Fe^{2+} is 0.78 Å, whereas Mg is 0.72 Å (Klein & Dutrow, 2008). In addition both Fe^{2+} and Mg are abundant elements in many minerals. The garnet-clinopyroxene geothermometer of Ellis & Green (1979) has a ΔV^0 of -0.9033 cm³Mole⁻¹ (Ellis & Green, 1979) and a ΔS^0 of 44.3 J K⁻¹Mole⁻¹ (After Robie & Hemingway, 1995). For barometry net-transfer reactions as the Albite = Jadeite + Quartz barometer (Holland, 1980) are most commonly used (Krogh Ravna & Paquin, 2003). ΔV^0 for the reaction is 17.34 cm³Mole⁻¹ and the ΔS^0 is 46.67 J K⁻¹Mole⁻¹ (Holland, 1980). Due to the high ΔS^0 the barometer (Holland, 1980) needs an temperature input.

In the literature used for this thesis (Ellis & Green (1979), Graham & Powell (1984), Powell (1985) and Krogh Ravna (2000)), the authors have empirically calibrated the geothermometers by correlating data from natural rocks or experiments with the pressure and temperature at equilibrium. From the experimental data, the constants in Eq. 8.1 can be determined (Ellis & Green, 1979), and one can derive a function from regression analysis, where P and T are the only unknowns.

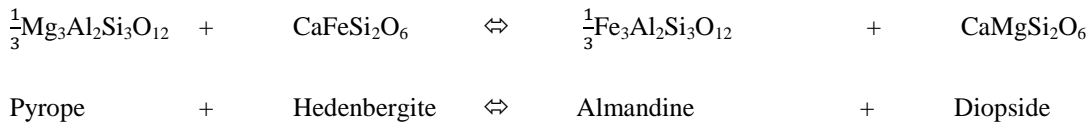
8.2 Applications of the general thermodynamics on natural systems

Below, three geothermometers and one geobarometer used for this thesis are explained. For the geothermometers, several references will be used, in order to see the difference between the models.

8.2.1 Garnet-Clinopyroxene geothermometer

Ellis and Green's (1979) geothermometer uses the Fe²⁺-Mg exchange between garnet and clinopyroxene. From Korneliussen *et al.* (1998) it worked well on the Engebøfjellet Eclogite and it is hence described here. Below, the results from Ellis and Green (1979) is compared to the results from the same data sets using the geothermometers from Graham (1985) and Krogh Ravna (2000).

The background for Ellis & Green's (1979) geothermometer is an experiment where a basaltic composition was crystallized to a Grt + Cpx mineral assemblage in the P-T range of 24-30 kbar and 750 – 1300°C. The experiment revealed that the Fe²⁺-Mg exchange reaction depended on the Ca-content. The geothermometer is based on the reaction



and Ellis & Green (1979) measured the K_D as a function of P,T and X_{Ca}^{Grt} and fitted these data to Eq. 8.5, yielding the temperature function

$$T(K) = \frac{3104X_{Ca}^{Grt} + 3030 + 10.86P(\text{kbar})}{\ln K_D + 1.9034} \quad (\text{Eq. 8.6, Ellis \& Green, 1979}).$$

Where X_{Ca}^{Grt} = Ca/(Ca + Mg + Fe²⁺) The equation requires a pressure, and from earlier work at Engebøfjellet (Korneliussen *et al.*, 1998) the pressure is estimated to 15-17 kbar. Hence both 15 and 20 kbar were used for calculating T.

Similar work was done by Powell (1985) and Krogh Ravna (2000), resulting in different equations than in Ellis & Green (1979):

$$T(K) = \frac{2790 + 10P(\text{kbar}) + 3140X_{Ca}^{Grt}}{\ln K_D + 1.735} \quad (\text{Eq. 8.7, Powell, 1985}).$$

$$X_{Ca}^{Grt} = \text{Ca}/(\text{Ca} + \text{Mg} + \text{Fe}^{2+}).$$

$$T(K) = \frac{1939.9 + 3270X_{Ca}^{Grt} - 1396(X_{Ca}^{Grt})^2 + 3319X_{Mn}^{Grt} - 3535(X_{Mn}^{Grt})^2 + 1105X_{Mg\#}^{Grt} - 3561(X_{Mg\#}^{Grt})^2 + 2324(X_{Mg\#}^{Grt})^3 + 169.4P(\text{GPa})}{\ln K_D - 1.223}$$

(Eq. 8.8, Krogh Ravna, 2000).

$$X_{Ca}^{Grt} = \text{Ca}/(\text{Ca} + \text{Mg} + \text{Fe}^{2+} + \text{Mn}), X_{Mn}^{Grt} = \text{Mn}/(\text{Ca} + \text{Mg} + \text{Fe}^{2+} + \text{Mn}) \text{ and } X_{Mg\#}^{Grt} = \text{Mg}/(\text{Mg} + \text{Fe}^{2+}).$$

8.2.2 Application of Grt-Cpx geothermometers on samples from Engebøfjellet

15 Grt-Cpx pairs were chosen from the EMP analyses. They represented rim analyses in the contact zone between the two minerals. This was done to increase the possibility of equilibrium between the points. Table 13 shows the composition and temperature calculated from them after eq. 8.6, eq.8.7 and eq. 8.8.

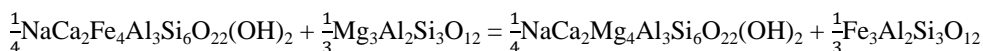
Table 13 - Cpx-Grt thermometry on samples from Engebøfjellet after Ellis & Green (1979), Powell (1985) and Krogh Ravna (2000).

Sample	Garnet						Cpx			Ellis & Green (1979)		Powell (1985)		Krogh Ravna (2000)	
	Mg	Fe2+	Ca	Mn	XCa	XMn	Mg	Fe2+	Kd	T°C (15 kb)	T°C (20 kb)	T°C (15 kb)	T°C (20 kb)	T°C (15 kb)	T°C (20 kb)
SK-7	0,52	1,75	0,70	0,03	0,23	0,01	0,48	0,08	20,25	526	537	502	513	433	453
	0,52	1,75	0,70	0,03	0,23	0,01	0,44	0,11	13,23	601	613	579	590	512	534
	0,52	1,69	0,73	0,03	0,25	0,01	0,46	0,12	12,48	622	634	600	612	533	556
	0,52	1,76	0,68	0,03	0,23	0,01	0,45	0,07	23,08	502	513	479	489	409	429
SK-28	0,41	1,75	0,81	0,03	0,27	0,01	0,43	0,13	14,76	606	618	585	596	520	541
	0,46	1,75	0,73	0,03	0,25	0,01	0,46	0,09	20,45	533	544	510	521	444	464
SK-29	0,50	1,71	0,73	0,03	0,25	0,01	0,45	0,16	9,39	683	696	662	675	599	623
	0,46	1,69	0,76	0,03	0,26	0,01	0,47	0,17	10,23	674	687	653	666	591	615
SK-6	0,39	1,75	0,81	0,04	0,27	0,01	0,44	0,12	17,06	580	592	559	570	495	515
SK-9	0,50	1,72	0,74	0,03	0,25	0,01	0,49	0,12	13,76	604	616	582	594	515	537
	0,51	1,73	0,72	0,03	0,24	0,01	0,47	0,12	13,59	602	614	580	591	511	533
SK-8	0,55	1,79	0,60	0,03	0,20	0,01	0,42	0,10	13,21	580	592	556	568	490	512
SK-2	0,46	1,70	0,77	0,02	0,26	0,01	0,46	0,09	19,57	549	560	527	538	457	477
SK-11	0,42	1,85	0,71	0,02	0,24	0,01	0,39	0,11	16,03	568	579	545	556	480	501
	0,48	1,77	0,67	0,04	0,23	0,01	0,43	0,08	21,19	516	526	492	503	427	447

From 15 data pairs the temperature calculated from Ellis & Green (1979) range from 502°C to 683°C at 15 kbar and 513°C to 696°C at 20 kbar. For comparison, the average from Korneliussen *et al.* (1998) at 15 kbar was 638±64°C. Relative to the results from Ellis & Green's (1979) geothermometer, Powell's (1979) geothermometer is systematic 21-24°C lower, and Krogh Ravna's (2000) geothermometer is systematic 79-93°C lower. The latter uses a far more complex empirical formula than the former two, adding more room for errors due to errors in data. In addition Krogh Ravna (2000) observed that Ellis & Green's (1979) and Powell's (1985) geothermometer showed increasing over-estimation of the temperature at lower temperature (<900°C). Based on the results from garnet-amphibole and Zr-in-rutile (see below), rather an under-estimation from Krogh Ravna (2000) appears to be the reason for the difference in temperature.

8.2.3 Garnet – Amphibole geothermometer

Graham and Powell's (1984) geothermometer uses the Fe²⁺-Mg exchange between garnet and hornblende, and is calibrated against Ellis & Green's (1979) garnet-clinopyroxene geothermometer. The geothermometer works on temperatures up to about 850°C on rocks with low spessartine garnets and for amphiboles of widely varying compositions (Graham & Powell, 1984). The thermometer is based on the reaction:



The Fe²⁺-Mg exchange reaction is fitted to the equation

$$\ln K_D = \frac{\Delta S^0}{R} - \frac{\Delta H^0}{RT} - \frac{P\Delta V^0}{RT} - \frac{W}{RT} (X_{Ca}^{Grt}) \quad (\text{Eq. 8.9, Graham \& Powell, 1985})$$

K_D is the Fe_{tot}-Mg distribution coefficient between garnet and amphibole:

$$K = K_D = \frac{X_{Fe}^{Grt} \cdot X_{Mg}^{Hbl}}{X_{Mg}^{Grt} \cdot X_{Fe}^{Hbl}} \quad (\text{Eq. 8.10, Graham \& Powell, 1984})$$

Eq. 3.3.8 is fitted to the experimental data by regression, yielding the empirical temperature equation

$$T(K) = \frac{2880 + 3280 X_{Ca}^{Grt}}{\ln K_D + 2.426} \quad (\text{Eq. 8.11, Graham \& Powell, 1984})$$

Where X_{Ca}^{Grt} = Ca/(Ca + Mg + Fe²⁺).

Since the Fe²⁺-Mg exchange is associated with a low ΔV, the pressure does not affect the geothermometer significantly, and is hence not included as it is in Ellis & Green's (1979) geothermometer.

Krogh Ravna (2000) also fitted a thermometer to the Garnet-amphibole Fe²⁺-Mg exchange reaction yielding

$$T(K) = \frac{1504 + 1784(X_{Ca}^{Grt} + X_{Mn}^{Grt})}{\ln K_D + 0.720} \quad (\text{Eq. 8.12, Krogh Ravna, 2000}).$$

This thermometer is compared to the thermometer from Graham & Powell (1984).

8.2.4 Application of Grt-Amp geothermometers on samples from Engebøfjellet

Graham & Powell's (1984) and Krogh Ravna's (2000) geothermometers were applied on 8 data pairs from 6 samples from Engebøfjellet, and the results are presented in table 14.

Table 14 - Grt-Amp thermometry on samples from Engebøfjellet. (After Graham & Powell (1984) and Krogh Ravna (2000)).

Sample	Garnet						Amphibole			Graham & Powell (1984)	Krogh Ravna (2000)
	Mg	Fe2+	Ca	Mn	XCa	XMn	Mg	Fe2+	Fe3+		
SK-7	0,52	1,69	0,73	0,03	0,25	0,012	2,79	1,26	0,33	5,70	614
	0,44	1,73	0,75	0,03	0,26	0,01	2,98	1,20	0,32	7,65	562
SK-28	0,41	1,75	0,75	0,03	0,26	0,01	2,48	1,50	0,21	6,16	606
	0,46	1,75	0,73	0,03	0,25	0,011	2,26	1,61	0,27	4,60	663
SK-6	0,39	1,75	0,81	0,04	0,27	0,013	2,79	1,29	0,34	7,75	572
SK-9	0,54	1,76	0,63	0,04	0,22	0,012	3,00	1,12	0,26	7,08	545
SK-2	0,45	1,70	0,77	0,04	0,26	0,015	2,40	1,51	0,33	4,98	656
SK-11	0,42	1,85	0,71	0,02	0,24	0,007	2,33	1,50	0,25	5,88	599
											460

The temperature from Graham & Powell (1984) varies from 545°C to 663°C. The Geothermometer from Krogh Ravna (2000) is systematic 117-176°C lower, possibly due to the fact that Krogh Ravna (2000) calibrated the geothermometer for amphiboles with Ca = [1.5, 2], whereas the amphiboles in Engebøfjellet range in Ca from 1.2 to 1.5. This shows how sensitive the geothermometer is for invalid amphiboles.

8.2.5 Zirconium-in-rutile geothermometer

The zirconium in rutile geothermometer (Tomkins *et al.*, 2007) is based on rutile coexisting with quartz and zircon. At equilibrium the rutile will incorporate ZrO₂, and the amount varies with respect to T and P. Tomkins *et al.* (2007) ran experiments from 1 atm to 30 kbar at temperatures between 1000 and 1500°C. The results were fitted to Eq. 8.5 for $X_{ZrO_2}^{Rt} < 0.01$, and yielded

$$T \text{ (°C)} = \frac{83.9 + 0.410P(\text{kbar})}{0.1428 - R\ln Zr(\text{ppm})} - 273 \quad (\text{Eq. 8.13, Tomkins } et al., 2007)$$

R is the gas constant (0.0083144 KJ K⁻¹).

8.2.6 Application of zirconium-in-rutile-geothermometer on samples from Engebøfjellet

The zirconium-in-rutile geothermometer was applied on 4 samples from the Engebøfjellet Eclogite, showing Zr concentration in rutile between 31 and 111 ppm. Both quartz and rutile were coexisting with the rutile with $X_{ZrO_2}^{Rt}$ below 0.01 fulfilling the requirements from Tomkins *et al.* (2007). The temperatures were calculated on pressures of 15 and 20 kbar (after Korneliussen *et al.*, 1998) and are presented in table 15.

Table 15 - Results from the zirconium-in-rutile geothermometer of Tomkins *et al.* (2007) applied on samples from the Engebøfjellet eclogite.

Sample	Zr in Rt, Tomkins <i>et al.</i> (2007)		
	Zr	T°C(15kbar)	T°C(20kbar)
SK2	92	583	602
SK2	73	568	587
SK2	63	558	577
SK6 wall-rock	111	596	616
SK6 wall-rock	63	558	577
SK6 wall-rock	93	584	603
SK6 wall-rock	100	589	608
SK12	89	581	600
SK12	69	564	583
SK12	66	561	580
SK28	52	546	565

The detection limit of Zr in rutile is 49 ppm (see section 7.6). Hence, the Zr concentration below 49 ppm is not included in table 15. The temperature ranges from 546°C 15 kbar to 616°C at 20 kbar.

8.2.7 Plagioclase-omphacite-quartz geobarometer

The Pl-Omp-Qz geobarometer is based on the Ab-Jd-Qz geobarometer of Holland (1980). Holland (1980) fitted the Ab = Jd + Qz reaction to Eq. 8.5 from high P and T experiments, in order to produce a barometer suitable for high temperature and pressure. The location of the reaction curve was earlier well known from 500-600°C (Newton & Smith, 1967), but Holland (1980) fitted the line up to 1200°C (Figure 75). The experimental data was fitted to an expression of T and P:

$$P(\text{Kbar}) = 0.0265T(\text{°C}) + 0.35 \pm 0.5 \quad (\text{Eq. 8.14, Holland, 1980}).$$

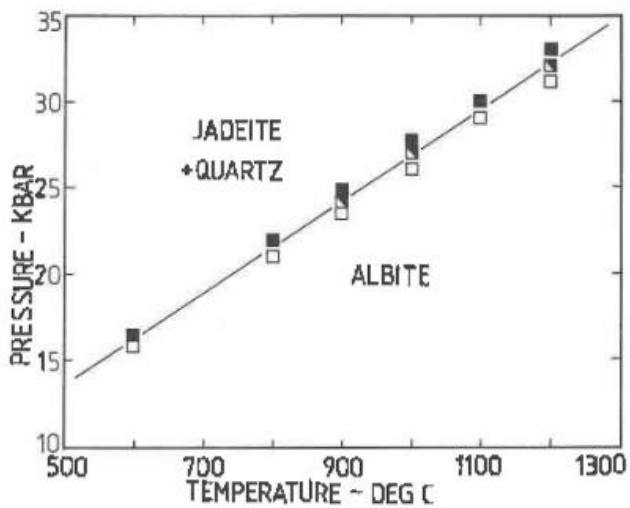


Figure 75 - The fitted line from Hollands (1980) experiment on the Albite = Jadeite + Quartz reaction between 600 and 1200°C.

When adding Ca to the system, the Pl - Omp - Qz equilibrium curve is displaced towards lower pressure. This is illustrated in figure 76 by Gasparik & Lindsley (1980). The Ab - Jd - Qz equilibrium curve is the same as proposed by Holland (1980) indicating pure Jd and Ab. Figure 76 shows several isopleths representing X_{Jd}^{Omp} and different isopleths yield different pressures for the same temperature.

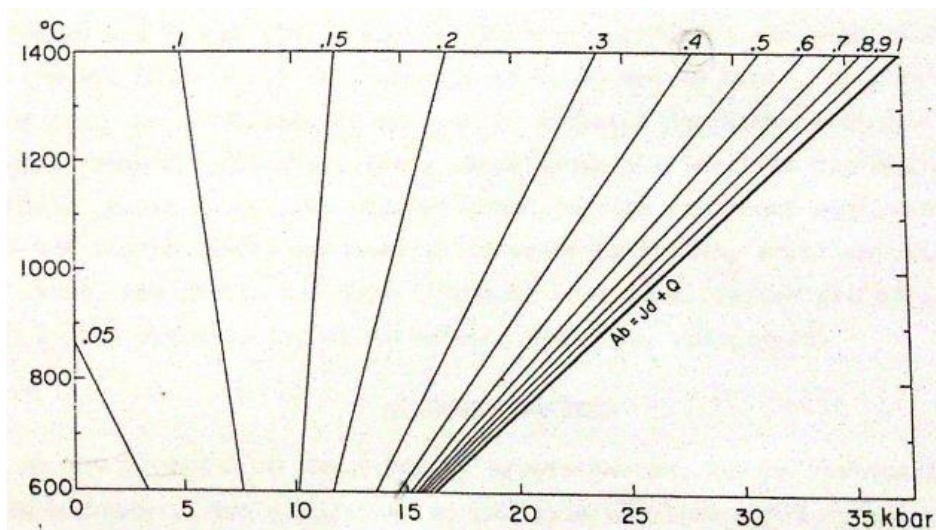


Figure 76 - Phase diagram for the system Di - Jd - SiO₂ for different molar concentrations of Jd in Omp (Gasparik & Lindsley, 1980). Note the difference in axes from figure XX.

8.2.8 Application of the Pl-Omp-Qz geobarometer for minimum pressure estimate at Engebøfjellet

Since no eclogitic plagioclase is found in the Engebøfjellet Eclogite, an absolute pressure cannot be calculated. However, by applying Gasparik & Lindsley (1980) at least a minimum pressure of formation can be found. Since the equilibrium curve of the Pl-Omp-Qz reaction increases in pressure with increasing X_{Jd}^{Omp} , applying Gasparik & Lindsley (1980) on the omphacite with the highest X_{Jd}^{Omp} will yield the minimum pressure. In order to estimate an upper pressure, the Grt-Omp-Ph geobarometer (Waters & Martin, 1993) was considered used. This is not done in this thesis because of lack of time.

Based on the EMP analyses, the highest X_{Jd}^{Omp} in a pyroxene is from SK-31 with $X_{Jd}^{Omp} = 0.425$. The temperature is calculated to approximately 600°C from Grt-Cpx, Grt-Amp and Zr-in-Rt geothermometers, yielding a minimum pressure from Gasparik & Lindsley (1980) of close to 15 kbar. X_{Jd}^{Omp} strongly depends on Fe³⁺ due to the occupation of Na in the Aeg component. At such low temperatures and high X_{Jd}^{Omp} , an error in Fe^{3+:}Fe²⁺ (calculated based on charge balance) will not affect the pressure significantly, at least not if the X_{Fe3+}^{Omp} is an overestimate.

8.3 Summary on thermobarometry

From the geobarometric calculations the temperature is calculated to approximately 600°C (± 100) °C, and the pressure to at least 15 kbar. The variations in the temperature are large, and the consequences of calculating Fe^{2+:}Fe³⁺ by charge balance is thought to be a source to this error. All the mineral pairs used for calculations are rim measurements, and should hence be equilibrated.

9. XMapTools

9.1 Introduction on XMapTools

XmapTools V 1.6.1 (Lanari *et al.*, 2013) is a Matlab based program designed for processing elemental X-ray maps from the EMP. By loading up matrices from elemental maps together with control points, the built in features in the program are able to detect mineral phases, recalculate structural formulas, plot the chemistry in both 2D and 3D and do thermobarometry together with a number of other possibilities.

High quality Al, Ca, Fe, Mg, Mn, Na, Si and Ti maps were made from a section of sample ME9-97A (BH 103/103.3, see figure 20) by using the EMP. In addition, 126 point analyses were done, covering the representative spread in mineral chemistry within the map. The mapping and analyses was done according to De Andrade *et al.* (2006). Sample ME9-97A is coarse grained eclogite from Engebøfjellet, as illustrated in figure 2 (Section 1.2). The reason that this thin section was chosen over collected samples, was that earlier investigation (Korneliussen *et al.* 1998) showed a strong zoning of these garnets. From microprobe analyses of collected sample, a weak zoning is observed in garnets, but most garnet appear to be recrystallized and close to homogeneous. The garnets in the sample showed numerous, larger eclogite facies inclusions (relative to the fine grained garnets). In addition Krogh (1980) used thermobarometry on similar garnets from Sunnfjord, yielding a prograde evolution of the garnet, as well as finding pre eclogite facies mineral assemblage. XMapTools was used for studying this thin section since it gives the possibility to work more accurately and systematic with an elemental map.

The intensity matrices for the different elemental maps were loaded into XMapTools, along with the coordination references and control points showing representative chemical variations on every mineral phase present. Each unique mineral phase was then selected, and the program identified all the selected phases within the map. Since maps created for this purpose are of high resolution, the grain boundaries are well defined and relative few pixels overlap two or more minerals.

When the structural formulas for the mineral phases are recalculated the program contains information on the number of atoms per formula unit in every pixel within the map. Mineral end members and cation positions are also included, giving the user a good opportunity to investigate the variation within and between mineral grains.

Along with the visual component, the thermobarometry feature is one of the XmapTools strongest tools. It contains different thermometers and barometers, usually with several references. When the wanted thermometer or barometer is chosen, the user is asked to first make a point on for example the garnet, and one at the other mineral of interest. The program then calculates the conditions based on the structural formula matrices, assuming equilibrium between the two points.

Below, observations on garnet, pyroxene and amphibole are described.

9.2 Application of XMapTools on a sample from Engebøfjellet

9.2.1 Garnet

Figure 77 A shows where the garnets plot within the pyrope-almandine-grossular triangle. 96% (figure 77 B) of the measurements lie within the $X\text{Alm}_{60-70}X\text{Pyr}_{5-23}X\text{Gro}_{15-30}$ field.

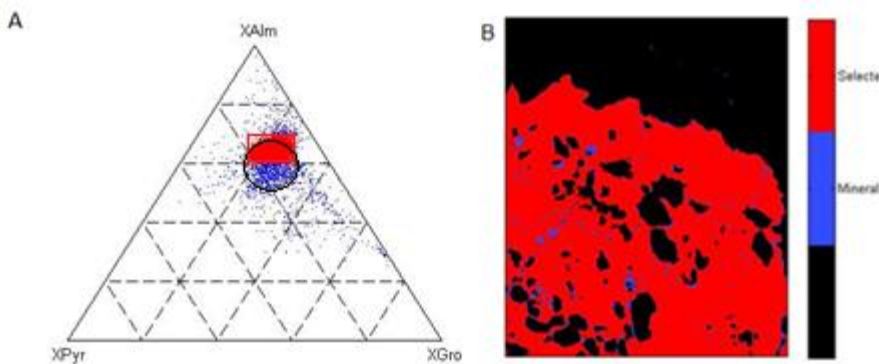


Figure 77 - A) Triangle plot of the Grt analyses. **B)** Amount of the Grt within the red rectangle in A. Black circle marks compositional spread from point analyses (see section 7.1).

The garnet displays a strong zoning with respect to Mn and Mg and a weaker Ca zoning (Figure 78 A, B and C respectively).

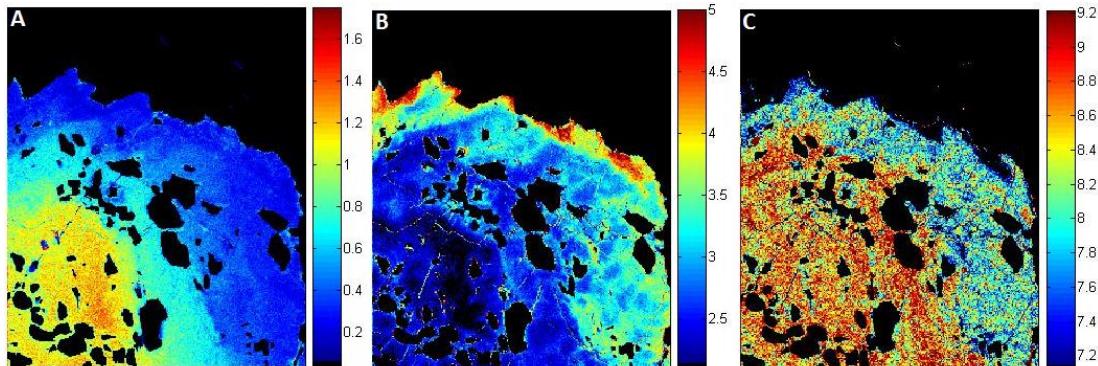


Figure 78 - Zoning in Grt with respect to A) Mn, B) Mg and C) Ca.

Figure 79 A and B show the zoning of MnO and MgO respectively in the garnet from the core (0 mm) to the rim (ca 1.2 mm). Based on core – rim ratio, these are the two oxides experiencing most zoning.

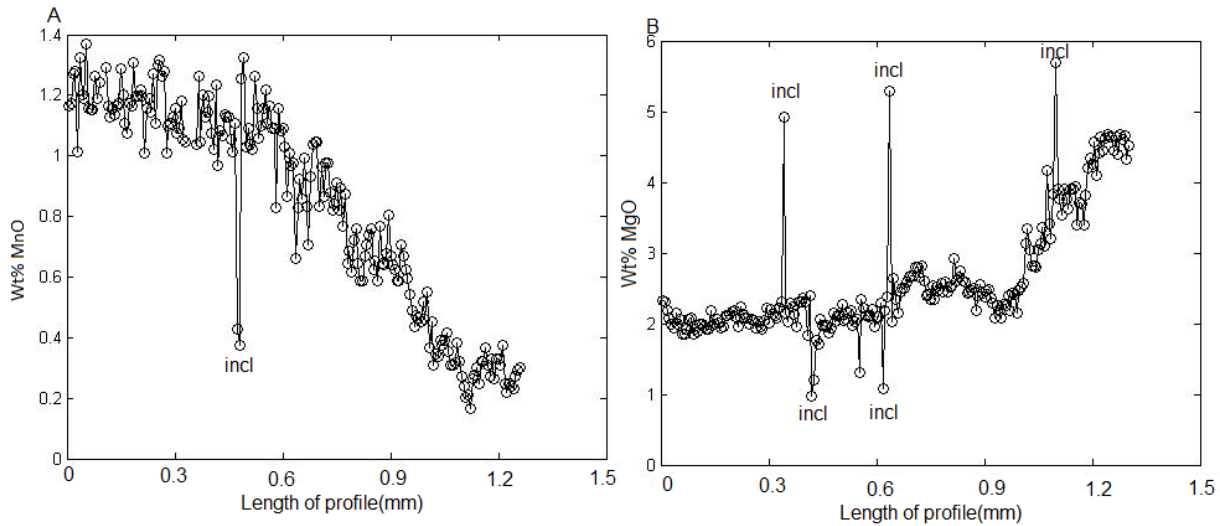


Figure 79 - Profile from core to rim in Grt, with respect to A) MnO and B) MgO.

MnO however, constitutes <1.5 weight percent, while MgO and CaO constitute up to 5 and 9.5 weight percent respectively, and can therefore not entirely account for the garnet zoning (Figure 80 A). Hence the two elements controlling the zoning of the garnet is Mg-Ca due to the Grossular-pyrope substitution at a nearly 1:1 ratio in the main cluster in (figure 80 B).

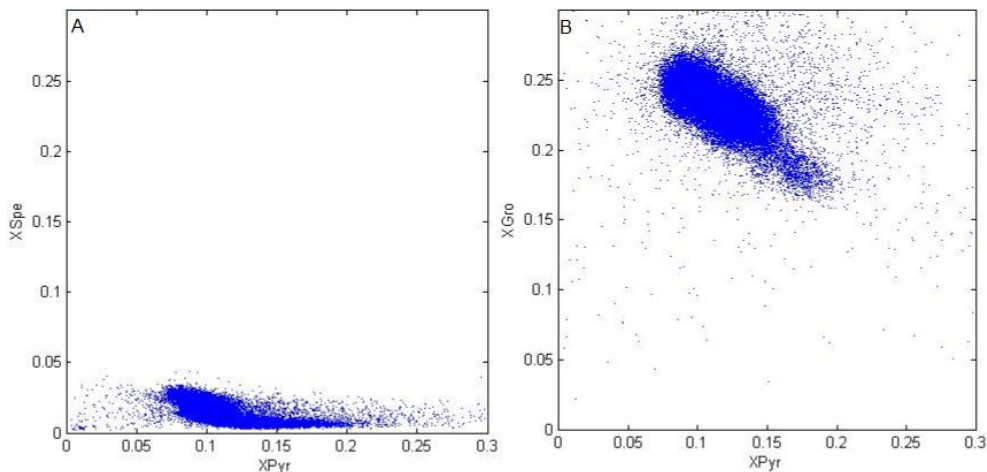


Figure 80 - 2D chemical plots of the Grt. A) XSpe-XPyr shows that relative to the XPyr, the XSpe is close to constant. B) XGro-XPyr shows that the negative correlation close to 1:1.

9.2.2 Pyroxene

From figure 81 A, the pyroxene in ME9-97A is omphacite. The omphacites in the section mapped are, however of two textural different types.

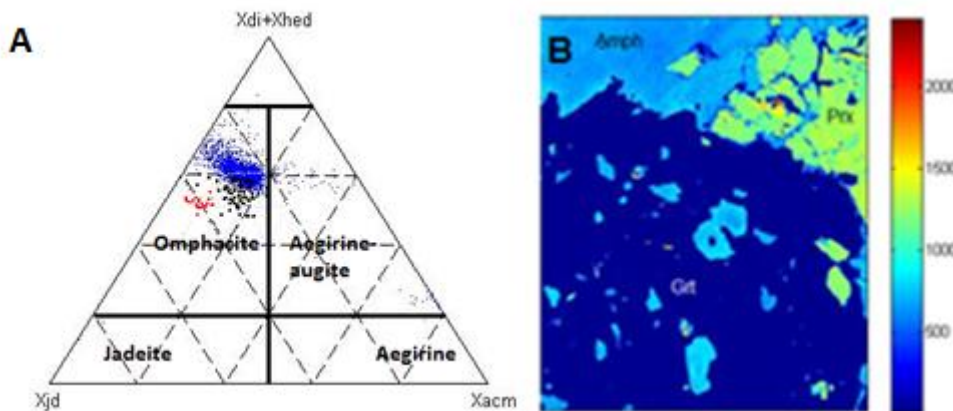


Figure 81 - A) Triangular plot in the XJd-XAcM-XDi+XHd system. Approximatley all points lie within the omphacite field, and red/blue dots represents point analyses (See section 7.2). B) Na map, showing the Omp as green/yellow.

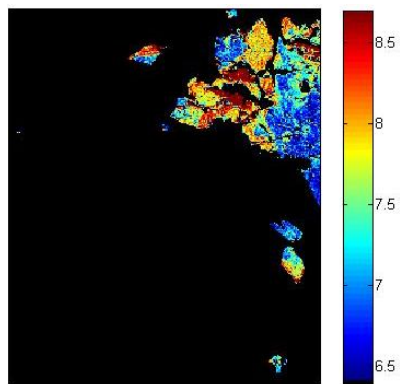


Figure 82 - Mg distribution in the Omp.

The omphacites occur in the matrix and as inclusions close to the rim of the garnet (Figure 81 B). Based on visual investigation of the elemental maps, the two textural different omphacites appear to be chemically identical.

Figure 82 shows the Mg-distribution in the omphacites, and clearly show a zoning into at least two distinct omphacites in both the matrix and inclusions. This is further proved by a scatter plot of XMg and Fe²⁺ (Figure 83 A).

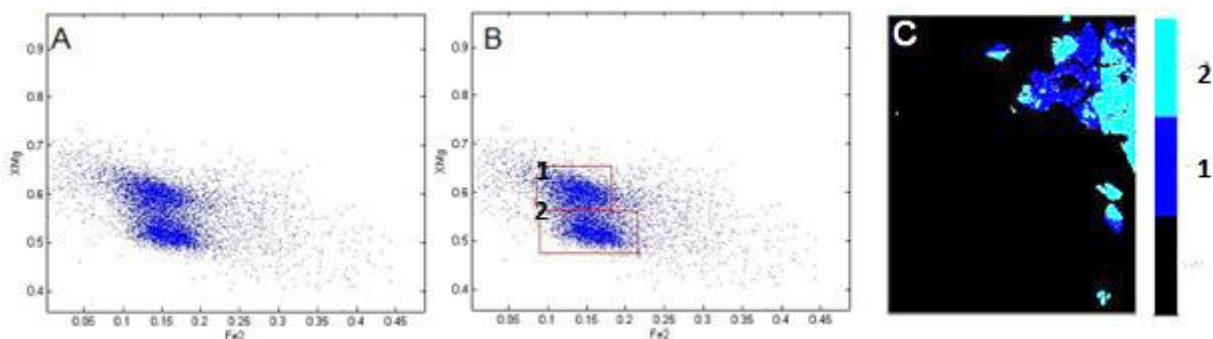


Figure 83 - A) 2D chemical plot of XMg-Fe²⁺ in the Omp. B) One group is selected in each cluster. C) Image showing where the two clusters are located.

The plot shows two clusters (Figure 83 B) separated by a Mg threshold. Figure 83 C shows where the two clusters from figure 83 B are located within the omphacites. Notice that both inclusion and matrix omphacite are zoned into the two groups.

At the contact between amphibole and omphacite there is a breakdown of omphacite into a symplectite appearing texture involving relics of the omphacite together with quartz, calcium rich carbonate (Figure 84 A) and amphibole (Figure 84 B). Since omphacite is richer in both Si and Ca than amphibole, a breakdown of

omphacite to amphibole would result in development of quartz and carbonate as bi products. A slight increase in Na content in amphibole towards the contact to omphacite and a slight decrease in the Na content of omphacite towards the amphibole (Figure 84 C) could indicate a minor Na exchange between the two minerals.

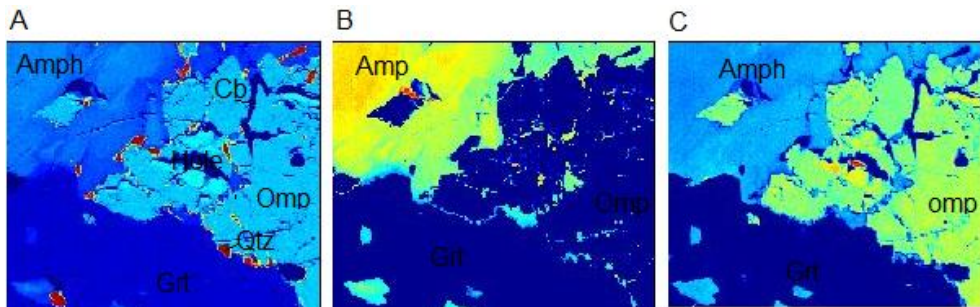


Figure 84 - A) Si map showing Qz as red. B) Ca map over Amp. C) Na map showing zoning in Omp towards Amp.

Since all the pyroxene is omphacite, the exchange reaction occurring within omphacite causing the strong zoning occurred at eclogite facies conditions. At lower P-T conditions the residue pyroxene would not be omphacite but rather an aegirine-augite as seen in section 7.2.

A breakdown of omphacite also appears to occur at the contact to the garnet, where a narrow rim of quartz (Figure 85 A) and amphibole (Figure 85 B) is found. Apart from this reaction no zoning of either the garnet or omphacite occurs in the contact zone.

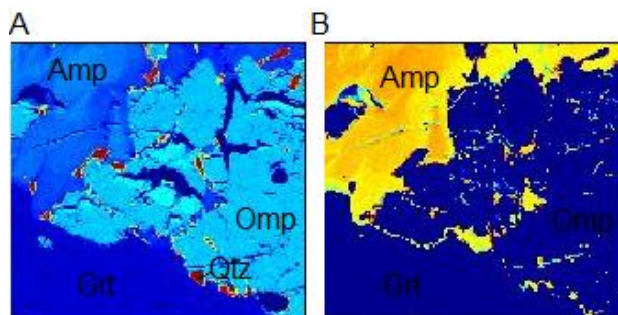
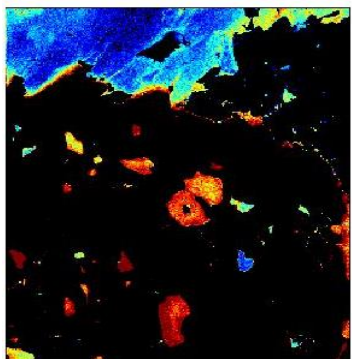


Figure 85 - A) Development of Qz in the contact between Omp and Grt. B) Development of Amp in the contact between Omp and Grt.

9.2.3 Amphibole

The amphibole within the mapped section is texturally within three groups. Figure 86 shows that the amphibole



occurs as 1) matrix amphibole, 2) amphibole inclusions in garnet and 3) amphibole as reaction product from decomposition of omphacite. Figure 86 also suggests that most of the inclusions are chemical different from the matrix amphibole, even in the cores. This difference is further confirmed by chemical scatter plots showing two clusters (Figure 87 A) corresponding to the matrix amphibole (Group 1 in figure 87 B) and inclusion amphibole (Group 2 in figure 87 B).

Figure 86 - Distribution of Amp in the map from a Fe-map.

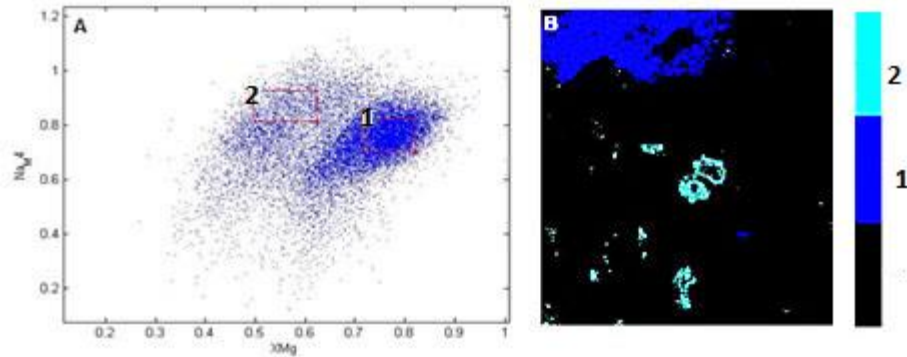


Figure 87 - NaM4-XMg plot for amphiboles gives two clusters that according to B separates the matrix Amp from the inclusion Amp.

When following a profile from the inclusions in the core towards the matrix amphibole (Figure 89 A) a strong Mg-Fe substitution occurs from the Fe rich inclusions to the Mg rich core of the matrix amphibole (figure 89 B and C, respectively). The profiles also show that the inclusions and matrix amphibole are zoned from rim to core, and that Fe-Mg exchange reactions strongly contribute to this zoning.

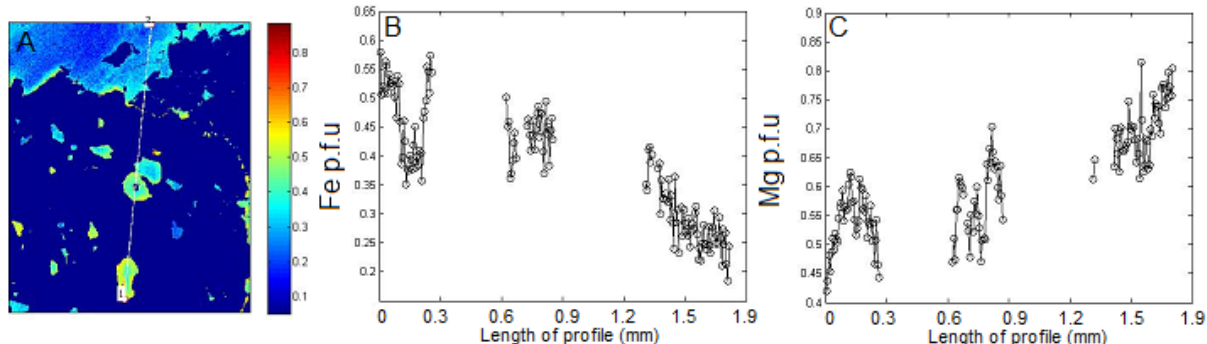


Figure 89 - A) Shows where the profile is located. B) Distribution of Fe along the profile. C) Distribution of Mg along the profile.

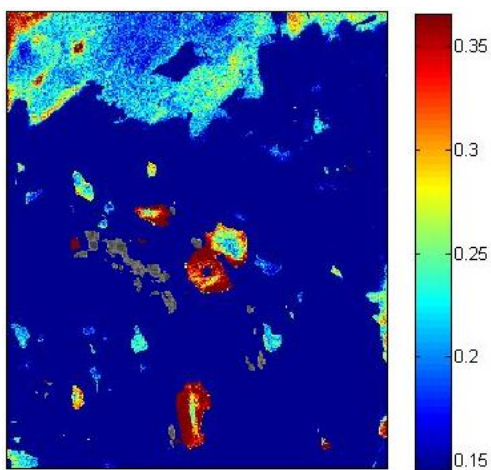


Figure 88 - Ti map on the Amp. Grey fields are rutile.

Figure 88 shows how sensitive amphiboles are for incorporating Ti when being in contact with rutile (grey areas in figure 88). The color bar shows weight percent TiO_2 in amphibole, and when in contact to rutile the TiO_2 content is often doubled at the rim of the amphibole.

9.2.4 Thermometry

Two thermometers were used; garnet-amphibole (Graham & Powell, 1984) and garnet-clinopyroxene (Ellis & Green, 1979). The garnet-amphibole thermometer is pressure independent whereas the garnet-clinopyroxene is pressure dependent, and requires a pressure input. Pressures is earlier interpreted to have been around 15 kbar,

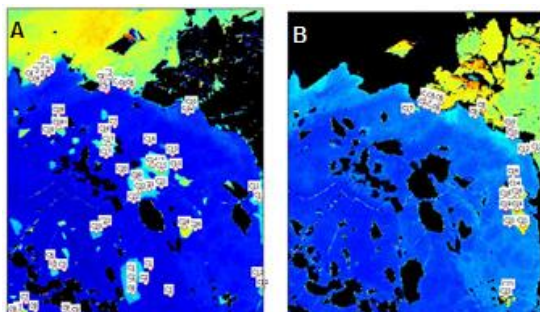


Figure 90 - A) Points for Grt-Amp thermometry. B) Points for Grt-Cpx thermometry.

The results from the thermometry calculations from XMapTools are presented in table 16 below.

Table 16 - Results from calculating temperature. For Grt-Cpx both 10 kbar and 15 kbar is used.

Garnet-Amphibole			Garnet-clinopyroxene		
Couple	P	T	Couple	P	T
Rim			Rim		
C1		568	C1	15	771
C2		590	C1	10	756
C3		596	C3	15	771
C4		589	C3	10	756
C5		556	C5	15	902
C6		579	C5	10	885
C10		607	C7	15	752
C11		620	C7	10	731
C12		589	C9	15	840
Average		588	C9	10	815
Intermediate			C11	15	927
C13		521	C11	10	883
C14		473	Average (10 kbar)		804
C15		505	Average (15 kbar)		827
C16		563	Intermediate		
C17		494	C13	15	872
C18		463	C13	10	854
C19		469	C15	15	809
C20		520	C15	10	794
C21		559	C17	15	761
C22		608	C17	10	747
C23		643	C19	15	784
C24		445	C19	10	769
Average		522	C21	15	773
Core			C21	10	758
C1		495	Average (10 kbar)		784
C2		485	Average (15 kbar)		800
C3		493			
C7		430			
C8		480			
C9		473			
Average		476			

and due to an uncertainty both 10 and 15 kbar were used as input pressure for the thermometry between the same points. Several garnet-amphibole/clinopyroxene couples were taken between the rim and core of the garnet, in order to see a general pattern. Positions of the thermometry calculations are pointed out in figure 90 A (Garnet-amphibole) and figure 90 B (Garnet-clinopyroxene).

The garnet-amphibole thermometer shows an increase in temperature from the core towards the rim, suggesting a garnet growth during prograde metamorphism. Since omphacite is not found near the core of the garnet, garnet-clinopyroxene temperatures from this region is not calculated. The two thermometers show a temperature difference of approximately 200°C. According to the classical thermobarometry (see section 8) the Grt-Amp geothermometer in table 16 is the most correct.

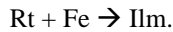
The reason for the error (relative to section 8.2.2) in the Grt-Cpx is due to the K_D . The K_D used by XMapTools ranges from 1.33 to 1.94, and K_D used for classical thermometry ranges from 2.52 to 3.05. Fe^{3+} is recalculated by XMapTools, so the error in the T could be a bug in the program. The pressure used for the calculation is set to 10 and 15 kbar, whereas in the thermometers in section 8 the pressures used are 15 and 20. Using 10 and 15 kbar is a mistake, but could not be redone due to the fact that coffee 3 weeks before dead line was spilled all over the laptop used, and all the Matlab files were lost. Because of lack of time, the data

could not be reproduced. Anyway, the Grt-Cpx geothermometer show the trend of increasing T towards the rim.

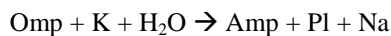
10. Discussion

10.1 Net mineral reaction from eclogite facies to Amphibole facies

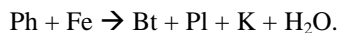
From section 6.2, several mineral reactions were described. From section 7, the chemistry of the minerals in these reactions is accounted for. From these results, more detailed mineral reactions can be written. When rutile breaks down to form ilmenite, it requires external Fe, hence



The breakdown of omphacite to amphibole and plagioclase within and close to amphibolite/greenschist facies veins requires external K and H₂O. Since the omphacite is rich in Na relative to amphibole and the amount of altered omphacite is large relative to the plagioclase, the reaction will produce excess Na:



In SK-28, phengite broke down to form biotite and plagioclase. Since the biotite is rich in Fe relative to phengite, the reaction requires Fe. Due to the formation of plagioclase, the reaction has the potential to free K and H₂O, yielding the reaction:



From the near isolated breakdown of garnet to amphibole (Edenite) in SK-6, break down of garnet to amphibole requires Na and H₂O, and will produce excess Fe:



The mineral reactions causing the alteration of the eclogite mineral assemblage to the amphibolite mineral assemblage (Table 17) may depend on each other.

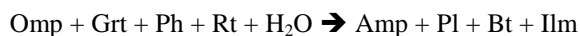
Table 17 - Observed mineral reactions from eclogite facies to Amphibolite facies.

Eclogite facies	→	Amphibolite facies
Omp + K + H ₂ O	→	Amp + Pl + Na
Grt + Na + H ₂ O	→	Amp + Fe
Ph + Fe	→	Bt + Pl + K + H ₂ O
Rt + Fe	→	Ilm

Adding the reactions from table 17, and assuming a closed system were only H₂O is added, the net reaction is



Cancelling the elements present at both sides of the reaction leaves the net reaction



There are no obvious reasons to assume a closed system, but as the reaction above shows, it is possible to have a transition from the observed eclogite facies assemblage to the observed amphibolite facies assemblage without

input of other elements. Several attempts on balancing apparently simple mineral reactions and breakdowns ($\text{Omp} + \text{Grt} = \text{Amp}$, $\text{Ph} = \text{Bt} + \text{Pl}$ and $\text{Grt} = \text{Amp}$ in vein) have failed, indicating an external source/sink of elements.

The alteration of primary amphibole to secondary amphibole is not included in the reaction above. The reason for excluding this breakdown is the complex and highly variable chemistry of the secondary Amphiboles. This variance in Amphibole chemistry, however, is an excellent sink for excess elements in the alteration of the eclogite facies assemblage.

Since the amount of H_2O required for the observed alteration of Omphacite and Garnet to Amphibole must be considerably larger than the H_2O released from breakdown of Ph to Bt –which in fact is minor–, external H_2O is required. The veins and fractures frequently found in the Engebøfjellet Eclogite is most likely the pathway of this external H_2O and possibly elements. The source for this metamorphic fluid may be the gneissic host rock.

10.2 The detection of rutile through image processing

From visual control, the Matlab program written to detect rutile was able to detect most of the rutile in the thin section. As seen in table 18, however, the amount of rutile detected in thin sections is often significantly lower than the amount of rutile detected through XRF and XRD. Since the rutile is proven to be chemically pure (see section 7.6) and that some of the total TiO_2 occurs in Amphiboles and ilmenite, the weight percent of rutile has to be lower than the TiO_2 from bulk rock XRF is. The program gives the amount of rutile in modal percent, and is therefore recalculated to weight percent by roughly calculating an eclogite density from modal abundances of minerals and the respective mineral densities (from www.mindat.org), and multiply the modal percent with the factor $\rho(\text{Rutile}) / \rho(\text{Eclogite})$.

Table 18 - Amount of rutile in samples based on three different methods.

	Modal % image processing	Cor. Image to weigh percent	Bulk rock % XRD	Bulk rock % XRF
SK-7	3,40	4,08	5,33	5,37
SK-8	3,64	4,37	4,31	4,89
SK-9	2,93	3,52	5,17	5,21
SK-11	2,78	3,34	3,16	3,04
SK-12	2,75	3,30	3,45	4,23
SK-20	1,12	1,34	3,2	3,34
SK-29	1,99	2,39	4,61	4,76
SK-30	0,89	1,07	1,98	2,19
SK-31	0,47	0,56	2,21	0,98

Assumed:

$$d(\text{ecl}) = 3.5$$

$$d(rt) = 4.2$$

A possible explanation for the underestimate of rutile in several samples is that the program is not able to detect the smallest rutile grains. The rutile grain size varies from sample to sample (see appendix 4.2), and how close the image processing program is to the XRD/XRF analyses correlates strongly with how coarse the rutile grains are. This may seem to be a strong weakness, but for an economical purpose it is better than blindly rely on results from XRD/XRF. Geologist in Nordic Mining ASA, Mona Schanche, said that the rutile yield strongly depends on the rutile grain size, since the smallest grains are difficult to separate. The most interesting fraction

was grains >75 μm in diameter. When the Matlab program struggles to detect small grains, in addition to morphological operations removing pixels not surrounded by a given number of other pixels (see appendix 6.1), there is an unspecified threshold in grain size. Assuming the rutile grains to be perfectly rounded, a 75 μm grain has an area of $4.4 \cdot 10^3 \mu\text{m}^2$. From the rutile grain size histograms (Appendix 4.2) no grains <10 $^3 \mu\text{m}^2$ are detected. Hence, nearly all rutile detected is above the grain size limit proposed by Nordic Mining ASA. The result from the image processing can therefore be interpreted as a more accurate measurement on the amount of mineable rutile relative to XRD/XRF.

10.3 Consequences of calculated Fe³⁺:Fe²⁺ ratio

When analyzing at the EMP, all Fe is calculated as ferrous (Fe²⁺). Since minerals often contain both ferrous and ferric (Fe³⁺) Fe, the proportion between the two valence states are be calculated by charge balance. When the recalculation of the structural formula is done (see appendix 5), the total cation charge is compared to the charge of ideal oxygen in order to see if the structural formula has a positive or negative charge. If the anion charge is greater, some ferrous Fe is changed into ferric Fe to balance the charge in the structural formula. This, however, will only assume the proportion between ferrous and ferric Fe, and may hence be wrong.

The fact that the Fe²⁺:Fe³⁺-ratio is calculated assuming an electrical neutral mineral, causes problems when treating the data. For end-member calculations the distribution of Fe²⁺ and Fe³⁺ is important, and small errors can affect the result significantly. The Cpx in the Engebøfjellet Eclogite is relative Fe-poor, and Fe_{tot} (as FeO) contributes only to <10 % for the weight. Typical ferro-gabbroic omphacite have around 0.1 Fe²⁺ pfu, and around 0.15 Fe³⁺ pfu. If Fe²⁺ is wrongly recalculated by as little as 0.05 pfu, it results in an increase in the hedenbergite component of 40%. The same error in Fe²⁺ for a garnet will on the other hand cause an increase in the almandine component of 1.5 %.

Thermobarometry (see section 8) is sensitive for the amount of Fe²⁺ since most geothermometers are based on the Mg-Fe²⁺ exchange reaction. The Garnet-Cpx thermometer from Ellis & Green (1979), for example, includes the $K_D = (\text{Fe}^{2+}/\text{Mg})^{\text{Grt}} / (\text{Fe}^{2+}/\text{Mg})^{\text{Cpx}}$. For accurate thermobarometric calculations, a precise Fe²⁺:Fe³⁺ ratio is required. 13 samples are sent to professor David Moecher at the University of Kentucky for analysis at a Mossbauer spectrometer. This technique will hopefully increase the precision of the Fe²⁺:Fe³⁺-ratio, for better thermobarometric studies. The result from Dave Moecher will not be available in this thesis.

10.4 Growth of garnets based on inclusions and thermometry

The garnet analyzed in XMapTools (Section 9.2.2) was zoned with respect to the distribution of amphibole and omphacites inclusions. Figure 91 shows that the inclusions close to the rim are omphacites, whereas the inclusions inside the rim zone are amphiboles.

This can be explained in either two ways:

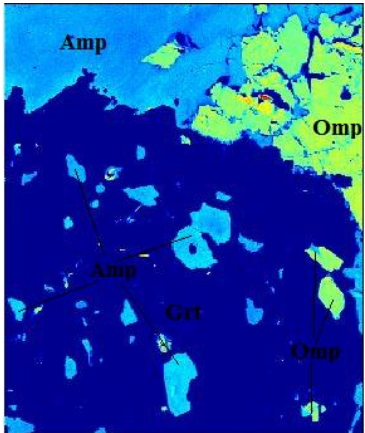


Figure 91 - Na map showing Garnet, Amphibole and Omphacite from sample ME 9.97-A.

1) The garnet grew from core and towards the rim, starting in garnet amphibolite facies where both garnet and amphibole were in equilibrium. Since omphacite is not stable at garnet-amphibolite facies, omphacite inclusions in the core zone could not occur. In the late phase of the garnet growth, eclogite facies was reached, allowing omphacite inclusions.

2) The distribution of amphibole and omphacite inclusions is controlled by the a_{H_2O} activity (a_{H_2O}). If the a_{H_2O} is high, Le Chatelier's principle will expand the stability field of hydrous phases as amphibole, and reduce the

stability of anhydrous phases as omphacite. Assuming eclogite facies conditions throughout the garnet crystallization, a_{H_2O} may have been too high in the incipient phase of the garnet growth, preventing omphacite to crystallize. Hydrous phases as amphiboles, however, could crystallize causing the core zone of the garnet to be dominated by amphibole inclusions. The crystallization of amphibole would eventually reduce the a_{H_2O} enough to allow omphacite to crystallize instead of amphibole, hence the omphacite dominated rim.

There are arguments strengthening theory 1 and weakening theory 2: 1) From section 9.2.4, the garnet-amphibole thermometer (Graham & Powell, 1984) shows an increase in temperature from core (476°C) to rim (588°C). From the metamorphic phase diagram (Figure 1) in the introduction, eclogite facies condition at 476°C is reached at about 18 kbar. According to Korneliussen *et al.* (1998) the pressure at Engebøfjellet is below 16-17 kbar. This suggests that the core of the garnet was crystallized at a lower metamorphic facies. From section 7.3 and 7.4, the eclogite facies amphiboles differ in chemistry relative to the amphiboles from lower facies. From section 9.2.3, the amphibole inclusions are chemically different from the matrix amphibole. The inclusions are richer in Al and Fe, and from section 7.4 and appendix 3 this is common for the lower facies amphiboles. 2) Assuming near constant metamorphic conditions is in disagreement with the geothermometry results from section 9.2.4. The difference in amphibole chemistry between the inclusions and matrix would possibly be minor given near constant conditions.

The zoning with respect to inclusions in the garnet is most likely to originate from a prograde metamorphism rather than being controlled by a_{H_2O} . In addition, the Mn zoning in the garnets showing a Mn rich core, and Mn poor rim is typical for a prograde growth of the garnet (Spear, 1995). Krogh (1980) concluded that the eclogites in the Sunnfjord region were formed during prograde metamorphosis, but this prograde evolution is previously not proved at the Engebøfjellet Eclogite.

10.5 Recrystallization of Garnet

As described above, the garnets show two very distinct textures. Common for all sample collected for this thesis is the weakly zoned fine grained garnets. In section 8 a larger garnet from ME 9.97-A was analyzed, showing a

strong zoning with respect to Mn Mg and Ca. The two types of garnet are apparently texturally different, but there are evidences relating the two. A 1 mm garnet in SK-6 was mapped for elements, and showed a weak zoning as expected. Notably, however, were the two isolated concentrations of Mn within the garnet (Figure 56, section 7.1). The magnitude of the zoning in the smaller garnet was smaller (core:rim = 2:1) than in the larger garnet (core:rim = 5:1).

In ME 9.97-A, a single concentric Mn zoning appears to be a result of the garnet growth. When two such high Mn domains are found away from the core of a garnet in the garnet in SK-6, it strongly indicates a garnet recrystallizing event where two garnets have coalesced. This is interpreted to have happened during the recrystallization associated with foliation developing mylonitization. The reason to believe that the mylonitization caused the recrystallization of the garnets, is that the rims of the recrystallized garnets in contact to amphibole or omphacite yield eclogite facies conditions. This excludes the possibility that the garnets recrystallized in later events.

10.6 Quantitative XRD on eclogites

As the quantitative XRD analyses are used in this thesis, it generally appears to give reasonable results based on thin section and BSE/EDS investigations and is hence a good tool for studying eclogites. In order to check the validity of the method, an extensive image processing could be done and compared to the quantitative XRD. From what is done in this thesis, the Matlab image processing program is able to detect rutile and garnet, but could probably be upgraded to detect omphacite and amphibole in addition to the sum of quartz, mica and feldspar.

The main difficulty on the quantification was to fit the minerals with respective mineral chemistry to the XRD diffractogram. Almost pure spessartine fitted perfectly well to the XRD-diffractogram, but from EMP analyses the garnets were in fact relatively poor in spessartine (see section 7.1). Hence a trying and failing process was required to fit the observed garnet chemistry to the XRD diffractogram. This was also the case for the other minerals that deviated from the mineral standards in the Bruker Structure Database.

In order to improve this method on eclogites, a more extensive work on the EMP should be done in order to detect all the phases present. The representative mineral chemistry is already found, and for further tuning of the quantitative XRD, all samples should be processed with refined structural formulas representing the samples.

10.7 Mobility of Ti in hydrothermal fluids

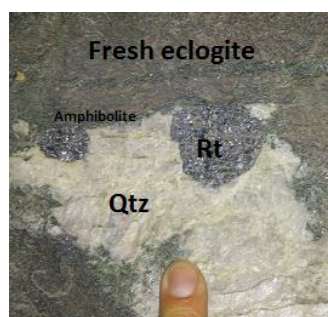


Figure 92 - Large rutile crystals in Qz + Omp vein in the tunnel.

TiO_2 is considered one of the least mobile components in a silicate rock, and Ti is therefore often used as a reference element in order to recognize chemical changes due to hydrothermal or metamorphic reaction (Audétat & Keppler, 2005). When relatively large amounts of rutile are found in eclogite facies veins at Engebøfjellet (Figure 92) a significant dissolution-reprecipitation is required, and hence the solubility of rutile and Ti in the high-P/T-fluids present should be considered. From EMP analyses and XMapTools, Ti is known to be mobile at least on a small scale since especially amphiboles are enriched in Ti when in contact to rutile, but abundant rutile in the veins require a mobility of Ti on a

scale larger than a few μm .

Under appropriate conditions, rutile can show elevated solubility in fluids, leading to significant Ti mobility. Under HP metamorphic conditions, rutile show evidence for this increased solubility due to crystals in fluid inclusions and rutile in veins as well as changes in whole rock TiO_2 -concentrations (Antignano & Manning, 2008). Several theories try to explain how larger amount of Ti can become mobilized in metamorphic rocks. Theories are increased solubility due to increase in P, extreme pH variations and high concentrations of complexing elements as fluorine, but it is unlikely that these theories can account for all occurrences (Antignano & Manning, 2008). This leaves the reason for the increase in Ti mobility uncertain.

Result from Audéat and Keppler (2005) show that the solubility of rutile increases with increasing P (Figure 93). Despite this, the solubility of rutile in pure H_2O at 820°C and 14 Kbar was only 10 ppm.

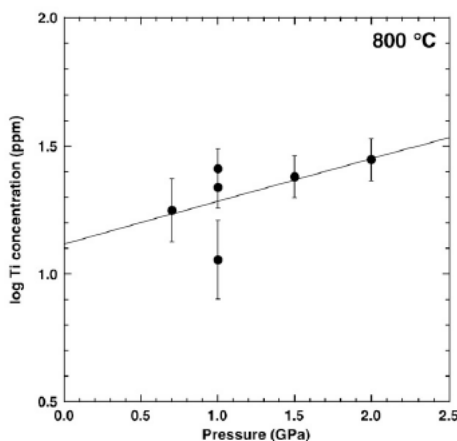


Figure 93 - Solubility of Ti from Rt in pure H_2O at 800°C at varying pressure (Antignano & Manning, 2008).

Since the solubility of rutile increase with increasing P, a drop in pressure would cause a decrease in solubility, and hence lead to precipitation of rutile in zones with lower pressure, for example in an open fracture in the eclogite.

Antignano and Manning (2008) showed that the solubility of rutile increases when NaCl or albite (Figure 94) is dissolved into the fluid. When 15 wt.% NaCl is dissolved into the H_2O at 814°C and 14 Kbar the solubility of rutile increased to 25 ppm. When 9.4 wt. % albite is dissolved into the H_2O at 815°C and 12 Kbar, the solubility of rutile increased to 96 ppm. Their work suggests that addition of fluorine into the H_2O would significantly increase the rutile solubility. F and Cl were analyzed using the EMP on amphiboles in fresh eclogite, alteration zones and within the veins, but none showed any signs of increasing F or Cl in the Amphiboles associated with rutile bearing veins. A further study of fluid inclusions in the quartz-pyroxene-rutile veins would be of interest in order to find what fluid components were present.

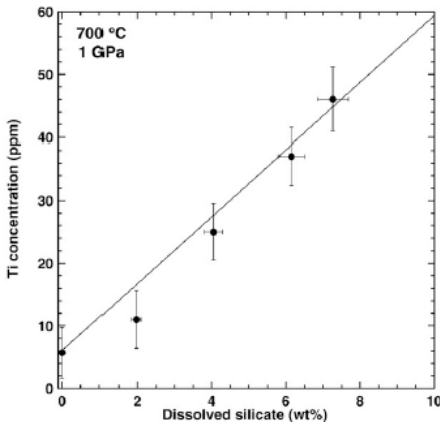


Figure 94 - Solubility of Ti from Rt at constant T and P with variable dissolved Ab (Antignano & Manning, 2008).

Antignano and Manning (2008) compared the solubility of rutile in a H₂O-system, a SiO₂-H₂O system and a NaAlSi₃O₈-system at various pressures. They concluded that rutile solubility increases with increasing P, does not show a systematic increase in solubility with increasing SiO₂, but show a linear solubility increase of rutile with increasing Na and Al content in the fluid at constant P and T. The report states that due to the high content of alkali feldspars in continental crust, metamorphic fluids from such rocks can contain significant amounts of dissolved Na, K, Al and Si. The gneissic rocks surrounding the Engebøfjellet Eclogite (Korneliussen *et al.*, 1998) can thus provide the metamorphic fluids circulating into the eclogite with dissolved material. Eclogite facies veins have omphacite, proving that at least Na, Al and Si were present in the fluid. When entering the veins, an associated pressure drop (Boiron *et al.*, 1990) may reduce the solubility of rutile in the fluid enough to cause precipitation of rutile.

10.8 Development of veins at eclogite facies

Most of the structures observed in eclogites are ductile structures. Ductile structures are developed due to the flowing properties of rocks common at eclogite facies conditions. Despite this, veins are observed at Engebøfjellet (Figure 95). They vary in width from 1 cm to >1 m and typically contain quartz, pyroxene, rutile



Figure 95 - Quartz vein cutting eclogite in the tunnel. Vein contains several larger rutile crystals.

and carbonate. From field observations and earlier works (Etc. Foreman *et al.*, 2005), many of them are interpreted to represent brittle deformation structures cemented with material from hydrothermal fluids. The veins at Engebøfjellet often cut the foliation, and is hence post-dated to the foliation developing event, but since they are composed of eclogite facies minerals, and do not alter the eclogite wall rock, they are considered eclogite facies veins.

Veins at lower crustal levels are often considered to originate from hydro fracturing of the rocks, where the pore fluid pressure exceeds the least principle stress. The veins are assumed to develop due to an increase in the stress with a concomitant drop in pore fluid pressure (Birtel & Stöckhert, 2008). The increased stress may be induced by a nearby seismic event. In order to cause an open cavity at such deep levels, a high rate of deformation is required. Ductile deformation structures are often observed in such rocks, and this is suggested to originate from the decreased stress after the seismic event, where the vein material could deform

ductile (Birtel & Stöckhert, 2005). The fluid responsible for the hydro fracturing can originate from metamorphic reactions (Strating & Vissers, 1991) dehydrating hydrous minerals, causing a significant release of fluids. Strating and Vissers (1991) claim that dehydration of antigorite in hydrated peridotites can cause brittle deformation at depths of 50-70 km. Since amphiboles contain one mole of $(OH)_2$ per formula unit, the dehydration of for example 1000 g actinolite ($Ca_2(Mg,Fe)_5Si_8O_{22}(OH)_2$) will release approximately 20 g of H_2O . When considering the amphibolite-eclogite transition where several million tons of amphiboles dehydrate to pyroxene, the amount of H_2O released is significant.

10.9 Lack of amphibolitized samples

Sample SK-30 (Figure 96) and SK-31 were collected as amphibolite in order to get an overview on the mineralogy and geochemistry of the completely retrograded equivalents to the eclogite. When these samples, from thin section studies, turned out to be eclogite, the sample collection did not contain any amphibolite.



Figure 96 – Hand specimen from SK-30. Sample appears to be amphibolite, but turned out to be fresh eclogite.

Hence, the amphibolitization of the eclogite could only be studied close to amphibolite/greenschist facies veins and fractures. Studying the small scale amphibolitization associated to the veins is an advantage, however, since both metamorphic facies assemblages are represented, and reactions are easier to track. On the down side, lack of whole rock amphibolite samples causes no bulk rock XRD and XRF to be available. For this reason eclogite facies bulk rock analyses are not compared to amphibolite bulk rock.

Since the eclogite to a large extent varies in visual appearance, in addition to being fine grained, care must be taken when classifying samples in field. Rocks earlier classified as amphibolite may hence actually be eclogite. If this is true, the resource potential of the Engebøfjellet increases since more volume than earlier proposed is actually fresh eclogite.

10.10 Problems due to bad thin section polish

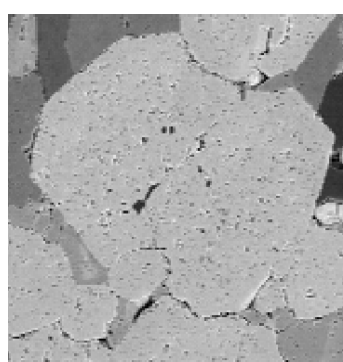


Figure 97 - Example on bad polishing of thins section from SK-6, Grt is ca. 0.5 mm across.

Several thin sections suffered from bad polishing, and especially the garnets had a very high pit density (Figure 97). When searching for zoning in garnets, profiles across garnets should contain 5-10 analyses. In most of the thin sections this was difficult to achieve due to the pits in the thin sections. When analyzing close to a pit, the analyses often yielded a weight percent total less than 98.5% and more than 101.5 % for garnets and pyroxenes, and the analysis had to be discarded.

11. Conclusion

The Engebøfjellet Eclogite is considered a rutile ore with up to 5.4 wt. % mineable rutile of high purity (>99.5 wt. % TiO₂). From an economical point of view, image processing gives a more correct result than XRD/XRF due to the problems the program has on detecting the smallest fraction (<10³ µm). The shape of the rutile is strongly dependent on the strain in each sample, from rounded grains in less deformed samples to elongated rutile clusters in deformed samples.

Based on bulk rock chemistry, primarily Fe, the eclogite can be divided into two groups: The low Fe leuco-eclogite and the high Fe ferro-eclogite. The difference in the bulk rock chemistry affects the mineralogy significantly but also the mineral chemistry. Both eclogite types contain sodium rich amphiboles (barroisite and magnesio-katophorite) and clinopyroxene (omphacite). The main difference in the mineralogy is that the ferro-eclogite is richer in rutile and almandine-grossular-pyrope garnet and lower in quartz and phengite.

From thermobarometric studies the eclogite facies metamorphic conditions are calculated to 600 (\pm ca. 100)°C and at least 15 kbar. Lack of good geobarometers and reliable Fe²⁺:Fe³⁺ ratios cause large uncertainties. Based on the distribution of amphibole and omphacite inclusions in larger Mn-zoned garnets and garnet-amphibole geothermometry, the eclogitization of the Engebøfjellet Eclogite protolith is interpreted to have occurred by prograde metamorphism. The temperatures range from 488°C in the core of the garnet to 574°C at the rim, indicating garnet amphibolite facies conditions in the incipient phases of garnet crystallization.

Due to fracturing with associated fluids during exhumation, smaller areas of the eclogite lens is partly to completely altered to amphibolite/greenschist facies. In completely altered areas, the eclogite mineral assemblage (Omphacite + garnet + primary amphibole + phengite + rutile) is replaced by symplectites of an amphibolite/greenschist facies mineral assemblage (Secondary amphibole + feldspar + biotite + ilmenite).

Many of the veins observed are eclogite facies veins with quartz, omphacite and rutile. Based on the presence of omphacite, the vein fluid must have contained dissolved Na, Al and Si, causing increased solubility of rutile. The pressure drop associated with the vein or in pressure shadows is thought to have caused the rutile precipitation.

12. Suggestions for further research

A fluid inclusion study on the rutile bearing veins is suggested in order to find the fluid chemistry. Since the rutile solubility increases with increasing F, Cl, Na and Al a study on this could increase the understanding on the dissolution-reprecipitation process taking place in the eclogite and these veins. A more systematic search for albite/plagioclase in the eclogite mineral assemblage could be done in order to use the albite-jadeite-quartz geobarometer more accurately. The samples sent to Dr. Dave Moechler for determination of Fe²⁺:Fe³⁺ should be reconsidered regarding (P-)T estimates. Further, more precise refinements should be done to get better quantitative XRD results. In addition, the image processing program should be upgraded to be able to detect more minerals from thin sections.

13. References

- Antignano, A. and Manning, C.E. 2008. Rutile solubility in H₂O, H₂O–SiO₂, and H₂O–NaAlSi₃O₈ fluids at 0.7–2.0 GPa and 700–1000 °C: Implications for mobility of nominally insoluble elements. *Chemical Geology* 255, 283-293.
- Audétat, A. and Keppler, H. 2005. Solubility of rutile in subduction zone fluids, as determined by experiments in the hydrothermal diamond anvil cell. *Earth and Planetary Science Letters* 232, 393-402.
- Austrheim, H.O. Erambert, M. and Engvik A.K. 1997. Processing of crust in the root of the Caledonian continent collision zone: the role of eclogitization. *Tectonophysics* 274, 129-153.
- Austrheim, H.O. Corfu, F. Bryhni, I. and Andersen, T.B. 2003. The Proterozoic Hustad igneous complex: a low strain enclave with a key to the history of the Western Gneiss Region of Norway. *Precambrian Research* 120 (1-2), 149-175.
- Birtel, S. and Stöckhert, B. 2008. Quartz veins record earthquake-related brittle failure and short term ductile flow in the deep crust. *Tectonophysics* 457 (1-2), 53-63.
- Boiron, M.C. Cathelineau, M. Dubessy, J. and Bastoul, A.M. 1990. Fluids in Hercynian Au veins from the French Variscan belt. *Mineralogical Magazine*, 54, 231-243.
- Brady, J. College, S. and Perkins, D. 2012. *Mineral Formulae Recalculation*. Available at http://serc.carleton.edu/research_education/equilibria/mineralformulaerecalculation.html (Accessed: 14.05.2013)
- Charlier, B. Duchesne, J.C. Vander Auwera, J. 2005. Magma chamber processes in the Tellnes ilmenite deposit (Rogaland Anorthosite Province, SW Norway) and the formation of Fe-Ti ores in massif-type anorthosites. *Chemical Geology* 234, 264-290.
- Cuthbert, S.J. Harvey, M.A. and Carswell, D.A. 1983. A tectonic model for the metamorphic evolution of the Basal Gneiss Complex, western south Norway. *Journal of Metamorphic Geology* 1, 63-90.
- Cuthbert, S.J. Carswell, D.A. Krogh-Ravna, E.J. and Wain, A. 2000. Eclogites and eclogites in the Western Gneiss Region, Norwegian Caledonides. *Lithos* 52, 165-195.
- De Andrade, V. Vidal, O. Lewin, E. O'Brien, P. and Agard, P. 2006. Quantification of electron microprobe compositional maps of rock thin sections: an optimized method and examples. *Journal of Metamorphic Geology*, 655-668.
- Dill, H.G. 2006. Grain morphology of heavy minerals from marine and continental placer deposits, With special references to Fe-Ti oxides. *Sedimentary geology* 198, 1-27.
- Dobrzhinetskaya, L.F. Eide, E.A. Larsen, L.B. Sturt, B.A. Trønnes, R.G. Smith, D.C. Taylor, W.R. and Posukhova, T.V. 1995. Microdiamond in high-grade metamorphic rocks of the Western Gneiss Region, Norway. *Geology* 23, 597-600.

Dutrow, B.L. and Clark, C.M. 2012. *X-ray Powder Diffraction*. (Accessed 28.05.2013 from http://serc.carleton.edu/research_education/geochemsheets/techniques/XRD.html)

Ellis, D.J and Green, D.H. 1979. An experimental study of the effect of Ca upon garnet-clinopyroxene Fe-Mg exchange equilibria. *Contributions to Mineralogy and Petrology* 71 (1), 13-22.

Foreman, R. Andersen, T.B. and Wheeler, J. 2005. Eclogite facies deformation of the Drøsdal eclogite, Western Gneiss Complex, Norway, and implications for exhumation. *Tectonophysics* 398 (1-2), 1-32.

Ganguly, J. 2001. Thermodynamic modeling of solid solutions. *EMU Notes in Mineralogy* 3, 37-69.

Gasparik, T. Lindsley, D.H. 1980. Phase equilibria at high pressure of pyroxenes containing monovalent and trivalent ions. In Prewitt, C.T. (ed.) *Pyroxenes*. Reviews in Mineralogy Volume 7, 309-340.

Graham, C.M and Powell, R. 1984. A garnet-hornblende geothermometer: calibration, testing, and application to the Pelona Schist, Southern California. *Journal of Metamorphic geology* 2, 13-31.

Hacker, B. 2007. Ascent of the ultrahigh-pressure Western Gneiss Region, Norway. *Geological Society of America. Special paper* 419, 171-184.

Hacker, R.B. Andersen, T.B. Johnston, S. Kylander-Clark, A.R.C. Peterman, E.M. Walsh, E.O. and David, Y. 2010. High temperature deformation during continental-margin subduction & exhumation: The ultrahigh-pressure Western Gneiss Region of Norway. *Tectonophysics* 480, 149-171.

Holland, T.J.B. 1980. The reaction albite = jadeite + quartz determined experimentally from 600-1200°C. *American Mineralogist* 65, 129-134.

Hossack, J.R. and Cooper, M.A. 1986. Collision tectonics in the Scandian Caledonides. *Geological Society of London, special publications* 19, 285-304.

Johnston, S.M. Hacker, B.R. and Andersen, T.B. 2007. Exhuming Norwegian ultrahigh-pressure rocks: Overprinting extensional structures and the role of the Nordfjord-Sogn Detachment Zone. *Tectonics* 26, 1-12.

Klein, C. Dutrow, B. and Flahive, R. (ed.). 2008. *The 23rd edition of the manual of mineral science*. John Wiley & Sons, Inc, USA. 675 pp.

Korneliussen, A. 2001. *Rutilressurser I Sunnfjord-regionen, Sogn og Fjordane*. Trondheim: NGU (2001.102). 28 pp.

Korneliussen, A. Braathen, A. Erambert, M. Lutro, O. and Ragnhildstveit, J. 1998. *The geology of the Engebøfjell eclogite deposit and its regional setting*. Trondheim: NGU (98.081). 121 pp.

Korneliussen, A. Furuhaug, L. Gautneb, H. and Ihlen, P. 1991. *Rutile deposits in Norway, Vol. 1: Text*. Trondheim: NGU (99.129). 61 pp.

Korneliussen, A. Wanvik, J.E. and Broekmans, M.A.T.M. 2007. *Engebøfjellet: prospect of a major rutile deposit*. Trondheim: NGU (2007.055). 19 pp. N.B (confidential).

- Krabbendam, M. and Dewey, J.F. 1998. Exhumation of UHP rocks by transtension in the Western Gneiss Region, Scandinavian Caledonides. *Geological Society of London, Special Publications* 135, 159-181.
- Krogh, E.J. 1980. Geochemistry and petrology of glaucophane-bearing eclogites and associated rocks from Sunnfjord, Western Norway. *Lithos* 13, 355-380.
- Krogh E.J. 1980. Metamorphic evolution of Norwegian country-rock eclogites, as deduced from mineral inclusions and compositional zoning in garnet. *Lithos* 15, 305-321.
- Krogh Ravna, E.J. 2000. The Garnet – clinopyroxene Fe²⁺-Mg geothermometer: an updated calibration. *Journal of Metamorphic Geology* 18, 211-219.
- Krogh Ravna, E.J. 2000. Distribution of Fe²⁺ and Mg between coexisting garnet and hornblende in synthetic and natural system: an empirical calibration of the garnet-hornblende Fe-Mg geothermometer. *Lithos* 53, 265-277.
- Krogh Ravna, E.J. and Paquin, J. 2003. Thermobarometric methodologies applicable to eclogites and garnet ultrabasites. *EMU Notes in Mineralogy* 5, 229-259.
- Kylander-Clark, A.R.C. Hacker, B.R. and Mattinson, J.M. 2008. Slow exhumation of UHP terranes: Titanite and rutile ages of the Western Gneiss Region, Norway. *Earth and Planetary Science Letter* 272, 531 – 540.
- Kylander-Clark, A.R.C. Hacker, B.R. Johnson, C.M. Beard, B.L. and Mahlen, N.J. 2009. Slow subduction of a thick ultrahigh-pressure terrane. *Tectonics* 28, 1-14.
- Lanari, P. Vidal, O. De Andrade, V. Dubacq, B. Lewin, E. Grosch, E. and Schwartz, S. (submitted) XMapTools: a MATLAB©-based program for electron microprobe X-ray image processing and geothermobarometry. *Computer and Geosciences*.
- Leake, B.E. Wooley, A.R. Arps, C.E.S. Birch, W.D. Gilbert, M.C. Grice, J.D. Hawthorne, F.C. Kato, A. Krivovichev, V.G. Linthout, K. Laird, J. Mandarino, J.A. Maresch, W.V. Nickel, E.H. Rock, N.M.S. Schumachere, J.C. Smith, D.C. Stephenson, N.C.K. Ungaretti, L. Whittaker, E.J.W. and Youzhi, G. 1997. Nomenclature of amphiboles: Report of the subcommittee on amphiboles of the international mineralogical association, commission on new minerals and mineral names. *The Canadian Mineralogist* 35, 219-246.
- Lutro, O. and Ragnhildstveit, J. 1996. *Geological map of the Førdefjord area, bedrock map, scale 1:50 000*. Trondheim: NGU.
- Milnes, A.G. Wennberg, O.P. Skår, Ø. Koestler, A.G. 1997. Contraction, extension and timing in the South Norwegian Caledonides: The Sognefjord transect. In: Burg J.P., Ford M (Eds.), *Orogeny Through Time. Geological Society Special Publication* 121. 123-148.
- Newton, R.C. and Smith, J.V. 1967. Investigations concerning the breakdown of albite at depth in the Earth. *The Journal of Geology* 75 (3), 268-286.
- Norton, M.G. 1986. Late Caledonian extension in western Norway: A response to extreme crustal thickening. *Tectonics* 5, 195-204.

Osmundsen, P.T. and Andersen, T.B. 2001. The middle Devonian basin of western Norway: a sedimentary response to large-scale transitional tectonics. *Tectonophysics* 332, 51-68.

Pouchou, J.L. and Pichoir, F. 1985. PAP $\Phi(\rho Z)$ procedure for improved quantitative microanalysis. In Armstrong, J.T (ed.) *Microbeam Analysis*. San Francisco Press, San Francisco , pp 104-106.

Powell, R. 1985. Regression diagnostics and robust regression in geothermometer/ geobarometer calibration: The garnet-clinopyroxene geothermometer revisited. *Journal of Metamorphic geology* 3, 231-243.

Powell, R. and Holland, T.J.B. 2008. On thermobarometry. *Journal of metamorphic geology* 26, 155-179.

Reed, S.J.B. 2005. *Electron Microprobe Analysis and Scanning Electron Microscopy in Geology*. University of Cambridge. 189 pp.

Robie, R.A and Hemingway, B.S. 1995. Thermodynamic properties of minerals and related substances at 298.15 K and 1 bar (10^5 Pascals) pressure and higher temperatures. *U.S Geological Survey Bulletin* 2131.

Skår, Ø. and Pedersen, R.B. 2003. Relations between granitoid magmatism and migmatization: U-Pb geochronological evidence from the Western Gneiss Complex, Norway. *Journal of the geological society of London* 160, 935-946.

Smith, D.C. (1984) – Coesite in clinopyroxene in the Caledonides and its implications for geodynamics. *Nature* 310, 641-644.

Spear, F.S. 1995. *Metamorphic phase equilibria and pressure-temperature-time path*. Mineralogical Society of America, Washington. 799 pp.

Stephens, M.B. 1988. The Scandinavian Caledonides: a complexity of collisions. *Geology Today*, 20-26.

Stipp, M. Stünitz, H. Heilbronner, R. and Schmid, S.M. 2002. The eastern Tonale fault zone: a ‘natural laboratory’ for crystal plastic deformation of quartz over a temperature range from 250 to 700°C. *Journal of Structural Geology* 24, 1861-1884.

Strating, E.H.H. and Vissers, R.L.M. 1991. Dehydration-induced fracturing of eclogite-facies peridotites: implications for the mechanical behavior of subducting oceanic lithosphere. *Tectonophysics* 200 (1-3), 187-198.

Tenold, H. 2009. Reguleringsplan med konsekvensutredning for utvinning av rutil i Engebøfjellet I Naustdal Kommune. *Impact analysis done by Asplan Viak*. (Accessed: 24.05.2013, from <https://www.naustdal.kommune.no/Filnedlasting.aspx?FilId=406&MId1=&MId2=&MId3=&>)

Tomkins H.S. Powell R. and Ellis D.J. 2007. The pressure dependence of the zirconium-in-rutile thermometer. *Journal of Metamorphic Geology* 25, 703-713.

Tucker, R.D. Robinson, P. Solli, A. Gee, D.G. Thorsnes, T. Krogh, T.E. Nordgulen, L. and Bickford, M.E. 2004. Thrusting and extension in the Scandian Hinterland, Norway: New U-Pb ages and tectonostratigraphic evidence. *American Journal of Science* 304, 477-532.

Walsh, E.O. and Hacker, B.R. 2004. The fate of subducted continental margins: Two-stage exhumation of the high-pressure to ultrahigh-pressure Western Gneiss Region, Norway. *Journal of Metamorphic Geology* 22, 671-687.

Walsh, E.O. Hacker, B.R. Gans, P.B. Grove, M. and Gehrels, G. 2007. Protolith ages and exhumation histories of (ultra)high-pressure rocks across the Western Gneiss Region, Norway. *GSA Bulletin* 119, 289-301.

Waters, D.J. and Martin, H.N. 1993. Geobarometry of phengite-bearing eclogites. *Terra Abstract 5 (1)*, 410-411.

Whitney, D.L and Evans, B.W. 2010. Abbreviations for names of rock-forming minerals. *American mineralogist* 95, 185-187.

Wilks, W.J. and Cuthbert, S.J. 1994. The evolution of the Hornelen Basin detachment system, western Norway: Implications for the style of late orogenic extension in the southern Scandinavian Caledonides. *Tectonophysics* 238, 1-30.

Winter, J.D. and Peters, D (eds.) (2010) - *Principles of Igneous and Metamorphic Petrology*. Pearson education, Inc. Withman College, US. 702 pp.

Wirth, K. and Barth, A. 2012. *X-Ray Fluorescence*. Accessed: 28.05.2013 from http://serc.carleton.edu/research_education/geochemsheets/techniques/XRF.html

www.azom.com: <http://www.azom.com/article.aspx?ArticleID=5251> (Accessed: 24.10.2012)

www.photonicmicrodevices.com: <http://www.photonicmicrodevices.com/XRD.html> (Accessed: 24.10.2012)

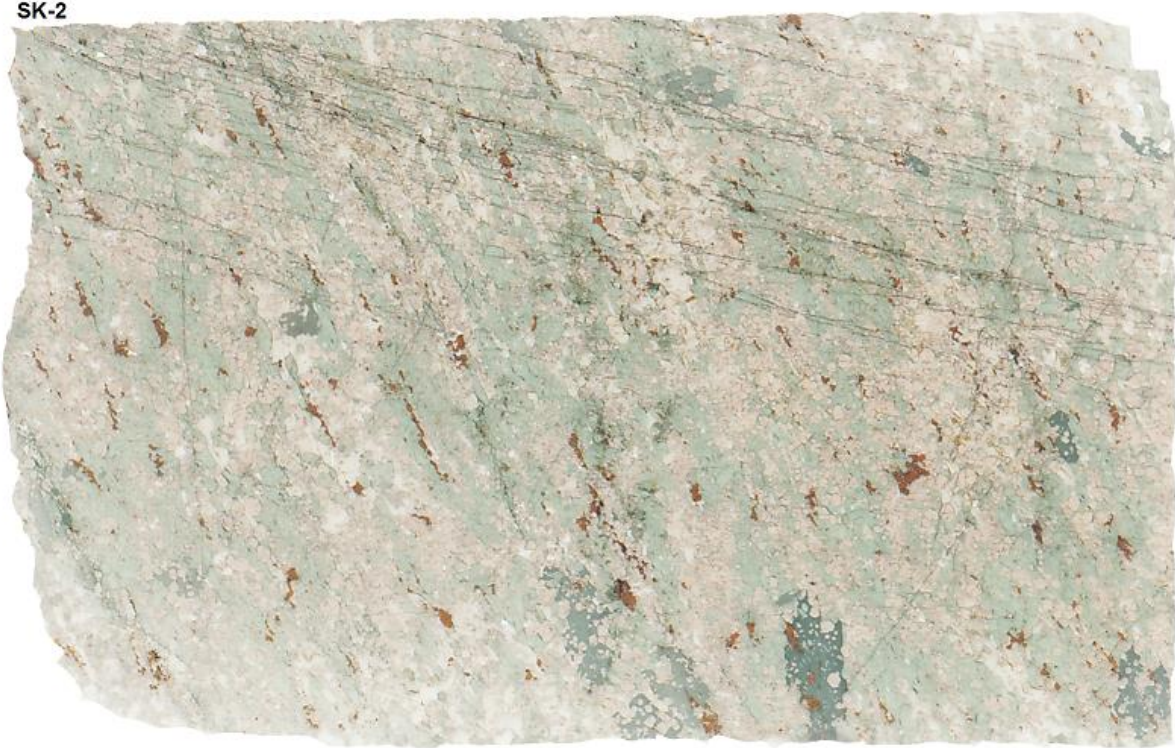
Appendix 1 – Mineral abbreviations

From Whitney and Evans (2010)

Act - Actinolite	Hd - Hedenbergite
Ab – Albite	Ilm – Ilmenite
Aeg – Aegerine	Jd – Jadeite
Alm – Almandines	Mhs – Magnesiohastingsite
Amp – Amphibole	Mhb – Magnesiohornblende
Brs – Barroisite	Mkt – Magnesiokatophorite
Bt – Biotite	Omp – Omphacite
Cal – Calcite	Pg – Paragonite
Cb – Carbonate	Prg – Pargasite
Cpx – Clinopyroxene	Ph – Phengite
Di – Diopside	Pl – Plagioclase
Ed – Edenite	Py – Pyrite
Ep – Epidote	Prp – Pyrope
Fsp – Feldspar	Qz – quartz
Fprg – Ferropargasite	Rt – Rutile
Fts – Ferrotschermakite	Sps – Spessartine
Grt – Garnet	Ttn - Titanite
Grs – Grossular	Zrn - Zircon

Appendix 2 – Thin section scans

SK-2



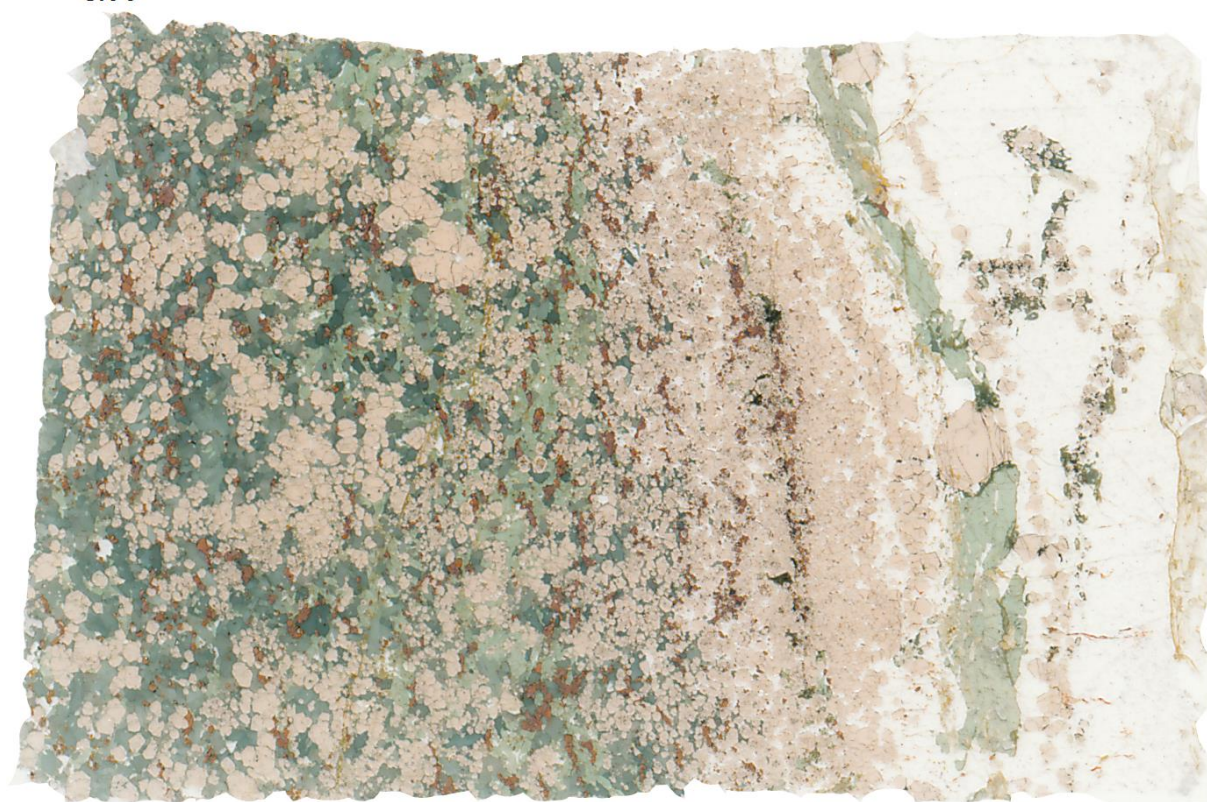
SK-3



SK-4



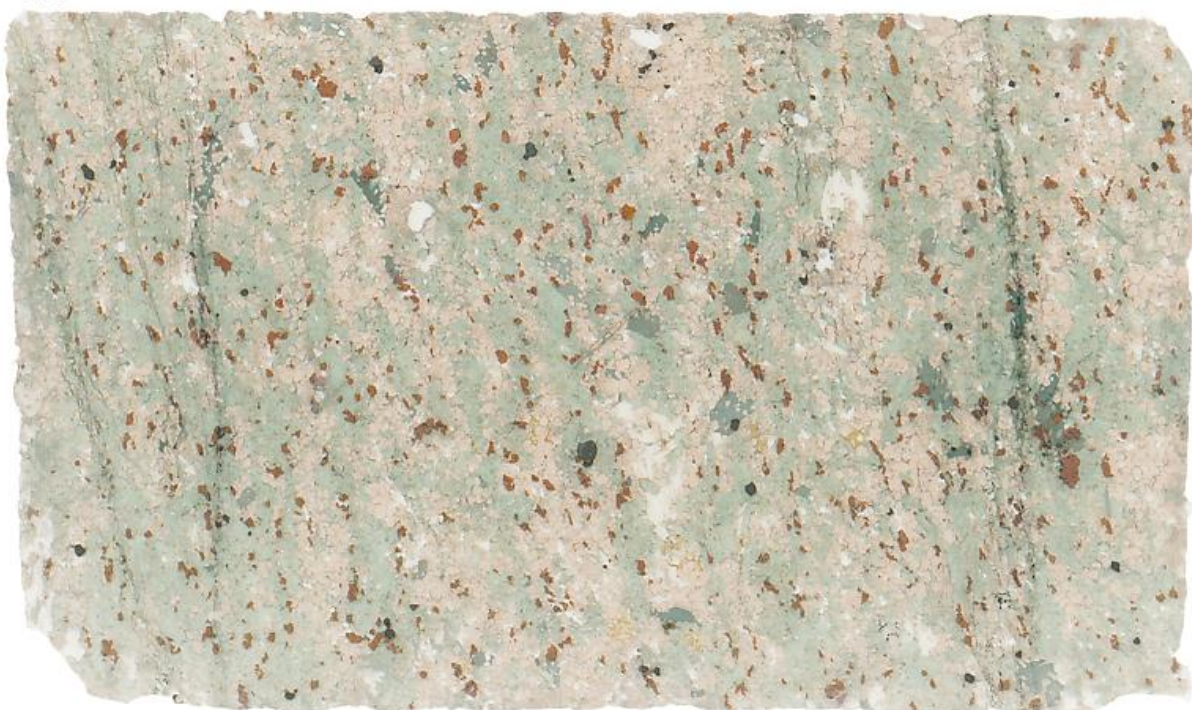
SK-6



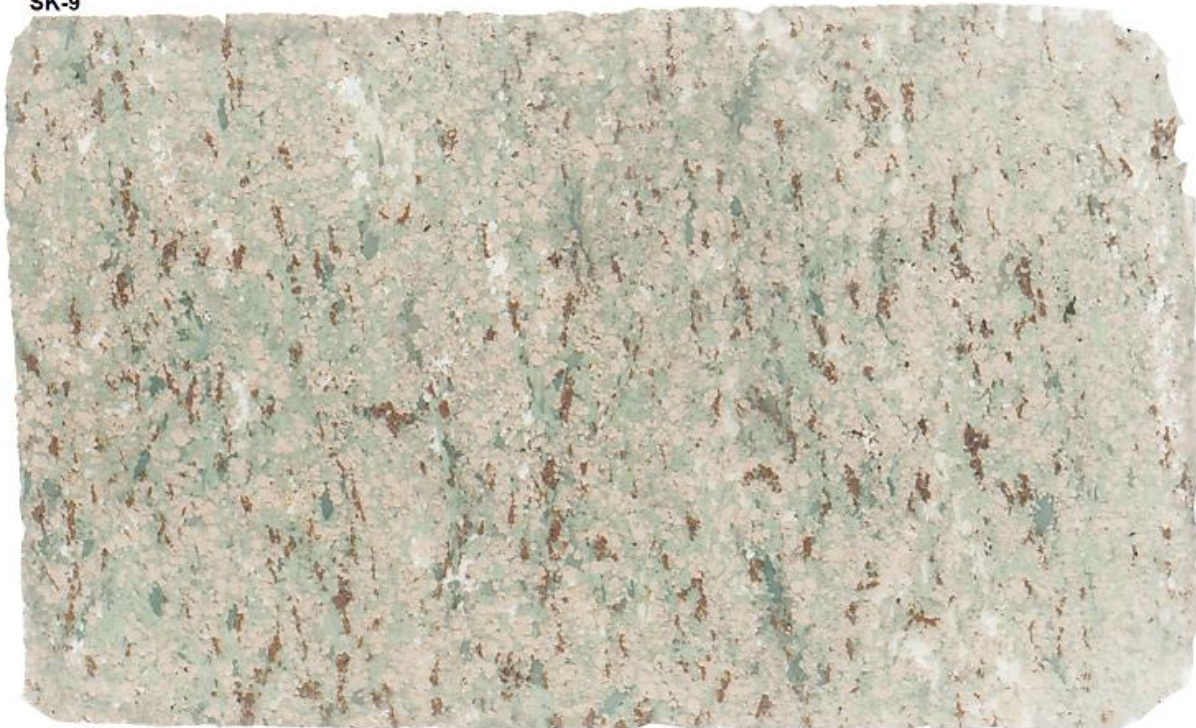
SK-7



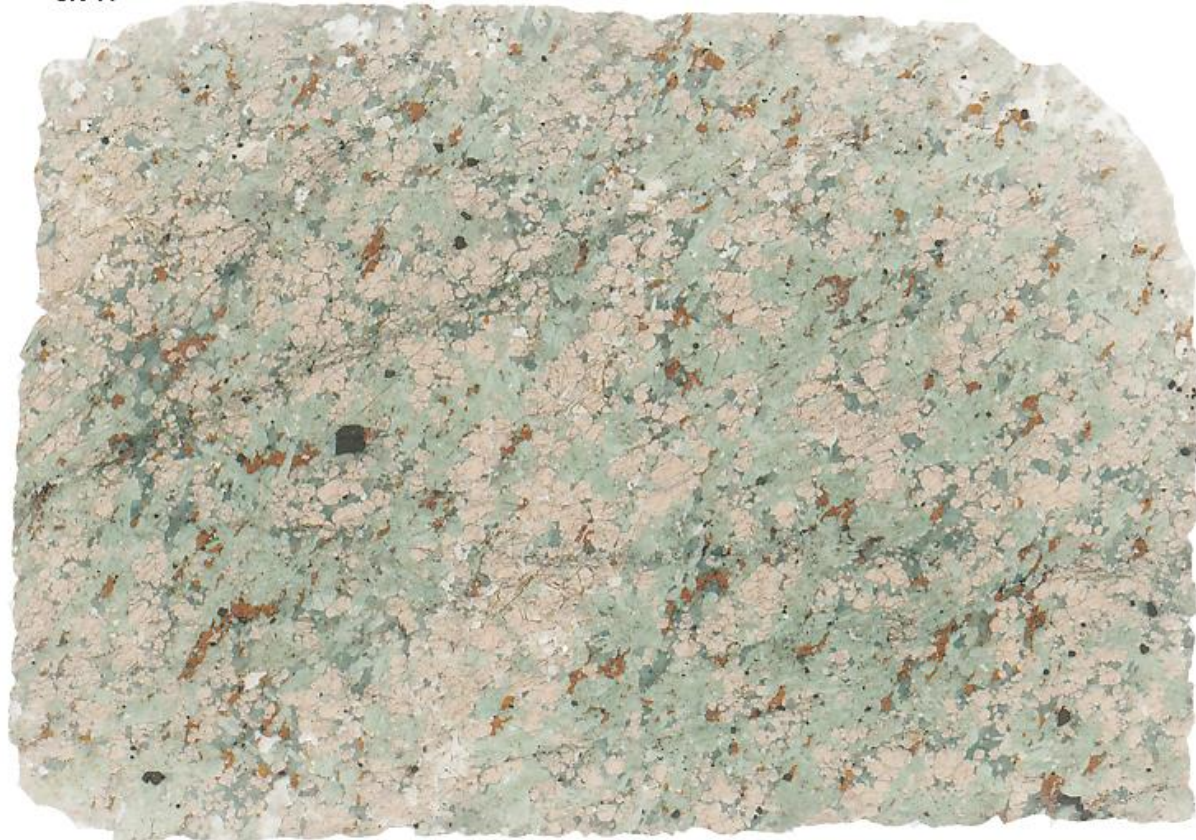
SK-8



SK-9



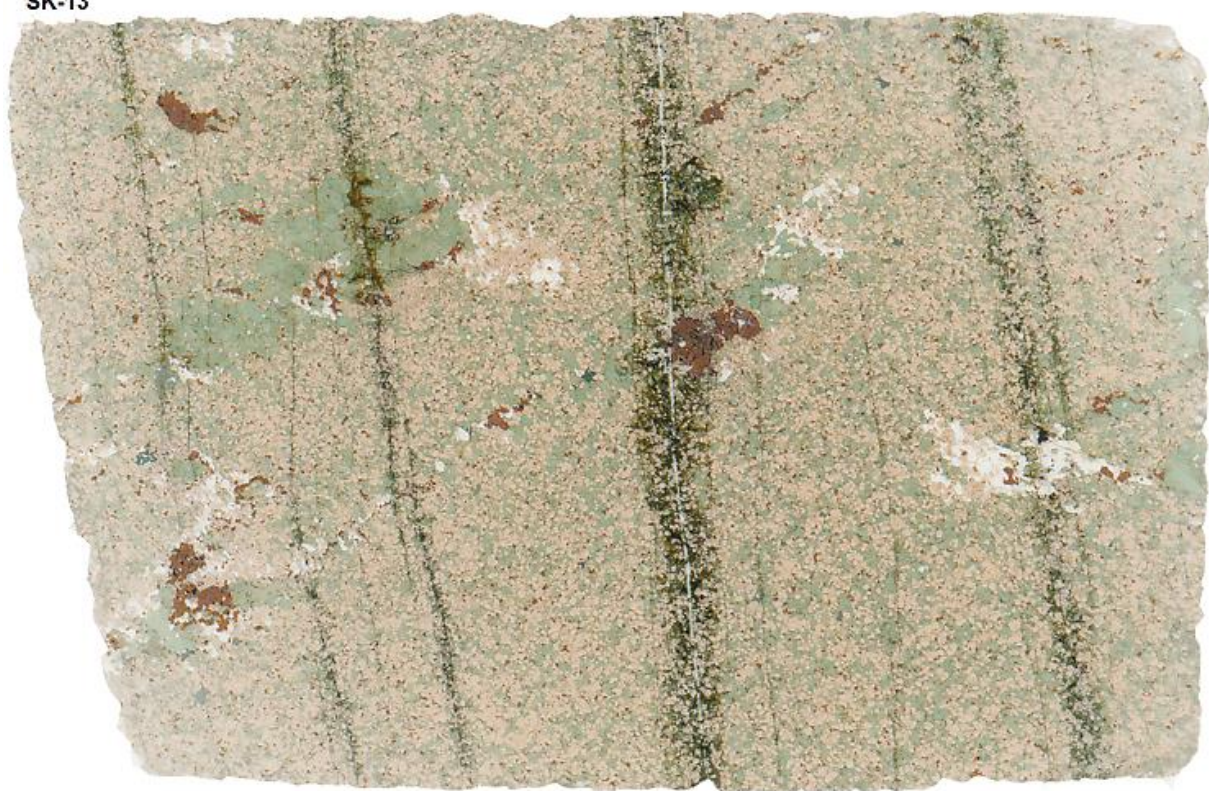
SK-11



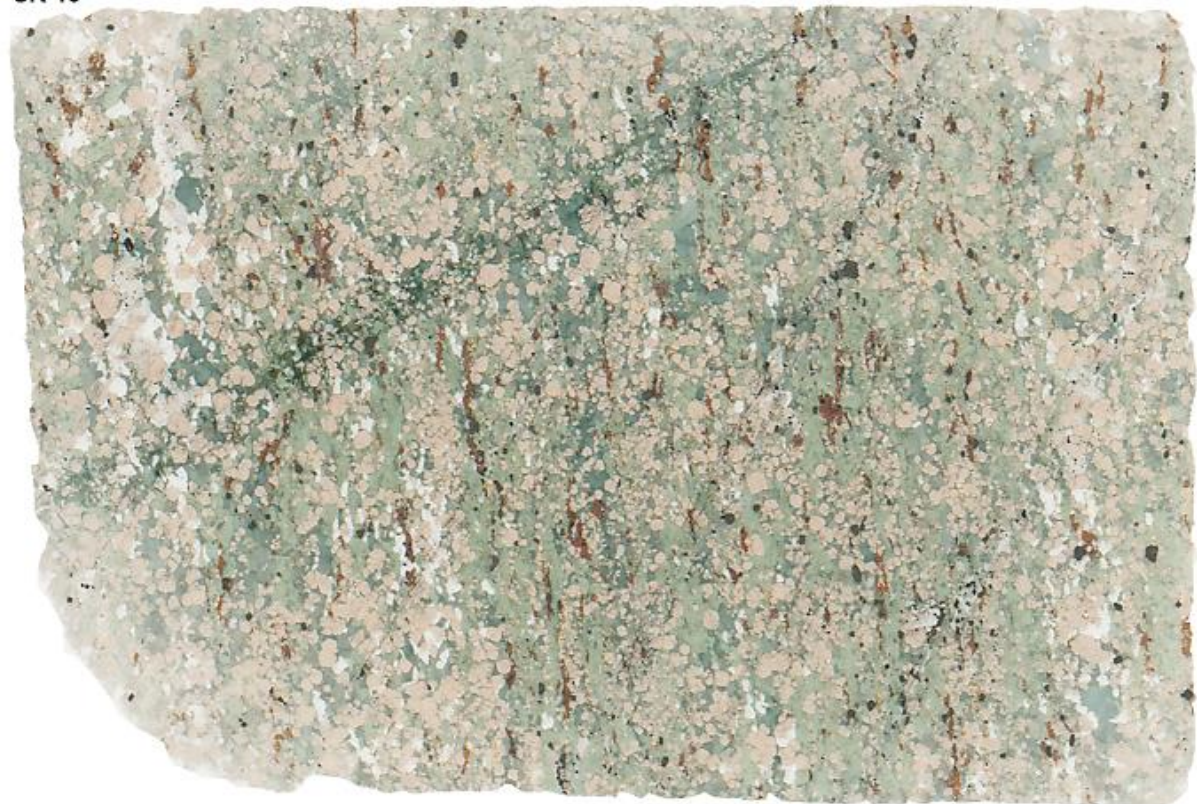
SK-12



SK-13



SK-15



SK-16



SK-19



SK-20



SK-27



SK-28



SK-29



SK-30



SK-31



Appendix 3 – Mineral chemical tables

- 3.1 – Ferro gabbroic garnets
- 3.2 – Leuco gabbroic garnets
- 3.3 – Ferro gabbroic Pyroxenes
- 3.4 – Leuco gabbroic pyroxenes
- 3.5 – Ferro gabbroic, primary amphiboles
- 3.6 – Leuco gabbroic, primary amphiboles
- 3.7 – Secondary amphiboles
- 3.8 – Mica
- 3.9 – Clinzoisite
- 3.10 – Feldspar

3.1 Ferro gabbroic garnets

Oxide Wt%	Sk-7						SK-28					
	Core	Core	Core	Rim	Rim	Rim	Core	Core	Core	Rim	Rim	Rim
SiO ₂	38,22	37,82	38,15	38,02	38,28	38,21	38,61	37,95	37,91	38,17	37,84	37,95
TiO ₂	0,08	0,06	0,01	0,04	0,02	0,00	0,01	0,17	0,16	0,06	0,02	0,03
Al ₂ O ₃	21,05	21,34	21,15	21,13	21,35	21,15	21,51	20,89	21,22	21,71	21,27	21,18
Cr ₂ O ₃	0,00	0,01	0,00	0,00	0,00	0,00	0,00	0,00	0,04	0,03	0,00	0,00
FeO	28,15	27,80	28,70	28,87	27,28	27,78	27,89	27,11	26,96	28,06	28,37	28,23
MnO	0,61	0,60	0,53	0,33	0,45	0,52	0,53	0,35	0,44	0,50	0,55	0,47
MgO	3,10	3,95	4,23	2,84	4,44	4,47	4,20	3,32	3,58	4,11	3,58	3,33
CaO	9,29	8,43	7,80	9,34	8,31	8,71	8,25	10,30	10,01	8,30	8,84	9,58
Na ₂ O	0,02	0,02	0,02	0,00	0,00	0,03	0,01	0,01	0,07	0,04	0,02	0,03
K ₂ O	0,00	0,01	0,01	0,00	0,00	0,00	0,00	0,01	0,00	0,00	0,01	0,00
Sum	100,51	100,02	100,60	100,56	100,13	100,88	101,00	100,12	100,41	100,98	100,49	100,80
Structural formula based on 8 cations and 12 oxygens												
Si	3,01	2,97	2,99	2,99	3,00	2,97	3,00	2,99	2,97	2,97	2,97	2,97
Ti	0,00	0,00	0,00	0,00	0,00	0,00	0,00	0,01	0,01	0,00	0,00	0,00
Al	1,95	1,98	1,95	1,96	1,97	1,94	1,97	1,94	1,96	1,99	1,97	1,95
Fe(III)	0,03	0,07	0,08	0,05	0,04	0,12	0,02	0,07	0,09	0,07	0,10	0,11
Fe(II)	1,82	1,76	1,80	1,85	1,75	1,69	1,79	1,71	1,67	1,76	1,76	1,74
Mn	0,04	0,04	0,03	0,02	0,03	0,03	0,04	0,02	0,03	0,03	0,04	0,03
Mg	0,36	0,46	0,49	0,33	0,52	0,52	0,49	0,39	0,42	0,48	0,42	0,39
Ca	0,78	0,71	0,65	0,79	0,70	0,73	0,69	0,87	0,84	0,69	0,74	0,80
Sum	8,00	8,00	8,00	8,00	8,00	8,00	8,00	8,00	7,99	7,99	8,00	8,00
Mg/Mg+Fe ₂₊	0,17	0,21	0,22	0,15	0,23	0,23	0,21	0,19	0,20	0,21	0,19	0,18
End members												
Almandine	61	59	60	62	58	57	60	57	56	59	60	59
Pyrope	12	16	17	11	17	17	16	13	14	16	14	13
Grossular	26	23	21	26	23	23	23	28	27	23	24	26
Sum	98	98	98	99	99	97	99	98	98	98	98	98

Oxide Wt%	SK-29						SK-6					
	Core	Core	Core	Rim	Rim	Rim	Core	Core	Core	Rim	Rim	Rim
SiO ₂	37,86	37,89	37,84	37,81	38,23	38,21	37,55	37,83	37,66	38,08	38,02	37,70
TiO ₂	0,13	0,16	0,16	0,02	0,11	0,04	0,14	0,06	0,03	0,00	0,01	0,03
Al ₂ O ₃	21,10	20,91	21,16	21,43	21,57	21,27	20,94	20,79	21,29	21,14	21,28	20,98
Cr ₂ O ₃	0,00	0,02	0,02	0,00	0,00	0,01	0,03	0,01	0,00	0,00	0,00	0,05
FeO	27,92	27,48	28,41	27,43	27,23	27,72	28,63	27,83	28,02	27,47	29,78	29,13
MnO	0,47	0,47	1,26	0,51	0,43	0,40	0,71	0,59	0,34	0,40	0,39	0,38
MgO	2,94	3,38	3,49	3,97	4,35	4,50	2,64	3,11	4,46	4,47	3,89	4,06
CaO	10,21	9,97	8,51	8,80	8,74	8,21	9,19	9,74	8,05	8,18	7,56	7,76
Na ₂ O	0,00	0,06	0,03	0,00	0,03	0,04	0,03	0,03	0,02	0,00	0,01	0,02
K ₂ O	0,02	0,00	0,00	0,01	0,00	0,06	0,01	0,01	0,01	0,01	0,00	0,00
Sum	100,64	100,34	100,89	99,97	100,67	100,46	99,88	100,01	99,89	99,75	100,93	100,10
Structural formula based on 8 cations and 12 oxygens												
Si	3,00	2,98	2,96	2,97	2,98	2,98	2,98	2,99	2,96	2,99	2,98	2,97
Ti	0,01	0,01	0,01	0,00	0,01	0,00	0,01	0,00	0,00	0,00	0,00	0,00
Al	1,97	1,94	1,95	1,99	1,98	1,96	1,96	1,94	1,97	1,96	1,96	1,95
Fe(III)	0,00	0,10	0,10	0,07	0,06	0,08	0,06	0,09	0,11	0,05	0,09	0,11
Fe(II)	1,85	1,70	1,76	1,74	1,71	1,72	1,84	1,75	1,73	1,75	1,86	1,81
Mn	0,03	0,03	0,08	0,03	0,03	0,03	0,05	0,04	0,02	0,03	0,03	0,03
Mg	0,35	0,40	0,41	0,46	0,50	0,52	0,31	0,37	0,52	0,52	0,45	0,48
Ca	0,87	0,84	0,71	0,74	0,73	0,69	0,78	0,82	0,68	0,69	0,63	0,65
Sum	8,08	7,99	7,99	8,00	8,00	7,99	7,99	7,99	8,00	8,00	8,00	7,99
Mg/Mg+Fe ²⁺	0,16	0,19	0,19	0,21	0,23	0,23	0,15	0,17	0,23	0,23	0,20	0,21
End members												
Almandine	60	57	59	58	58	58	62	59	59	59	63	61
Pyrope	11	13	14	16	17	18	10	12	18	18	15	16
Grossular	28	27	23	24	24	22	25	26	22	22	20	21
Sum	99	97	96	98	98	98	97	97	98	98	98	98

Oxide Wt%	SK-9			SK-8			SK-2							
	Core	Core	Rim	Rim	Rim	Core	Core	Rim	Core	Core	Core	Rim	Rim	Rim
SiO ₂	38,35	37,80	37,95	38,00	38,28	38,07	37,49	37,78	37,55	37,73	38,29	37,69	37,39	38,17
TiO ₂	0,02	0,06	0,04	0,31	0,03	0,02	0,08	0,05	0,08	0,04	0,04	0,02	0,02	0,00
Al ₂ O ₃	21,52	21,47	21,18	21,21	21,18	21,51	20,86	21,12	21,28	21,14	21,16	21,34	20,91	21,58
Cr ₂ O ₃	0,00	0,00	0,00	0,00	0,00	0,00	0,01	0,00	0,01	0,00	0,01	0,01	0,00	0,02
FeO	28,59	28,42	28,51	26,98	27,29	28,56	28,14	27,44	27,62	27,72	26,60	27,64	27,67	27,88
MnO	0,53	0,55	0,55	0,47	0,46	0,50	0,41	0,41	0,55	0,51	0,58	0,34	0,34	0,47
MgO	4,70	4,28	4,63	3,79	4,31	4,69	3,30	3,80	3,41	3,51	4,13	3,89	4,10	4,48
CaO	7,04	7,60	7,52	9,65	8,86	7,12	9,13	8,93	9,51	9,07	8,71	9,18	8,60	7,70
Na ₂ O	0,00	0,02	0,03	0,04	0,00	0,03	0,04	0,01	0,01	0,02	0,02	0,03	0,00	0,04
K ₂ O	0,01	0,00	0,00	0,00	0,00	0,00	0,00	0,02	0,00	0,00	0,00	0,00	0,00	0,00
Sum	100,76	100,20	100,41	100,45	100,42	100,50	99,48	99,57	100,03	99,73	99,55	100,15	99,04	100,33
Structural formula based on 8 cations and 12 oxygens														
Si	2,99	2,97	2,97	2,97	2,99	2,97	2,97	2,99	2,96	2,98	3,02	2,96	2,97	2,98
Ti	0,00	0,00	0,00	0,02	0,00	0,00	0,00	0,00	0,00	0,00	0,00	0,00	0,00	0,00
Al	1,98	1,99	1,95	1,96	1,95	1,98	1,95	1,97	1,98	1,97	1,97	1,97	1,96	1,99
Fe(III)	0,04	0,08	0,11	0,07	0,06	0,07	0,10	0,06	0,10	0,07	0,00	0,11	0,11	0,05
Fe(II)	1,83	1,79	1,76	1,70	1,72	1,79	1,77	1,75	1,72	1,76	1,75	1,70	1,73	1,77
Mn	0,04	0,04	0,04	0,03	0,03	0,03	0,03	0,03	0,04	0,03	0,04	0,02	0,02	0,03
Mg	0,55	0,50	0,54	0,44	0,50	0,55	0,39	0,45	0,40	0,41	0,49	0,46	0,49	0,52
Ca	0,59	0,64	0,63	0,81	0,74	0,60	0,78	0,76	0,80	0,77	0,74	0,77	0,73	0,65
Sum	8,00	8,00	8,00	8,00	8,00	8,00	7,99	8,00	8,00	8,00	8,00	8,00	8,00	7,99
Mg/Mg+Fe2+	0,23	0,22	0,24	0,21	0,23	0,23	0,18	0,20	0,19	0,19	0,22	0,21	0,22	0,23
End members														
Almandine	61	60	59	57	57	60	60	59	58	59	58	58	58	60
Pyrope	18	17	18	15	17	18	13	15	14	14	16	15	16	18
Grossular	19	21	20	26	24	19	25	25	26	25	24	25	23	21
Sum	98	98	98	98	98	98	98	98	97	98	99	98	98	98

	SK-3			SK-11				SK-12						SK-20		
Oxide Wt%	Core	Core	Rim	Core	Core	Core	Rim	Core	Core	Core	Rim	Rim	Rim	Core	Core	Core
SiO ₂	37,70	37,93	37,63	37,26	37,59	37,49	37,79	37,54	37,65	37,74	37,64	37,75	38,10	38,19	38,00	37,93
TiO ₂	0,14	0,09	0,04	0,13	0,05	0,07	0,05	0,13	0,08	0,04	0,10	0,12	0,01	0,07	0,05	0,05
Al ₂ O ₃	21,11	21,10	20,96	20,67	20,97	20,84	20,94	21,03	20,91	20,88	21,05	20,85	21,52	21,05	21,20	21,12
Cr ₂ O ₃	0,03	0,03	0,01	0,03	0,00	0,00	0,03	0,04	0,00	0,02	0,01	0,08	0,02	0,01	0,01	0,00
FeO	26,29	26,61	26,76	29,16	27,94	30,00	28,67	27,47	28,78	27,62	28,15	28,29	29,10	28,97	28,70	28,29
MnO	0,64	0,69	0,59	0,44	1,85	0,23	0,60	0,57	0,34	0,42	0,40	0,37	0,37	0,37	0,34	0,30
MgO	4,13	3,69	3,82	2,14	2,83	2,45	4,05	3,47	3,20	3,43	3,26	3,13	4,46	4,31	4,22	4,09
CaO	9,97	9,61	9,66	10,41	8,82	9,44	7,99	9,44	8,79	9,35	9,22	9,68	7,07	7,56	7,65	7,97
Na ₂ O	0,03	0,04	0,00	0,02	0,04	0,03	0,03	0,04	0,05	0,02	0,04	0,05	0,00	0,02	0,00	0,00
K ₂ O	0,02	0,00	0,00	0,00	0,00	0,01	0,02	0,00	0,00	0,00	0,00	0,00	0,00	0,00	0,00	0,01
Sum	100,06	99,78	99,47	100,26	100,07	100,56	100,17	99,73	99,81	99,53	99,86	100,32	100,64	100,57	100,16	99,76
Structural formula based on 8 cations and 12 oxygens																
Si	2,95	2,99	2,97	2,95	2,98	2,96	2,97	2,97	2,98	2,99	2,98	2,97	2,98	2,99	2,99	2,99
Ti	0,01	0,01	0,00	0,01	0,00	0,00	0,00	0,01	0,00	0,00	0,01	0,01	0,00	0,00	0,00	0,00
Al	1,95	1,96	1,95	1,93	1,96	1,94	1,94	1,96	1,95	1,95	1,96	1,94	1,98	1,94	1,96	1,96
Fe(III)	0,13	0,06	0,10	0,14	0,09	0,13	0,11	0,10	0,08	0,07	0,08	0,11	0,06	0,07	0,06	0,05
Fe(II)	1,59	1,69	1,67	1,79	1,76	1,85	1,77	1,72	1,83	1,76	1,78	1,76	1,84	1,83	1,83	1,82
Mn	0,04	0,05	0,04	0,03	0,12	0,02	0,04	0,04	0,02	0,03	0,03	0,02	0,02	0,02	0,02	0,02
Mg	0,48	0,43	0,45	0,25	0,33	0,29	0,48	0,41	0,38	0,41	0,38	0,37	0,52	0,50	0,49	0,48
Ca	0,84	0,81	0,82	0,88	0,75	0,80	0,67	0,80	0,75	0,79	0,78	0,82	0,59	0,63	0,64	0,67
Sum	7,99	7,99	8,00	8,00	8,00	8,00	7,99	7,99	8,00	8,00	7,99	7,99	8,00	8,00	8,00	8,00
Mg/Mg+Fe ²⁺	0,23	0,20	0,21	0,12	0,16	0,13	0,21	0,19	0,17	0,19	0,18	0,17	0,22	0,22	0,21	0,21
End members																
Almandine	54	57	56	61	59	63	60	58	61	59	60	59	62	61	61	61
Pyrope	16	15	15	9	11	10	16	14	13	14	13	12	17	17	17	16
Grossular	26	26	26	28	24	25	21	26	24	26	25	26	19	20	21	22
Sum	97	98	97	97	95	98	97	97	98	98	98	98	99	98	99	99

3.2 Leuco gabbroic garnets

	SK-31						SK-30				SK-4					
Oxide Wt%	Core	Core	Core	Rim	Rim	Core	Core	Rim	Rim	Core	Core	Core	Rim	Rim	Rim	
SiO ₂	38,56	38,22	38,44	38,32	38,27	38,39	38,30	38,66	38,06	38,21	38,32	38,06	38,40	38,46	38,08	
TiO ₂	0,06	0,07	0,11	0,07	0,00	0,06	0,08	0,11	0,08	0,09	0,12	0,14	0,05	0,03	0,05	
Al ₂ O ₃	21,41	21,59	21,57	21,60	21,31	21,73	21,54	21,63	21,65	21,53	21,33	21,36	21,59	21,64	21,69	
Cr ₂ O ₃	0,00	0,01	0,00	0,02	0,01	0,00	0,02	0,00	0,00	0,02	0,02	0,01	0,04	0,01	0,03	
FeO	25,46	25,69	24,57	25,34	26,27	24,39	25,35	24,46	25,26	27,00	27,13	27,80	26,06	26,01	24,41	
MnO	0,70	0,87	0,91	0,62	0,62	0,69	0,60	0,56	0,53	0,61	0,62	0,67	0,42	0,52	0,43	
MgO	4,84	4,60	5,06	4,38	5,70	4,87	5,50	4,81	5,37	5,16	5,17	5,10	5,65	5,15	4,42	
CaO	9,49	9,18	9,22	9,81	7,14	10,03	8,49	10,26	8,72	7,70	7,21	6,76	7,81	8,34	10,92	
Na ₂ O	0,04	0,02	0,06	0,01	0,01	0,10	0,01	0,04	0,03	0,02	0,06	0,05	0,02	0,03	0,02	
K ₂ O	0,01	0,00	0,00	0,00	0,00	0,01	0,00	0,01	0,00	0,00	0,00	0,00	0,00	0,00	0,00	
Sum	100,57	100,24	99,95	100,16	99,33	100,27	99,89	100,54	99,70	100,35	99,97	99,93	100,05	100,18	100,06	
Structural formula based on 8 cations and 12 oxygens																
Si	2,99	2,98	2,99	2,99	3,00	2,98	2,98	2,99	2,97	2,98	3,00	2,99	2,99	2,99	2,96	
Ti	0,00	0,00	0,01	0,00	0,00	0,00	0,00	0,01	0,00	0,01	0,01	0,00	0,00	0,00	0,00	
Al	1,96	1,98	1,98	1,98	1,97	1,99	1,98	1,97	1,99	1,98	1,97	1,99	1,98	1,98	1,99	
Fe(III)	0,06	0,05	0,03	0,03	0,03	0,07	0,05	0,04	0,07	0,07	0,03	0,02	0,05	0,03	0,08	
Fe(II)	0,00	0,00	0,00	0,00	0,00	0,00	0,00	0,00	0,00	0,00	0,00	0,00	0,00	0,00	0,00	
Mn	1,59	1,62	1,56	1,62	1,69	1,51	1,60	1,54	1,58	1,69	1,74	1,66	1,65	1,66	1,51	
Mg	0,05	0,06	0,06	0,04	0,04	0,05	0,04	0,04	0,04	0,04	0,04	0,03	0,03	0,03	0,03	
Ca	0,56	0,53	0,59	0,51	0,67	0,56	0,64	0,55	0,62	0,60	0,60	0,60	0,66	0,60	0,51	
Sum	0,79	0,77	0,77	0,82	0,60	0,83	0,71	0,85	0,73	0,64	0,60	0,69	0,65	0,69	0,91	
Mg/Mg+Fe ²⁺	0,00	0,00	0,00	0,00	0,00	0,00	0,00	0,00	0,00	0,00	0,00	0,00	0,00	0,00	0,00	
End members	0,00	0,00	0,00	0,00	0,00	0,00	0,00	0,00	0,00	0,00	0,00	0,00	0,00	0,00	0,00	
Almandine	7,99	8,00	7,99	8,00	8,00	7,98	8,00	7,99	8,00	8,00	7,99	8,00	8,00	8,00	8,00	
Pyrope	0,26	0,25	0,27	0,24	0,28	0,27	0,29	0,26	0,28	0,26	0,26	0,27	0,28	0,26	0,25	
Grossular																
Sum	53	54	52	54	56	51,1	53,5	51,7	53,2	56,9	58,2	55,6	55,3	55,5	51,0	
	19	18	20	17	22	19,1	21,4	18,6	21,0	20,2	20,2	20,2	22,0	20,0	17,3	
	26	25	25	27	20	27,2	23,0	27,8	23,7	20,8	19,8	23,0	21,3	22,9	29,5	
	98	97	97	98	98	97	98	98	98	98	98	99	99	98	98	

3.3 Ferro gabbroic, primary pyroxenes

Oxide Wt%	SK-7						SK-28					
	Core	Core	Core	Rim	Rim	Rim	Core	Core	Core	Rim	Rim	Rim
SiO ₂	54,66	55,00	55,16	54,55	54,86	54,64	54,78	55,00	55,04	54,70	55,44	55,06
TiO ₂	0,04	0,07	0,05	0,07	0,05	0,09	0,07	0,07	0,06	0,11	0,05	0,06
Al ₂ O ₃	7,67	7,39	7,00	7,19	7,40	7,70	7,72	7,77	8,06	8,09	7,95	8,09
Cr ₂ O ₃	0,00	0,08	0,04	0,00	0,05	0,02	0,00	0,00	0,00	0,01	0,00	0,00
FeO	8,74	8,73	8,00	8,34	8,37	8,49	9,16	7,82	7,20	8,55	7,45	7,65
MnO	0,02	0,01	0,00	0,02	0,01	0,01	0,02	0,02	0,01	0,01	0,03	0,01
MgO	8,18	8,36	9,28	8,93	8,50	8,41	7,75	8,68	8,78	8,03	8,71	8,63
CaO	14,13	14,16	14,86	14,84	14,23	14,51	13,28	13,97	14,17	13,69	14,14	14,14
Na ₂ O	6,54	6,58	5,93	5,96	6,11	6,39	6,88	6,49	6,33	6,37	6,42	6,46
K ₂ O	0,02	0,00	0,00	0,02	0,00	0,00	0,01	0,01	0,01	0,00	0,00	0,00
Sum	100,00	100,39	100,32	99,91	99,57	100,26	99,66	99,81	99,66	99,54	100,2	100,1
Structural formula based on 4 cations and 8 oxygens												
Si	1,97	1,97	1,98	1,97	1,99	1,96	1,98	1,98	1,98	1,98	1,99	1,97
Ti	0,00	0,00	0,00	0,00	0,00	0,00	0,00	0,00	0,00	0,00	0,00	0,00
Al	0,33	0,31	0,30	0,31	0,32	0,33	0,33	0,33	0,34	0,35	0,34	0,34
Fe(III)	0,19	0,19	0,15	0,17	0,13	0,19	0,19	0,16	0,14	0,13	0,14	0,16
Cr	0,00	0,00	0,00	0,00	0,00	0,00	0,00	0,00	0,00	0,00	0,00	0,00
Fe(II)	0,07	0,07	0,09	0,08	0,12	0,07	0,08	0,07	0,08	0,13	0,09	0,07
Mn	0,00	0,00	0,00	0,00	0,00	0,00	0,00	0,00	0,00	0,00	0,00	0,00
Mg	0,44	0,45	0,50	0,48	0,46	0,45	0,42	0,47	0,47	0,43	0,46	0,46
Ca	0,55	0,54	0,57	0,57	0,55	0,56	0,51	0,54	0,55	0,53	0,54	0,54
Na	0,46	0,46	0,41	0,42	0,43	0,45	0,48	0,45	0,44	0,45	0,45	0,45
K	0,00	0,00	0,00	0,00	0,00	0,00	0,00	0,00	0,00	0,00	0,00	0,00
Sum	4,00	4,00	4,00	4,00	4,00	4,00	4,00	4,00	4,00	4,00	4,00	4,00
Mg/(Mg+Fe ²⁺)	0,86	0,87	0,85	0,86	0,79	0,87	0,83	0,87	0,85	0,78	0,84	0,86
End members												
Diop+Heden	53	53	59	57	57	54	51	54	56	56	55	54
Jadeite	27	27	26	25	29	27	29	29	31	31	31	30
Aegirine	20	20	15	18	13	20	20	17	14	13	14	16

Oxide Wt%	SK-29						SK-6					
	Core	Core	Core	Rim	Rim	Rim	Core	Core	Core	Rim	Rim	
SiO ₂	55,10	55,25	54,70	55,27	54,60	54,77	54,97	54,75	54,57	54,85	54,84	
TiO ₂	0,05	0,05	0,07	0,08	0,11	0,08	0,29	0,11	0,05	0,04	0,08	
Al ₂ O ₃	7,75	8,05	7,88	9,43	7,75	7,66	7,52	7,53	6,94	6,97	7,59	
Cr ₂ O ₃	0,03	0,02	0,01	0,00	0,00	0,02	0,01	0,01	0,00	0,04	0,00	
FeO	7,18	7,69	7,72	7,42	8,51	7,87	8,76	8,92	7,98	8,51	8,72	
MnO	0,07	0,00	0,03	0,00	0,04	0,02	0,03	0,05	0,00	0,01	0,06	
MgO	8,70	8,38	8,52	7,85	8,32	8,80	8,33	8,42	9,22	8,73	8,15	
CaO	14,50	14,01	14,16	13,35	14,87	14,30	14,44	14,09	15,11	14,98	14,30	
Na ₂ O	6,18	6,55	6,48	7,15	6,24	6,28	6,20	6,25	5,91	5,97	6,35	
K ₂ O	0,01	0,00	0,00	0,00	0,01	0,01	0,01	0,02	0,00	0,01	0,00	
Sum	99,58	100,00	99,56	100,54	100,45	99,80	100,57	100,14	99,77	100,10	100,09	
Structural formula based on 4 cations and 8 oxygens												
Si	1,96	1,98	1,97	1,97	1,96	1,97	1,97	1,97	1,97	1,98	1,98	
Ti	0,00	0,00	0,00	0,00	0,00	0,00	0,01	0,00	0,00	0,00	0,00	
Al	0,33	0,34	0,33	0,40	0,33	0,33	0,32	0,32	0,30	0,30	0,32	
Fe(III)	0,18	0,14	0,17	0,16	0,18	0,16	0,15	0,17	0,18	0,16	0,16	
Cr	0,00	0,00	0,00	0,00	0,00	0,00	0,00	0,00	0,00	0,00	0,00	
Fe(II)	0,07	0,09	0,06	0,06	0,07	0,07	0,12	0,10	0,06	0,10	0,10	
Mn	0,00	0,00	0,00	0,00	0,00	0,00	0,00	0,00	0,00	0,00	0,00	
Mg	0,45	0,45	0,46	0,42	0,45	0,47	0,45	0,45	0,50	0,47	0,44	
Ca	0,57	0,54	0,55	0,51	0,57	0,55	0,56	0,54	0,58	0,58	0,55	
Na	0,43	0,46	0,45	0,49	0,43	0,44	0,43	0,44	0,41	0,42	0,44	
K	0,00	0,00	0,00	0,00	0,00	0,00	0,00	0,00	0,00	0,00	0,00	
Sum	4,00	4,00	4,00	4,00	4,00	4,00	4,00	4,00	4,00	4,00	4,00	
Mg/(Mg+Fe2+)	0,86	0,84	0,88	0,88	0,86	0,87	0,80	0,81	0,88	0,83	0,81	
End members												
Diop+Heden	55	54	53	49	55	55	57	56	58	58	55	
Jadeite	27	31	29	34	27	28	29	27	24	24	29	
Aegirine	19	15	18	17	19	17	15	17	18	18	17	

Oxide Wt%	SK-9					SK-8				
	Core	Core	Core	Rim	Rim	Core	Core	Core	Rim	Rim
SiO ₂	55,39	55,35	54,95	55,01	55,01	55,16	54,87	54,88	54,69	54,99
TiO ₂	0,06	0,07	0,06	0,46	0,08	0,05	0,06	0,09	0,04	0,09
Al ₂ O ₃	7,25	7,85	7,43	7,19	7,32	7,71	7,77	7,47	6,85	7,87
Cr ₂ O ₃	0,03	0,04	0,01	0,00	0,01	0,01	0,00	0,01	0,04	0,05
FeO	7,70	7,96	9,00	8,04	8,06	7,93	9,17	8,16	7,13	7,92
MnO	0,02	0,02	0,00	0,04	0,00	0,00	0,04	0,02	0,00	0,02
MgO	9,11	8,57	8,11	8,74	8,75	8,22	7,75	8,83	9,77	8,66
CaO	14,90	14,23	13,83	14,87	14,87	14,22	13,37	14,89	15,81	14,70
Na ₂ O	5,79	6,43	6,69	5,99	5,89	6,57	6,75	6,07	5,39	6,22
K ₂ O	0,01	0,00	0,00	0,01	0,00	0,00	0,00	0,01	0,00	0,00
Sum	100,26	100,51	100,09	100,35	100,01	99,86	99,78	100,42	99,72	100,53
Structural formula based on 4 cations and 8 oxygens										
Si	1,99	1,98	1,98	1,98	1,98	1,99	1,98	1,97	1,98	1,97
Ti	0,00	0,00	0,00	0,01	0,00	0,00	0,00	0,00	0,00	0,00
Al	0,31	0,33	0,32	0,30	0,31	0,33	0,33	0,32	0,29	0,33
Fe(III)	0,11	0,15	0,19	0,13	0,13	0,16	0,17	0,16	0,13	0,16
Cr	0,00	0,00	0,00	0,00	0,00	0,00	0,00	0,00	0,00	0,00
Fe(II)	0,12	0,09	0,08	0,11	0,12	0,08	0,10	0,08	0,08	0,08
Mn	0,00	0,00	0,00	0,00	0,00	0,00	0,00	0,00	0,00	0,00
Mg	0,49	0,46	0,43	0,47	0,47	0,44	0,42	0,47	0,53	0,46
Ca	0,57	0,55	0,53	0,57	0,57	0,55	0,52	0,57	0,61	0,56
Na	0,40	0,45	0,47	0,42	0,41	0,46	0,47	0,42	0,38	0,43
K	0,00	0,00	0,00	0,00	0,00	0,00	0,00	0,00	0,00	0,00
Sum	4,00	4,00	4,00	4,00	4,00	4,00	4,00	4,00	4,00	4,00
Mg/(Mg+Fe2+)	0,80	0,84	0,85	0,81	0,80	0,84	0,80	0,85	0,86	0,85
End members										
Diop+Heden	60	55	52	58	59	53	52	57	62	56
Jadeite	29	30	28	29	29	31	30	27	25	28
Aegirine	11	15	20	13	13	16	18	17	13	16

Oxide Wt%	SK-2						SK-3					
	Core	Core	Core	Rim	Rim	Rim	Core	Core	Rim	Rim	Rim	
SiO ₂	55,26	55,01	54,94	55,20	55,22	54,95	54,59	55,16	54,82	54,59	54,81	
TiO ₂	0,05	0,05	0,07	0,06	0,08	0,07	0,08	0,06	0,07	0,08	0,05	
Al ₂ O ₃	8,17	8,23	8,21	9,38	8,01	8,04	7,83	8,33	7,87	7,83	8,16	
Cr ₂ O ₃	0,02	0,00	0,00	0,00	0,02	0,00	0,01	0,00	0,00	0,01	0,00	
FeO	7,21	8,60	7,34	7,74	8,22	8,65	8,42	7,59	7,63	8,42	7,55	
MnO	0,00	0,00	0,01	0,03	0,07	0,02	0,00	0,05	0,00	0,00	0,01	
MgO	8,83	7,78	8,49	7,35	8,25	7,60	8,14	8,40	8,72	8,14	8,71	
CaO	14,36	13,11	13,97	12,61	14,17	13,35	14,55	14,32	14,71	14,55	14,34	
Na ₂ O	6,39	6,99	6,43	7,39	6,47	6,90	6,43	6,41	6,32	6,43	6,49	
K ₂ O	0,00	0,00	0,00	0,01	0,01	0,00	0,01	0,00	0,00	0,01	0,01	
Sum	100,29	99,77	99,46	99,77	100,50	99,58	100,05	100,32	100,14	100,05	100,13	
Structural formula based on 4 cations and 8 oxygens												
Si	1,97	1,98	1,98	1,98	1,98	1,99	1,97	1,98	1,97	1,97	1,96	
Ti	0,00	0,00	0,00	0,00	0,00	0,00	0,00	0,00	0,00	0,00	0,00	
Al	0,34	0,35	0,35	0,40	0,34	0,34	0,33	0,35	0,33	0,35	0,34	
Fe(III)	0,15	0,18	0,13	0,16	0,15	0,17	0,18	0,14	0,17	0,16	0,18	
Cr	0,00	0,00	0,00	0,00	0,00	0,00	0,00	0,00	0,00	0,00	0,00	
Fe(II)	0,07	0,08	0,09	0,07	0,09	0,09	0,07	0,09	0,06	0,07	0,05	
Mn	0,00	0,00	0,00	0,00	0,00	0,00	0,00	0,00	0,00	0,00	0,00	
Mg	0,47	0,42	0,46	0,39	0,44	0,41	0,44	0,45	0,47	0,45	0,46	
Ca	0,55	0,51	0,54	0,48	0,54	0,52	0,56	0,55	0,57	0,55	0,55	
Na	0,44	0,49	0,45	0,51	0,45	0,48	0,45	0,45	0,44	0,45	0,45	
K	0,00	0,00	0,00	0,00	0,00	0,00	0,00	0,00	0,00	0,00	0,00	
Sum	4,00	4,00	4,00	4,00	4,00	4,00	4,00	4,00	4,00	4,00	4,00	
Mg/(Mg+Fe2+)	0,87	0,83	0,84	0,84	0,82	0,81	0,86	0,84	0,89	0,87	0,91	
End members												
Diop+Heden	55	51	55	48	54	51	53	55	54	54	53	
Jadeite	30	32	32	36	30	32	28	31	28	29	28	
Aegirine	15	18	14	16	15	17	19	14	18	17	19	

Oxide Wt%	SK-11				SK-12			SK-20					
	Core	Core	Core	Rim	Rim	Core	Core	Core	Core	Core	Core	Rim	Rim
SiO ₂	55,03	54,81	55,19	54,74	54,83	54,85	54,37	55,03	55,10	55,48	54,88	54,74	55,06
TiO ₂	0,07	0,04	0,05	0,09	0,07	0,09	0,05	0,07	0,08	0,06	0,06	0,03	0,06
Al ₂ O ₃	8,17	7,81	8,36	8,60	7,93	7,00	8,15	8,36	8,02	8,07	8,03	8,22	7,84
Cr ₂ O ₃	0,00	0,02	0,05	0,04	0,00	0,03	0,02	0,03	0,02	0,03	0,02	0,04	0,00
FeO	7,98	9,34	8,20	7,97	9,73	9,12	10,31	8,89	8,50	7,92	8,22	8,34	8,41
MnO	0,04	0,02	0,00	0,01	0,01	0,04	0,01	0,03	0,01	0,00	0,03	0,04	0,02
MgO	8,25	7,52	7,80	8,05	7,26	8,35	6,83	7,56	7,83	8,30	8,04	8,04	8,26
CaO	13,71	12,74	13,26	13,39	12,27	13,86	12,44	12,76	13,33	13,82	13,64	13,41	13,97
Na ₂ O	6,58	7,04	6,83	6,79	7,20	6,43	7,37	7,16	6,79	6,53	6,66	6,82	6,55
K ₂ O	0,00	0,00	0,01	0,00	0,00	0,01	0,00	0,00	0,00	0,00	0,00	0,00	0,00
Sum	99,84	99,33	99,73	99,69	99,3	99,77	99,55	99,89	99,68	100,21	99,57	99,68	100,18
Structural formula based on 4 cations and 8 oxygens													
Si	1,98	1,99	1,99	1,97	1,99	1,98	1,97	1,98	1,99	1,99	1,97	1,97	1,98
Ti	0,00	0,00	0,00	0,00	0,00	0,00	0,00	0,00	0,00	0,00	0,00	0,00	0,00
Al	0,35	0,33	0,35	0,36	0,34	0,30	0,35	0,35	0,34	0,34	0,36	0,35	0,33
Fe(III)	0,15	0,19	0,14	0,16	0,19	0,18	0,23	0,18	0,15	0,13	0,19	0,18	0,17
Cr	0,00	0,00	0,00	0,00	0,00	0,00	0,00	0,00	0,00	0,00	0,00	0,00	0,00
Fe(II)	0,09	0,10	0,10	0,08	0,11	0,09	0,08	0,09	0,10	0,11	0,05	0,07	0,09
Mn	0,00	0,00	0,00	0,00	0,00	0,00	0,00	0,00	0,00	0,00	0,00	0,00	0,00
Mg	0,44	0,41	0,42	0,43	0,39	0,45	0,37	0,41	0,42	0,44	0,42	0,43	0,44
Ca	0,53	0,49	0,51	0,52	0,48	0,54	0,48	0,49	0,52	0,53	0,51	0,52	0,54
Na	0,46	0,49	0,48	0,47	0,51	0,45	0,52	0,50	0,47	0,45	0,49	0,48	0,46
K	0,00	0,00	0,00	0,00	0,00	0,00	0,00	0,00	0,00	0,00	0,00	0,00	0,00
Sum	4,00	4,00	4,00	4,00	4,00	4,00	4,00	4,00	4,00	4,00	4,00	4,00	4,00
Mg/(Mg+Fe2+)	0,83	0,81	0,80	0,85	0,78	0,83	0,81	0,83	0,80	0,80	0,89	0,86	0,84
End members													
Diop+Heden	54	50	52	52	50	55	47	50	52	55	49	51	54
Jadeite	31	31	33	32	32	27	30	32	32	32	32	30	29
Aegirine	15	19	14	17	19	18	23	18	15	13	19	19	17

3.4 Leuco gabbroic, primary pyroxenes

Oxide Wt%	SK-31			SK-30				SK-4					
	Core	Core	Rim	Core	Core	Core	Rim	Core	Core	Core	Rim	Rim	Rim
SiO ₂	56,43	56,56	56,35	56,34	55,53	56,11	56,05	55,77	55,78	55,27	56,07	55,83	55,83
TiO ₂	0,05	0,05	0,03	0,07	0,04	0,04	0,07	0,07	0,07	0,07	0,05	0,03	0,04
Al ₂ O ₃	10,74	10,45	10,84	10,47	10,65	10,39	10,38	10,30	10,55	9,83	10,41	10,96	9,27
Cr ₂ O ₃	0,08	0,02	0,02	0,05	0,05	0,02	0,02	0,00	0,02	0,03	0,02	0,04	0,03
FeO	3,95	4,29	4,30	5,10	4,70	4,98	4,90	4,98	5,07	5,21	5,03	5,01	5,32
MnO	0,05	0,00	0,02	0,04	0,00	0,04	0,01	0,02	0,04	0,04	0,02	0,03	0,04
MgO	8,72	8,51	8,64	8,15	8,40	8,38	8,46	8,41	8,23	8,71	8,34	8,03	9,00
CaO	13,57	13,78	13,69	13,59	13,08	13,52	13,32	13,32	12,86	13,66	13,38	12,71	14,18
Na ₂ O	6,99	7,07	7,09	6,91	7,09	6,95	7,02	7,14	7,10	6,74	7,18	7,46	6,58
K ₂ O	0,00	0,00	0,02	0,01	0,00	0,00	0,00	0,00	0,00	0,00	0,01	0,00	0,00
Sum	100,58	100,75	101,00	100,74	99,55	100,43	100,22	100,01	99,71	99,57	100,49	100,11	100,27
Structural formula based on 4 cations and 8 oxygens													
Si	1,99	1,99	1,98	1,99	1,98	1,99	1,99	1,98	1,99	1,97	1,98	1,98	1,98
Ti	0,00	0,00	0,00	0,00	0,00	0,00	0,00	0,00	0,00	0,00	0,00	0,00	0,00
Al	0,45	0,43	0,45	0,44	0,45	0,43	0,43	0,43	0,44	0,41	0,43	0,46	0,39
Fe(III)	0,05	0,06	0,08	0,05	0,09	0,07	0,07	0,10	0,07	0,10	0,10	0,10	0,10
Cr	0,00	0,00	0,00	0,00	0,00	0,00	0,00	0,00	0,00	0,00	0,00	0,00	0,00
Fe(II)	0,06	0,06	0,04	0,10	0,05	0,08	0,07	0,05	0,08	0,06	0,05	0,05	0,06
Mn	0,00	0,00	0,00	0,00	0,00	0,00	0,00	0,00	0,00	0,00	0,00	0,00	0,00
Mg	0,46	0,45	0,45	0,43	0,45	0,44	0,45	0,44	0,44	0,46	0,44	0,42	0,48
Ca	0,51	0,52	0,51	0,51	0,50	0,51	0,51	0,51	0,49	0,52	0,51	0,48	0,54
Na	0,48	0,48	0,48	0,47	0,49	0,48	0,48	0,49	0,49	0,47	0,49	0,51	0,45
K	0,00	0,00	0,00	0,00	0,00	0,00	0,00	0,00	0,00	0,00	0,00	0,00	0,00
Sum	4,00	4,00	4,00	4,00	4,00	4,00	4,00	4,00	4,00	4,00	4,00	4,00	4,00
Mg/(Mg+Fe ²⁺)	0,91	0,88	0,91	0,81	0,89	0,85	0,87	0,91	0,85	0,89	0,89	0,90	0,89
End members													
Diop+Heden	52	51	51	53	51	52	52	50	51	53	50	48	54
Jadeite	42	42	41	42	41	41	41	40	42	37	40	42	36
Aegirine	5	7	8	5	9	7	7	10	7	10	10	10	10

3.5 Ferro gabbroic, primary amphiboles

Oxide Wt%	SK-7						SK-28					
	Core	Core	Core	Rim	Rim	Rim	Core	Core	Rim	Rim	Rim	
SiO₂	49,81	50,87	50,27	48,89	50,51	48,29	47,00	46,84	47,05	43,99	44,87	
TiO₂	0,24	0,16	0,23	0,31	0,15	0,32	0,37	0,36	0,36	0,43	1,12	
Al₂O₃	8,03	6,88	7,78	9,89	7,60	9,63	11,08	11,41	11,25	13,31	12,16	
Cr₂O₃	0,02	0,00	0,00	0,00	0,00	0,02	0,03	0,00	0,00	0,01	0,01	
FeO	12,80	12,50	12,89	13,28	12,65	13,01	14,13	14,56	14,11	15,12	15,12	
MnO	0,00	0,01	0,03	0,04	0,07	0,03	0,03	0,01	0,05	0,01	0,02	
MgO	14,00	14,26	13,73	13,05	13,88	12,93	11,43	11,23	11,33	10,16	10,08	
CaO	8,50	8,88	8,88	8,78	8,80	8,46	8,33	8,42	8,34	9,04	9,13	
Na₂O	3,16	2,93	3,14	3,43	3,04	3,46	3,92	3,84	3,84	3,65	3,78	
K₂O	0,43	0,34	0,34	0,41	0,29	0,44	0,48	0,48	0,48	0,55	0,55	
Sum	96,98	96,83	97,29	98,08	97,00	96,60	96,79	97,15	96,82	96,28	96,83	
Structural formula based on average of all Fe as Fe²⁺ and sum cat - (Na+K+Ca) = 13												
Si	7,18	7,33	7,24	7,01	7,27	7,02	6,89	6,85	6,89	6,55	6,67	
Ti	0,03	0,02	0,03	0,03	0,02	0,04	0,04	0,04	0,04	0,05	0,13	
Al IV	0,82	0,67	0,76	0,99	0,73	0,98	1,11	1,15	1,11	1,45	1,33	
Al VI	0,54	0,50	0,56	0,68	0,56	0,67	0,80	0,81	0,83	0,89	0,80	
Fe³⁺	0,41	0,32	0,30	0,33	0,32	0,34	0,26	0,28	0,26	0,27	0,12	
Fe²⁺	1,14	1,19	1,25	1,26	1,20	1,24	1,47	1,50	1,47	1,61	1,76	
Mn	0,00	0,00	0,00	0,00	0,01	0,00	0,00	0,00	0,01	0,00	0,00	
Mg	3,01	3,06	2,95	2,79	2,98	2,80	2,50	2,45	2,47	2,26	2,23	
Ca	1,31	1,37	1,37	1,35	1,36	1,32	1,31	1,32	1,31	1,44	1,45	
NaA	0,31	0,28	0,33	0,40	0,30	0,39	0,50	0,49	0,47	0,57	0,58	
NaM4	0,57	0,54	0,54	0,56	0,55	0,58	0,62	0,60	0,62	0,48	0,51	
K	0,08	0,06	0,06	0,08	0,05	0,08	0,09	0,09	0,09	0,10	0,10	
Sum	15,39	15,35	15,39	15,47	15,35	15,47	15,59	15,58	15,56	15,68	15,68	
Mg/Mg+Fe²⁺	0,73	0,72	0,70	0,69	0,71	0,69	0,63	0,62	0,63	0,58	0,56	
Name	Brs	Brs	Brs	Brs	Brs	Brs	Mkt	Mkt	Mkt	Mkt	Mkt	

Brs = Barroisite, Mkt = Magnesio-katophorite

Oxide Wt%	SK-29		SK-6						SK-9				
	Rim	Rim	Core	Core	Core	Rim	Rim	Rim	Core	Core	Core	Rim	
SiO₂	47,82	44,20	48,25	47,90	48,99	48,19	48,30	47,55	50,93	50,92	49,94	50,99	
TiO₂	0,33	0,46	0,25	0,28	0,27	0,39	0,23	0,35	0,19	0,19	0,26	0,23	
Al₂O₃	10,83	13,17	8,82	9,21	8,80	9,39	9,27	10,12	7,61	7,92	8,32	8,34	
Cr₂O₃	0,00	0,00	0,02	0,00	0,04	0,00	0,01	0,00	0,00	0,03	0,03	0,00	
FeO	12,82	14,38	13,35	13,22	13,85	14,51	13,45	14,40	11,96	11,71	12,13	11,58	
MnO	0,04	0,05	0,02	0,04	0,00	0,07	0,06	0,06	0,05	0,05	0,03	0,02	
MgO	12,08	10,60	12,75	12,30	12,49	11,95	12,65	11,74	14,46	14,25	13,90	14,15	
CaO	8,43	9,36	8,70	8,53	8,44	8,49	8,58	8,58	8,77	8,68	8,73	8,74	
Na₂O	3,90	3,71	3,43	3,21	3,36	3,61	3,36	3,59	3,11	3,19	3,28	3,22	
K₂O	0,44	0,60	0,40	0,43	0,42	0,44	0,32	0,51	0,36	0,39	0,43	0,36	
Sum	96,71	96,53	96,01	95,13	96,68	97,05	96,23	96,88	97,45	97,33	97,05	97,63	
Structural formula based on average of all Fe as Fe²⁺ and sum cat - (Na+K+Ca) = 13													
Si	6,97	6,89	7,09	7,09	7,14	7,04	7,06	6,96	7,28	7,28	7,19	7,26	
Ti	0,04	0,04	0,03	0,03	0,03	0,04	0,03	0,04	0,02	0,02	0,03	0,02	
Al IV	1,03	1,11	0,91	0,91	0,86	0,96	0,94	1,04	0,72	0,72	0,81	0,74	
Al VI	0,83	0,80	0,62	0,70	0,65	0,66	0,66	0,71	0,56	0,62	0,61	0,66	
Fe³⁺	0,20	0,25	0,28	0,28	0,30	0,29	0,33	0,28	0,33	0,28	0,29	0,26	
Fe²⁺	1,36	1,37	1,36	1,35	1,38	1,48	1,31	1,48	1,10	1,12	1,17	1,12	
Mn	0,00	0,01	0,00	0,01	0,00	0,01	0,01	0,01	0,01	0,01	0,01	0,00	
Mg	2,62	2,61	2,79	2,71	2,71	2,60	2,76	2,56	3,08	3,04	2,99	3,00	
Ca	1,32	1,31	1,37	1,35	1,32	1,33	1,34	1,35	1,34	1,33	1,35	1,33	
NaA	0,48	0,50	0,43	0,35	0,36	0,43	0,39	0,45	0,30	0,30	0,35	0,30	
NaM4	0,63	0,61	0,55	0,57	0,59	0,59	0,56	0,57	0,56	0,59	0,57	0,59	
K	0,08	0,09	0,08	0,08	0,08	0,08	0,06	0,09	0,06	0,07	0,08	0,07	
Sum	15,56	15,59	15,50	15,44	15,43	15,52	15,45	15,54	15,36	15,37	15,43	15,36	
Mg/Mg+Fe²⁺	0,66	0,66	0,67	0,67	0,66	0,64	0,68	0,63	0,74	0,73	0,72	0,73	
Name	Mkt	Mkt	Mkt	Mkt	Brs	Mkt	Brs	Mkt	Brs	Brs	Brs	Brs	

Brs = Barroisite, Mkt = Magnesio-katophorite

	SK-8		SK-2				SK-3		SK-11				
Oxide Wt%	Core	Core	Core	Core	Rim	Rim	Core	Core	Core	Core	Core	Rim	Rim
SiO₂	49,80	51,05	49,89	48,82	44,63	48,94	48,28	46,37	48,02	47,71	51,50	47,02	44,18
TiO₂	0,27	0,19	0,22	0,26	0,38	0,32	0,32	0,29	0,35	0,33	0,12	0,41	0,28
Al₂O₃	9,18	8,15	8,83	9,59	12,41	9,65	10,58	11,43	9,99	10,98	7,38	12,32	13,77
Cr₂O₃	0,01	0,00	0,01	0,00	0,04	0,00	0,04	0,01	0,03	0,02	0,00	0,00	0,01
FeO	12,04	11,48	11,93	12,22	14,78	12,52	12,98	14,07	13,27	13,98	12,01	13,88	14,18
MnO	0,05	0,02	0,04	0,03	0,03	0,01	0,00	0,05	0,01	0,05	0,00	0,06	0,02
MgO	13,48	14,44	13,80	13,38	10,84	12,81	12,33	11,82	11,95	11,69	14,01	11,24	10,54
CaO	8,42	8,64	8,18	8,26	8,47	8,38	8,31	8,90	8,08	8,29	7,58	8,40	8,75
Na₂O	3,49	3,31	3,68	3,74	3,84	3,74	3,73	3,72	3,92	4,01	3,82	4,09	3,83
K₂O	0,38	0,34	0,40	0,40	0,77	0,46	0,36	0,24	0,40	0,47	0,25	0,62	0,84
Sum	97,10	97,63	96,98	96,69	96,19	96,83	96,92	96,88	96,02	97,53	96,67	98,03	96,40
Structural formula based on average of all Fe as Fe²⁺ and sum cat - (Na+K+Ca) = 13													
Si	7,16	7,26	7,17	7,06	6,63	7,09	7,00	6,78	7,05	6,93	7,39	6,80	6,55
Ti	0,03	0,02	0,02	0,03	0,04	0,04	0,03	0,03	0,04	0,04	0,01	0,04	0,03
Al IV	0,84	0,74	0,83	0,94	1,37	0,91	1,00	1,22	0,95	1,07	0,61	1,20	1,45
Al VI	0,71	0,63	0,67	0,70	0,81	0,74	0,81	0,75	0,78	0,80	0,64	0,90	0,95
Fe₃+	0,28	0,29	0,31	0,32	0,33	0,23	0,28	0,32	0,23	0,26	0,32	0,22	0,25
Fe₂+	1,17	1,08	1,12	1,16	1,51	1,29	1,30	1,40	1,40	1,44	1,12	1,46	1,50
Mn	0,01	0,00	0,01	0,00	0,00	0,00	0,00	0,01	0,00	0,01	0,00	0,01	0,00
Mg	2,89	3,06	2,96	2,88	2,40	2,77	2,66	2,58	2,61	2,53	3,00	2,43	2,33
Ca	1,30	1,32	1,26	1,28	1,35	1,30	1,29	1,39	1,27	1,29	1,17	1,30	1,39
NaA	0,35	0,31	0,38	0,42	0,55	0,42	0,42	0,54	0,45	0,49	0,32	0,51	0,56
NaM4	0,62	0,60	0,65	0,63	0,56	0,63	0,63	0,51	0,66	0,64	0,74	0,64	0,54
K	0,07	0,06	0,07	0,07	0,15	0,09	0,07	0,04	0,08	0,09	0,05	0,11	0,16
Sum	15,42	15,38	15,45	15,49	15,70	15,50	15,48	15,59	15,53	15,58	15,37	15,62	15,72
Mg/Mg+Fe₂+	0,71	0,74	0,73	0,71	0,61	0,68	0,67	0,65	0,65	0,64	0,73	0,62	0,61
Name	Brs	Brs	Brs	Brs	Mkt	Brs	Brs	Mkt	Mkt	Mkt	Mkt	Mkt	Mkt

Brs = Barroisite, Mkt = Magnesio-katophorite

Oxide Wt%	SK-12					SK-20		
	Core	Core	Core	Rim	Rim	Core	Core	Rim
SiO₂	50,92	51,45	50,67	49,58	49,92	46,55	46,59	48,11
TiO₂	0,19	0,19	0,21	0,22	0,28	0,39	0,33	0,37
Al₂O₃	7,92	7,39	7,72	8,68	8,62	11,59	11,57	10,70
Cr₂O₃	0,06	0,00	0,05	0,04	0,03	0,01	0,00	0,03
FeO	13,35	13,12	13,59	13,79	13,91	15,34	14,05	13,82
MnO	0,00	0,04	0,00	0,04	0,04	0,01	0,01	0,06
MgO	12,74	13,23	12,94	12,67	12,26	10,86	11,59	11,93
CaO	7,72	7,63	7,65	7,81	7,75	8,19	8,31	8,04
Na₂O	3,64	3,50	3,68	3,94	3,74	3,55	3,84	3,95
K₂O	0,19	0,20	0,30	0,35	0,36	0,13	0,26	0,38
Sum	96,72	96,75	96,80	97,12	96,91	96,62	96,54	97,39

Structural formula based on average of all Fe as Fe²⁺ and sum cat -

(Na+K+Ca) = 13

Si	7,36	7,40	7,33	7,18	7,24	6,82	6,82	6,97
Ti	0,02	0,02	0,02	0,02	0,03	0,04	0,04	0,04
Al IV	0,64	0,60	0,67	0,82	0,76	1,18	1,18	1,03
Al VI	0,71	0,66	0,64	0,66	0,71	0,82	0,81	0,79
Fe³⁺	0,29	0,34	0,34	0,33	0,29	0,42	0,35	0,31
Fe²⁺	1,33	1,24	1,31	1,34	1,39	1,46	1,37	1,36
Mn	0,00	0,00	0,00	0,00	0,01	0,00	0,00	0,01
Mg	2,74	2,84	2,79	2,74	2,65	2,37	2,53	2,58
Ca	1,19	1,18	1,18	1,21	1,20	1,29	1,30	1,25
NaA	0,30	0,25	0,31	0,41	0,34	0,42	0,49	0,44
NaM4	0,72	0,73	0,72	0,69	0,71	0,59	0,60	0,66
K	0,04	0,04	0,06	0,07	0,07	0,02	0,05	0,07
Sum	15,33	15,29	15,37	15,48	15,41	15,44	15,54	15,51
Mg/Mg+Fe²⁺	0,67	0,70	0,68	0,67	0,66	0,62	0,65	0,65
Name	Mkt							

Brs = Barroisite, Mkt = Magnesio-katophorite

3.6 Leuco gabbroic, primary amphiboles

Oxide Wt%	SK-31						SK-30		SK-4					
	Core	Core	Core	Rim	Rim	Rim	Core	Core	Core	Core	Core	Rim	Rim	Rim
SiO₂	52,41	49,84	51,56	45,45	52,82	51,10	49,54	50,43	48,57	47,19	49,40	46,75	48,39	49,67
TiO₂	0,20	0,23	0,15	0,49	0,14	0,21	0,23	0,26	0,34	0,45	0,25	0,60	0,28	0,22
Al₂O₃	10,61	11,67	10,82	14,49	10,43	11,42	12,20	11,86	10,88	12,40	10,60	12,64	11,43	10,45
Cr₂O₃	0,05	0,02	0,00	0,10	0,06	0,00	0,00	0,00	0,01	0,01	0,04	0,00	0,03	0,02
FeO	9,02	9,97	10,07	10,29	9,28	9,70	9,72	9,39	12,55	12,21	11,19	12,52	11,49	11,54
MnO	0,08	0,09	0,05	0,09	0,11	0,07	0,05	0,00	0,07	0,04	0,03	0,05	0,00	0,06
MgO	14,04	13,55	13,52	12,62	13,88	13,53	13,37	14,13	12,82	12,02	13,23	11,70	12,85	13,15
CaO	6,64	7,69	6,96	9,46	6,51	6,96	7,77	7,58	7,86	7,98	7,72	8,26	7,83	7,66
Na₂O	4,43	4,17	4,46	3,76	4,39	4,45	4,11	4,07	3,56	3,78	3,80	3,81	3,96	3,66
K₂O	0,16	0,30	0,21	0,52	0,17	0,25	0,32	0,26	0,37	0,52	0,35	0,53	0,41	0,36
Sum	97,65	97,52	97,81	97,25	97,79	97,69	97,28	98,00	97,02	96,59	96,61	96,85	96,67	96,78
Structural formula based on average of all Fe as Fe²⁺ and sum cat - (Na+K+Ca) = 13														
Si	7,32	7,05	7,24	6,56	7,36	7,17	7,02	7,05	6,98	6,84	7,09	6,79	6,97	7,11
Ti	0,02	0,02	0,02	0,05	0,01	0,02	0,02	0,03	0,04	0,05	0,03	0,07	0,03	0,02
Al IV	0,68	0,95	0,76	1,44	0,64	0,83	0,98	0,95	1,02	1,16	0,91	1,21	1,03	0,89
Al VI	1,06	1,00	1,03	1,02	1,08	1,06	1,05	1,01	0,82	0,96	0,88	0,95	0,91	0,88
Fe³⁺	0,23	0,24	0,22	0,15	0,24	0,23	0,21	0,29	0,41	0,30	0,30	0,25	0,29	0,34
Fe²⁺	0,82	0,94	0,96	1,09	0,84	0,91	0,94	0,81	1,10	1,18	1,04	1,27	1,09	1,05
Mn	0,01	0,01	0,01	0,01	0,01	0,01	0,01	0,00	0,01	0,01	0,00	0,01	0,00	0,01
Mg	2,92	2,86	2,83	2,71	2,88	2,83	2,82	2,95	2,75	2,60	2,83	2,53	2,76	2,81
Ca	0,99	1,17	1,05	1,46	0,97	1,05	1,18	1,14	1,21	1,24	1,19	1,28	1,21	1,18
NaA	0,26	0,38	0,33	0,56	0,23	0,33	0,37	0,32	0,32	0,39	0,33	0,43	0,40	0,29
NaM4	0,94	0,77	0,89	0,49	0,96	0,89	0,76	0,78	0,67	0,67	0,73	0,64	0,71	0,73
K	0,03	0,05	0,04	0,10	0,03	0,04	0,06	0,05	0,07	0,10	0,06	0,10	0,07	0,07
Sum	15,29	15,43	15,36	15,65	15,26	15,37	15,43	15,37	15,39	15,48	15,39	15,53	15,48	15,35
Mg/Mg+Fe²⁺	0,78	0,75	0,75	0,71	0,77	0,76	0,75	0,78	0,71	0,69	0,73	0,67	0,72	0,73
Name	Brs	Brs	Brs	Mkt	Brs	Brs	Mkt	Mkt	Brs	Brs	Brs	Mkt	Brs	Brs

Brs = Barroisite, Mkt = Magnesio-katophorite

3.7 Secondary amphiboles

	SK-31			SK-28						SK-6		SK-9
Oxide Wt%												
SiO₂	49,20	40,06	52,74	38,64	45,11	39,70	42,04	46,98	52,69	44,52	46,14	40,58
TiO₂	0,20	0,18	0,30	0,20	0,34	0,19	0,26	0,27	0,15	0,11	0,36	0,40
Al₂O₃	8,52	20,34	4,78	19,24	10,59	13,52	11,29	10,69	3,78	11,53	10,79	16,45
Cr₂O₃	0,05	0,02	0,05	0,00	0,01	0,03	0,03	0,03	0,03	0,00	0,00	0,00
FeO	9,14	14,00	8,92	17,53	17,23	19,54	17,84	12,80	10,92	15,25	14,75	14,92
MnO	0,09	0,11	0,05	0,14	0,08	0,15	0,17	0,09	0,05	0,10	0,11	0,07
MgO	15,90	8,50	17,39	7,17	9,98	8,34	10,09	12,20	16,21	11,73	11,42	9,63
CaO	10,95	10,00	11,79	9,71	9,27	10,34	10,25	8,50	11,24	10,75	9,77	9,84
Na₂O	2,47	3,72	1,44	4,04	3,63	3,20	2,96	3,94	1,75	2,27	2,73	3,71
K₂O	0,30	0,89	0,17	0,32	0,30	1,45	1,15	0,43	0,28	0,65	0,73	0,76
Sum	96,82	97,83	97,64	97,00	96,54	95,00	96,07	95,92	97,09	96,91	96,80	96,36
Structural formula based on average of all Fe as Fe₂₊ and sum cat - (Na+K+Ca) = 13												
Si	7,07	5,90	7,47	5,82	6,77	6,11	6,43	6,92	7,58	6,59	6,81	6,09
Ti	0,02	0,02	0,03	0,02	0,04	0,02	0,03	0,03	0,02	0,01	0,04	0,05
Al IV	0,93	2,10	0,53	2,18	1,23	1,89	1,57	1,08	0,42	1,41	1,19	1,91
Al VI	0,51	1,42	0,27	1,23	0,64	0,56	0,47	0,77	0,22	0,61	0,69	1,00
Fe₃₊	0,17	0,16	0,12	0,36	0,27	0,59	0,39	0,23	0,11	0,37	0,26	0,27
Fe₂₊	0,93	1,56	0,93	1,85	1,89	1,92	1,90	1,34	1,21	1,51	1,56	1,60
Mn	0,01	0,01	0,01	0,02	0,01	0,02	0,02	0,01	0,01	0,01	0,01	0,01
Mg	3,41	1,87	3,67	1,61	2,23	1,91	2,30	2,68	3,47	2,59	2,51	2,15
Ca	1,69	1,58	1,79	1,57	1,49	1,70	1,68	1,34	1,73	1,71	1,54	1,58
NaA	0,42	0,69	0,22	0,83	0,62	0,68	0,66	0,53	0,25	0,46	0,40	0,74
NaM4	0,27	0,38	0,18	0,35	0,43	0,27	0,22	0,59	0,24	0,19	0,38	0,34
K	0,05	0,17	0,03	0,06	0,06	0,28	0,22	0,08	0,05	0,12	0,14	0,14
Sum	15,47	15,85	15,25	15,89	15,68	15,97	15,88	15,61	15,30	15,59	15,54	15,89
Mg/Mg+Fe₂₊	0,79	0,54	0,80	0,47	0,54	0,50	0,55	0,67	0,74	0,63	0,62	0,57
Name	Prg	Mhb	Fprg	Ed	Hst	Prg	Ed	Act		Ed	Ed	Prg
Facies	A	E	A	E	A	A	A	A-G		A	A	E

Facies: E = eclogite facies, A = amphibolite facies, C = Greenschist facies

Name: Prg = Pargasite, Mhb = Magnesio-hornblende, Fprg = Ferro-pargasite, Ed = Edenite, Hst = Hastingsite, Act = actinolite

	SK-29							SK-11	SK-20			SK-30
Oxide Wt%												
SiO₂	38,93	44,62	46,25	38,00	44,20	43,59	46,06	44,18	47,72	38,63	45,37	43,59
TiO₂	0,30	0,52	0,09	0,08	0,39	0,41	0,74	0,28	0,08	0,22	0,96	0,26
Al₂O₃	15,49	9,83	7,99	18,10	11,49	10,49	8,34	13,77	6,00	15,52	9,45	16,83
Cr₂O₃	0,00	0,00	0,03	0,00	0,00	0,02	0,00	0,01	0,00	0,00	0,04	0,01
FeO	20,59	18,25	18,16	20,11	18,50	19,15	17,52	14,18	17,52	21,19	18,48	11,89
MnO	0,09	0,14	0,15	0,11	0,11	0,15	0,19	0,02	0,21	0,17	0,15	0,07
MgO	6,71	10,00	11,03	6,25	9,24	9,21	11,15	10,54	12,06	6,18	9,59	10,92
CaO	10,04	10,02	10,16	10,54	9,70	10,43	9,80	8,75	11,57	10,86	9,49	9,11
Na₂O	3,57	2,82	2,55	3,49	3,08	3,06	2,76	3,83	1,59	3,03	2,92	4,12
K₂O	0,51	0,29	0,21	0,45	0,34	0,35	0,38	0,84	0,03	0,08	0,29	0,70
Sum	96,23	96,49	96,64	97,12	97,06	96,86	96,92	96,40	96,79	95,88	96,73	97,50
Structural formula based on average of all Fe as Fe²⁺ and sum cat - (Na+K+Ca) = 13												
Si	6,01	6,73	6,93	5,80	6,63	6,62	6,87	6,55	7,14	6,02	6,82	6,33
Ti	0,03	0,06	0,01	0,01	0,04	0,05	0,08	0,03	0,01	0,03	0,11	0,03
Al IV	1,99	1,27	1,07	2,20	1,37	1,38	1,13	1,45	0,86	1,98	1,18	1,67
Al VI	0,83	0,48	0,35	1,06	0,66	0,50	0,34	0,95	0,19	0,88	0,49	1,21
Fe₃₊	0,45	0,36	0,41	0,41	0,35	0,27	0,39	0,25	0,26	0,24	0,32	0,18
Fe₂₊	2,21	1,94	1,86	2,15	1,97	2,16	1,80	1,50	1,93	2,52	2,00	1,26
Mn	0,01	0,02	0,02	0,01	0,01	0,02	0,02	0,00	0,03	0,02	0,02	0,01
Mg	1,54	2,25	2,47	1,42	2,06	2,09	2,48	2,33	2,69	1,44	2,15	2,36
Ca	1,66	1,62	1,63	1,72	1,56	1,70	1,57	1,39	1,85	1,81	1,53	1,42
NaA	0,81	0,55	0,49	0,83	0,56	0,68	0,48	0,56	0,41	0,85	0,47	0,63
NaM4	0,26	0,28	0,25	0,21	0,34	0,22	0,32	0,54	0,05	0,07	0,38	0,53
K	0,10	0,05	0,04	0,09	0,07	0,07	0,07	0,16	0,00	0,02	0,06	0,13
Sum	15,91	15,60	15,53	15,91	15,62	15,74	15,55	15,72	15,43	15,87	15,53	15,76
Mg/Mg+Fe₂₊	0,41	0,54	0,57	0,40	0,51	0,49	0,58	0,61	0,58	0,36	0,52	0,65
Name	Prg	Ed	Mkp	Fprg	Ed	Fed	Mhs	Mkp	Mhb	Fts	Mhb	Mtm
Facies	A-G	E	A-G	A-G	A-G	E						

Facies: E = eclogite facies, A = amphibolite facies, C = Greenschist facies

Names: Prg = Pargasite, Mhb = Magnesio-hornblende, Fprg = Ferro-pargasite, Ed = Edeneite, Mhs = Magnesio-hastingsite

Mkp = Magnesio-katophorite, Fts = Ferro-tschermakite, Mtm = Magnesio-taramite

3.8 Micas

	SK-7	SK-31			SK-28				SK-8		SK-2		SK-3
Oxide Wt%	Ph	Pg	Pg	Ph	Ph	Ph	Bt	Bt	Ph	Ph	Ph	Ph	Bt
SiO ₂	50,59	47,95	47,13	50,27	50,16	50,09	36,43	35,74	48,84	50,77	49,12	51,22	37,27
TiO ₂	0,50	0,08	0,11	0,35	0,45	0,46	1,58	0,87	0,47	0,44	0,48	0,46	0,11
Al ₂ O ₃	26,15	40,73	40,24	28,55	25,94	25,90	16,97	17,63	27,36	26,74	27,66	27,29	25,66
Cr ₂ O ₃	0,02	0,05	0,04	0,24	0,00	0,05	0,00	0,00	0,00	0,00	0,01	0,01	0,03
FeO	3,22	0,46	0,58	1,91	3,29	3,43	15,54	15,55	3,42	3,23	3,08	3,11	8,82
MnO	0,00	0,00	0,00	0,00	0,00	0,00	0,12	0,05	0,00	0,03	0,01	0,00	0,03
MgO	4,08	0,17	0,19	3,48	3,76	3,67	13,03	13,27	3,70	3,98	3,76	3,81	0,05
CaO	0,00	0,34	0,24	0,00	0,00	0,00	0,00	0,00	0,00	0,01	0,03	0,00	22,96
Na ₂ O	0,33	7,31	7,06	0,75	0,31	0,41	0,10	0,10	0,30	0,26	0,46	0,31	0,01
K ₂ O	11,06	0,74	0,98	10,06	10,66	10,59	9,99	9,97	10,79	10,86	10,25	10,24	0,00
Sum	95,96	97,83	96,58	95,61	94,58	94,60	93,76	93,17	94,87	96,32	94,84	96,46	94,94
Structural formula based on 22 oxygens													
Si	3,39	2,99	2,98	3,34	3,40	3,40	2,78	2,74	3,31	3,38	3,31	3,38	2,69
Ti	0,03	0,00	0,01	0,02	0,02	0,02	0,09	0,05	0,02	0,02	0,02	0,02	0,01
Al	2,06	2,99	3,00	2,23	2,07	2,07	1,53	1,60	2,19	2,10	2,20	2,13	2,19
Cr	0,00	0,00	0,00	0,01	0,00	0,00	0,00	0,00	0,00	0,00	0,00	0,00	0,00
Fe(II)	0,18	0,02	0,03	0,11	0,19	0,19	0,99	1,00	0,19	0,18	0,17	0,17	0,53
Mn	0,00	0,00	0,00	0,00	0,00	0,00	0,01	0,00	0,00	0,00	0,00	0,00	0,00
Mg	0,41	0,02	0,02	0,34	0,38	0,37	1,48	1,52	0,37	0,39	0,38	0,38	0,01
Ca	0,00	0,02	0,02	0,00	0,00	0,00	0,00	0,00	0,00	0,00	0,00	0,00	1,78
Na	0,04	0,88	0,87	0,10	0,04	0,05	0,01	0,01	0,04	0,03	0,06	0,04	0,00
K	0,94	0,06	0,08	0,85	0,92	0,92	0,97	0,98	0,93	0,92	0,88	0,86	0,00
Sum	7,05	6,98	6,99	7,00	7,02	7,03	7,86	7,90	7,06	7,03	7,03	6,98	7,21
Mg/(Mg+Fe ²⁺)	0,69	0,40	0,37	0,76	0,67	0,66	0,60	0,60	0,66	0,69	0,69	0,69	0,01

Ph = phengite, Pg = Paragonite, Bt = biotite

Oxide Wt%	SK-11			SK-30			SK-4		
	Ph	Ph	Ph	Ph	Ph	Pg	Ph	Ph	Ph
SiO ₂	50,63	49,58	50,11	49,51	49,73	47,13	48,96	50,20	49,89
TiO ₂	0,47	0,50	0,46	0,41	0,30	0,10	0,50	0,38	0,38
Al ₂ O ₃	26,89	27,46	27,22	29,74	28,65	40,14	29,19	27,64	27,06
Cr ₂ O ₃	0,02	0,00	0,01	0,04	0,03	0,01	0,00	0,00	0,01
FeO	3,29	3,49	2,98	1,80	1,69	0,47	2,64	2,39	2,63
MnO	0,00	0,00	0,05	0,03	0,02	0,01	0,04	0,01	0,00
MgO	3,83	3,35	3,57	3,42	3,63	0,18	3,12	3,89	3,47
CaO	0,01	0,00	0,00	0,00	0,01	0,27	0,00	0,00	0,00
Na ₂ O	0,40	0,50	0,50	0,77	0,64	6,80	0,65	0,58	0,44
K ₂ O	10,00	10,36	10,49	9,91	10,34	1,03	10,35	10,38	10,56
Sum	95,54	95,24	95,37	95,65	95,03	96,14	95,43	95,47	94,44
Structural formula based on 22 oxygens									
Si	3,38	3,34	3,36	3,28	3,32	2,99	3,28	3,35	3,37
Ti	0,02	0,03	0,02	0,02	0,02	0,00	0,02	0,02	0,02
Al	2,12	2,18	2,15	2,32	2,26	3,00	2,30	2,17	2,16
Cr	0,00	0,00	0,00	0,00	0,00	0,00	0,00	0,00	0,00
Fe(II)	0,18	0,20	0,17	0,10	0,09	0,03	0,15	0,13	0,15
Mn	0,00	0,00	0,00	0,00	0,00	0,00	0,00	0,00	0,00
Mg	0,38	0,34	0,36	0,34	0,36	0,02	0,31	0,39	0,35
Ca	0,00	0,00	0,00	0,00	0,00	0,02	0,00	0,00	0,00
Na	0,05	0,06	0,06	0,10	0,08	0,83	0,08	0,08	0,06
K	0,85	0,89	0,90	0,84	0,88	0,08	0,88	0,88	0,91
Sum	6,99	7,03	7,02	7,00	7,02	6,97	7,03	7,02	7,01
Mg/(Mg+Fe ²⁺)	0,67	0,63	0,68	0,77	0,79	0,41	0,68	0,74	0,70

Ph = phengite, Pg = Paragonite

3.9 Clinzoisites

	SK-31			SK-28		SK-29	SK-6		
Oxide Wt%									
SiO ₂	38,57	38,70	37,69	37,96	37,52	37,24	37,90	37,83	38,14
TiO ₂	0,10	0,08	0,09	0,14	0,07	0,12	0,07	0,04	0,11
Al ₂ O ₃	28,28	28,78	26,61	24,86	23,45	23,14	25,07	25,48	25,03
Cr ₂ O ₃	0,07	0,02	0,11	0,04	0,00	0,00	0,00	0,00	0,01
FeO	5,92	5,90	6,90	10,94	12,06	12,50	10,42	9,86	9,82
MnO	0,02	0,05	0,02	0,01	0,12	0,12	0,03	0,03	0,03
MgO	0,05	0,01	0,40	0,05	0,00	0,00	0,03	0,01	0,09
CaO	23,95	24,47	21,89	23,24	23,80	23,56	22,65	23,80	22,68
Na ₂ O	0,00	0,00	0,03	0,02	0,01	0,00	0,00	0,02	0,01
K ₂ O	0,00	0,00	0,00	0,00	0,00	0,01	0,00	0,00	0,00
Sum	96,95	98,01	93,74	97,25	97,01	96,69	96,17	97,08	95,92
Strutural formula based on 12,5 oxygens and 8 cations									
Si	2,99	2,97	3,01	2,96	2,95	2,94	2,98	2,95	3,00
Ti	0,01	0,00	0,01	0,01	0,00	0,01	0,00	0,00	0,01
Al	2,58	2,60	2,51	2,28	2,17	2,15	2,32	2,34	2,32
Fe(III)	0,43	0,42	0,51	0,79	0,88	0,92	0,76	0,72	0,72
Mn	0,00	0,00	0,00	0,00	0,01	0,01	0,00	0,00	0,00
Mg	0,01	0,00	0,05	0,01	0,00	0,00	0,00	0,00	0,01
Ca	1,99	2,01	1,87	1,94	2,00	1,99	1,91	1,99	1,91
Sum	8,00	8,01	7,96	7,99	8,02	8,02	7,98	8,01	7,97
Pistacite	0,14	0,14	0,17	0,26	0,29	0,30	0,25	0,23	0,24

Pistacite = Fe(III)/ (Fe(III) + Al)

	SK-8			SK-2	SK-30		SK-4		
Oxide Wt%									
SiO ₂	37,92	37,96	38,09	37,65	38,50	38,76	38,16	38,05	37,65
TiO ₂	0,13	0,12	0,09	0,11	0,06	0,05	0,11	0,14	0,08
Al ₂ O ₃	25,53	24,88	24,88	25,41	27,42	28,12	27,17	26,19	25,77
Cr ₂ O ₃	0,01	0,03	0,01	0,00	0,01	0,00	0,01	0,00	0,03
FeO	9,44	10,27	9,74	9,32	6,90	6,46	6,97	8,44	8,64
MnO	0,00	0,00	0,03	0,01	0,00	0,00	0,00	0,01	0,03
MgO	0,08	0,02	0,05	0,08	0,09	0,12	0,05	0,06	0,11
CaO	22,97	23,21	23,43	22,78	23,52	23,97	23,69	23,33	23,22
Na ₂ O	0,01	0,00	0,01	0,00	0,01	0,01	0,02	0,02	0,02
K ₂ O	0,00	0,00	0,00	0,00	0,01	0,02	0,01	0,01	0,00
Sum	96,09	96,49	96,32	95,36	96,50	97,51	96,19	96,24	95,55
Strutural formula based on 12,5 oxygens and 8 cations									
Si	2,98	2,98	2,99	2,98	3,00	2,99	2,99	2,98	2,98
Ti	0,01	0,01	0,01	0,01	0,00	0,01	0,01	0,01	0,00
Al	2,36	2,30	2,30	2,37	2,52	2,55	2,51	2,42	2,40
Fe(III)	0,69	0,75	0,71	0,69	0,50	0,46	0,51	0,62	0,63
Mn	0,00	0,00	0,00	0,00	0,00	0,00	0,00	0,00	0,00
Mg	0,01	0,00	0,01	0,01	0,01	0,01	0,01	0,01	0,01
Ca	1,93	1,95	1,97	1,93	1,96	1,98	1,99	1,96	1,97
Sum	7,98	7,99	7,99	7,99	7,99	8,00	8,00	7,99	8,00
Pistacite	0,23	0,25	0,24	0,22	0,17	0,15	0,17	0,20	0,21

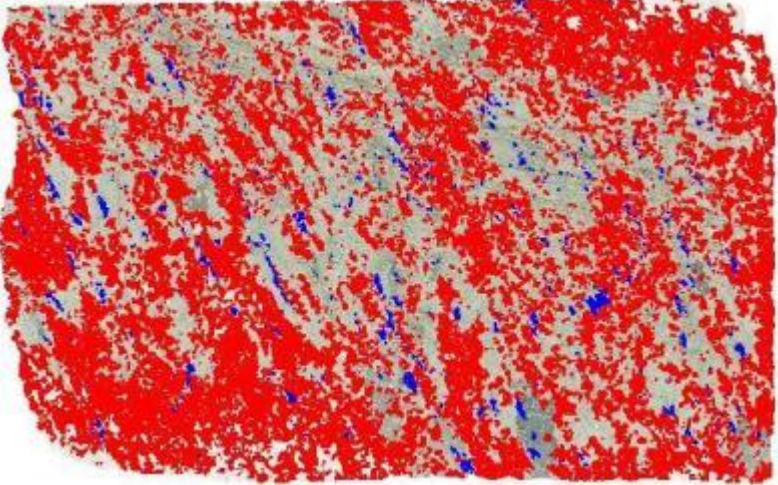
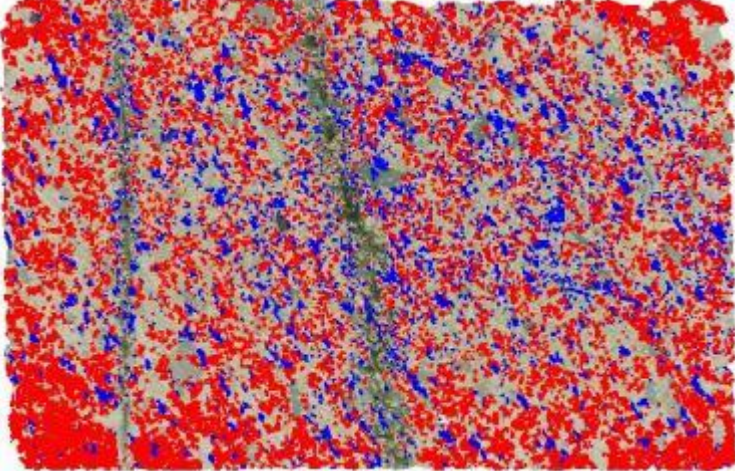
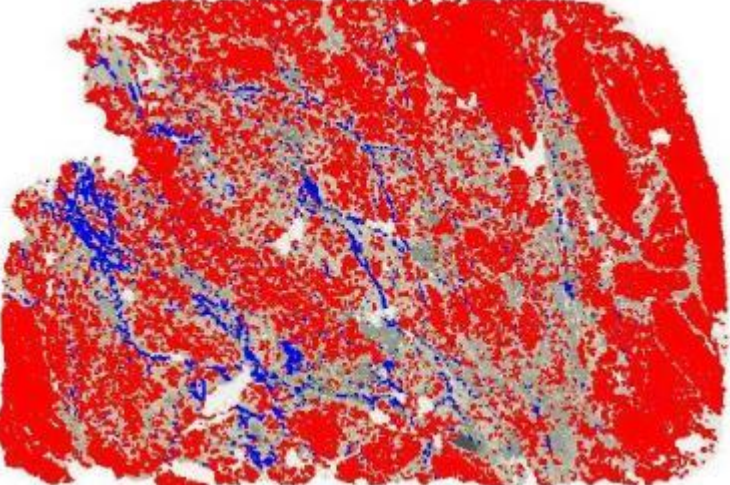
Pistacite = Fe(III)/ (Fe(III) + Al)

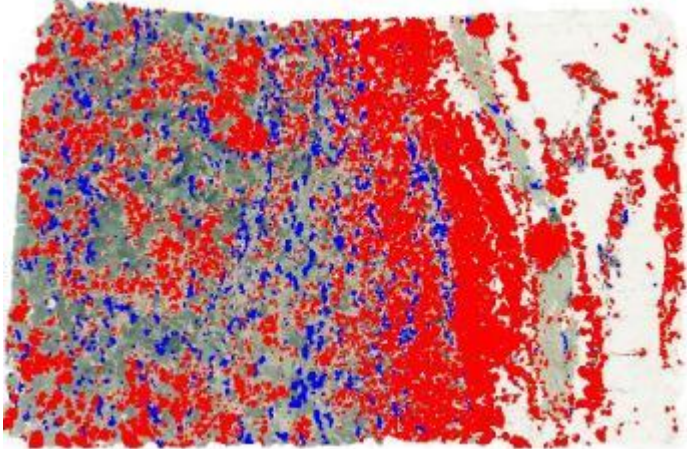
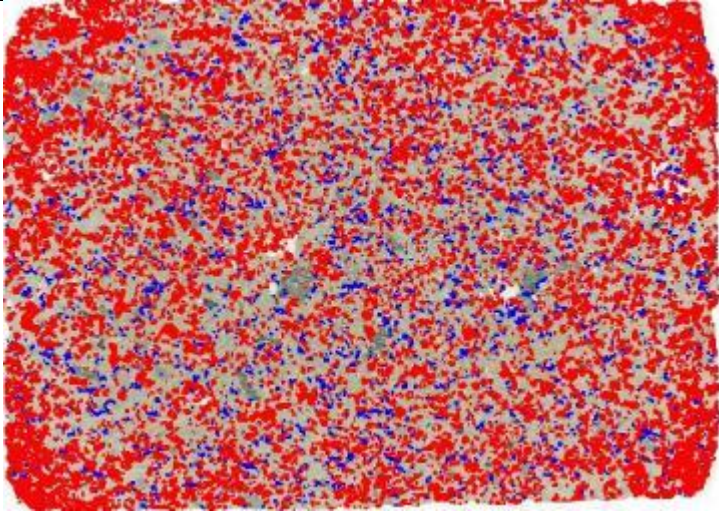
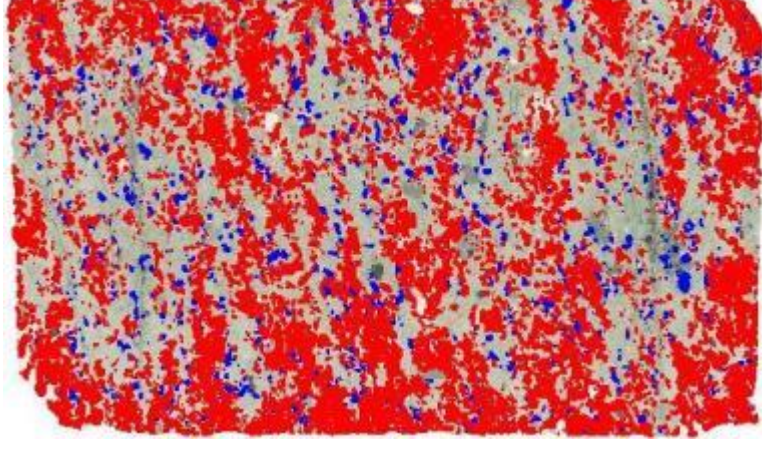
3.10 Feldspars

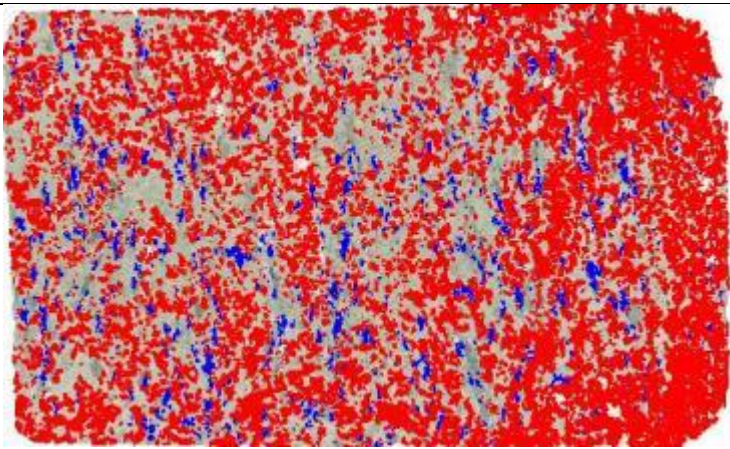
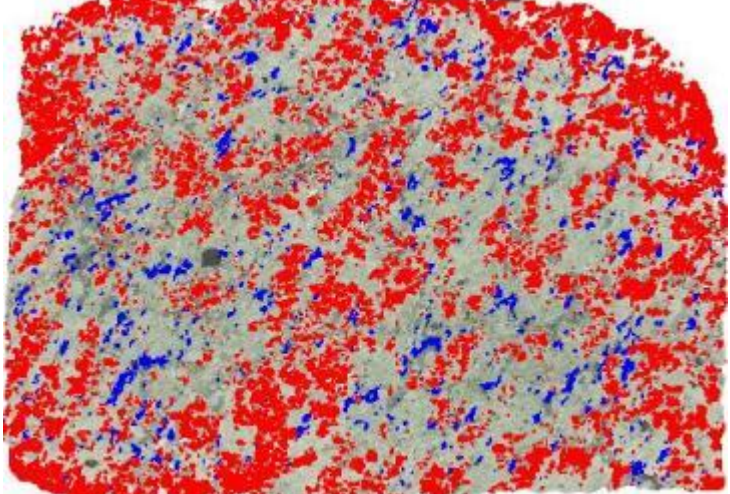
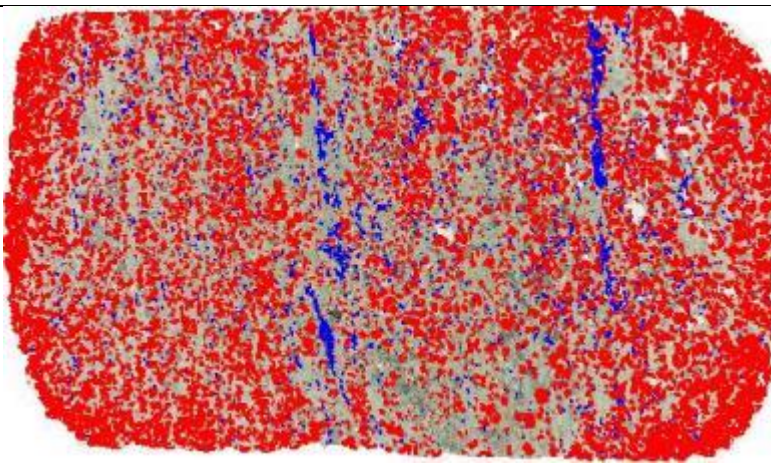
Oxide Wt%	SK-28				SK-31	
SiO ₂	63,82	63,67	67,18	67,76	69,05	69,12
TiO ₂	0,02	0,00	0,00	0,02	0,00	0,00
Al ₂ O ₃	22,43	22,53	20,68	20,38	19,63	19,75
Cr ₂ O ₃	0,01	0,01	0,00	0,00	0,02	0,00
FeO	0,23	0,21	0,08	0,08	0,26	0,27
MnO	0,02	0,03	0,00	0,00	0,00	0,02
MgO	0,00	0,00	0,00	0,00	0,00	0,00
CaO	3,60	3,85	1,49	0,95	0,20	0,30
Na ₂ O	9,76	9,78	10,50	11,19	12,07	12,01
K ₂ O	0,11	0,10	0,07	0,13	0,05	0,04
Sum	99,99	100,17	100,00	100,52	101,27	101,52
Structural formula based on 5 cations and 8 oxygens						
Si	2,81	2,80	2,96	2,95	2,97	2,97
Ti	0,00	0,00	0,00	0,00	0,00	0,00
Al	1,17	1,17	1,07	1,05	1,00	1,00
Fe(III)	0,01	0,01	0,00	0,00	0,01	0,01
Cr	0,00	0,00	0,00	0,00	0,00	0,00
Fe(II)	0,00	0,00	0,00	0,00	0,00	0,00
Mn	0,00	0,00	0,00	0,00	0,00	0,00
Mg	0,00	0,00	0,00	0,00	0,00	0,00
Ca	0,17	0,18	0,07	0,04	0,01	0,01
Na	0,83	0,83	0,90	0,95	1,01	1,00
K	0,01	0,01	0,00	0,01	0,00	0,00
Sum	5,00	5,00	5,00	5,00	5,00	5,00
End members						
Anorthite	16,8	17,8	7,3	4,5	0,9	1,4
Albite	82,6	81,7	92,3	94,8	98,9	98,4
Orthoclase	0,6	0,5	0,4	0,7	0,3	0,2

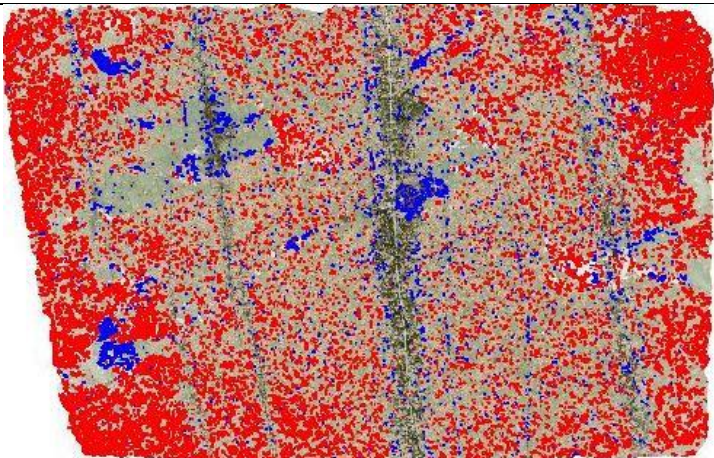
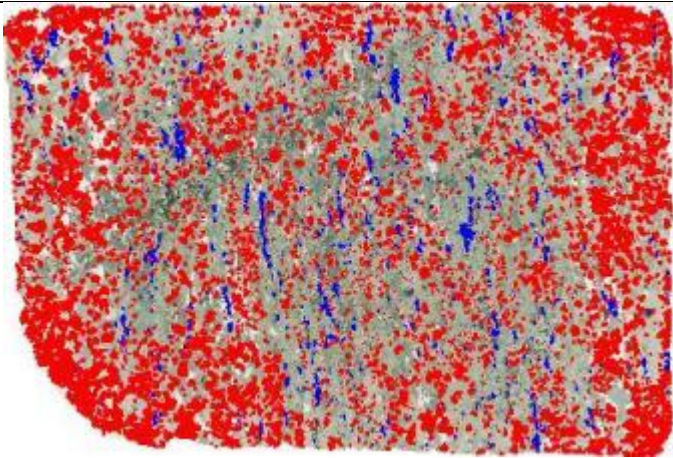
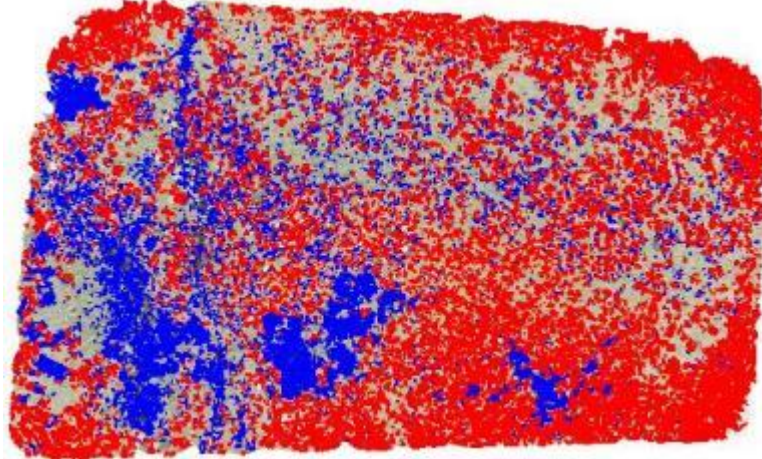
Appendix 4 – Results from image processing in MATLAB

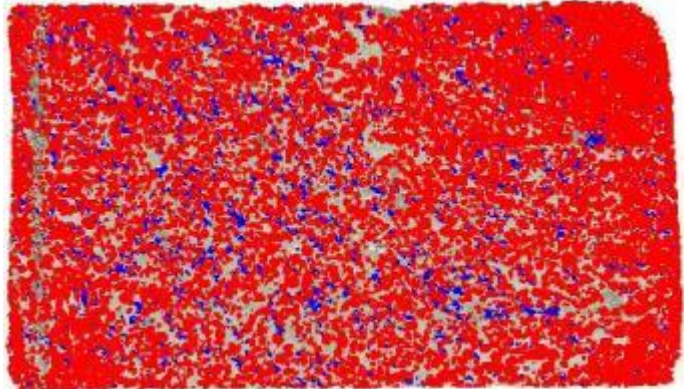
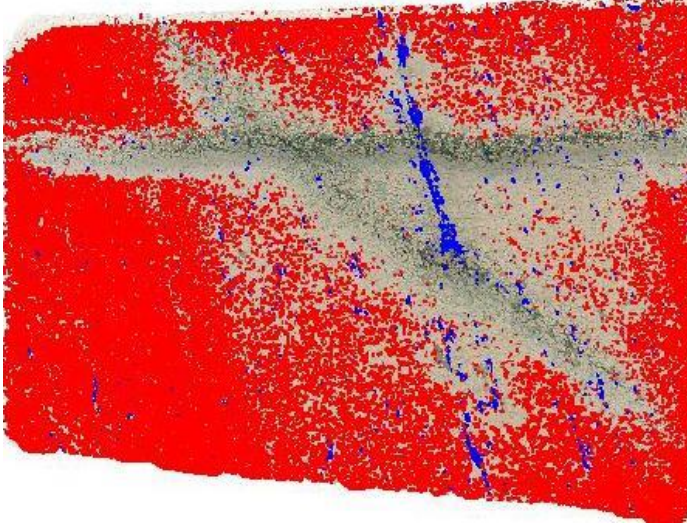
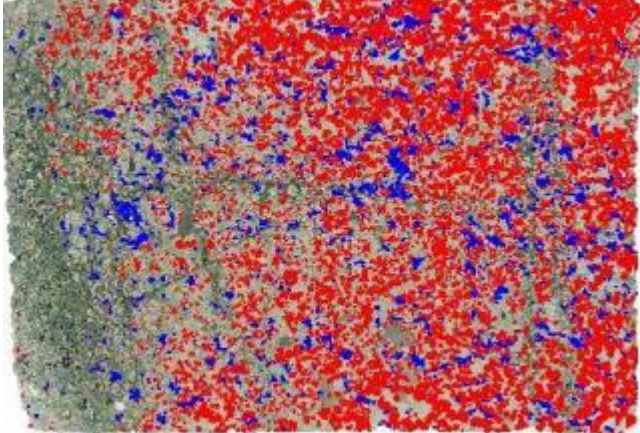
4.1 Modal percentages of rutile and garnet

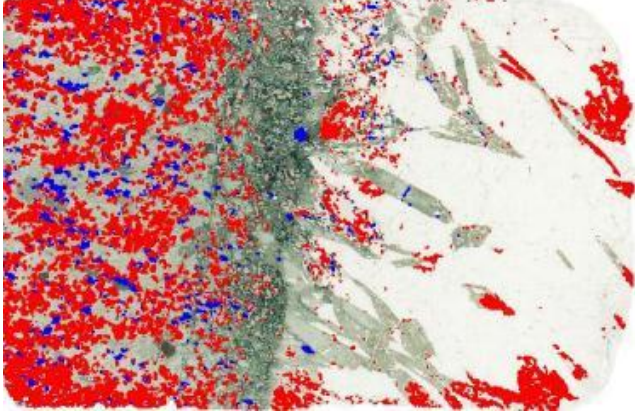
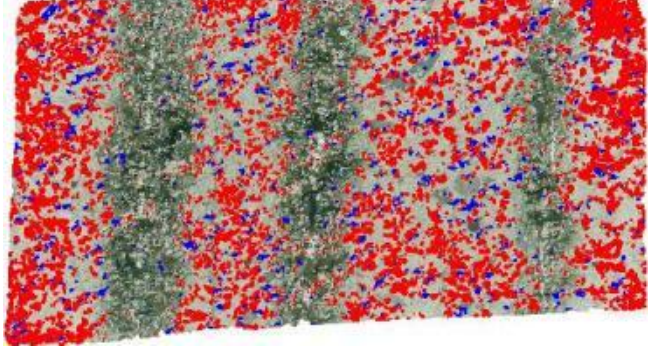
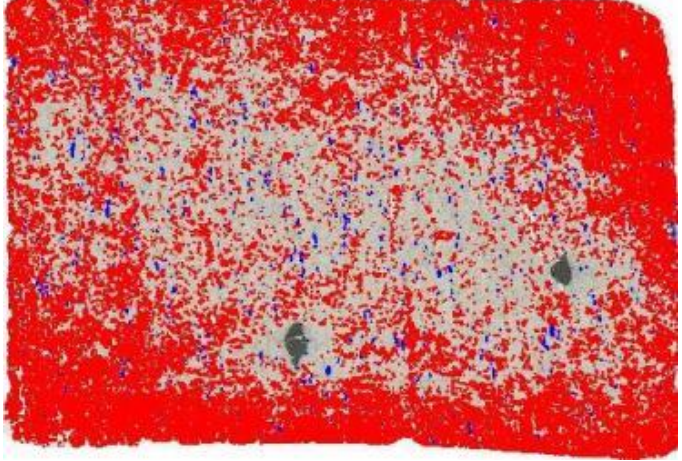
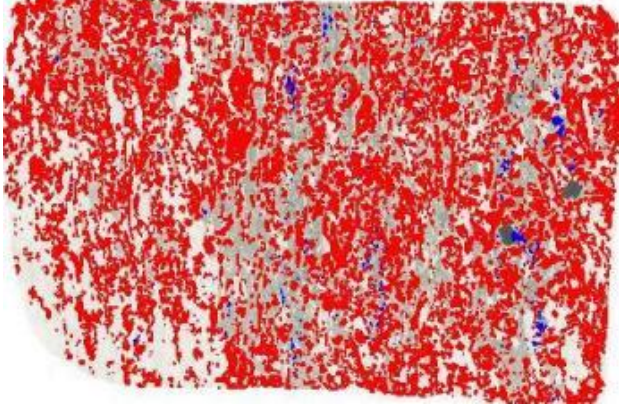
Sample	Rutile	Garnet	Processed image. Rutile: Blue. Garnet: Red.
SK-2	1,40	48,08	
Sk-3	6,63	39,52	
SK-4	2,20	45,83	

Sample	% Rutile	%Garnet	Processed image. Rutile: Blue. Garnet: Red.
SK-6	3,46	33,59	
SK-7	3,40	44,08	
SK-8	3,64	49,82	

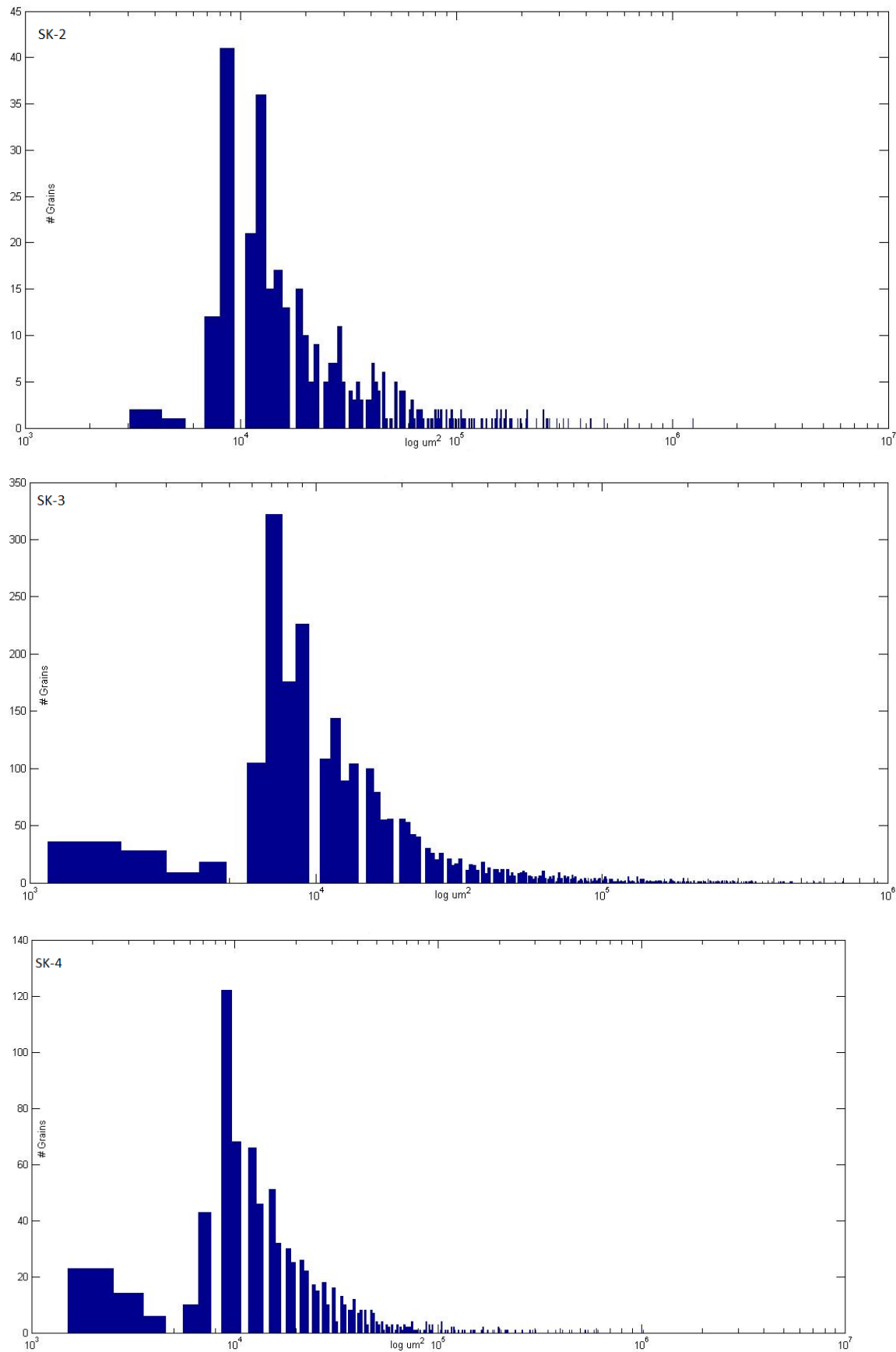
Sample	% Rutile	%Garnet	Processed image. Rutile: Blue. Garnet: Red.
SK-9	2,93	50,71	
SK-11	2,78	30,06	
SK-12	2,75	37,11	

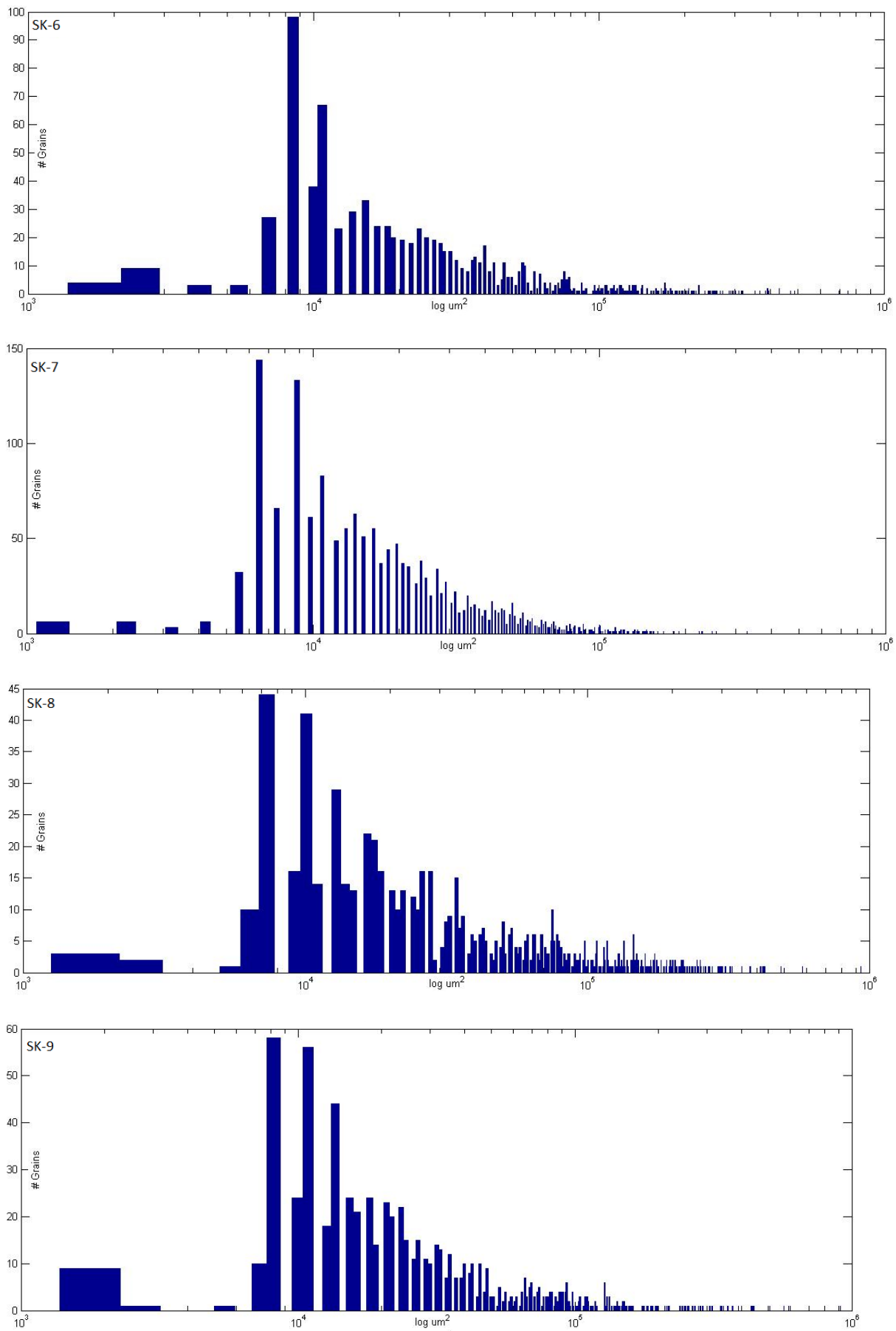
Sample	% Rutile	%Garnet	Processed image. Rutile: Blue. Garnet: Red.
SK-13	2,95	35,83	
SK-15	1,80	27,40	
SK-16	13,58	38,58	

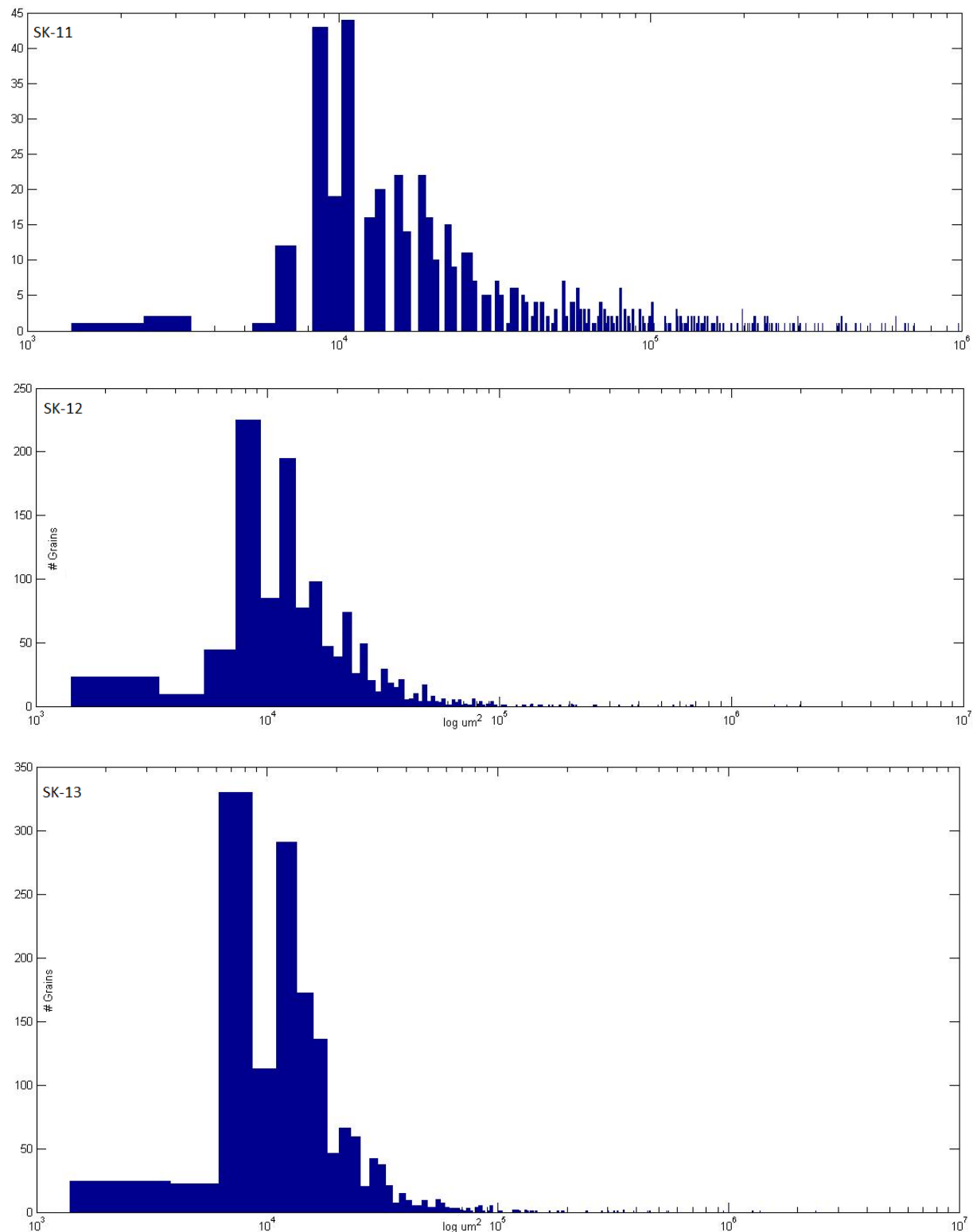
Sample	% Rutile	%Garnet	Processed image. Rutile: Blue. Garnet: Red.
SK-19	3,67	60,68	
SK-20	1,12	60,74	
SK-27	4,52	30,88	

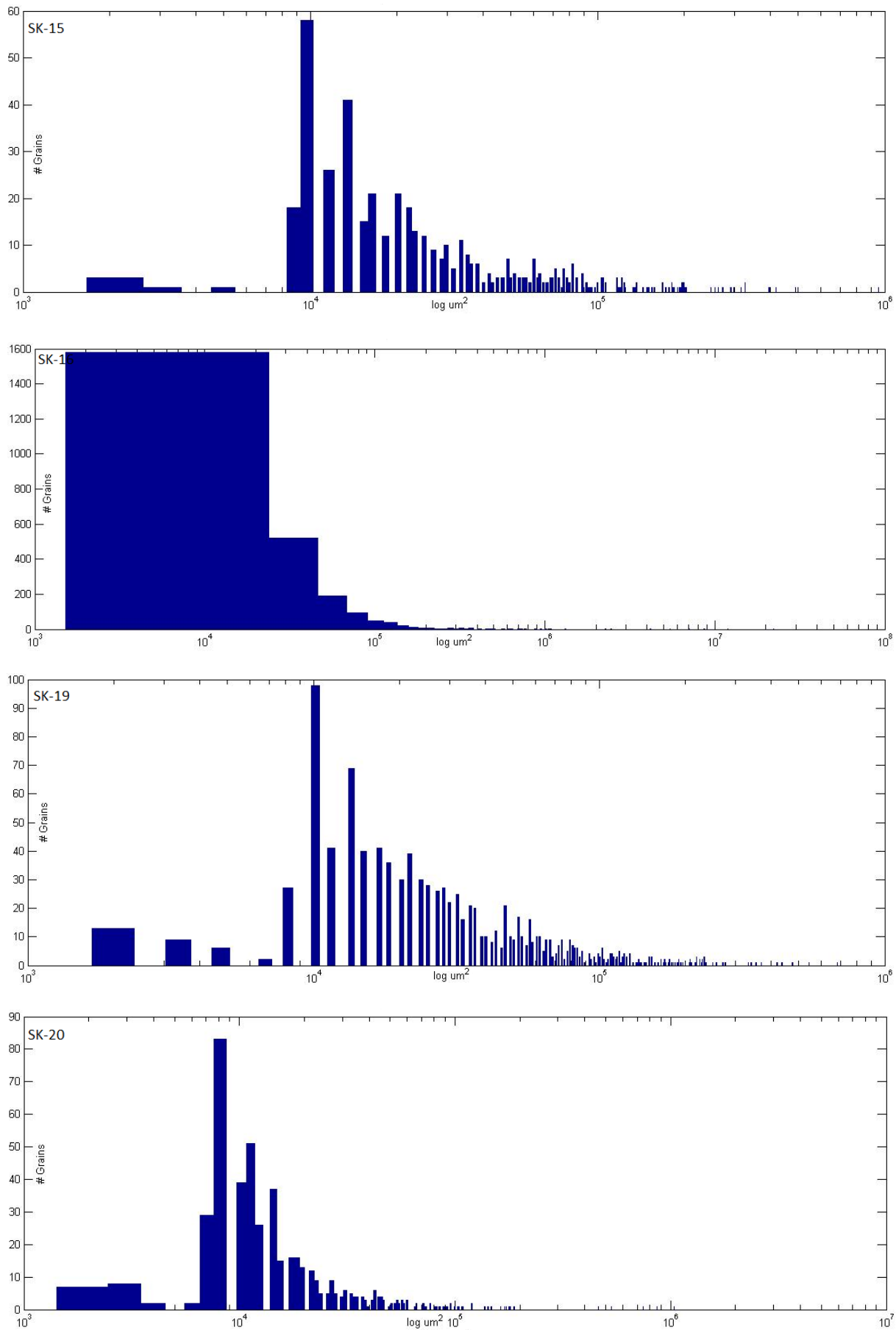
Sample	% Rutile	%Garnet	Processed image. Rutile: Blue. Garnet: Red.
SK-28	1,71	19,97	
SK-29	1,99	26,76	
SK-30	0,89	72,53	
SK-31	0,47	18,78	

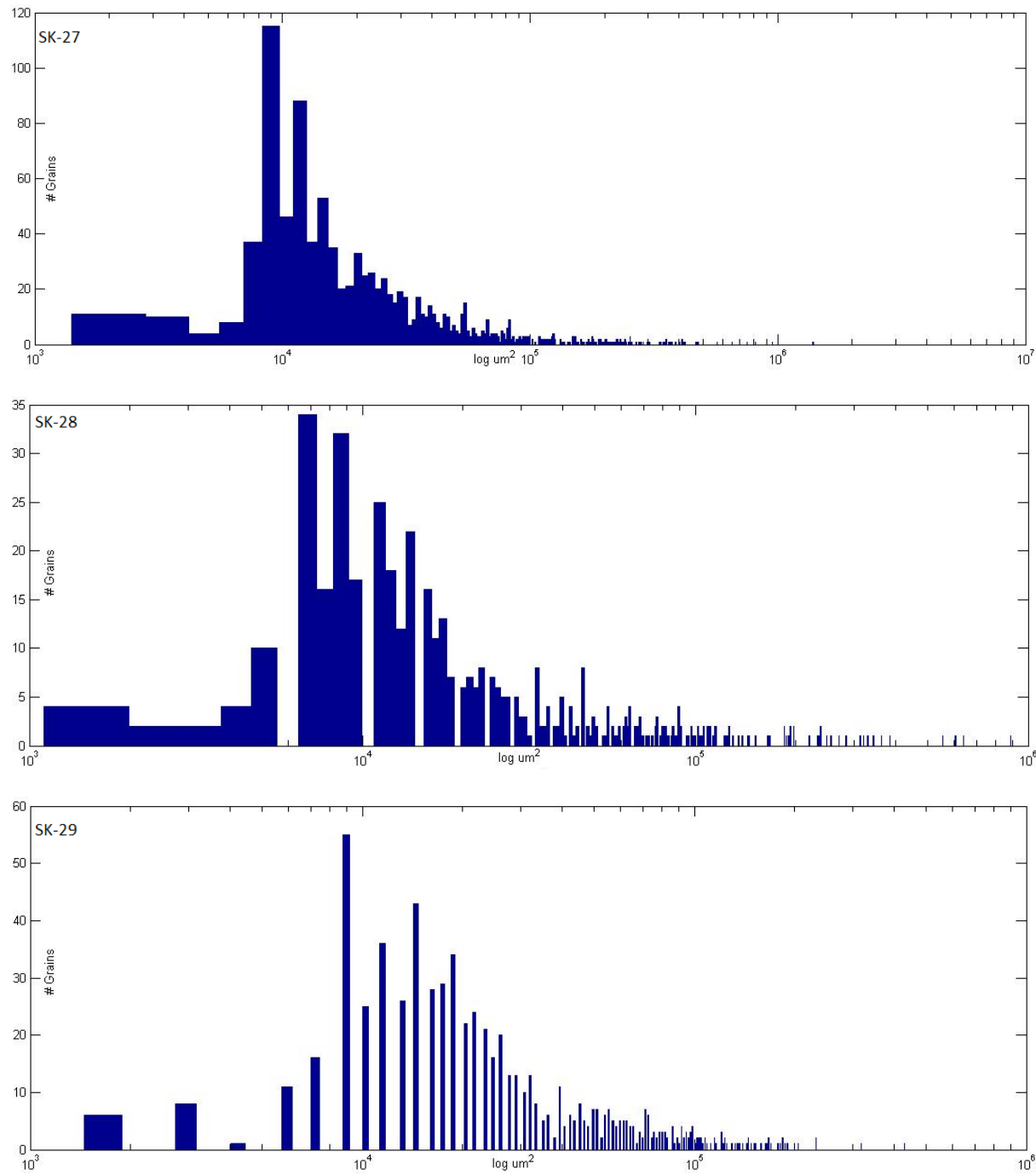
4.2 Rutile grain size distribution

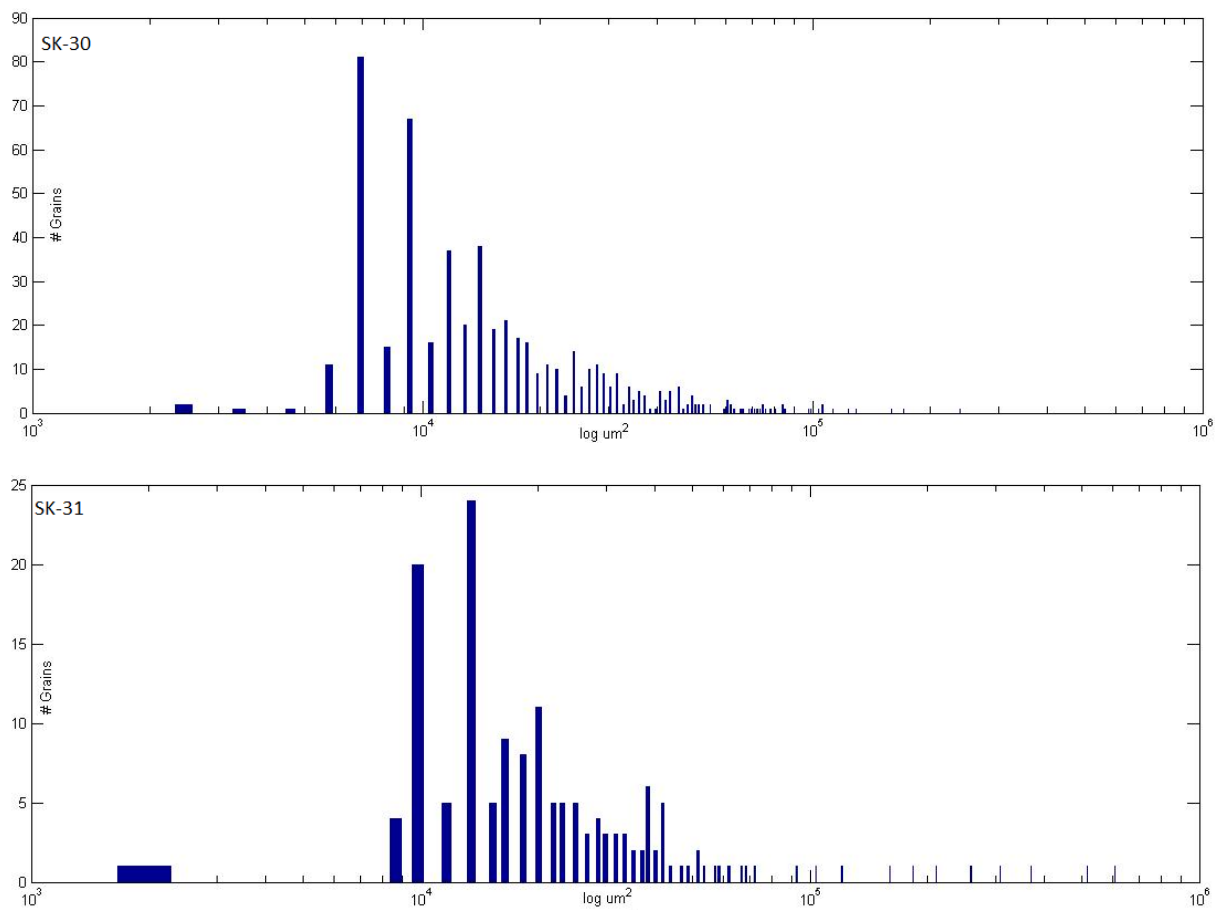












Appendix 5 – Structural formula recalculations

5.1 Preparation of analyses for recalculation

The EMP analyses were sorted into different spread sheets for different minerals. The coordinates and total values were then deleted before copied into a notebook file where the “,” used in Excel were replaced with “.” used in Matlab.

5.2 Recalculation structural formula

The notebook files (.txt) were loaded into the Matlab programs written for the different minerals (Appendix 6). These programs contain information about oxide weights, number of cations in oxide, number of oxygens in oxide, the charge on the cations, and the ideal number of cations and oxygens in structural formula. Table 19 gives the number of ideal cations and oxygens for the different minerals recalculated.

Table 19 - Ideal cations and oxygens used for mineral fomulae recalculations.

Mineral	Ideal Cations	Ideal oxygens
Garnet	8	12
Feldspar	5	8
Mica	-	15
Clinopyroxene	4	6
Amphibole	-	23
Clinozoisite	-	12,5

The mineral recalculation programs are written after Brady *et al.* (2012). The minerals are recalculated by calculating the moles of cations and oxygens, and then normalizing them to the pre-defined ideal number of cations and oxygens. For most of the minerals recalculated, Fe is differentiated into Fe^{2+} and Fe^{3+} . This is done by converting some of the Fe^{2+} to Fe^{3+} based on charge balance. The program checks if the total charge of the cations is equal to the total charge of the oxygens. Since there typically is some Fe^{3+} in a mineral structure, assuming all Fe to be Fe^{2+} will result in a lower charge than in reality. The difference in calculated charge and ideal charge (from the ideal number of oxygens) will be equalized by converting Fe^{2+} to Fe^{3+} , and hence gain one extra charge per conversion.

5.3 Calculating end-members

For triangular plots or for a better view on the mineral chemistry, end-members on the different mineral groups were calculated for garnet, pyroxene, clinozoisite and feldspar. The procedures used for calculating end-members for these minerals are presented in table 20.

Table 20 - Criteria used for end-member calculations.

Garnet	
Almandine	Fe(2+) / Ca + Fe(2+) + Mn + Mg
Pyrope	Mg / Ca + Fe(2+) + Mn + Mg
Grossular	(Ca / Ca + Fe(2+) + Mn + Mg) * (Al / Al + Cr + Ti + Fe(3+))
Spessartine	Mn / Ca + Fe(2+) + Mn + Mg
Uvarovite	(Ca / Ca + Fe(2+) + Mn + Mg) * (Cr / Al + Cr + Ti + Fe(3+))
Andradite	(Ca / Ca + Fe(2+) + Mn + Mg) * (Fe(3+) / Al + Cr + Ti + Fe(3+))
Ca-Ti Garnet	(Ca / Ca + Fe(2+) + Mn + Mg) * (Ti / Al + Cr + Ti + Fe(3+))
Clinopyroxene	
Jadeite	Na-Fe(3+) / Na + Fe(2+) + Mg
Aegerine	Fe(3+) / Na + Fe(2+) + Mg
Diopside+ Hedenbergite	Fe(2+) + Mg / Na + Fe(2+) + Mg
Feldspar	
Anorthite	Ca / Na + K + Ca
Albite	Na / Na + K + Ca
Orthoclase	K / Na + K + Ca
Clinozoisite	
Pistacite	Fe (3+) / (Fe(3+) + Al)

5.4 Calculating amphiboles

Since amphiboles show a wide range in cation distribution, finding the right configuration requires additional processing of the recalculated structural formula. In the Matlab program all amphiboles were calculated with all the Fe as Fe²⁺. An Excel spread sheet was made for finding the most precise structural formula. The spread sheet made for this thesis is a modification of one received from Muriel Erambert, and is found in figure 98. The only input required is the recalculated structural formula where all Fe is calculated as Fe²⁺.

The values are copied into the spread sheet in the column marked by “All Fe as Fe2+”. If the cation sums to between 15 and 16, it is marked with OK. Below, the Fe³⁺ is calculated from charge balance, as described in the section above. If this Fe³⁺ is ≥ 0.00 , it is marked with OK. The amount of Fe³⁺ is subtracted from the amount of Fe² in the analysis. If the recalculated amount of Fe²⁺ is ≥ 0.00 , it is marked with OK. Further down, the Al in the tetrahedral position is calculated by subtracting the amount of Si from 8. The rest of the Al goes into octahedral position. 15 cations and the amount of K are subtracted from the total of cations, and gives Na in A position. If this is a positive number less than 1, it is marked with OK. If there is more Na left, this goes into M4 position together with Ca. If this sum is between 0 and 2, it is marked with OK. All other cations go into octahedral and tetrahedral sites. If the sum of these cations is between 13 and 15, it is marked with OK. In order to have a valid amphibole, all points mentioned above needs to be marked with OK, and all statements are summed up in the top of the spread sheet.

This process is done for several predefined scenarios for cation distribution in the amphiboles. The different scenarios are: The sum of the cations = 16, the sum of the cations except Na and K = 15, the sum of the cations except Na, K and Ca = 13, the sum of the cations except K = 15, The sum of Si + Al = 8 (all Al in tetrahedral site), the sum of Si = 8 (only Si in tetrahedral site) and All Fe as Fe^{3+} . The structural formula is recalculated for every of these scenarios.

Final Check (6 x OK is required)	OK	OK	OK	OK	OK	Not OK	Not OK	OK
	OK	OK	OK	OK	Not OK	Not OK	OK	OK
	OK	OK	OK	OK	Not OK	Not OK	Not OK	Not OK
	OK	OK	OK	OK	Not OK	Not OK	Not OK	Not OK
	OK	Not OK	Not OK	OK	OK	OK	Not OK	OK
	OK	OK	OK	OK	Not OK	Not OK	OK	OK
<hr/>								
All Fe as		Sum	Sum Cat	Sum Cat	Sum Cat	Sum	Sum	All Fe as
Fe2+		Cat = 16	- (Na+K) = 15	(Na+K+Ca) = 13	-K = 15	Si+Al = 8	Si = 8	Fe3+
Element	100%	1,007	0,992	0,958	0,916	1,248	0,961	
Si	6,40889	6,504	6,454	6,359	6,142	5,868	8,000	6,160
Na	0,75599	0,767	0,761	0,750	0,724	0,692	0,944	0,727
Al	2,32887	2,363	2,345	2,311	2,232	2,132	2,907	2,238
K	0,11349	0,115	0,114	0,113	0,109	0,104	0,142	0,109
Ca	1,79318	1,820	1,806	1,779	1,718	1,642	2,238	1,723
Fe	1,86231	1,890	1,875	1,848	1,785	1,705	2,325	1,790
Mn	0,0061	0,006	0,006	0,006	0,006	0,006	0,008	0,006
Ti	0,09578	0,097	0,096	0,095	0,092	0,088	0,120	0,092
Mg	2,40103	2,437	2,418	2,382	2,301	2,198	2,997	2,308
Sum cat = [15,16]	15,766	16,000	15,876	15,642	15,109	14,434	19,680	15,152
Check	OK	OK	OK	OK	OK	Not OK	Not OK	OK
<hr/>								
Fe3+	0,000	-0,684	-0,321	0,361	1,917	3,884	-11,420	1,790
Check	OK	Not OK	Not OK	OK	OK	OK	Not OK	OK
Fe2+	1,862	2,574	2,196	1,486	-0,132	-2,179	13,745	0
Check	OK	OK	OK	OK	Not OK	Not OK	OK	OK
Al (C.N=8)	1,591	1,496	1,546	1,641	1,858	2,132	0,000	1,840
Al (C.N=6)	0,738	0,868	0,799	0,669	0,374	0,000	2,907	0,398
Mg/Fe2+	0,563	0,486	0,524	0,616	1,061	113,167	0,179	
NaA ≤ 1	0,652	0,767	0,761	0,529	0,000	-0,669	0,944	0,043
Check	OK	OK	OK	OK	Not OK	Not OK	OK	OK
NaM4≤2	0,104	0,000	0,000	0,221	0,724	1,362	0,000	0,683
Ca,NaM4≤2	1,897	1,820	1,806	2,000	2,443	3,003	2,238	2,407
Check	OK	OK	OK	OK	Not OK	Not OK	Not OK	Not OK
Si+Al ≥ 8	8,738	8,868	8,799	8,669	8,374	8,000	10,907	8,398
Sum FM = [13,15]	13,103	13,298	13,194	13,000	12,557	11,997	16,356	12,593
Check	OK	OK	OK	OK	Not OK	Not OK	Not OK	Not OK

Figure 98 - Spread sheet for determining cation positions in amphiboles.

When an analysis is copied into this spread sheet, and only one configuration is correct, this one is used as the final amphibole structural formula. If more than one is correct, as is the case in figure 98, the average of these are used to produce the most correct structural formula.

Appendix 6 – Matlab scripts written for this thesis

- 6.1 – Rutile and Garnet detection
- 6.2 – Structural formula recalculation of garnet
- 6.3 – Structural formula recalculation of feldspar
- 6.4 – Structural formula recalculation of mica.
- 6.5 – Structural formula recalculation of clinopyroxene
- 6.6 – Structural formula recalculation of amphibole
- 6.7 – Structural formula recalculation of epidote

6.1 Rutile and Garnet detection

```
%Loading the bright rutile standard and defying the min and max values.  
Ib=imread('C:\Users\Stubbebryter\Desktop\Masteroppgave\Matlab\bright rutile.png');  
Rb_min = min(min(Ib(:,:,1)));  
Rb_max = max(max(Ib(:,:,1)));  
Gb_min = min(min(Ib(:,:,2)));  
Gb_max = max(max(Ib(:,:,2)));  
Bb_min = min(min(Ib(:,:,3)));  
Bb_max = max(max(Ib(:,:,3)));  
  
%Loading the dark rutile standard and defying the min and max values.  
Id = imread('C:\Users\Stubbebryter\Desktop\Masteroppgave\Matlab\dark rutile.png');  
Rd_min = min(min(Id(:,:,1)));  
Rd_max = max(max(Id(:,:,1)));  
Gd_min = min(min(Id(:,:,2)));  
Gd_max = max(max(Id(:,:,2)));  
Bd_min = min(min(Id(:,:,3)));  
Bd_max = max(max(Id(:,:,3)));  
  
%Loading the pink rutile standard and defying the min and max values.  
Ip = imread('C:\Users\Stubbebryter\Desktop\Masteroppgave\Matlab\pink rutile.png');  
Rp_min = min(min(Ip(:,:,1)));  
Rp_max = max(max(Ip(:,:,1)));  
Gp_min = min(min(Ip(:,:,2)));  
Gp_max = max(max(Ip(:,:,2)));  
Bp_min = min(min(Ip(:,:,3)));  
Bp_max = max(max(Ip(:,:,3)));  
  
%Loading the garnet standard and defying the min and max values.  
Ib=imread('C:\Users\Stubbebryter\Desktop\Masteroppgave\Matlab\garnet.png');  
Rg_min = min(min(Ib(:,:,1)));  
Rg_max = max(max(Ib(:,:,1)));  
Gg_min = min(min(Ib(:,:,2)));  
Gg_max = max(max(Ib(:,:,2)));  
Bg_min = min(min(Ib(:,:,3)));  
Bg_max = max(max(Ib(:,:,3)));  
  
%Loading the thin section scan, and scan through it to find the pixels that %coincides with the either of the three rutile standards.  
Im = imread('C:\Users\Stubbebryter\Desktop\Masteroppgave\Egne tynnslip\Tilkutta for matlab\SK-7.png');  
no_pixels = size(Im,1)*size(Im, 2);  
RUTILE= ...  
    Im(:,:,1)>Rp_min & Im(:,:,1)<Rp_max & Im(:,:,2)>Gp_min & Im(:,:,2)<Gp_max & Im(:,:,3)>Bp_min & Im(:,:,3)<Bp_max | ...  
    Im(:,:,1)>Rb_min & Im(:,:,1)<Rb_max & Im(:,:,2)>Gb_min & Im(:,:,2)<Gb_max & Im(:,:,3)>Bb_min & Im(:,:,3)<Bb_max | ...  
    Im(:,:,1)>Rd_min & Im(:,:,1)<Rd_max & Im(:,:,2)>Gd_min & Im(:,:,2)<Gd_max & Im(:,:,3)>Bd_min & Im(:,:,3)<Bd_max;  
  
% Processing the image with different operations.  
RUTIL2 = bwmorph(RUTILE,'clean');  
RUTIL3 = bwmorph(RUTIL2,'hbreak');
```

```

RUTIL4 = bwmorph(RUTIL3,'majority');
RUTIL5 = bwmorph(RUTIL4,'spur');
RUTIL7 = bwareaopen(RUTIL5,5);
[L,numR] = bwlabel(RUTIL7,4);

Scan through the image and find all pixels that coincides with the garnet standard.
GARNET = Im(:,:,1)>Rg_min & Im(:,:,1)<Rg_max & Im(:,:,2)>Gg_min & Im(:,:,2)<Gg_max & Im(:,:,3)>Bg_min & Im(:,:,3)<Bg_max;

% Processing the image with different operations.
GARNET2 = bwmorph(GARNET,'clean');
GARNET3 = bwmorph(GARNET2,'hbreak');
GARNET4 = bwmorph(GARNET3,'majority');
GARNET5 = bwmorph(GARNET4,'spur');
GARNET7 = bwareaopen(GARNET5,5);
[G,numG] = bwlabel(GARNET7,4);

% Finding the white pixels in order to subtract the rim in the image.
WHITE = Im(:,:,1)==255 & Im(:,:,2)==255 & Im(:,:,3)==255;
[W,numW] = bwlabel(WHITE,4);
WHITE_size = NaN*ones(numW,1);
for i=1:numW
    WHITE_size(i) = sum(W(:)==i);
end

%Plotting the rutile grains on top of the thin section image, and add the
%percentage of rutile in the sample.
figure(1)
imshow(Im)
hold on
spy(RUTIL7,'b')
hold on
spy(GARNET7,'r')
Percent_rutile = (sum(RUTIL7(:))/(no_pixels-(max(WHITE_size))))*100;
Percent_garnet = (sum(GARNET7(:))/(no_pixels-(max(WHITE_size))))*100;
title(['Rutile(blue): ', sprintf('%0.2f', Percent_rutile), '% and Garnet(red): ', sprintf('%0.2f', Percent_garnet), '%']);

%Counting up the pixels in each of the rutile grains detected.
Rutile_size = NaN*ones(numR,1);
for i=1:numR
    Rutile_size(i) = sum(L(:)==i);
end

Garnet_size = NaN*ones(numG,1);
for i=1:numG
    Garnet_size(i) = sum(G(:)==i);
end

%Calculating the physical size of each rutile grain, based on the physical
%size of the thin section.
scale = (48*28)/no_pixels;
Rutile_size=Rutile_size*scale;
Garnet_size = Garnet_size*scale;

%Plotting a histogram containing the distribution of rutile grains of
%various sizes.
figure(2)
clf;
hist([Rutile_size]*1000000,1000)
xlabel('log um^2');
ylabel('# Grains');



## 6.2 Structural formula recalculation of garnet


% Give information about the molar weight, name of cation, number of
% cations in oxide, number of oxygen in oxide and charge of cations.
Weighth = [60.0843, 61.97894, 101.96128, 94.196, 56.0794, 71.8464, 70.9374, 151.9902, 79.8988, 40.3044, 159.6922];
Cation = ['sample', 'Si', 'Na', 'Al', 'K', 'Ca', 'Fe2+', 'Mn', 'Cr', 'Ti', 'Mg', 'Fe3+'];
N_Cat = [0,1,2,2,2,1,1,1,2,1,1,2];
N_Ox = [0,2,1,3,1,1,1,1,3,2,1,3];
Charge_cat = [0,4,1,3,1,2,2,2,3,4,2,3];

%Give information on the ideal number of cations and oxygens in structural
%formula.
Ideal_cat = 8;
Ideal_ox = 12;

%Load and prepare the raw data for processing.
A = dlmread('C:\Users\Stubbebryter\Desktop\Masteroppgave\Mikrosonde\Matlab-mat\garnets 240113.txt');
extra = zeros((size(A(:,1))));


```

```

Analysis = [A,extra];
An_number = Analysis(:,1);
%Create empty matrices for further use.
Result = zeros (length(An_number),11);
Result(:,1) = An_number;
Comp = zeros(length(An_number), 7);
Comp (:,1) = An_number;
Struc_form = zeros(length(An_number),10);
Struc_form(:,1) = An_number;
Triangular = zeros (length(An_number),4);
Triangular (:,1) = An_number;

%Run through the raw data and recalculate the structural formula.
for i = 1:length (An_number)

Mole_cat = N_Cat(2:12).*Analysis(i,2:12)./Weighth(2:12);
Sum_cat = sum(Mole_cat);
Charge_MC = sum(Charge_cat(2:12).*Mole_cat);
Mole_ox = N_Ox(2:12).*Analysis(i,2:12)./Weighth(2:12);
Charge_Mox = -2* sum(Mole_ox);
Norm_cat = Ideal_cat/Sum_cat .*Mole_cat;
Sum_Ncat = sum(Norm_cat);
Charge_NC = sum(Charge_cat(2:12).*Norm_cat);
Norm_ox = N_Ox(2:12)./N_Cat(2:12) .* Norm_cat;
Charge_NOX = -2*sum(Norm_ox);
Atom_units = Norm_cat;
%Make some Fe(2+) into Fe(3+) to achieve charge balance.
if 2*Ideal_ox - Charge_NC > 0
    Atom_units(11) = 2*Ideal_ox - Charge_NC;
    Atom_units (6) = Atom_units(6)- (2*Ideal_ox - Charge_NC);
else Atom_units (11) = 0;
end

%Sort the cations.
Result(i,2:12) = [Atom_units];
Struc_form(i,2:10) = [Atom_units(6), Atom_units(5), Atom_units(10), Atom_units(7), Atom_units(3), Atom_units(11), Atom_units(9), Atom_units(8), Atom_units(1)];

%Calculate the percentage of the end-members.
Sum_8 = Atom_units(5)+Atom_units(6)+Atom_units(7)+Atom_units(10);
Sum_6 = Atom_units(3)+Atom_units(8)+Atom_units(9)+Atom_units(11);

Almandine = 100 * Atom_units(6)/Sum_8;
Pyrope = 100 * Atom_units(10)/Sum_8;
Grossular = 100 * (Atom_units(3)/Sum_6) * (Atom_units(5)/Sum_8);
Spessartine = 100 * Atom_units(7)/Sum_8;
Uvarovite = 100 * Atom_units(8)/Sum_6 * Atom_units(5)/Sum_8;
Andradite = 100 * Atom_units(11)/Sum_8 * Atom_units(5)/Sum_6;
Ca_Ti_Garnet = 100 * Atom_units(9)/Sum_6 * Atom_units(5)/Sum_8;
Comp (i,2:8) = [Almandine,Pyrope,Grossular,Spessartine,Uvarovite,Andradite,Ca_Ti_Garnet];

%Calculate the three most common end-members for triangular plot.
Sum_comp = Almandine + Pyrope + Grossular;
Alm = (100/Sum_comp)*Almandine;
Pyr = (100/Sum_comp)*Pyrope;
Gross = (100/Sum_comp)*Grossular;
Triangular(i,2:4) = [Alm, Pyr, Gross];

end

Atom_units = [0,Atom_units];
Norm_ox = N_Ox./N_Cat .* Atom_units;

```

6.3 Structural formula recalculation of feldspar

```

% Give information about the molar weight, name of cation, number of
% cations in oxide, number of oxygen in oxide and charge of cations.
Weighth = [0 60.0843, 61.97894, 101.96128, 94.196, 56.0794, 71.8464, 70.9374, 151.9902, 79.8988, 40.3044, 159.6922];
Cation = ['sample', 'Si', 'Na', 'Al', 'K', 'Ca', 'Fe2+', 'Mn', 'Cr', 'Ti', 'Mg', 'Fe3+'];
N_Cat = [0,1,2,2,2,1,1,1,2,1,1,2];
N_Ox = [0,2,1,3,1,1,1,1,3,2,1,3];
Charge_cat = [0,4,1,3,1,2,2,2,3,4,2,3];
%Give information on the ideal number of cations and oxygens in structural
%formula.
Ideal_cat = 5;
Ideal_ox = 8;

```

```

%Load and prepare the raw data for processing.
A      = dlmread('C:\Users\Stubbebryter\Desktop\Masteroppgave\Mikrosonde\Matlab-mat\feldspar 041212.txt');
extra  = zeros((size(A(:,1))));
Analysis = [A,extra];
An_number = Analysis(:,1);
%Create empty matrices for further use.
Result  = zeros (length(An_number),11);
Result(:,1) = An_number;
Struc_form = zeros(length(An_number),12);
Struc_form(:,1) = An_number;
Triangular = zeros (length(An_number),4);
Triangular (:,1) = An_number;

%Run through the raw data and recalculate the structural formula.
for i = 1:length (An_number)

Mole_cat  = N_Cat(2:12).*Analysis(i,2:12)./Weigh(2:12);
Sum_cat   = sum(Mole_cat);
Charge_MC = sum(Charge_cat(2:12).*Mole_cat);
Mole_ox   = N_Ox(2:12).*Analysis(i,2:12)./Weigh(2:12);
Charge_Mox = -2* sum(Mole_ox);
Norm_cat  = Ideal_cat/Sum_cat .*Mole_cat;
Sum_Ncat  = sum(Norm_cat);
Charge_NC = sum(Charge_cat(2:12).*Norm_cat);
Norm_ox   = N_Ox(2:12)./N_Cat(2:12) .* Norm_cat;
Charge_NOX = -2*sum(Norm_ox);
Atom_units = Norm_cat;
%Make some Fe(2+) into Fe(3+) to achieve charge balance.
if 2*Ideal_ox - Charge_NC > 0
    Atom_units(11) = 2*Ideal_ox - Charge_NC;
    Atom_units (6) = Atom_units(6)- (2*Ideal_ox - Charge_NC);
else Atom_units (11) = 0;
end

Result(i,2:12) = [Atom_units];

%Calculate the percentage of the end-members.
S      = Atom_units(2)+ Atom_units(4) + Atom_units(5);
Anorthite = 100*Atom_units(5)/S;
Albite   = 100*Atom_units(2)/S;
Orthoclase = 100*((Atom_units(10)+ Atom_units(4))/S);
Triangular(i,2:4) = [Anorthite,Albite,Orthoclase];
end

Atom_units = [0,Atom_units];
Norm_ox   = N_Ox./N_Cat .* Atom_units;

```

6.4 Structural formula recalculation of mica

```

% Give information about the molar weight, name of cation, number of
% cations in oxide, number of oxygen in oxide and charge of cations.
Weighth  = [0 60.0843, 61.97894, 101.96128, 94.196, 56.0794, 71.8464, 70.9374, 151.9902, 79.8988, 40.3044];
Cation   = ['sample', 'Si', 'Na', 'Al', 'K', 'Ca', 'Fe2+', 'Mn', 'Cr', 'Ti', 'Mg'];
N_Cat    = [0,1,2,2,2,1,1,1,2,1,1];
N_Ox     = [0,2,1,3,1,1,1,1,3,2,1];
Charge_cat = [0,4,1,3,1,2,2,2,3,4,2];
%Give information on the ideal number of oxygens in structural
%formula.
Ideal_ox  = 15;
%Load and prepare the raw data for processing.
A      = dlmread('C:\Users\Stubbebryter\Desktop\Masteroppgave\Mikrosonde\Matlab-mat\mica 240113.txt');
Analysis = [A];
An_number = Analysis(:,1);
%Create empty matrices for further use.
Result  = zeros (length(An_number),11);
Result(:,1) = An_number;
Struc_form = zeros(length(An_number),11);
Struc_form(:,1) = An_number;

%Run through the raw data and recalculate the structural formula.
for i = 1:length (An_number)

Mole_units = Analysis(i,2:11)./Weighth(2:11);
Ox_units  = Mole_units.*N_Ox(2:11);
Charge_Mox = sum(Ox_units);
Norm_Ox   = (Ideal_ox/Charge_Mox) *Ox_units;

```

```

Num_Ox    = sum(Norm_Ox);
Atom_units = Norm_Ox.*N_Cat(2:11)./N_Ox(2:11);

Result(i,2:11) = [Atom_units];

end

Atom_units = [0,Atom_units];
Norm_ox   = N_Ox./N_Cat .* Atom_units;

6.5 Structural formula recalculation of clinopyroxene

% Give information about the molar weight, name of cation, number of
% cations in oxide, number of oxygen in oxide and charge of cations.
Weigth   = [0 60.0843, 61.97894, 101.96128, 94.196, 56.0794, 71.8464, 70.9374, 151.9902, 79.8988, 40.3044, 159.6922];
Cation   = ['sample', 'Si', 'Na', 'Al', 'K', 'Ca', 'Fe2+', 'Mn', 'Cr', 'Ti', 'Mg', 'Fe3+'];
N_Cat    = [0,1,2,2,2,1,1,1,2,1,1,2];
N_Ox     = [0,2,1,3,1,1,1,1,3,2,1,3];
Charge_cat = [0,4,1,3,1,2,2,2,3,4,2,3];
%Give information on the ideal number of cations and oxygens in structural
%formula.
Ideal_cat = 4;
Ideal_ox  = 6;
%Load and prepare the raw data for processing.
A       = dlmread('C:\Users\Stubbebryter\Desktop\Masteroppgave\Mikrosonde\Matlab-mat\pyroxenes 240113.txt');
extra   = zeros((size(A(:,1))));
Analysis = [A,extra];
An_number = Analysis(:,1);
%Create empty matrices for further use.
Result  = zeros (length(An_number),11);
Result(:,1) = An_number;
Struc_form = zeros(length(An_number),12);
Struc_form(:,1) = An_number;
Triangular = zeros (length(An_number),4);
Triangular (:,1) = An_number;

%Run through the raw data and recalculate the structural formula.
for i = 1:length (An_number)

Mole_cat  = N_Cat(2:12).*Analysis(i,2:12)./Weigth(2:12);
Sum_cat   = sum(Mole_cat);
Charge_MC = sum(Charge_cat(2:12).*Mole_cat);
Mole_ox   = N_Ox(2:12).*Analysis(i,2:12)./Weigth(2:12);
Charge_Mox = -2* sum(Mole_ox);
Norm_cat  = Ideal_cat/Sum_cat .*Mole_cat;
Sum_Ncat  = sum(Norm_cat);
Charge_NC = sum(Charge_cat(2:12).*Norm_cat);
Norm_ox   = N_Ox(2:12)./N_Cat(2:12) .* Norm_cat;
Charge_NOX = -2*sum(Norm_ox);
Atom_units = Norm_cat;
%Make some Fe(2+) into Fe(3+) to achieve charge balance.
if 2*Ideal_ox - Charge_NC > 0
    Atom_units(11) = 2*Ideal_ox - Charge_NC;
    Atom_units (6) = Atom_units(6)- (2*Ideal_ox - Charge_NC);
else Atom_units (11) = 0;
end

%Sort the cations.
Result(i,2:12) = [Atom_units];
Struc_form(i,2:12) = [Atom_units(2), Atom_units(4), Atom_units(5), Atom_units(10), Atom_units(3), Atom_units(11), Atom_units(6),
Atom_units(9), Atom_units(7), Atom_units(8), Atom_units(1)];

%Calculate the percentage of the end-members.
S      = Atom_units(11)+(Atom_units(2) - Atom_units(11)) + Atom_units(6)+ Atom_units(10);
Jadeite = 100*(Atom_units(2)-Atom_units(11))/S;
Aegerine = 100*Atom_units(11)/S;
DiHe   = 100*((Atom_units(10)+ Atom_units(6))/S);
Triangular(i,2:4) = [DiHe,Jadeite,Aegerine];
end

Atom_units = [0,Atom_units];
Norm_ox   = N_Ox./N_Cat .* Atom_units;

```

6.6 Structural formulae recalculation of amphibole

% Give information about the molar weight, name of cation, number of

```

% cations in oxide, number of oxygen in oxide and charge of cations.
Weighth = [0 60.0843, 61.97894, 101.96128, 94.196, 56.0794, 71.8464, 70.9374, 79.8988, 40.3044, 159.6922];
Cation = ['sample', 'Si', 'Na', 'Al', 'K', 'Ca', 'Fe2+', 'Mn', 'Ti', 'Mg'];
N_Cat = [0,1,2,2,2,1,1,1,1,1];
N_Ox = [0,2,1,3,1,1,1,1,2,1];
Charge_cat = [0,4,1,3,1,2,2,2,4,2]
% Give information on the ideal number of oxygens in structural
% formula.
Ideal_ox = 23;
% Load and prepare the raw data for processing.
A = dlmread('C:\Users\Stubbebryter\Desktop\Masteroppgave\Mikrosonde\Matlab-mat\Amphiboles 240113.txt');
Analysis = [A];
An_number = Analysis(:,1);
% Create empty matrix for further use.
Result = zeros(length(An_number),10);
Result(:,1) = An_number;

% Run through the raw data and recalculate the structural formula.
for i = 1:length (An_number)

Mole_units = Analysis(i,2:10)./Weighth(2:10);
Ox_units = Mole_units.*N_Ox(2:10);
Charge_Mox = sum(Ox_units);
Norm_Ox = (Ideal_ox/Charge_Mox) *Ox_units;
Num_Ox = sum(Norm_Ox);
Atom_units = Norm_Ox.*N_Cat(2:10)./N_Ox(2:10);

Result(i,2:10) = [Atom_units];

end

```

6.7 Structural formula recalculation of clinzozoisite

```

% Give information about the molar weight, name of cation, number of
% cations in oxide, number of oxygen in oxide and charge of cations.
Weighth = [0 60.0843, 61.97894, 101.96128, 94.196, 56.0794, 71.8464, 70.9374, 151.9902, 79.8988, 40.3044];
Cation = ['sample', 'Si', 'Na', 'Al', 'K', 'Ca', 'Fe3+', 'Mn', 'Cr', 'Ti', 'Mg',];
N_Cat = [0,1,2,2,2,1,1,1,2,1];
N_Ox = [0,2,1,3,1,1,1,1,3,2,1];
Charge_cat = [0,4,1,3,1,2,2,2,3,4,2];
% Give information on the ideal number of oxygens in structural
% formula.
Ideal_ox = 12.5;
% Load and prepare the raw data for processing.
A = dlmread('C:\Users\Stubbebryter\Desktop\Masteroppgave\Mikrosonde\Matlab-mat\epidotes 240113.txt');
extra = zeros((size(A(:,1))));
Analysis = [A,extra];
An_number = Analysis(:,1);
% Create empty matrices for further use.
Result = zeros(length(An_number),10);
Result(:,1) = An_number;
Struc_form = zeros(length(An_number),11);
Struc_form(:,1) = An_number;

% Run through the raw data and recalculate the structural formula.
for i = 1:length (An_number)

Mole_units = Analysis(i,2:11)./Weighth(2:11);
Mole_units(6) = Mole_units(6)/2;
Ox_units = Mole_units.*N_Ox(2:11);
Ox_units(6) = Ox_units(6)*3;
Sum_ox = sum(Ox_units);
Norm_ox = (Ideal_ox/Sum_ox).*Ox_units;
Atom_units = Norm_ox.*N_Cat(2:11)./N_Ox(2:11);
Atom_units(6) = Atom_units(6)/1.5;

% Sort the cations.
Result(i,2:11) = [Atom_units];
Struc_form(i,2:11) = [Atom_units(2), Atom_units(4), Atom_units(5), Atom_units(10), Atom_units(3), Atom_units(6), Atom_units(9),
Atom_units(7), Atom_units(8), Atom_units(1)];

end

Atom_units = [0,Atom_units];
Norm_ox = N_Ox./N_Cat .* Atom_units;

```

Appendix 7 – List of figures and tables

Figure 1 - Phase diagram showing the locations of the metamorphic facies (Winter, 2010).....	1
Figure 2 - Typical eclogite minerals from Engebøfjellet. Grain size in the rock is larger than in typical eclogite at Engebøfjellet. Hammer head as scale.....	2
Figure 3 - Helicopter view of Engebøfjellet (Korneliussen et al., 2007)	3
Figure 4 - Petrographic map of the coastal part of the WGR and the distribution of eclogites (Cuthbert et al., 2000)	4
Figure 5 - Map showing the direction of the subduction and exhumation during and after the Caledonian orogeny (Kylander-Clark et al., (2008).....	5
Figure 6 - Geological map of WGR with T-gradients and eclogite localities. Red dot marks Engebøfjellet. (Krabbendam and Dewey, 1998)	6
Figure 7 - Metamorphic overview of the WGR (Hacker et al, 2010).	7
Figure 8 - P-T path for several HP to UHP eclogites in the WGR (Hacker et al., 2010).....	7
Figure 9 - Geological map of the Førdefjord area (Korneliussen et al., 2001).....	8
Figure 10 - Simplified geological map of Engebøfjellet (Korneliussen et al., 2007)	9
Figure 11 - Illustration of the process from ionizing the atom to the emitting of a characteristic X-ray. (www.azom.com)	11
Figure 12 - Figure shows how Bragg's equation is fulfilled when positive interference occurs. (www.photonicmicrodevices.com)	12
Figure 13 - BSE image of partly altered rutile in amphibole from SK-7.	13
Figure 14 - The garnet and the three different rutile standards used in the classification.....	15
Figure 15 - Image showing how well the program detects rutile and garnet in SK-2.	16
Figure 16 - Example of how the program wrongly can classify rusty garnet and amphibole in sample SK-16 as rutile. Original thin section scan to left, and processed image to the right.	16
Figure 17 - Figure showing how pale thin sections can be problematic for identifying garnet correctly. Sample SK-20.....	16
Figure 18 - Output histogram of the grain size distribution in SK-19.....	17
Figure 19 - Air photo of Engebøfjellet shows how well exposed the rock is. (Photo from Norgeskart.no).....	18
Figure 20 - Geological map showing where the samples were collected (white dots). Map is from Korneliussen et al (1998).	19
Figure 21 - Eclogite facies vein in SK-28 containing omphacite.....	21
Figure 22 - Field image of the garnet veins.....	21
Figure 23 - Stereonet plot of the strikes of the garnet veins (Rick Allmendinger's Stereonet)	22
Figure 24 - Layer with large omphacite crystals in amphibole matrix.....	22
Figure 25 - A) Quartz, omphacite, rutile vein possibly developed in a pressure shadow between boudins (B).....	23
Figure 26 - 1 cm large rutile crystal in quartz vein. Notice the absence of alteration of the wall rock.	23
Figure 27 - Eclogite inclusion in quartz/mica vein. The eclogite behaved rigid during ductile deformation of the vein.	24
Figure 28 - quartz/mica vein developed in the flank of asymmetric fold.....	24
Figure 29 - Stereonet plot of the strikes of 7 quartz/mica veins (Rick Allmendinger's Stereonet)	25
Figure 30 - Rutile layering following the foliations in garnet rich zone of the eclogite.	25
Figure 31 - Outcrop from thin section of sample SK-20, showing part of a rutile layer in garnet rich eclogite.	25
Figure 32 - Stereonet plot showing orientation of 6 rutile veins. (Rick Allmendinger's Stereonet)	26
Figure 33 - A) Furrow found in the Engebøfjellet Eclogite due to weathering of late fractures. B) How the late fractures appear on unaltered surfaces. Hammer head as scale.....	26
Figure 34 - Later vein of considerably larger size than normal.	26
Figure 35 - Stereonet plot of A) Strike/dip of late veins and B) Strike directions of late veins. (Rick Allmendinger's Stereonet)	27
Figure 36 - BSE image from sample SK-28.....	35
Figure 37 - Figure showing difference in modal abundance of Omphacite and Amphibole. A is from SK-6, and B is from SK-28.....	35
Figure 38 - BSE image of ca. 1 mm Grt with several different inclusions. Sample SK-6.....	36
Figure 39 - A) Large Omp from SK-4. B) Matrix foliation developing Omp from SK-2.	36
Figure 40 - A) Matrix amphibole from SK-12. B) Porphyroblastic amphibole from SK-3.....	37
Figure 41 - BSE image showing late eclogitic amphibole after reaction of Grt and Omp.....	37
Figure 42 - Rutile cluster composed of several smaller rutile crystals from SK-29.....	37
Figure 43 - A) Elongated rutile in mylonitized samples (SK-30) and B) rounded rutile from less deformed sample (SK-8)....	37
Figure 44 - Rt - Grt corona in SK-16.	38
Figure 45 - BSE image showing symplectitic Amp and Ab from SK-29.	38
Figure 46 - Large symplectitic area from SK-27.....	38
Figure 47 - Micrometer scale symplectites around relict Omp and Amp from SK-4.....	39
Figure 48 - Relict Ph with symplectitic Bt+Pl corona from SK-28.	39
Figure 49 - A) Relict Rt with Ilm corona from alteration zone in SK-28. B) Alteration of Rt along fracture in SK-8.	39
Figure 50 - Section of SK-6 with fresh eclogite (left), Grt concentration (middle) and Qz+Grt vein (right).....	40
Figure 51 - Alteration of garnet to amphibole in quartz vein i SK-6.	40
Figure 52 - Garnets from SK-6.	40
Figure 53 - Triangular plot in the Alm-Pyr-Gro system.	41
Figure 54 - Chemical profile across 1 mm Grt from SK-6.	41
Figure 55 - Garnet from ME9.97-A showing strong Mn zoning.	41
Figure 56 - Mn map of 1 mm garnet from sample SK-6.	42
Figure 57 - Triangular plot of pyroxenes in the Jd-Aeg-Di+Hd system.....	43
Figure 58 - Chemical profile across large vein Omp in SK-28.....	44
Figure 59 - Triangular plot of Core, intermediate and rim of large vein Omp in SK-28.	44
Figure 60 - Image showing the visual difference in the vein Omp (SK-28) and matrix Omp (SK-7).	45
Figure 61 - Triangular plot of core of vein Omp (black squares) and matrix Omp (red squares) both from SK-28. Background points are from figure 59.....	45
Figure 62 - Figure showing the textural difference in porphyroblastic Amp (SK-3) and matrix Amp (SK-27). Amp(I) is the amphibole from reaction between Grt and Omp, while Amp (II) is the common matrix amphibole.	47
Figure 63 - Primary sodic-calcic amphiboles from the Engebøfjellet Eclogite (After Leake et al.1997). Arrows show trends from core to rim.	47
Figure 64 - Image showing how late amphiboles occur (SK-20).	49
Figure 65 - Zoning to, and secondary amphiboles from the Engebøfjellet Eclogite (After Leake et al 1997).	49
Figure 66 - Chemical profile across zoned primary Amp, cut by later vein causing development of a secondary amphibole (SK-28).	50
Figure 67 - Primary epidote within symplectite between Grt and Omp in SK-6.	50
Figure 68 - Carbonate clast in quartz+mica vein from the Vevring tunell.	52
Figure 69 - A) Large quartz from SK-4. B) Small quartz inclusion in SK-6.	52

Figure 70 - Quartz showing GBM in vein in SK-28.....	53
Figure 71 - Ab occurring in both vein and in symplectite in SK-20.	55
Figure 72 - Albite occurring close to contact between vein and wall rock in SK-28.	55
Figure 73 - Pyrite in SK-7 in reflected light.....	56
Figure 74 - Zircon inclusions in SK-2.....	56
Figure 75 - The fitted line from Hollands (1980) experiment on the Albite = Jadeite + Quartz reaction between 600 and 1200oC.....	63
Figure 76 - Phase diagram for the system Di - Jd - SiO ₂ for different molar concentrations of Jd in Omp (Gasparik & Linsley, 1980). Note the difference in axes from figure XX.....	63
Figure 77 - A) Triangle plot of the Grt analyses. B) Amount of the Grt within the red rectangle in A. Black circle marks compositional spread from point analyses (see section XX).....	65
Figure 78 - Zoning in Grt with respect to A) Mn, B) Mg and C) Ca.	65
Figure 79 - Profile from core to rim in Grt, with respect to A) MnO and B) MgO.	66
Figure 80 - 2D chemical plots of the Grt. A) XSpe-XPyr shows that relative to the XPyr, the XSpe is close to constant. B) XGro-XPyr shows that the negative correlation close to 1:1.	66
Figure 81 - A) Triangular plot in the XJd-XAcM-XDi+XHd system. Approximatley all points lie within the omphacite field, and red/blue dots represents point analyses (See section XX). B) Na map, showing the Omp as green/yellow.	67
Figure 82 - Mg distribution in the Omp.	67
Figure 83 - A) 2D chemical plot of XMg-Fe2+ in the Omp. B) One group is selected in each cluster. C) Image showing where the two clusters are located.....	67
Figure 84 - A) Si map showing Qz as red. B) Ca map over Amp. C) Na map showing zoning in Omp towards Amp.	68
Figure 85 - A) Development of Qz in the contact between Omp and Grt. B) Development of Amp in the contact between Omp and Grt.	68
Figure 86 - Distribution of Amp in the map from a Fe-map.....	68
Figure 87 - NaM4-XMg plot for amphiboles gives two clusters that according to B separates the matrix Amp from the inclusion Amp.....	69
Figure 88 - Ti map on the Amp. Grey fields are rutile.	69
Figure 89 - A) Shows where the profile is located. B) Distribution of Fe along the profile. C) Distribution of Mg along the profile.	69
Figure 90 - A) Points for Grt-Amp thermometry. B) Points for Grt-Cpx thermometry.	70
Figure 91 - Na map showing Garnet, Amphibole and Omphacite from sample ME 9.97-A.	74
Figure 92 - Large rutile crystals in Qz + Omp vein in the tunnel.	75
Figure 93 - Solubility of Ti from Rt in pure H ₂ O at 800oC at varying pressure (Antignano and Manning, 2008).	76
Figure 94 - Solubility of Ti from Rt at constant T and P with variable dissolved Ab (Antignano and Manning, 2008).	77
Figure 95 - Quartz vein cutting eclogite in the tunnel. Vein contains several larger rutile crystals.	77
Figure 96 - Hand specimen from SK-30. Sample appears to be amphibolite, but turned out to be fresh eclogite.	78
Figure 97 - Example on bad polishing of thins section from SK-6, Grt is ca. 0.5 mm across.	78
Figure 98 - Spread sheet for determining cation positions in amphiboles.....	133

Table 1-Overview of the deformation history at Engebøfjellet (After Korneliussen et al., 1998).	10
Table 2 - Table giving the weight of the samples used for XRD/XRF.	14
Table 3 - GPS coordinates for samples, with brief descriptions.	20
Table 4 - Bulk rock chemistry from XRF of 9 samples from the Engebøfjellet Eclogite.	27
Table 5 - Results from quantitative XRD of samples from the Engebøfjellet Eclogite. Quantification is done using a Rietveld method.	28
Table 6 - Selection of analyses of garnets from ferro- and leuco-eclogite.	42
Table 7 - Table with several Omp analyses from both ferro- and leuco-eclogite.	46
Table 8 - Analyses of amphiboles from ferro- and leuco-eclogite.	48
Table 9 - Table with analyses of epidotes from ferro- and leuco-eclogites at Engebøfjellet.	51
Table 10 - Chemical analyses of four rutile grains from the Engebøfjellet Eclogite.	51
Table 11 - Trace element analyses of rutile from Engebøfjellet, primarily of thermobarometric purposes.	52
Table 12 - Analyses of mica from the Engebøfjellet Eclogite.	54
Table 13 - Cpx-Grt thermometry on samples from Engebøfjellet after Ellis & Green (1979), Powell (1985) and Krogh Ravna (2000).	60
Table 14 - Grt-Amp thermometry on samples from Engebøfjellet. (After Graham & Powell (1984) and Krogh Ravna (2000).	61
Table 15 - Results from the zirconium-in-rutile geothermometer of Tomkins et al. (2007) applied on samples from the Engebøfjellet eclogite.	62
Table 16 - Results from calculating temperature. For Grt-Cpx both 10 kbar and 15 kbar is used.	70
Table 17 - Observed mineral reactions from eclogite facies to Amphibolite facies.	71
Table 18 - Amount of rutile in samples based on three different methods.	72
Table 19 - Ideal cations and oxygens used for mineral formulae recalculations.	131
Table 20 - Criteria used for end-member calculations.....	132